Universitat Autònoma de Barcelona

THREE-DIMENSIONAL ATLAS OF VASCULAR NETWORKS IN HUMAN GLIOBLASTOMA

George Paul Cribaro

THREE-DIMENSIONAL ATLAS OF VASCULAR NETWORKS IN HUMAN GLIOBLASTOMA

A doctoral dissertation presented

by

George Paul Cribaro

Submitted to the *Institut de Neurociències* in Partial Fulfillment
of the Requirements for the Degree of Doctor of Philosophy
at the *Universitat Autònoma de Barcelona*

Carlos Barcia González
Thesis Director

José Aguilera Ávila
Tutor

September 2018

DEDICATION

Perhaps more than anything else in life, a mother's presence defines us. Unfortunately, the primordial nature of that presence, like many other things in life, is only fully evident when it becomes an absence. I lovingly dedicate this thesis to my mother, who saw me through its conception but sadly will not enjoy the satisfaction of its fruition.

EPIGRAPH

Despacito y buena letra:

el hacer las cosas bien

importa más que el hacerlas.

- Antonio Machado

PROVERBIOS Y CANTARES
(Nuevas Canciones) (XXIV)

TABLE OF CONTENTS

LIST OF TABLES

LIST OF FIGURES

LIST OF APPENDICES

LIST OF ABBREVIATIONS

3D	three dimensional
ANOVA	analysis of variance
APC	antigen presenting cells
BBB	blood brain barrier
BMDC	bone marrow derived cells
BV	blood vessel
CD3	Cluster of differentiation 3
CSV	Comma separated values
DAPI	4,6-diamidino-2-phenylindole
DNA	deoxyribonucleic acid
EC	endothelial cell
EGFR	epidermal growth factor receptor
EORTC	European Organization for Research and Treatment of Cancer
EPC	endothelial precursor cell
GBM	glioblastoma multiforme
GFAP	glial fibrillary acidic protein
HLA-DP, DQ, DR	human leukocyte antigen complex – DP, DQ and DR isotypes
HS	horse serum
Iba-1	ionized calcium-binding adapter molecule 1
IDH	isocitrate dehydrogenase
IFP	interstitial fluid pressure
IHC	immunohistochemistry
KPS	Karnofsky performance status
LOH	loss of heterozygosity
MDM2	mouse double minute 2
MET	microentorno tumoral
MHCII	major histocompatibility complex class II
MMAT	microglia y macrófagos asociados a tumores
NCIC	National Cancer Institute of Canada
NOS	not otherwise specified
ns	not significant
NSC	neural stem cell
PCR	polymerase chain reaction
PECAM-1	platelet endothelial cell adhesion molecule-1
PSF	point spread function

PTEN	phosphatase and tensin homolog
ROI	region of interest
SAGE	serial analysis of gene expression
SEM	standard error of the mean
SVZ	subventricular zone
TABV	tumor-associated blood vessels
TAMM	tumor associated microglia/macrophages
TIL	tumor infiltrating lymphocyte
TME	tumor microenvironment
TMZ	temozolomide
VEGF	vascular endothelial growth factor
WHO	World Health Organization

ABSTRACT

Glioblastoma multiforme (GBM) presents activation of neuroinflammatory markers, which promotes local glial cell activation and monocyte and lymphocyte infiltration. This inflammatory activation and local angiogenesis are thought together to promote tumor growth, and this angiogenesis appears critical to tumor survival and propagation. Blood vessel networks are believed to act as paths for alternatively activated M2 macrophages and tumorigenic cells to enter naïve brain areas. GBM blood vessels show important morphological alterations yet the significance of these changes is poorly understood.

As such, revisiting the basic microarchitecture of glioma vasculature is opportune. Here, we analyze the microvasculature three-dimensionally (3D) in 60-μm thick, free-floating human biopsy tissue blocks, visualizing basement membrane and endothelial cell components and examining several tumor microenvironment (TME) populations. After immunohistochemical detection, samples were imaged in 3D with a laser scanning confocal microscope and the resulting 3D image stacks were analyzed with specialized software (Imaris and Fiji) to quantify relevant morpho- and topological parameters which were compared with normal tissue and correlated with tumor severity.

Our analysis shows evidence of profound basement membrane disruption, i.e. altered collagen IV deposition and consequent vessel wall discontinuity and CD31/collagen IV disassociation, resulting in blood vessels apparently without intact endothelial cell lining. Vessels seem clearly aberrant with larger, more variable diameters, uneven, irregular collagen IV distribution and vessel wall fenestration. We identified primary tumor vascularization patterns (cooption, looping, intussusception and silent corollary vessels) and predominant branching strategies. Our data confirms that the human glioma environment utilizes multiple vasculogenesis strategies and many tumor vasculature alterations correlate positively with increased tumor severity. We established that T cells increase in GBM conditions and may enter more deeply into the tumor with increasing severity, increased penetration correlating positively with vessel wall discontinuity. TAMMs increase with tumorigenicity; $MHCII^+$ and $GFAP^+$ cells occupy distinct TME niches.

We have developed a reliable and replicable sample immunostaining technique that preserves structural relationships, allowing us to study the glioma vasculature and MET cell populations and collect relevant data on spatial relationships. Such a deep analysis of human tissue is essential to understand brain diseases in their natural environment and to look beyond experimental models.

RESUMEN

El glioblastoma multiforme (GBM) presenta activación de marcadores neuroinflamatorios, que promueven la activación de las células gliales locales y la infiltración de monocitos y linfocitos. Esta activación inflamatoria y la angiogénesis local se considera que pueden promover el crecimiento del tumor conjuntamente, y la angiogénesis parece ser crítica para la supervivencia y propagación del tumor. Se cree que las redes de vasos sanguíneos actúan como vías para que los macrófagos M2 activados alternativamente y las células tumorigénicas entren en áreas cerebrales sanas. Los vasos sanguíneos en el GBM muestran notables alteraciones morfológicas, aunque la importancia de estos cambios aún no se comprende bien.

Como tal, es oportuno revisar la microarquitectura básica de la vasculatura del glioma. Aquí, analizamos la microvasculatura tridimensional (3D) en bloques de tejido de biopsias humanas de 60 μm de espesor y flotantes. Mediante inmunofluorescencia, visualizamos los componentes de la membrana basal y de las células endoteliales, examinando varias poblaciones del microambiente tumoral (MET). Después de la detección inmunohistoquímica, las muestras se visualizaron con un microscopio confocal de barrido láser y las imágenes 3D resultantes se analizaron con software especializado (Imaris y Fiji) para cuantificar los parámetros morfo- y topológicos relevantes. Posteriormente, estos parámetros se compararon con el tejido normal y se correlacionaron con la severidad del tumor.

Nuestro análisis muestra evidencia de una profunda alteración de la membrana basal, probablemente por una deposición alterada de colágeno IV y consecuentemente vemos discontinuidad de la pared del vaso y disociación de CD31/colágeno IV, resultando en vasos sanguíneos aparentemente sin revestimiento de células endoteliales. Los vasos tienen apariencia aberrante, con diámetros más grandes y variables, distribución desigual e irregular del colágeno IV y fenestración de la pared del vaso. Se identificaron patrones de vascularización tumoral primaria (cooptación, looping, intususcepción y vasos corolarios silenciosos) y estrategias de ramificación predominantes.

Nuestros datos confirman que el glioma humano utiliza múltiples estrategias de vasculogénesis, y muchas alteraciones de la vasculatura tumoral se correlacionan positivamente con la gravedad del tumor. Se estableció que las células T aumentan en el GBM y pueden entrar más profundamente en los tumores de mayor severidad. Además, una mayor penetración se correlaciona positivamente con una mayor discontinuidad de las paredes de los vasos sanguíneos. Los macrófagos y microglia también aumentan con la tumorigenicidad; y las células MHCII+ y GFAP+ ocupan nichos tumorales distintos.

Hemos desarrollado una técnica de inmunotinción de muestras fiable y replicable que preserva las relaciones estructurales, lo que nos permite estudiar la vasculatura del glioma y las poblaciones de células del MET y recopilar datos relevantes sobre las relaciones intercelulares en el espacio. Un análisis tan profundo del tejido humano es esencial para comprender las enfermedades cerebrales en su entorno natural y mirar más allá de los modelos experimentales.

ACKNOWLEDGEMENTS

Firstly, I would like to express my sincere gratitude to my thesis director Carlos Barcia for his continuous support of my PhD study and related research, for his patience, his motivation, his capacity to be critical and demanding without hurting and inspire a will to improve rather than a sense of defeat, and of course for his immense knowledge which he is always ready to share. He has stood by me throughout the long process of researching and writing this thesis and my good fortune in having him as advisor and mentor often felt equivalent to having won the lottery. I could not imagine having anyone better in this role.

Besides my director, I would like to thank my tutor, José Aguilera Ávila, and the members of my annual follow-up commission: Beatriz Almolda, Cristina Muñoz and Victor Yuste for their insightful comments and encouragement, but also for their hard questions which gave me incentive to widen my research from various perspectives and ultimately improve it.

I thank my fellow lab mates, Elena Saavedra, Paola Casanova, Meri Roig, Laura Díaz, Paola Heman, Alba Frías and Leire Romarate for the weekly lab meetings and all that those entailed, for sharing the anxieties of working under deadlines, for their collaboration on our joint article submissions, and for all the variety of experiences we have lived together over the past four years. I thank Elena for having accompanied me since the days of the Master at UAB and in particular for carrying a bit of my load at a crucial moment in helping with some necessary lab work and thus making my life infinitely easier.

Many thanks to Isabel Fernández and Vanessa Leo in the Neuroscience Department for their help and advice. I owe a deep debt and huge gratitude to Núria Barba in the Microscopy Core for her generous help and warm friendship. Saioa Mendizuri, Mar Castillo and Javier Carrasco have also been warmly supportive and encouraging and I appreciate their kind help. Naroa Mendizuri also generously aided me in performing some lab work vital to the thesis and in doing so saved me huge logistics problems in rearranging my work schedule, so for that I thank her.

I am deeply indebted to my former professors at UCLA, John Garcia and John Liebeskind, in whose labs I worked when I first became fascinated by neuroscience. It seems like a lifetime

ago, but their influence kindled a long-standing interest that finally comes somewhat full circle in this thesis.

I thank my friends at my day job, Anne Koski, Jonatan Rapaport, Barbara Befani and Diana Ramírez, for having patiently endured my ups and downs during the last four years and providing relief (sometimes comic), encouragement, support (and transportation) when needed.

Though unknown to me, I thank posthumously the nine patients whose devastating illness indirectly provided a means for me to study this lethal adversary and hopefully contribute towards advancing the knowledge that will one day give patients a better prognosis.

Finally, I would like to thank my family, my brothers and sisters for their life-long support, Sophie and her two beautiful daughters, Noha and Emma for their irreplaceable presence in my life and last but certainly not least, my sister Lynne for her unwavering help and generosity, not only while writing this thesis but throughout my life, I would not be who or where I am without her.

1 INTRODUCTION

1.1 Glioblastoma Multiforme - Historical Perspective

Although descriptions of primary brain tumors certainly pre-date Virchow, his description of these tumors in the mid-1800s marks an inflection point in the study of glioblastoma multiforme (GBM). Virchow not only first coined the name "glioma" but also initiated the combined micro- and macroscopic study of these tumors and his methods predominated for nearly a half a century. Early investigations led to numerous systems for classifying cerebral tumors but Bailey and Cushings' "*A Classification of the Tumors of the Glioma Group on Histogenetic Basis with Correlated Study of Prognosis*" (Bailey & Cushing, 1926) emerged as the most notable and durable. In fact, histological classification largely founded on the Bailey and Cushing schemata remains today the predominant means of categorizing tumors clinically.

Advances in the study of glioma also parallel developments in medical technique, as access to brain tissue is essential to its study, and until surgical and anesthetic techniques developed sufficiently, study of tumors was necessarily post mortem with tissue from autopsies. As intracranial surgery became possible after the innovative work of Godlee and Bennet in 1884 (Kirkpatrick, 1984), tumor tissue could be studied more thoroughly and also correlated with patient outcome.

The progressive improvement in surgical technique and ever evolving technical possibilities have been fundamental to glioma research over the last century. Diverse advances including electron microscopy, immunohistochemistry, DNA and chromosome analysis, polymerase chain reaction (PCR), serial analysis of gene expression (SAGE) and microarray technology applied to the study of glioma have all added multiple dimensions to characterizing glioma. For example, primary (de novo) and secondary (progressing from lower-grade astrocytoma) glioblastoma have been further subtyped by integrated genomic analysis as proneural, neural, classical or mesenchymal depending on particular molecular alterations (Agnihotri et al., 2013; Verhaak et al., 2010).

The 2016 World Health Organization (WHO) Classification of Tumors of the Central Nervous System (Louis et al., 2016) reflects the technological progress described above. As noted therein, for the past century, brain tumors have been categorized mainly according to histogenesis, i.e. according to microscopic similarities with distinct alleged cells of origin and their presumed degree of differentiation. Light microscopy of hematoxylin and eosin stained sections, immunohistochemical expression of lineage-associated proteins and ultrastructural

definition underlie this assumption of histological similarity. By including molecular parameters, the current classification scheme represents an important departure from the prevailing diagnostic principles based solely on microscopy. Under the 2016 classification system, glioblastoma is grouped as IDH-wildtype (isocitrate dehydrogenase) (approximately 90% of cases and most frequently corresponding to clinically defined de novo or primary GBM) and IDH-mutant (about 10% of cases and corresponding clinically to secondary GBM arising from lower grade glioma). Remaining instances not included in the above two categories because a full IDH evaluation was not possible are diagnosed NOS (not otherwise specified) (Cohen, Holmen, & Colman, 2013; Louis et al., 2016).

Yet despite the wealth of information from all these expanding possibilities for describing and categorizing GBM, one perspective that has perhaps been somewhat neglected is the in-depth morphometric study of GBM, visualizing tumors contextually and providing detailed physical characterizations of tumors and their components.

1.2 Pathological Features of GBM

GBM is a highly aggressive cerebral tumor whose effects are devastating. Its invasiveness and resistance to therapy make prognosis bleak and despite significant research advances, effective therapeutic options are limited. As the name "multiforme" implies, they are phenotypically diverse with varied gene expression and it is precisely this heterogeneity that at least partially accounts for the difficulties in characterizing tumors and in standardizing effective treatments. The most reliable prognostic indicators for GBM are extent of tumor resection, age at diagnosis and Karnofsky performance status (KPS) scale index (Bauchet et al., 2010; Lacroix et al., 2001). The KPS rates functional impairment on a scale from 0 to 100, 100 being perfect health and 0 being death. Treatment typically involves maximal surgical excision followed by combined radiation and chemotherapy with temozolomide (TMZ). A 2004 trial reported by the European Organization for Research and Treatment of Cancer (EORTC) in collaboration with the National Cancer Institute of Canada (NCIC) showed a survival advantage for GBM patients treated concurrently with temozolimide and post-surgical radiation (Stupp et al., 2005). At present this remains the standard for primary GBM treatment. Median patient survival is between 12 and 15 months after diagnosis (Wen & Kesari, 2008) and fewer than 5% of patients survive at five years post-diagnosis (Ostrom et al., 2014).

Glioblastoma is characteristically proliferative, highly invasive and resistant to apoptosis and shows extensive neovascularization (Stacey Watkins & Sontheimer, 2012) or new blood vessel (BV) growth, a process which is still poorly understood and actively under study. GBM contains both neoplastic and stromal tissue and shows hypercellularity, atypical nuclei, high mitotic activity, necrotic foci and necrotic palisades (Stacey Watkins & Sontheimer, 2012; Wen & Kesari, 2008), glomeruloid vessels (capillary tufts lined with hyperplastic endothelial cells) (Rojiani & Dorovini-Zis, 1996; Stacey Watkins & Sontheimer, 2012) and gemistocytic bodies (Kros, Schouten, Janssen, & van der Kwast, 1995) (astrocytic cells in pathological conditions characterized by voluminous, homogeneous, milky cytoplasm, fattened cell processes and an eccentric nucleus).

Genetic alterations are also thought to be involved, and EGFR (epidermal growth factor receptor) gene amplification and mutation; loss of heterozygosity (LOH) of chromosome 10q containing phosphatase and tensin homolog (PTEN); MDM2 (mouse double minute 2) overexpression; and p16 deletion are commonly associated with GBM (Agnihotri et al., 2013; Brennan et al., 2009; Wen & Kesari, 2008; Zhu & Parada, 2002).

While there is no consensus on the cellular origin of glioblastoma, prevailing opinion favors several alternatives. The first posits that mature glia dedifferentiate to acquire unregulated stem-cell-like properties by acquiring mutations or epigenetic lesions. According to the second, restricted neural progenitors, which have limited self-renewal potential, must acquire mutations that then lead them to gain unregulated stem-cell-like properties. A third alternative is that adult neural stem cells (NSCs), whose proliferative and differentiation potential is normally tightly regulated, acquire mutations which make them tumorigenic (Jiang & Uhrbom, 2012; Li, Wang, Eyler, Hjelmeland, & Rich, 2009; Sanai, Alvarez-Buylla, & Berger, 2005; Siebzehnrubl, Reynolds, Vescovi, Steindler, & Deleyrolle, 2011; Tabatabai & Weller, 2011). There is some evidence that astrocyte-like NSCs that carry driver mutations migrate from the subventricular zone (SVZ) to other brain regions where high-grade malignant gliomas then develop (Lee et al., 2018). In fact, proximity to or contact with the SVZ has been associated with negative prognostic implications (Adeberg et al., 2014; Jafri, Clarke, Weinberg, Barani, & Cha, 2013; Lim et al., 2007).

1.3 Tumor survival and invasion mechanisms - implications for cerebral vasculature

Whatever its origin, glioblastomas are the quintessential survivors and have highly effective mechanisms for surviving, diffusing and disabling immunological barriers to foster tumor growth and spread. One of the primary challenges developing GBM must overcome is to procure nutrients and oxygen once tumor size exceeds 1-2 mm in diameter (Carmeliet & Jain, 2000; Hillen & Griffioen, 2007). Once tumor size exceeds that limit, nutrient diffusion from the surrounding parenchyma is insufficient to maintain survival and growth so to meet increasing energy needs, gliomas stimulate the growth of new vasculature by interacting closely with their microenvironment.

It has long been postulated that GBM takes advantage of existing vascular networks or white matter tracts to migrate into the surrounding parenchyma (Montana & Sontheimer, 2011; Scherer, 1938; Stacey Watkins et al., 2014) where it commingles with native cells. The inability to remove all infiltrating tumor cells makes thorough surgical resection nearly impossible and is one of the principal causes for relapse (Cheng et al., 2011; Soda, Myskiw, Rommel, & Verma, 2013).

Normal cerebral vasculature comprises three cell types: endothelial cells, pericytes and astrocytes (see Figure 1). Pericytes embedded in the basement membrane make contact with endothelial cells while astrocyte end-feet make contact with the external basement membrane, all of which jointly constitute and support the blood brain barrier (BBB).

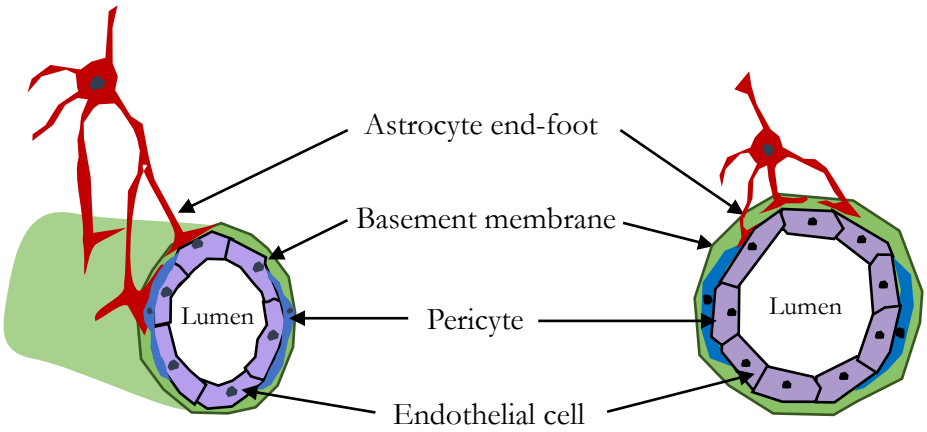

Figure 1. Healthy blood vessels have intact structure and help maintain the blood brain barrier. Schematic representation of normal relation of vascular cellular components showing basement membrane (green), astrocyte (red), pericytes (blue), nuclei (dark blue) and endothelial cells lining the lumen (light purple). Figure by author.

The glioma cell invasion process is believed to disrupt the intact BBB and render tight junctions more permeable, accounting along with highly expressed vascular endothelial growth factor (VEGF) (a major permeability and proangiogenic factor) for leakage of serum components into surrounding parenchyma (Abbott, Rönnbäck, & Hansson, 2006; Carmeliet & Jain, 2000; Dubois et al., 2014; Jain et al., 2007; Stacey Watkins et al., 2014).

A

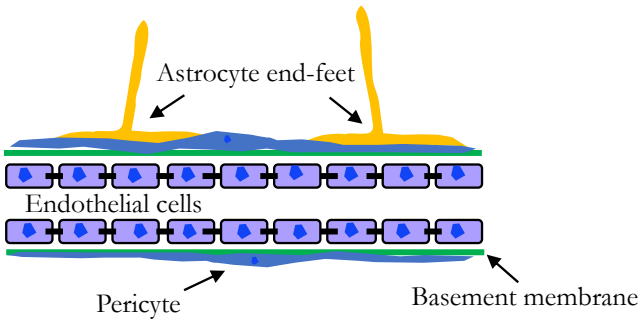

B

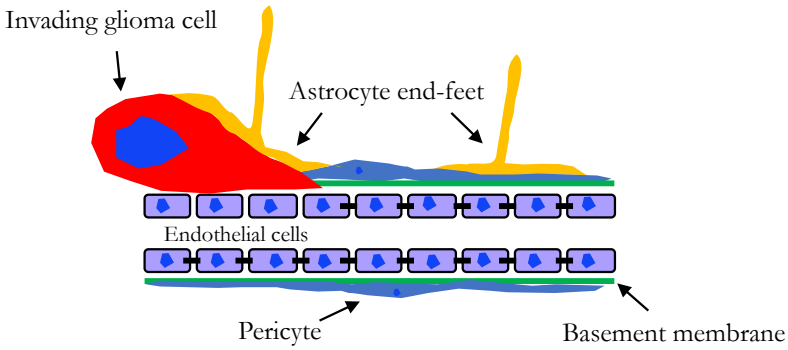

Figure 2. GBM invades healthy tissue along vessel walls. Schematic depiction of normal relation of vascular cellular components (**A**) and the tumor invasion process (**B**) whereby the tumor cell theoretically migrates along existing vessels, displacing astrocyte end feet, disrupting the tight junctions and finally leading to leakiness of the basement membrane. Basement membrane (green), astrocytes (orange), pericytes (light blue), tumor cell (red), nuclei (dark blue) and tight junctions (black dashes). Figure A by author and Figure B adapted from (Cuddapah, Robel, Watkins, & Sontheimer, 2014).

GBM is believed to interact with the existing vasculature in several ways. Murine studies have shown that tumor cells initially maneuver along white matter tracts or blood vessels (see Figure 2), in some cases losing up to one third of total cell volume to move in highly restricted interstitial spaces (S. Watkins & Sontheimer, 2011). This phenomenon has yet to be demonstrated in human tissue as it can only be studied using still images and not in vivo.

Studies with human glioma cells implanted in mice have shown that tumor cells can associate with all types and sizes of blood vessels but show a clear preference for smaller diameter

capillaries (Stacey Watkins et al., 2014). Invading glioma cells initiate a process whereby astrocyte end feet are displaced, disrupting the pericyte coverage and ultimately affecting tight junctions and basement membrane integrity. As a final stage in this cooption process, the perivascular glioma cells presumably assume control of vascular tone (Stacey Watkins et al., 2014).

After using pre-existing vasculature as a migratory pathway and coopting host vessels during initial growth, coopted vessels eventually die off and gliomas promote angiogenesis primarily by releasing VEGF at the borders of the tumor mass (Jain et al., 2007; Stacey Watkins et al., 2014). Recent studies suggest that tumor cells may even differentiate into blood-vessel-like endothelial cells thus also self-inducing de novo blood vessel growth (Wang et al., 2010; Stacey Watkins & Sontheimer, 2012).

1.4 Neovascularization in GBM

GBM is one of the most highly vascularized tumors known (Soda et al., 2013). Given the primordial importance of a continuous nutrient and oxygen supply to tumor survival and growth and given that neovascularization in its various manifestations is fundamental to maintaining this supply, the angiogenic process and the tumor microvasculature are central to understanding tumor biology.

After having reached a size at which the tumor's metabolic needs exceed the diffusion capacity for nutrients and oxygen, tumors switch to an angiogenic phenotype (Bergers & Benjamin, 2003; Carmeliet & Jain, 2000). Brain tumors rely primarily on four distinct mechanisms to generate new vasculature, 1) cooption-induced, 2) angiogenesis, 3) vasculogenesis and 4) intussusception (Carmeliet & Jain, 2000; Hillen & Griffioen, 2007; Jain et al., 2007; Soda et al., 2013). Complementary mechanisms include the recruitment of silent collateral vessels, transdifferentiation of tumor cells into endothelial cells (ECs) and vasculogenic mimicry (Y. S. Chen & Chen, 2014; Kreuger & Phillipson, 2016; Soda et al., 2011, 2013).

Cooption-induced neovascularization, as mentioned previously, is widely accepted as the process by which tumor cells initially populate brain parenchyma by navigating along BVs, displacing astrocyte feet and disrupting pericyte coverage which in turn is believed to affect BBB permeability (Carmeliet & Jain, 2000; Jain et al., 2007; Stacey Watkins et al., 2014; Holash et al., 1999). Continued tumor growth compresses vessels, causing constriction and reduced perfusion in turn leading to vessel degradation and tumor cell death. The resulting hypoxic

state contributes to the secretion of growth factors that initiate angiogenesis by tipping the balance between pro- and antiangiogenic factors in favor of angiogenesis, what is referred to as the "angiogenic switch". Figure 3 illustrates cooption-induced neovascularization.

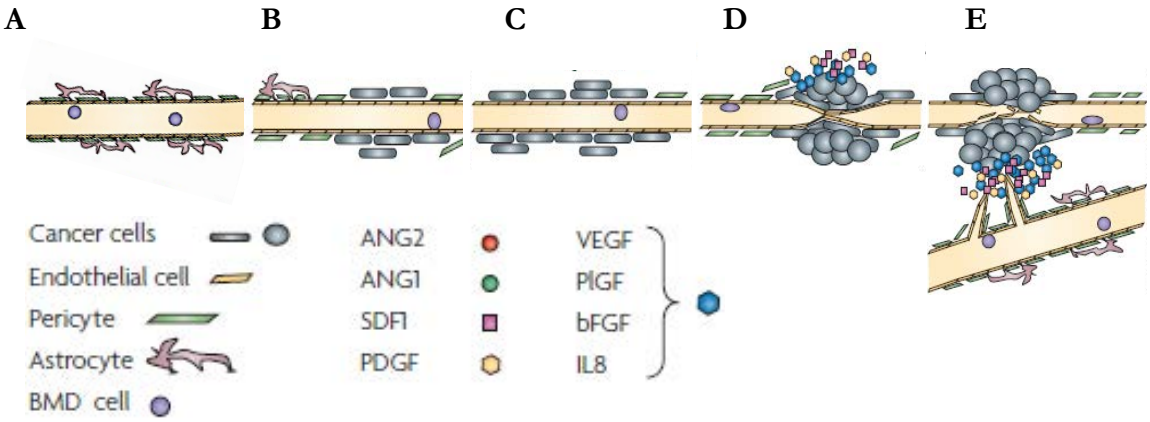

Figure 3. Tumor cells initially spread by migrating along and coopting preexisting blood vessels. Schematic representation showing a normal vessel (**A**), tumor cell invasion along the vessel and cooption (**B** and **C**), vessel compression and constriction as the tumor grows (**D**) leading to hypoxia which induces the release of growth factors and the resulting angiogenesis (**E**). Drawing adapted from Jain et al. (2007).

Standard **angiogenesis** is the process of new vessel formation by recruitment of circulating local endothelial precursor cells (EPCs) and their incorporation into newly formed vessels. Under normal circumstances there is a tightly-regulated balance between pro- and anti-angiogenic signals and new vessels develop rapidly and stabilize. On the contrary, in tumors the balance shifts in favor of pro-angiogenesis. This "angiogenic switch" derives from the nascent tumor's need for more copious blood supply and is induced by various factors including mutations in the cancer cells and the hypoxia resulting from tumor expansion by coopting vessels as described above (Bergers & Benjamin, 2003; Jain et al., 2007). A corollary to this distorted angiogenic balance is that tumor blood vessels are aberrant not only morphologically but also functionally, in terms of irregular blood flow and altered blood flow dynamics, and architecturally, with disrupted and disorganized capillary networks (Bergers & Benjamin, 2003; Carmeliet & Jain, 2000; Jain et al., 2007). This impairs blood delivery and has an impact on oxygen supply to the tumor which may exacerbate the hypoxia that in part led to proangiogenic signaling in the first place and induce further secretion of factors to help the tumor overcome the hypoxic conditions (Bergers & Benjamin, 2003; Maxwell, Pugh, & Ratcliffe, 2001).

Vasculogenesis describes new vessel formation by VEGF-recruited endothelial precursor cells from bone marrow (BMDCs) that can enter the blood circulation and differentiate and incorporate into tumor vessels (Duda et al., 2006; Hillen & Griffioen, 2007; Jain et al., 2007; Santarelli et al., 2006; Soda et al., 2013).

Intussusception (i.e. "growth within itself") is a process whereby preexisting vessels split into two new vessels by forming intraluminal pillars. The process comprises four distinct steps (see Figure 4): 1) opposing capillary walls protrude into the lumen and endothelial cells (ECs) make initial contact, 2) intercellular junctions are reorganized and the endothelial bilayer is perforated, 3) the interstitial pillar core forms and is populated by pericytes and myofibroblasts and 4) the pillar diameter increases and endothelial cells retract leading to the formation of two separate vessels (Hillen & Griffioen, 2007; Jain et al., 2007; Kurz, Burri, & Djonov, 2003). A distinct advantage of this angiogenic strategy is its rapidity (on the order of hours or even minutes), as it occurs without the need for endothelial cell proliferation (Hillen & Griffioen, 2007).

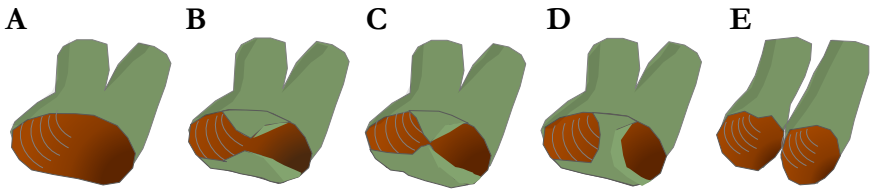

Figure 4. Intussusceptive angiogenesis is an efficient and rapid means of creating new blood vessels. The four basic stages of intussusceptive angiogenesis: (**A**) original vessel (**B** and **C**) opposing vessel walls protrude into the lumen and make contact, (**D**) intercellular junctions reorganize, the endothelial bilayer perforates and an interstitial pillar forms, (E) the pillar thickens, endothelial cells retract, and two separate vessels are formed. Drawing adapted from Kurz et al. (2003).

Alternative strategies

Additional angiogenic strategies include sprouting, looping and recruitment of silent collateral vessels (see Figure 5).

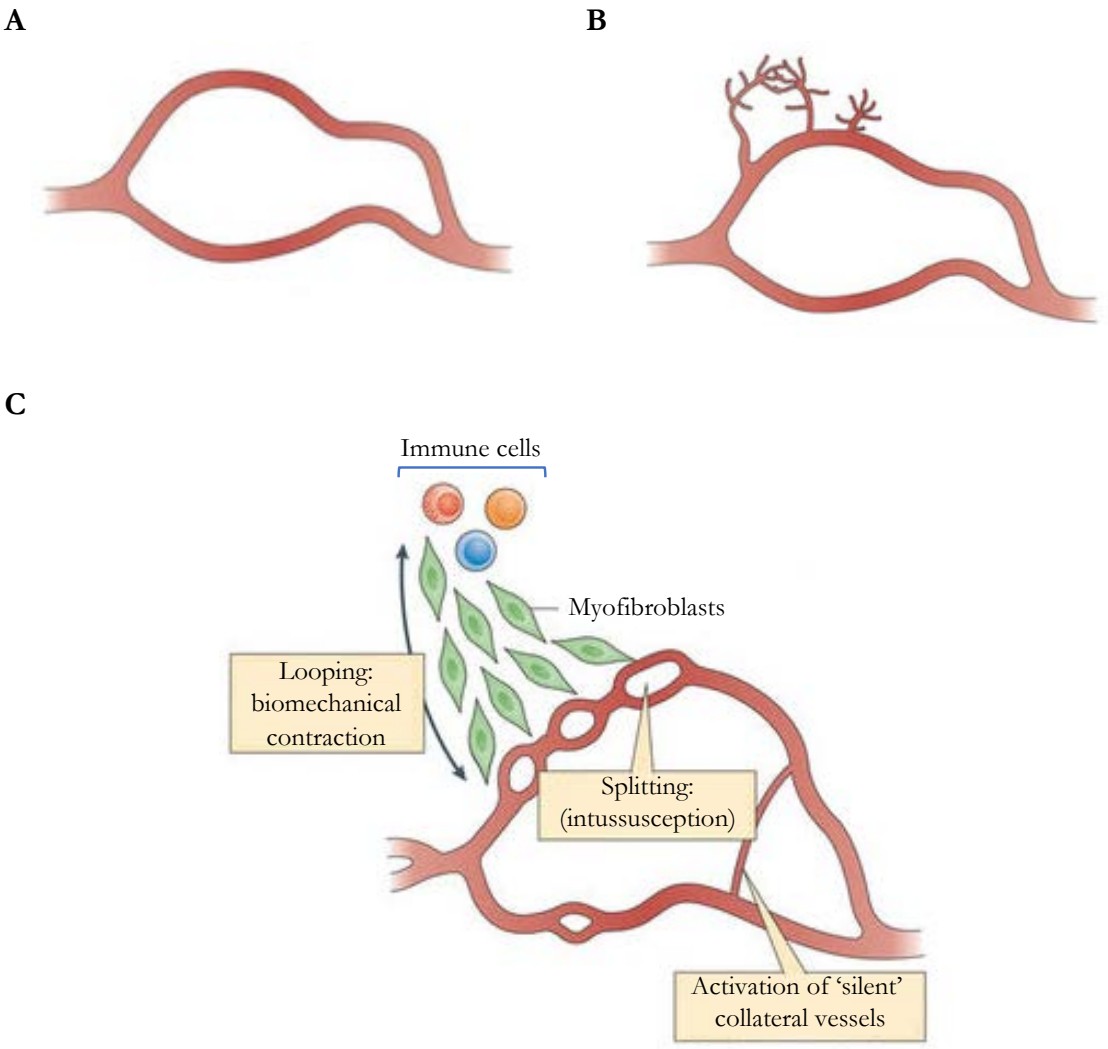

Figure 5. Alternative angiogenic strategies for creating new blood vessels add various tools for creating new blood supply to tumors. The figure depicts schematically a normal vascular bed (**A**), sprouting angiogenesis (**B**) and looping, splitting and recruitment of silent collateral vessels (**C**). Figure adapted from Kreuger & Phillipson (2016).

Other alternative strategies like vasculogenic mimicry and the transdifferentiation of tumor cells into endothelial cells (ECs) are worth mentioning in the context of tumor neovascularization, not only for their important contribution to the process but also to underline the complexity of the processes at work and the consequent difficulties in creating effective antiangiogenic therapeutic strategies when tumors have such wide options for evading and resisting therapies.

Vasculogenic mimicry describes the process by which tumor cells form de facto non-endothelial-cell-dependent vessel-like structures. First reported by Maniotis et al. in human melanoma (Maniotis et al., 1999), it has subsequently been reported in various cancer types,

which hypothetically include GBM (Y. Chen et al., 2012; Y. S. Chen & Chen, 2014; El Hallani et al., 2010; Qiao et al., 2015). Figure 6 shows a schematic representation of vascular mimicry.

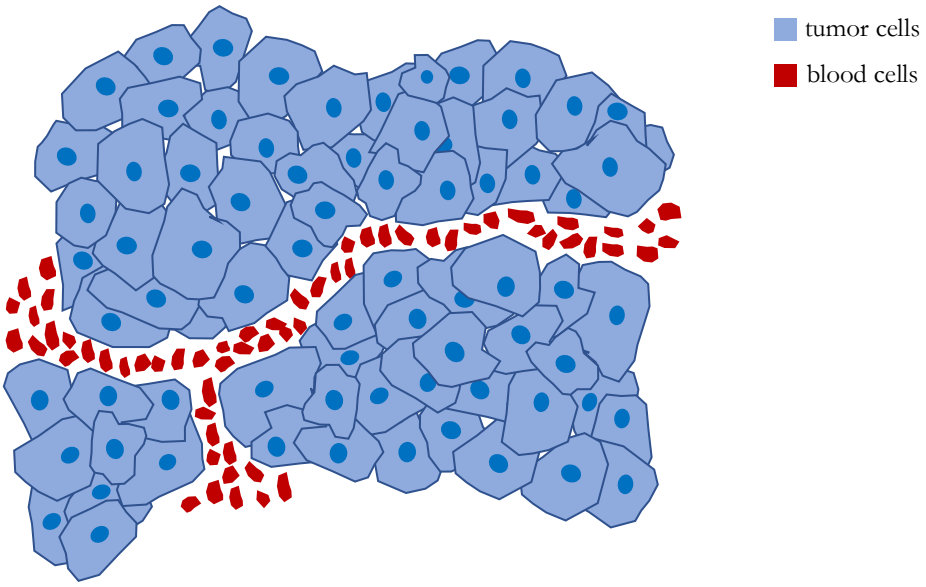

Figure 6. Tumors can form alternative circulatory systems in the absence of endothelial cells. In a process described as vasculogenic mimicry, melanoma cells have been observed to form networks of tubular structures lined with a layer of extracellular matrix instead of endothelial cells creating what is essentially an alternative non-endothelial derived circulatory system. This is well-characterized in melanoma cells and seen in other types of cancer, among which hypothetically is GBM. Drawing by author.

Transdifferentiation of tumor cells into endothelial cells is a recently described process by which the growing tumor itself provides cells for the de novo formation of blood vessels (Soda et al., 2011; Wang et al., 2010; Stacey Watkins & Sontheimer, 2012). While these studies in rodents indicate that GBM are highly versatile and suggest remarkable pluripotency of glioma cells, further study of the contribution of this process to neovascularization in human tumors is needed.

1.5 Neovascularization and hemodynamics

On the one hand, creation of new vasculature leads to increased overall vascularization in tumors but equally important is the quality of the newly created vessels and de novo vessels in GBM are widely believed to be aberrant (Hardee & Zagzag, 2012). What is essential in the context of this research is that BV morphology and integrity are also fundamental to hemodynamics. Though studying hemodynamics is not an objective of this research, nonetheless we postulated that any alterations in BV characteristics or structure may be accompanied by disrupted hemodynamics thus affecting nutrient and oxygen delivery to

tumors and in the case of chemotherapy, drug delivery. To understand this, a slight digression into some basic concepts is necessary to demonstrate how the parameters under investigation in this thesis are directly associated with physiologically effective fluid dynamics.

The most prominent principles applied to hemodynamics that are relevant here are Bernoulli's principle, Poiseuille's law, the Young–Laplace equation and Reynold's number. These concepts address the relationship between velocity and pressure, pressure gradients and changes, vessel wall characteristics and pressure and turbulent or laminar flow, respectively.

Blood flow velocity at each circulatory system level is determined mainly by the cross-sectional area of vessels at that level (Figure 7). Mathematically the relation is the following:

$$v = \frac{Q}{A}$$

where

v = velocity
Q = blood flow rate
A = cross sectional area

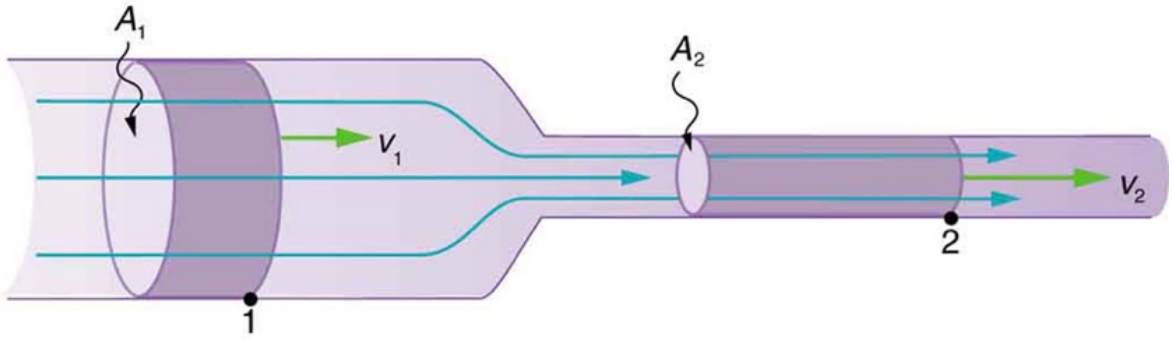

Figure 7. Flow velocity is related to cross-sectional area of blood vessels. This image shows a tube that narrows at one end and illustrates how the same volume occupies a greater length in the narrower portion than the wider one. For the same volume to pass points 1 and 2 in a given time, the velocity must be greater at point 2. Image from ©College Physics. OpenStax CNX. 6 August. 2018. Textbook content produced by OpenStax is licensed under a Creative Commons Attribution License 4.0 license.

Moreover, Bernoulli's principle states that flow velocity of a fluid is inversely proportional to pressure. Bernoulli's equation, valid at any arbitrary point along a streamline, is:

$$\frac{v^2}{2} + \frac{p}{\rho} + gz = constant$$

where:

v = velocity
g = acceleration due to gravity
z = elevation above a reference plane
p = pressure
ρ = fluid density

Relevant here is that velocity and pressure are inversely proportional, meaning that changes in cross-sectional area, which is dependent on vessel caliber, affect flow pressure. Figure 8 illustrates this relation.

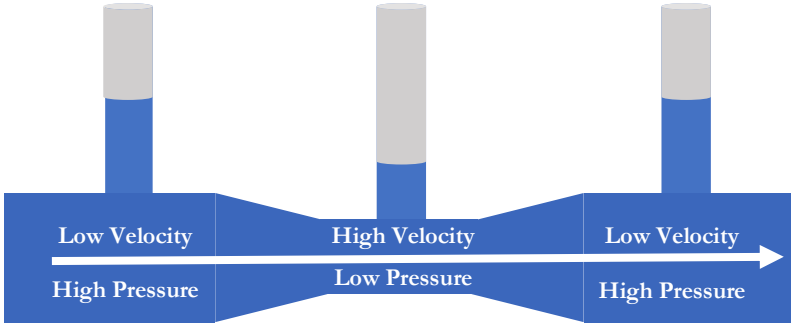

Figure 8. According to Bernoulli's principle higher velocity means lower pressure and vice versa. This image shows a tube that narrows in the middle and illustrates how fast-moving fluid generates low pressure and slow-moving fluid generates high pressure. Drawing by author.

Poiseuille's law states that flow rate is proportional to the radius to the fourth power. This assumes that the flow is laminar (smooth) through a tube of constant circular cross-section and substantially longer than its diameter. For velocities and pipe diameters above a certain threshold, actual fluid flow is not laminar but turbulent (chaotic) leading to larger pressure drops than calculated. The mathematical equation is the following:

$$Q = \frac{\Delta P \pi r^4}{8 \mu l}$$

where:

Q = blood flow rate
ΔP = pressure drop/gradient

r = radius of the vessel
μ = viscosity
l = length of tube

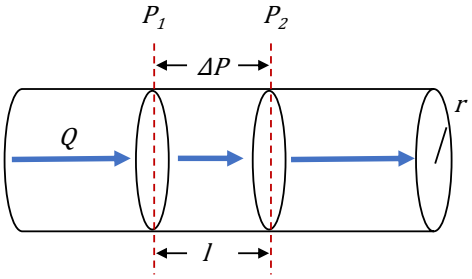

Figure 9. According to Poiseuille's law, flow rate is proportional to radius to the fourth power. Flow through a tube is dependent on the radius and small changes in vessel caliber could have profound effects on flow rate. Drawing by author.

The key point here is that a small increase in the internal diameter of a vessel yields a significant increase in fluid flow rate.

The Young–Laplace equation (Figure 10) relates pressure difference to the shape of the surface or wall and it is basic to the study of static capillary surfaces. Again, the key point here is that pressure differences are related to vessel wall thickness and vessel length and caliber.

A

$$\sigma_\theta = \frac{Pr}{t}$$

where

P = blood pressure
t = wall thickness
r = inside cylinder radius
σ_θ = cylinder stress

B

$$\sigma_\theta = \frac{F}{tl}$$

where

F = force exerted circumferentially on an area of the cylinder wall that has t and l as sides
t = radial thickness of cylinder
l = axial length of cylinder
σ_θ = cylinder stress

C

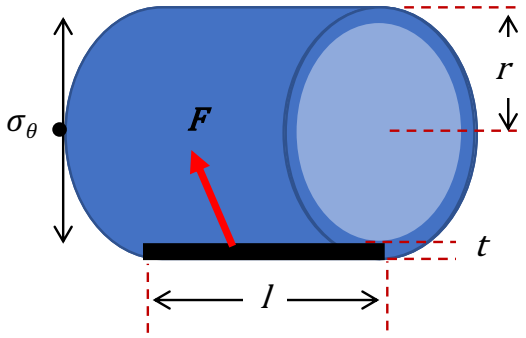

Figure 10. Young–Laplace equation relates pressure differences to vessel wall characteristics. Flow pressure (shown schematically in **C**) is dependent on vessel wall thickness, vessel radius and cylinder stress, a force component exerted circumferentially Cylinder stress referred to in equation **A** is the average force exerted circumferentially and is described in equation **B**. Drawing by author.

The Reynolds number (NR) is used in fluid mechanics to make predictions about different types of flow. The Reynold's number is directly proportional to the velocity and diameter of the vessel (tube). Lower Reynold's numbers indicate laminar flow (smooth constant fluid motion), whereas higher numbers indicate turbulent flow (chaotic, with eddies and other flow instabilities). The Reynolds number is defined as:

$$NR = \frac{\rho v L}{\mu}$$

where:

ρ = density of blood
v = mean velocity
l = characteristic dimension of vessel, in this case vessel diameter
μ = blood viscosity

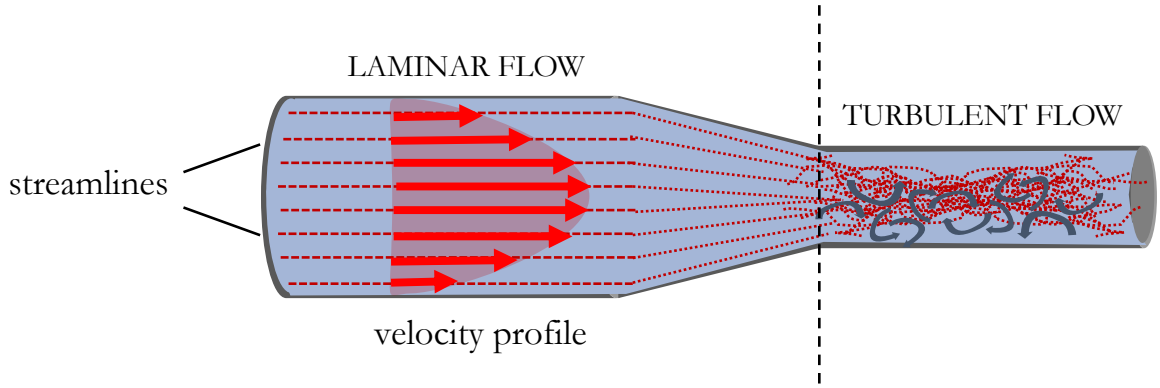

Figure 11. Reynold's number is a means of predicting certain flow characteristics such as whether flow is laminar or turbulent. Whether flow through a tube is laminar or turbulent is dependent on the radius. Generally speaking, a large diameter with rapid flow tends towards turbulence. Rapid changes in vessel diameter may lead to turbulent flow, as when a narrower vessel widens. Drawing by author.

To sum up, fundamental hemodynamic principles are integrally linked to vessel size (radius and length) and vessel wall integrity (cylinder stress) making the parameters that we are measuring here (see Sections 4.5 and 4.6) highly relevant to correct and effective vascular function.

1.6 Immunological Component of GBM

The immunological component is fundamental to the study of GBM, not only because immunotherapy is one of the most promising therapeutic strategies for fighting GBM but also because the mechanisms by which GBM defeats or usurps normal immune function is of vital interest. In fact, T cells are essential for effective antitumor response, but they may be particularly affected in GBM. T cell dysfunction in the form of senescence, ignorance, anergy, tolerance and exhaustion have been well-characterized and are hallmarks of GBM (Ausiello et al., 1991; Fecci et al., 2006; Mirzaei, Sarkar, & Yong, 2017; Woroniecka et al., 2018). Insufficient or ineffective immune response to GBM impedes halting tumor growth and spread and this could be due among other things to poor immune cell infiltration (Kmiecik et al., 2013) or to GBM's notorious capacity to subvert local and systemic immune responses (Dix, Brooks, Roszman, & Morford, 1999; Fecci, Heimberger, & Sampson, 2014). Although immunotherapy as treatment for GBM is encouraging, little is known about T cell location and niches in GBM. Careful study of T cell distribution in tumors and factors affecting leukocyte extravasation, or diapedesis, is particularly relevant to improving immunotherapies and elucidating how GBM manages to evade effective immune response.

Notwithstanding that microglial interactions with infiltrated T cells (Díaz et al., 2018) may partially explain why despite the increased presence of T cells in malignant areas, tumors still manage to thrive and spread, tumor-associated microglia/macrophages (TAMMs) crucial role in CNS immune response activation and wound healing is unquestionable. There is substantial evidence that TAMMs home to developing glioma and interact in a complex fashion with the TME to promote tumor growth in mouse models and human patients (Hambardzumyan, Gutmann, & Kettenmann, 2015). Activation of neuro-inflammatory markers is believed to promote local glial cell activation, in particular microglia, and monocyte and lymphocyte infiltration. Inflammatory activation is thought to be protumoral, aiding tumor cell proliferation and survival, promoting angiogenesis, impeding adaptive responses and modifying responses to therapeutic agents (Mantovani, Allavena, Sica, & Balkwill, 2008). Studies in rats indicate that microglia and other neuroglia like astrocytes are distributed in

extended, non-overlapping areas (Bushong, Martone, Jones, & Ellisman, 2002). TAMMs are intimately involved in the inflammatory response in GBM and the consequent molecular scenario that develops therefrom. Given the physical limits that the skull imposes, cerebral tumors are somewhat unique compared to other solid tumors and GBM has developed strategies to clear space for growth and propagation. Glioma have long been thought to be wounds that do not heal (Dvorak, 1986; Halliday & Holland, 2011). Some have even proposed that cerebral tumors be considered as a form of neurodegenerative disease in contrast to other solid tumors (Stacey Watkins & Sontheimer, 2012).

1.7 Thesis Research Implications and Rationale

Regardless that all of the research cited above implies highly significant advances in our understanding of gliomas, progress has been slow in prolonging life expectancy of patients and most characterizations represent a deconstructive or decontextualized approach to elucidating important facets of this formidable disease. At the diagnostic level, histological grading mainly derives from examination of paraffinized, 5-μm sections of tumor biopsy tissue and the detail of and relation to the surrounding parenchyma are largely lost. Moreover, given the essential nature of angiogenesis and tumor microvasculature to tumor survival, interestingly, studies specifically analyzing the vascular network in the human GBM scenario are rare.

As early as the 1940s, Scherer (Scherer, 1940) expressed frustration that tumor classification had somehow become an intellectual endeavor often based on unsubstantiated histogenetic schemata and somewhat divorced from anatomical and physiological reality, thus impelling him to undertake his broad whole-brain studies of tumors in their context. Understandably, there are many obstacles to studying tumor growth and angiogenesis in situ but that notwithstanding, there are compelling arguments in favor of evaluating and characterizing tumors in the context of the tumor microenvironment (TME) and surrounding parenchyma. The spatial limitations imposed by the enclosed area of the skull have ensured that gliomas have adapted by developing mechanisms to not only infiltrate the confined space but also to interact with the parenchyma to liberate space for expansion and coopt microvasculature as well as induce neovascularization to foster their growth. All these stratagems require an intimate and interactive relation with the TME and argue for studying gliomas in their biological context. The long trajectory of work by Rakesh Jain and colleagues has focused heavily on context in studying solid tumors, considering them not merely as a collection of

mutated cancer cells but rather as an intact organ comprising tumor cells and their stroma, the TME (Jain, 2013).

Molecular, immunological and genetic studies are rapidly defining and elucidating the TME from their respective viewpoints and contributing greatly towards developing more focused and effective therapies, however they do not offer much by way of characterizing and understanding tumor topography. Yet a precise knowledge of where target tumor cells are located can only aid in maximizing accurate delivery of novel anti-tumor immunotherapies or antiangiogenic therapies, consequently enhancing treatment efficacy. It may seem a formidable task to depict an idealized "generic" TME model because gliomas are extremely heterogenous and their microenvironments, highly individualized (Aum et al., 2014; Inda, Bonavia, & Seoane, 2014; Parker et al., 2016; Patel et al., 2014; Soeda et al., 2015). Nonetheless, by studying the morphology and topography of a large number of distinct samples, it may eventually be feasible to better understand how the various TME structures are related and mapped three-dimensionally in human glioblastoma. Interestingly, there are few in-depth morphological studies of human GBM and what is known has largely been gleaned from histological study of thin-section, paraffinized samples, which certainly cannot offer the same level of realism as our protocol for free-floating thick sections, visualized in three dimensions (3D).

Consequently, the tumor microvascular network and particularly the context in which GBM develops are a prominent focus of study for this thesis. Whatever other arguments can be made for studying GBM in its biological context, one of the central problems addressed by the research presented in this thesis is the flat-world approach characterized by many glioma studies. Diagnosis, for example, is predominantly made from thin-section (approximately 5 μm) biopsy samples which necessarily imposes a somewhat two-dimensional vision of glioma histopathology. Consider that looking at a blood vessel in a typical histopathological preparation gives the impression of seeing a doughnut-shaped object in two dimensions rather than a three-dimensional tubular structure. So, one of the main impulses behind this thesis research project is to characterize the GBM microvasculature and cell populations more realistically in 3D.

As a final consideration, many of the studies discussed in this thesis have employed mouse cancer models as a platform for mechanistic investigations of molecular or cellular players

involved in tumor angiogenesis so it is important to note that the results presented herein derive from careful analysis of human GBM samples.

At its core, this thesis describes research to explore the 3D morphometry and topographical organization of the human GBM microenvironment with particular emphasis on tumor microvasculature and the spatial distribution of prominent TME components. To achieve this objective, it was necessary to employ suitable tools for accurate imaging and careful analysis of the results. In the first place, creating convincing 3D renderings to visualize thick, extended areas of human GBM samples requires much thicker biopsy sections than are normally used for diagnostic purposes and working with this type of biological preparation carries inherent complications in handling the samples to maintain their structure intact without damaging them. Moreover, to visualize various structures simultaneously requires application of multiple antibody-fluorophore pairs. Commercial multiplex immunostaining procedures are available but typically require heat treatment of samples to strip them of antibodies between the sequential application of different fluorophores and the fragility of the free-floating sections used here makes this type of handling too aggressive and destructive (Coutu, Kokkaliaris, Kunz, & Schroeder, 2017). Obviously, to accurately characterize morphological features, it is imperative that the morphology of the tissue under study remain intact. The importance and difficulty of achieving a balance between sufficient and effective antibody penetration while maintaining structural integrity cannot be overemphasized. Hence, the first challenge was to develop and implement a multiplex immunostaining protocol which preserved the original morphometric characteristics of biopsy tissues and permitted accurate, realistic topographic analysis of GBM samples.

When imaging using multiple fluorophores, it is crucial that the laser emission spectra be sufficiently separate so as to avoid interference and bleeding of signals from one channel into the adjacent one. That along with the fact that the Zeiss LSM 700 (Carl Zeiss AG, Germany) confocal microscope used for image acquisition has four laser lines (405 nm, 488 nm, 555 nm and 639 nm) meant that only four maximum antibody-fluorophore combinations could be used at any one time. Because more than four structures were planned for study, the protocol had to be designed to use different combinations of antibody-fluorophore pairs that were derived from different species so that staining would be unique and separate for each structure. Image acquisition in itself did not present any particular technical problems but because the maximum depth possible was desired and considering the sample thickness, acquiring images comprising z-stack depths with 20-80 individual slices was time-consuming.

Additionally, because the highest detail possible was desired in the resulting images, once acquired each image was deblurred by deconvolution to remove artifacts introduced by the microscopy equipment in the image acquisition process.

Having obtained high quality multicolor confocal image stacks, several additional tools were required to quantify parameters of interest and to handle and analyze the large data sets generated. Specialized image analysis software was used to quantify some parameters and in other cases manual methods were employed using standard stereological techniques and criteria. Data was handled primarily using spreadsheets for recording raw data. To clean, sort and perform preliminary calculations on the data sets, individual data was read into MATLAB (MATLAB and Statistics Toolbox Release 2017b, The MathWorks, Inc., Natick, Massachusetts, United States.), a numerical computing environment with a proprietary programming language that allows matrix manipulations and plotting of functions and data among many other operations. Although many of the more straightforward data analyses and plotting were performed using GraphPad Prism version 6.00 for Mac (GraphPad Software, La Jolla California USA) or Microsoft® Excel for Mac version 16.10, some additional more complex analyses or specialized data plots were performed within MATLAB.

Finally, 3D isosurfaces for quantifying various parameters and measuring colocalization of certain structures were created using Imaris version 8.1 software and associated modules (Bitplane AG, Zurich, Switzerland). This software was also used to generate 3D projections and models of normal cortical tissue and GBM samples. Large-area hyperphotomosaics were either generated directly with a confocal microscope equipped with a motorized stage or were assembled using a Fiji (Schindelin et al., 2012) image stitching plugin (Preibisch, Saalfeld, & Tomancak, 2009) after acquiring a grid of overlapping images.

Comprehensive descriptions of the methods employed, including equipment, materials and software, and the results obtained with these tools are presented in the following sections.

2 OBJECTIVES

The principal objectives of this thesis are these:

1. Develop and optimize a multiplex immunostaining protocol for visualizing multiple structures in thick, free-floating, normal human cortical tissue and human GBM biopsy samples.
2. Topographic and morphometric evaluation and comparative analysis of microvasculature in normal human cortical tissue and GBM biopsy samples.
3. Comprehensive 3D morphometric rendering of vascular networks in microenvironments of glioblastoma samples.
4. Topographic evaluation and 3D rendering of astroglia-blood vessel interactions in distinct glioblastoma microenvironments.
5. Topographic evaluation and comparative analysis of distinct cell subpopulations including astroglia, microglia/macrophages, endothelial cells and T cells in normal human cortical tissue and GBM biopsy samples.

3 WORKFLOW

This workflow diagram provides an overview of the methodology employed in performing the research on which this thesis is based.

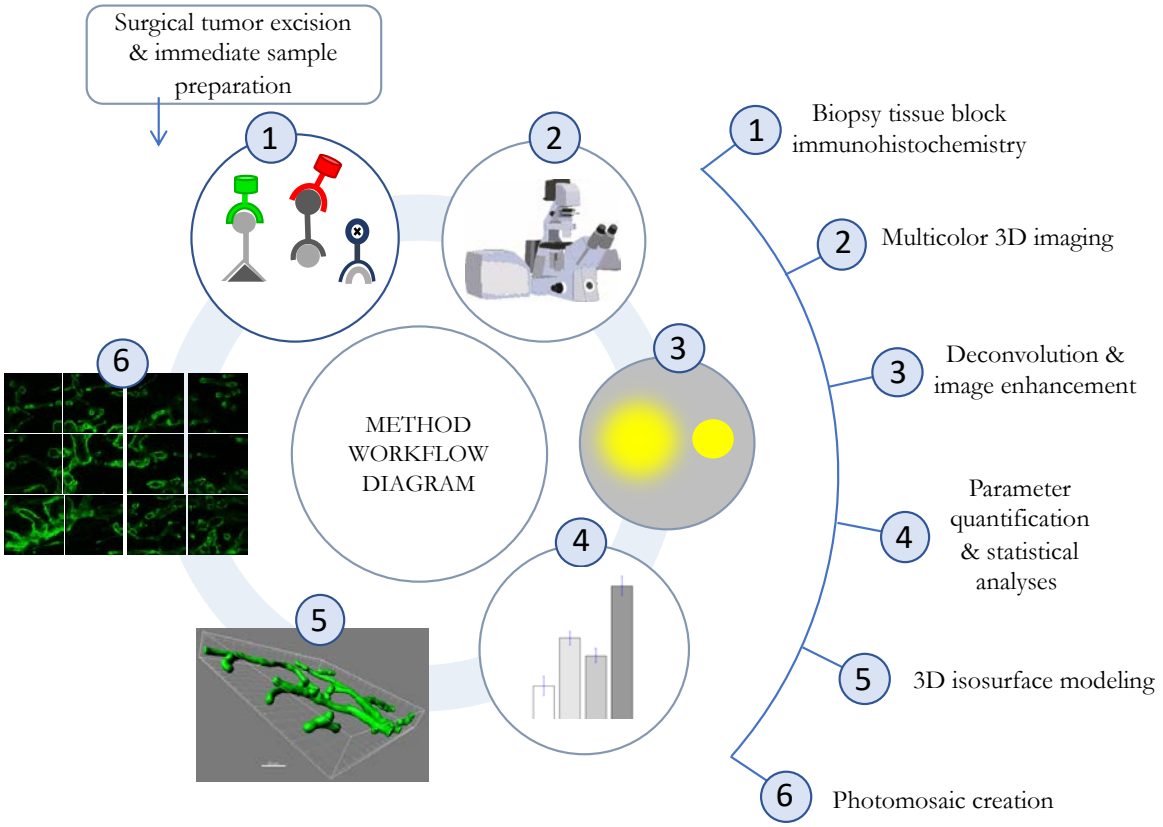

Figure 12. Schematic representation of methodology employed shows the complex series of processes involved in examining normal cortical and GBM samples. This diagram outlines the consecutive work stages which are described fully in the accompanying text. As will be seen in the sections that follow, the process is labor- and time-intensive.

4 MATERIALS AND METHODS

In order to bring the research described in this thesis to term, it was first necessary to overcome various technical challenges involving working with thick, free-floating tissue sections and applying multiple immunostains to each sample to mark the maximum possible number of structures. This section describes the immunostaining procedure developed to successfully carry out the objectives of this thesis and further describes measurement and quantification methodologies, image acquisition and processing techniques, 3D reconstruction of isosurfaces and the creation of large image mosaics. The full immunostaining protocol including an exhaustive list of reagents and preparation procedures is in Appendix 1.

4.1 Samples

Human glioblastoma samples were excised surgically at the General Hospital of Valencia (Spain). Tumors were excised and prepared following the protocol described in a previous publication and approved by the institutions involved (Barcia et al., 2009). It should be emphasized that tumors were excised and immediately fixed, cryo-protected and sectioned in a cryostat (Leica Microsystems, Wetzlar, Germany) thus preventing any significant tissue autolysis and preserving intact structure, an essential requirement for the type of analysis described herein. Tumors were graded in-hospital and the Ki-67 labeling index was assigned. All tumors studied and imaged as part of this thesis are grade IV glioblastoma with Ki67 indices ranging from 10 to 50% (see Table 1). In choosing the sample cohort size, we were less interested in power than in the level of detail required for the comprehensive analyses planned, a point which will be further addressed below (see Section 2.5 Limitations). Therefore, most comparisons are between normal tissue groups (N=5 or 6) and four or five tumor groups of different Ki67% indices (N=5 or 6, each).

Table 1. Detailed sample list

Sample no.	Lab reference no.	Glioma grade	Ki67 index (%)	Location
1	11	4	10	right temporal - frontal
2	2		20	right temporal - frontal
3	3.2			left frontal
4	3.4			left parietal
5	3.1		30	left temporal
6	3.6			left temporal
7	4			insular
8	12		50	right temporal - frontal

4.2 Immunohistochemistry

Box 1. Primary antibodies

Tissue target	Molecular target	Species	Manufacturer	Proportion
Basement membrane	Collagen IV	rabbit	Abcam, Cambridge, UK	1:200
Astrocyte, tumor cells	GFAP	mouse	Millipore, Temecula, CA, USA	1:500
		chicken	Abcam, Cambridge, UK	1:200
Endothelial cells	CD31	mouse	Abcam, Cambridge, UK	1:400
Antigen-presenting cells	HLA-DP, DQ, DR (MHCII)	mouse	Dako Cytomation; Glostrup, Denmark	1:100
T cells	CD3	rabbit	Dako Cytomation; Glostrup, Denmark	1:100
Microglia/macrophages	Iba-1	rabbit	Wako Pure Chemical Industries, Ltd.; Osaka, Japan	1:500

The 60-µm tumor sections were cut serially through the entire sample, and immunofluorescence was performed using various combinations of primary antibodies (see Box 1).

Secondary fluorescent antibodies (see Box 2) diluted in 1% HS were used accordingly with the host of the primary antibodies and 4,6-diamidino-2-phenylindole (DAPI) (1:1000, Invitrogen, Carlsbad, CA, USA) was used to stain nuclei. Immunohistochemical detection methods were previously optimized to achieve full and homogenous antibody penetration of the whole sections while substantially sparing tissue damage and keeping structural relationships intact, something absolutely critical to perform the analyses undertaken in this research.

Box 2. Secondary antibodies

Target	Species	Manufacturer	Proportion	Per mL
AlexaFluor® α-rabbit 488	goat	Invitrogen, Carlsbad, CA, USA	1:1000	1 µL
AlexaFluor® α-mouse 555	goat	Invitrogen, Carlsbad, CA, USA	1:500	2 µL
AlexaFluor® α-chicken 555	goat	Invitrogen, Carlsbad, CA, USA	1:500	2 µL
AlexaFluor® α-mouse 647	goat	Invitrogen, Carlsbad, CA, USA	1:500	2 µL

The full IHC protocol spans four days and comprises antigen retrieval in citrate buffer, blocking promiscuous binding sites with horse serum, marking target structures with a combination of primary and secondary antibodies and counterstaining nuclei with DAPI. Depending on the structures or cell types to be marked and bearing in mind the need to avoid duplicating antibody species in an individual multistaining procedure, the following antibody combinations were used:

1. Collagen IV-GFAP-CD31-DAPI
2. CD31-CD3-GFAP-DAPI
3. Collagen IV-MHCII-GFAP-DAPI
4. CD31-Iba1-GFAP-DAPI

Incubation for 48 hours with primary antibodies was followed by 24 hours of incubation with the appropriate secondary antibodies. After washing, sections were incubated with DAPI in solution for 30 minutes. The sections were washed again, mounted on non-gelatinized glass slides and cover-slipped with ProLong® Gold antifade (Invitrogen; Carlsbad, CA, USA) or Fluoprep reagent (bioMérieux SA, F-69280 Marcy l'Etoile, France) and once dry, examined by confocal microscope (Leica TCS SP5 or Zeiss LSM 700, at the Universidad Autónoma de Barcelona Microscopy Service and the Institut de Neurociències, respectively). Consult the supplementary material in Appendix 1 for the full immunofluorescence protocol.

4.3 Confocal Imaging

Images were acquired using a Zeiss LSM 700 laser scanning confocal microscope with four lasers lines (405 nm, 488 nm, 555 nm and 639 nm), three objectives (Plan-Apochromat 20x/0.8, Plan-Apochromat 40x/1.3 oil DIC and Plan-Apochromat 63x/1.4 oil DIC) and Zen image acquisition software (Carl Zeiss AG, Germany).

Images for large photo mosaics were acquired with a Leica TCS SP5 with a motorized stage, five laser lines (458, 476, 488, 496 and 514 nm), six objectives (Plan-Apochromat 10x/0.4 CS, Plan-Apochromat 20x/0.7 CS, Plan-Apochromat 40x/1.25-0.75 oil CS, Plan-Apochromat 63x/1.4-0.6 oil CS, Plan-Apochromat 63x/1.4-0.6 glycerol Corr CS and HC PL Fluorar 50x/0.80) and LAS AF software (Leica Microsystems CMS GmbH, Germany).

4.4 Image Processing

Deconvolution is an image processing technique to restore an object from an image that is degraded by blurring and noise, artifacts inherent to any image acquisition system. The degree of blurring of a single, sub-resolution point-like object is a measure of an optical system's quality and the blurred 3D image of this single point light source is known as the point spread function (PSF). Therefore, to counteract the effects of this blurring and to optimize image quality and subsequent quantifications, all images were processed using Huygens Professional image processing software package (Scientific Volume Imaging b.v., Hilversum, The Netherlands) or AutoQuant X3 image deconvolution software (Bitplane AG, Zurich, Switzerland).

Once images were processed to maximize quality, the relevant parameters were measured using Imaris 8.1 image visualization and analysis software (Bitplane AG, Zurich, Switzerland) or the Fiji (Schindelin et al., 2012) distribution of ImageJ (Rueden et al., 2017) software. Full descriptions of methodology and parameters studied are given in the subsequent sections.

4.5 Parameter Characterization and Quantification

The parameters measured included total cellularity; total units, surface area and volume of GFAP-positive astrocytes and tumor cells; total units, surface area and volume of type-IV collagen in basement membranes, blood vessel calibers; vessel branching types and totals; vessel wall continuity; total units, areas and volumes of CD31-positive endothelial cells; colocalization of CD31 and type-IV collagen; Iba-1-positive units, surface areas and volumes; and MHCII-positive units, surface areas and volumes and colocalization of MHCII and GFAP; and total T cells (expressing CD3) and their contact with or distance from blood vessels.

4.6 Quantification Methodologies

In line with the various research objectives of this thesis to closely examine the topographical and morphological relationships of human GBM microenvironment components and compare them across tumors with normal cortical tissue, we adopted the following strategy. First, we examined overall cellularity which is known to increase in GBM. We then centered on glial-lineage cells like astrocytes and tumor cells for which we measured GFAP expression in total area, volume and units. Next, given the fundamental role of vascular networks in

GBM, we performed a detailed analysis of BVs including type-IV collagen surface areas and volumes, vessel diameters, branching, vessel wall integrity, CD31 surface areas and volumes and the colocalization of collagen IV and CD31. Microglia and macrophage populations were then examined for which we measured Iba-1 and MHCII expression as total areas, volumes and units as well as interaction of MHCII with GFAP. Total T cells were counted, and T cell distribution was calculated as contact with or distance from nearest BVs. As a final component of our overall strategy, individual parameters were analyzed statistically, and Pearson correlation coefficients were calculated comparing individual parameters among themselves. Details of each step in this strategy are presented in the following sections.

4.6.1 Cellularity

Dense cellularity is characteristic of gliomas and measuring this parameter in the current context served a two-fold purpose: to corroborate the Ki67% indices assigned to the tumors when excised and, depending on the concordance of our cell counts with the hospital-designated Ki67% index, to indirectly validate our staining procedure. It also allowed us to examine how total cell count varied with the Ki67% index and other parameters. The Imaris software "Spots" module was used to generate spherical isosurfaces coinciding with DAPI-stained nuclei in each sample to estimate the total number of cells (see Figure 13).

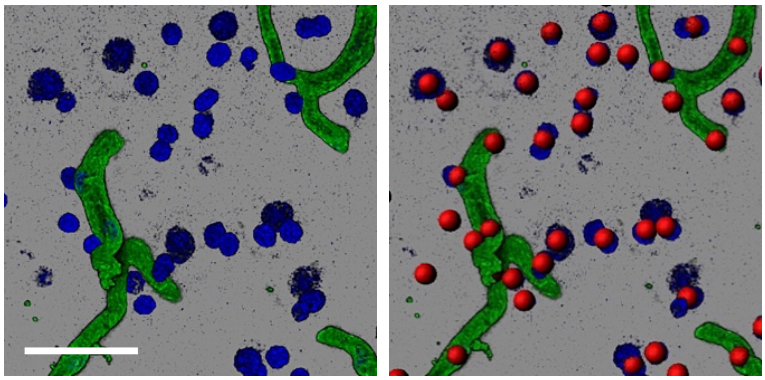

Figure 13. Imaris' "Spots" module used to count DAPI-stained nuclei in confocal images. Two confocal microphotographs of normal cortical tissue exported from Imaris software in a blend view. The image on the left shows blood vessels (green) and nuclei (blue). The image on the right shows the same superimposing the spots (red) generated by Imaris' "Spots" module. Note that not all nuclei coincide with a red spot in the image, i.e. some spots are masked because they are in a lower Z-plane in the original confocal stack. Scale bar 50 μm. Photos by author.

4.6.2 GFAP area and density

Glial fibrillary acidic protein (GFAP) is a member of the cytoskeletal protein family and is widely expressed in astroglial cells and in neural stem cells and also expressed in astroglial tumors, such as astrocytoma and GBM (Doetsch, 2003; Eng, Vanderhaeghen, Bignami, & Gerstl, 1971; Jung et al., 2007). GFAP surface area, units and volume were measured in confocal images by importing them into Bitplane's Imaris software and creating 3D isosurfaces (see Figure 14) using the "Surfaces" module.

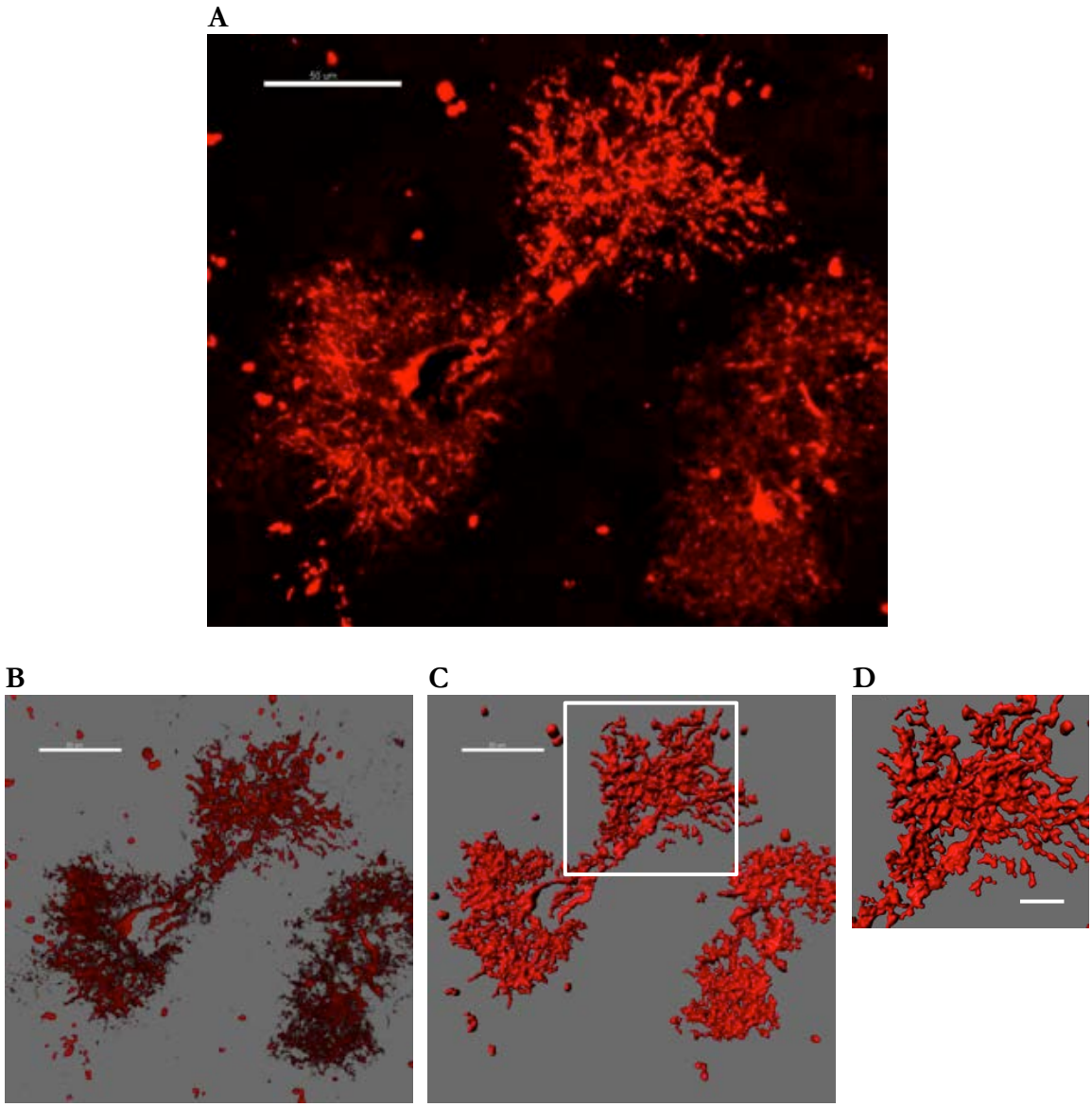

Figure 14. Creating 3D isosurfaces of GFAP-positive cells. Photo **A** is a maximum intensity projection of the red (GFAP) channel from a confocal image stack showing GFAP-positive protoplasmic astrocytes in normal cortical tissue. Photo **B** is a blend view of the same image and **C** is a 3D isosurface showing the reconstruction of the same area. Photo **D** on the right details the form of a single astrocyte. Scale bar A-C, 50 μm and D, 20 μm. Photos by author.

4.6.3 Collagen IV area and density

Type-IV collagen is an integral component of blood vessel basement membranes and a reliable marker for blood vessels in tissue. Assuming that increased vascularization necessarily implies increased collagen IV, we quantified the amount of collagen IV in confocal images by importing them into Imaris and creating 3D isosurfaces (see Figure 15) using the "Surfaces" module. Statistics for total area, total volume and total units were generated by the program and exported as CSV files for calculations and statistical analysis.

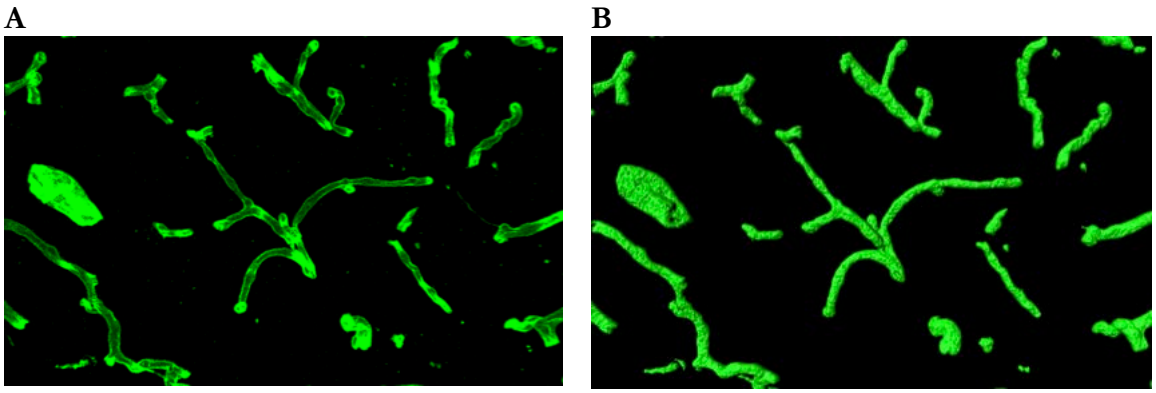

Figure 15. Replicating BVs to calculate surface areas and volumes by creating 3D isosurfaces of collagen-IV-positive basement membranes. Two images showing type-IV collagen (green) in basement membranes of normal cortical tissue in a confocal microphotograph (**A**) and a 3D reconstruction (**B**) of the same vessels. Scale bar 50 μm. Photos by author.

4.6.4 Vessel Diameter

To assess vessel diameters, confocal images were imported into Imaris and the measurement points tool was used to measure the widths of all visible vessels in each image (see Figures 16 and 17). Measurement data was exported to a CSV file to later calculate statistical parameters in MATLAB.

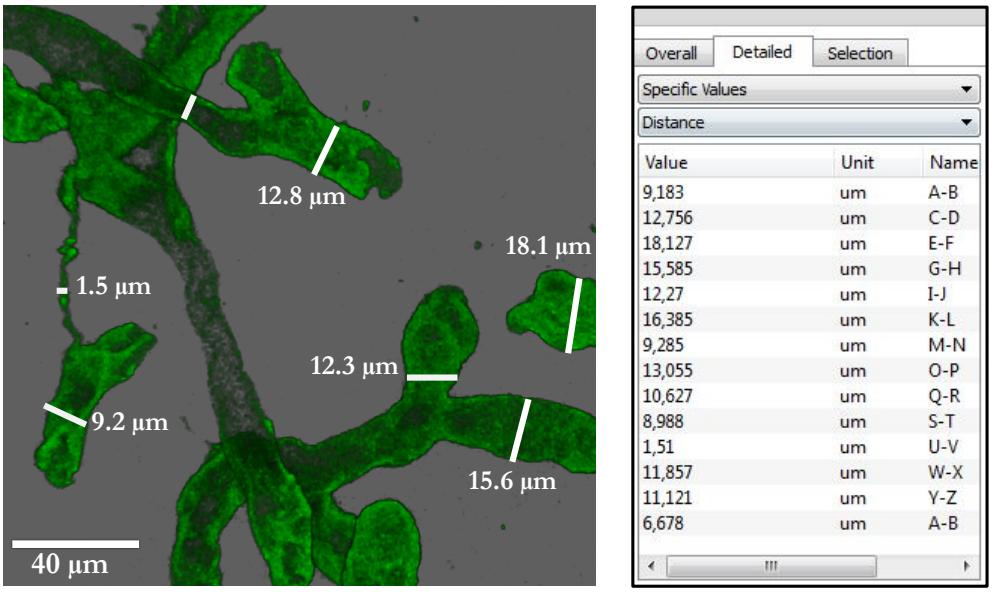

Figure 16. Imaris' "Measurement Points" tool used to measure blood vessel diameters in confocal images and generate values for calculations. The image on the left shows blood vessels (green) in a blend view of a confocal microphotograph. Using the measurement tool, diameters of each vessel (and different diameters of single vessels) are measured. The image on the right shows a list of point pairs and the corresponding diameters. Photo by author.

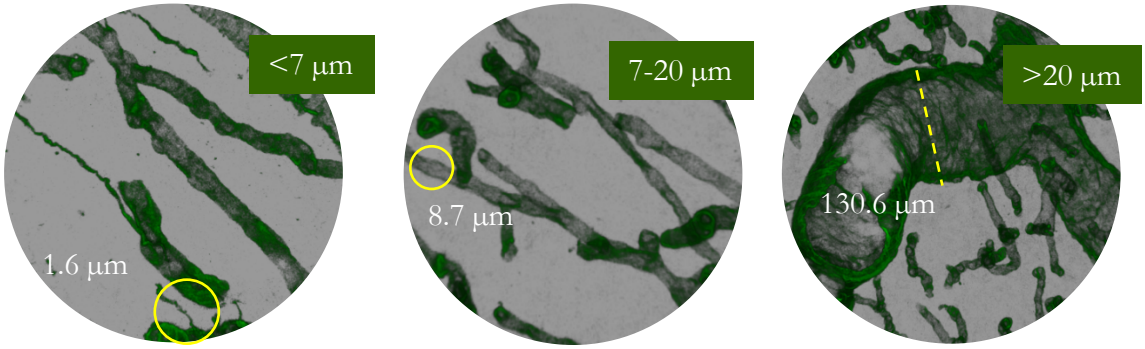

Figure 17. Vessel sizes vary greatly from silent collateral vessels to large, often deformed GBM vessels. The images above show several examples of blood vessels (green) in a blend view of a confocal micro-photograph. Sizes vary from small "silent" collateral vessels of approximately 5-7 µm (diameter insufficient to accommodate cell passage) to much larger vessels. Photos by author.

4.6.5 Branching

To quantify and categorize branching, vessel ramifications were divided into single and multiple branching types (see Figure 18), the former simple bifurcations and the latter more complex, multi-branching with two or more ramifications. Confocal images were imported into the Fiji distribution (Schindelin et al., 2012) of ImageJ (Rueden et al., 2017) software and the total single and multiple branches in each image were counted manually. Figure 19 shows a selection of different branching examples.

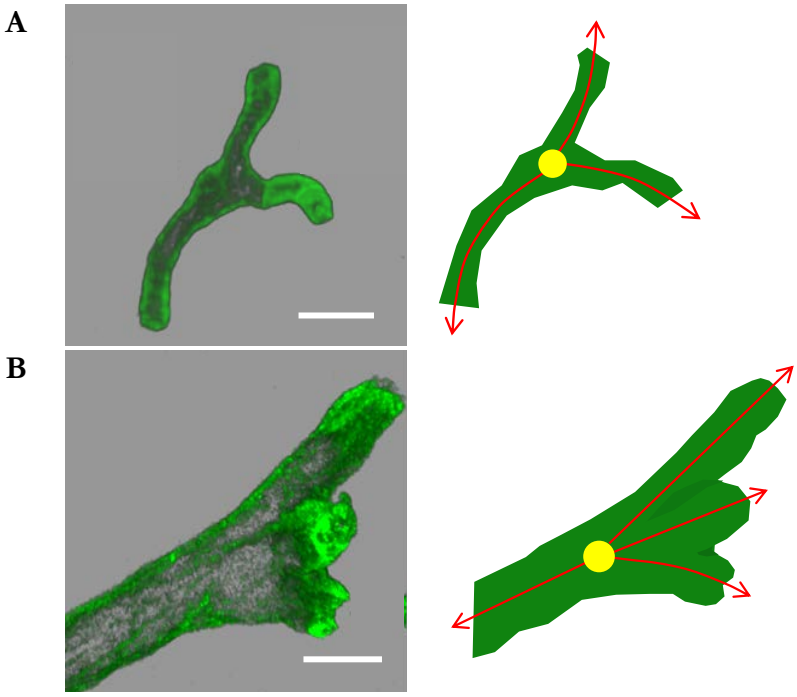

Figure 18. Vessels show great variety in branching but can be classified as having single or multiple ramifications to simplify calculations. Branches were divided into simple bifurcations (**A** - single) or those with two or more ramifications (**B** - multiple). Scale bar upper figure 15 μm and lower figure 30 μm. Drawings and photos by author.

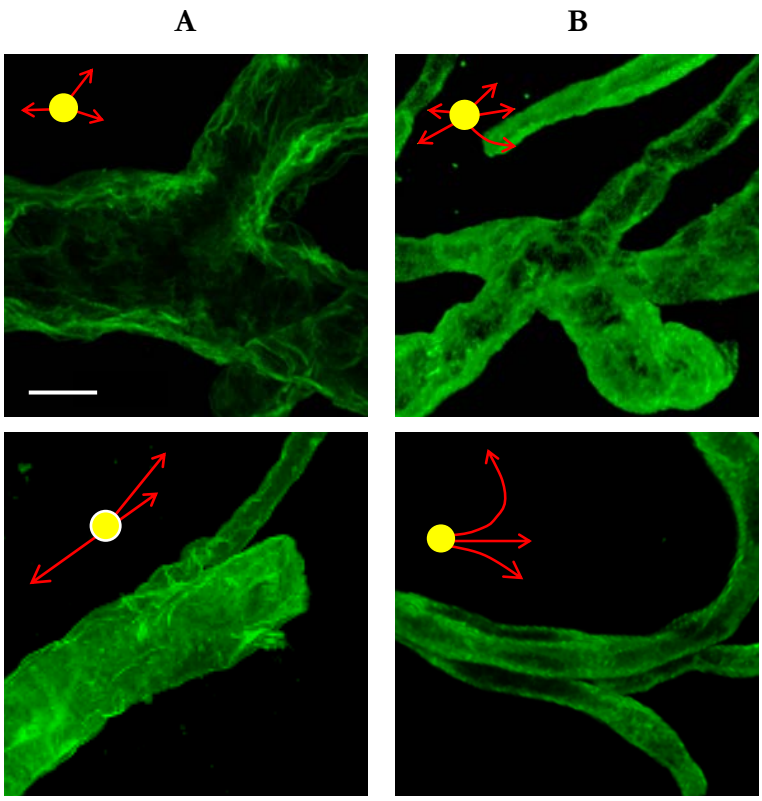

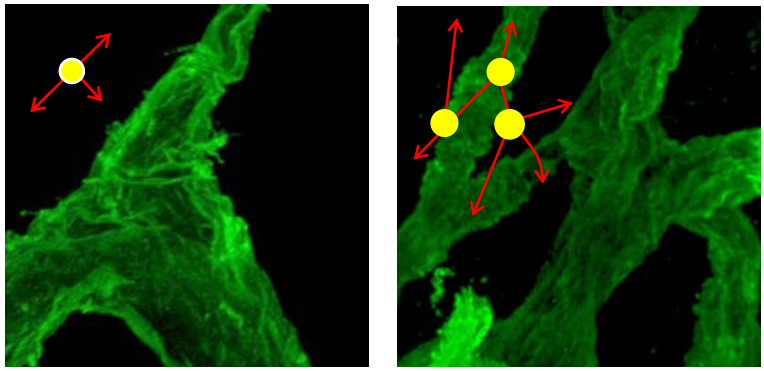

Figure 19. Branching is highly diverse even in normal cortical tissue but particularly in GBM vascular networks. Branches exhibit a wide range of variations as seen in the above confocal microphotographs. Column **A**, single branches; column **B**, multiple branches. Photos by author. Scale bar 10 μm.

Initially, we attempted to count and categorize branching using the Imaris "Filament Tracer" tool (see Figure 20) but most of the GBM images were so complex that the program could not generate accurate replicas of the vessel structure and branching points. As a result, using Imaris to recreate filaments and count branching points was ruled out and branching points were counted manually using stereological techniques (Nyengaard, Bendtsen, & Gundersen, 1988) and the Fiji implementation of ImageJ.

A

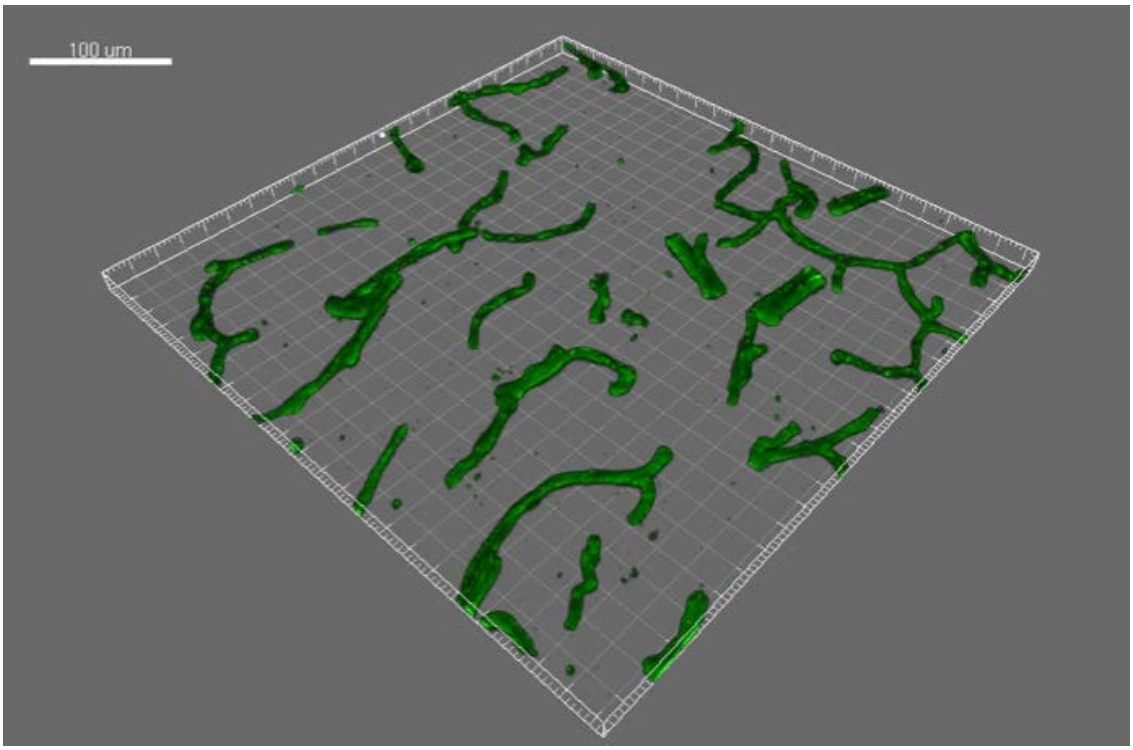

B

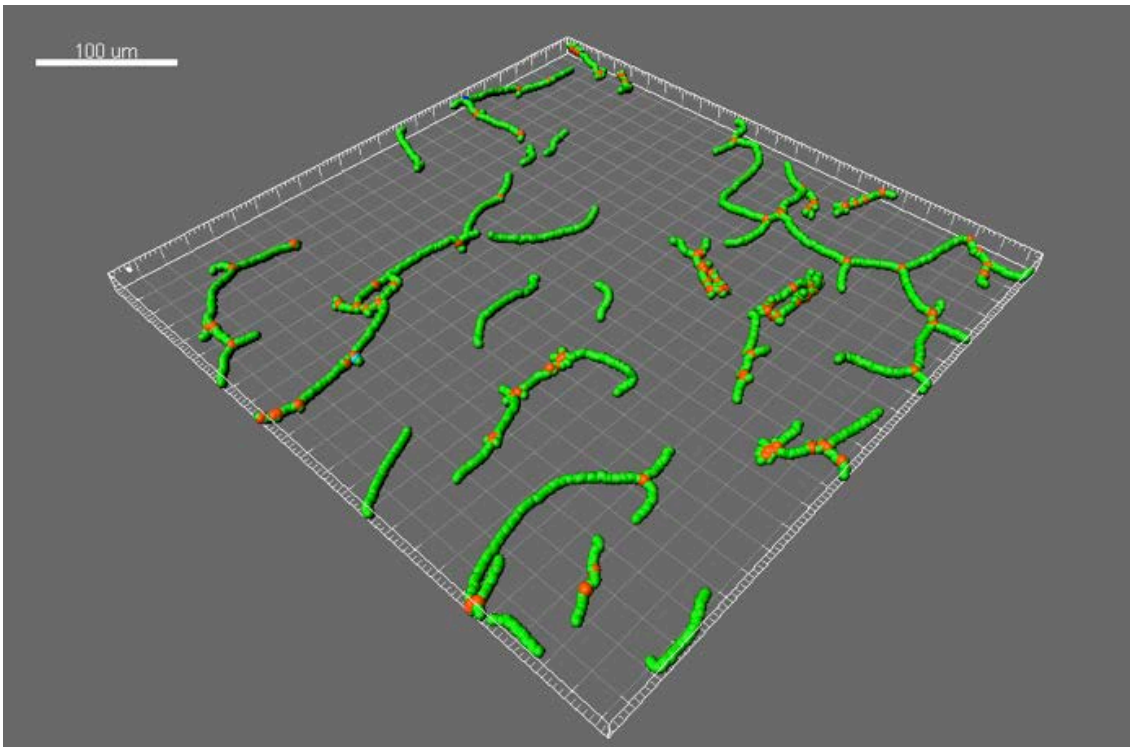

C

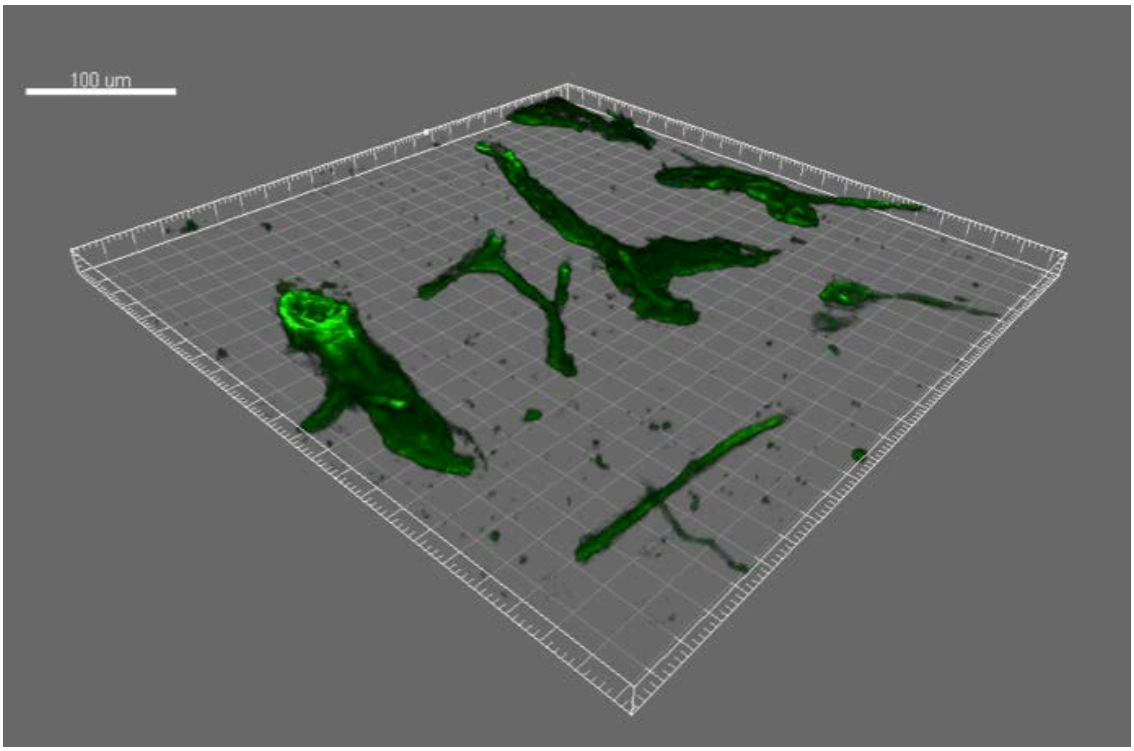

D

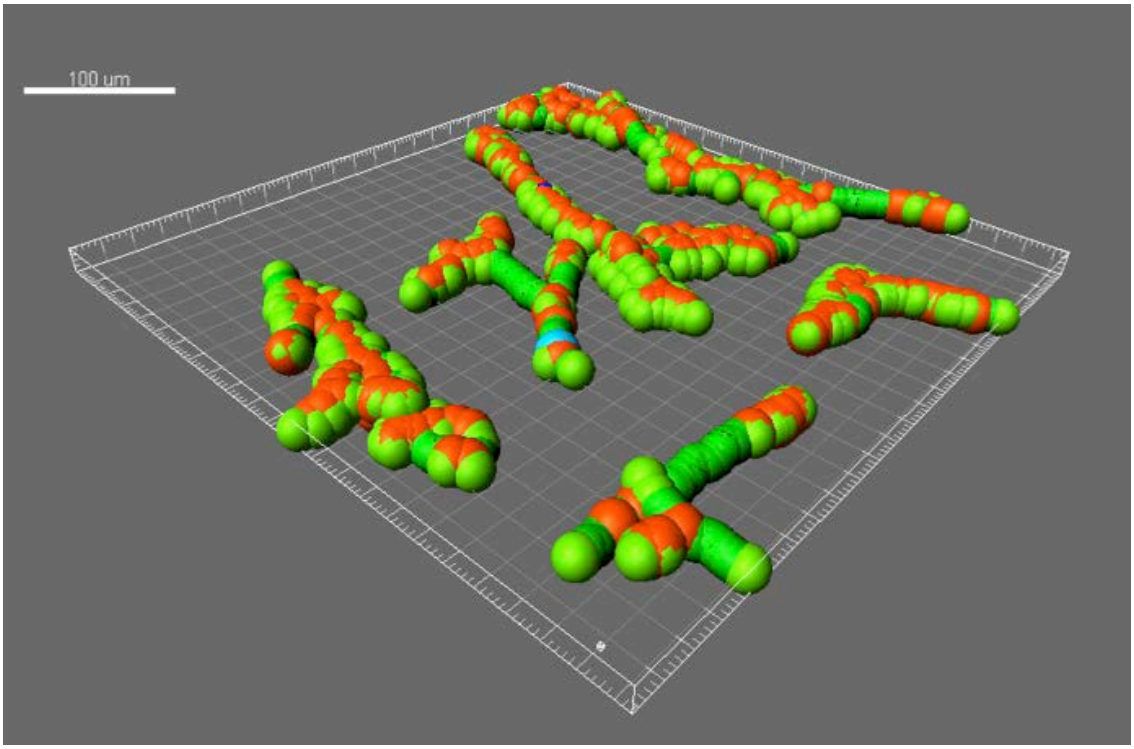

Figure 20. Two examples of 3D reconstructions of blood vessels generated using Imaris' "Filament Tracer" tool showing BVs and branching points in normal cortical tissue and GBM. With a relatively simple normal vessel network (**A** and **B**) and uncomplicated branching structure, the program is fairly accurate but in GBM vessels (**C** and **D**) many extraneous points are added. Given these technical problems, branching counts and types were quantified manually. Collagen IV (green,) A and C. Branch points (orange), vessel filaments (green), B and D. Scale bar 100 μm.

4.6.6 Vessel wall integrity

To quantify the vessel surface disruption and irregularities, we measured variations in fluorescence intensity along small segments of vessel walls assuming that the continuity and integrity of a vessel wall would be reflected indirectly in this variation (i.e. more variation, less vessel integrity). Single, approximately 1-µm slices, were exported from confocal image stacks and small segments of five vessel walls in each image were measured by tracing approximately 40-µm lines along blood vessel walls using ImageJ's "Freehand line" tool and generating a series of values for fluorescence levels along the respective lines with the application's "Plot Profile" analysis function. Individual line lengths varied slightly but the fluorescence value profiles were harmonized after exporting by taking the values corresponding to the first 40 microns measured from the list of fluorescence intensities created and plotted by the tool for each sample (see Figure 21).

A

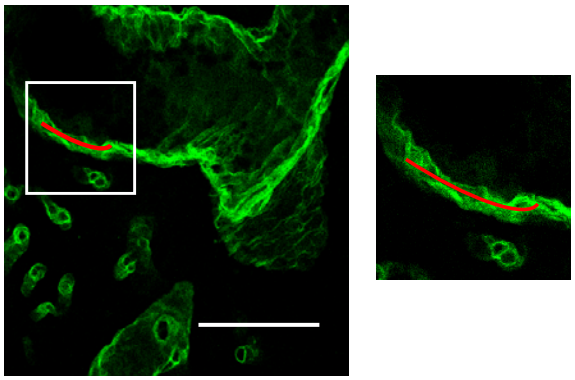

B

Distance from start (µ)	Gray value (intensity)
0	107.00
0.625	151.22
1.25	149.26
1.875	154.32
2.5	138.50
(⋯)	(⋯)
37.5	160.49
38.125	137.02
38.75	119.00
39.375	129.73
40	145.39

C

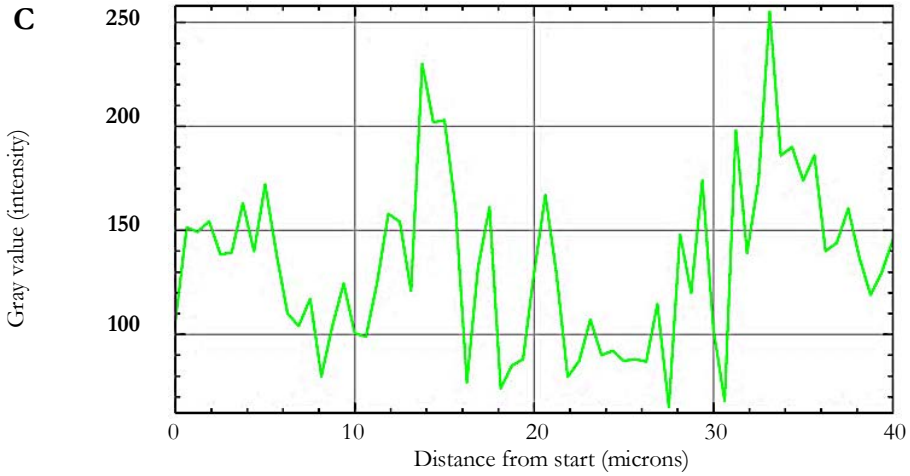

Figure 21. Vessel wall disruption estimated by plotting and comparing variations in fluorescence along vessel walls. Vessel wall segments were marked in ImageJ (Fiji) by drawing lines along the curvature of the blood vessel (**A**). Corresponding relative fluorescence values (**B**) were plotted (**C**) and then exported for calculations and analyses. Scale bar 100 µm. Collagen IV (green) in photographs. Photos by author.

4.6.7 CD31 area and density

CD31, also known as platelet endothelial cell adhesion molecule-1 (PECAM-1) is a membrane protein expressed on the surface of endothelial cells, which are known to proliferate in GBM. To quantify any changes in CD31 expression relative to increasing tumorigenicity, we captured confocal images and imported them into Imaris to create 3D isosurfaces (see Figure 22) using the "Surfaces" module and then exported the statistics of the isosurface surface areas and volumes for calculations and statistical analyses.

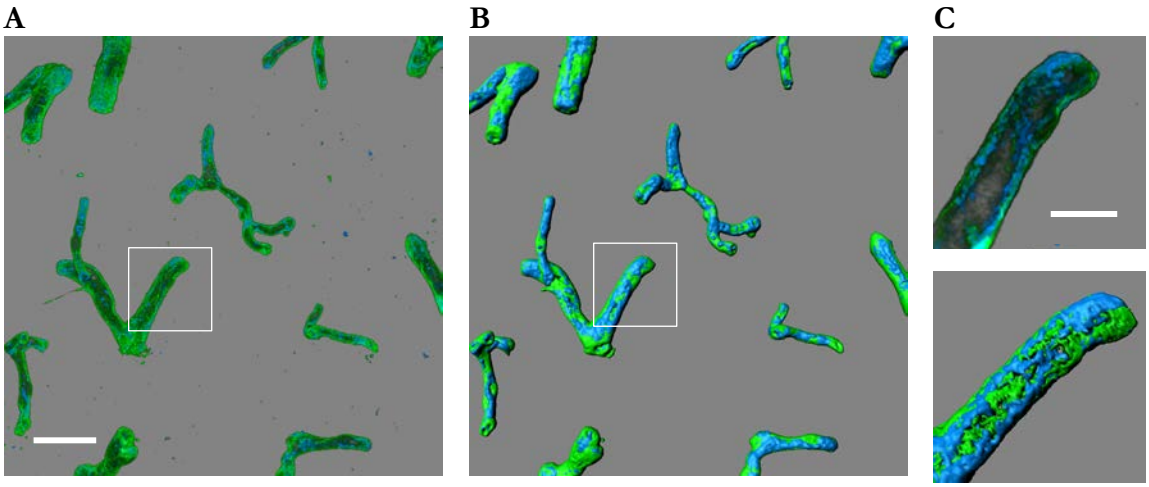

Figure 22. Creating 3D isosurfaces of CD31-positive endothelial cells to calculate surface areas and volumes. Normal cortical vessels (**A**) immunostained for collagen IV (green) and CD31 (blue) and a 3D isosurface (**B**) of the CD31 (blue) and collagen IV (green) structures in image **A**. Two amplified views (**C**) of the areas surrounded by the white squares in A (upper) and B (lower) panels, respectively, in C which show the spatial relationship between collagen IV and CD31. Scale bars A and B, 50 μm and C 20 μm. Photos by author.

4.6.8 Colocalization of CD31 and collagen IV

In intact blood vessels, pericytes are integral to the vascular basement membrane which is lined with endothelial cells (refer to Figure 1). During angiogenesis, endothelial cells proliferate rapidly and this proliferation is associated with basement membrane degradation (Kalluri, 2003). To examine this effect, images from samples immunostained for both type-IV collagen and CD31 were acquired and imported into Imaris software. Three-dimensional isosurfaces were created from the collagen IV and CD31 channels and a mask was created separately for each channel from the respective 3D isosurface to eliminate artifacts from the original confocal channels. A new channel was then generated from the colocalization of the masked collagen IV and CD31 channels in the confocal image stack and a 3D isosurface of this overlapping area was created (see Figure 23). From this latter, total colocalization areas were extracted.

A

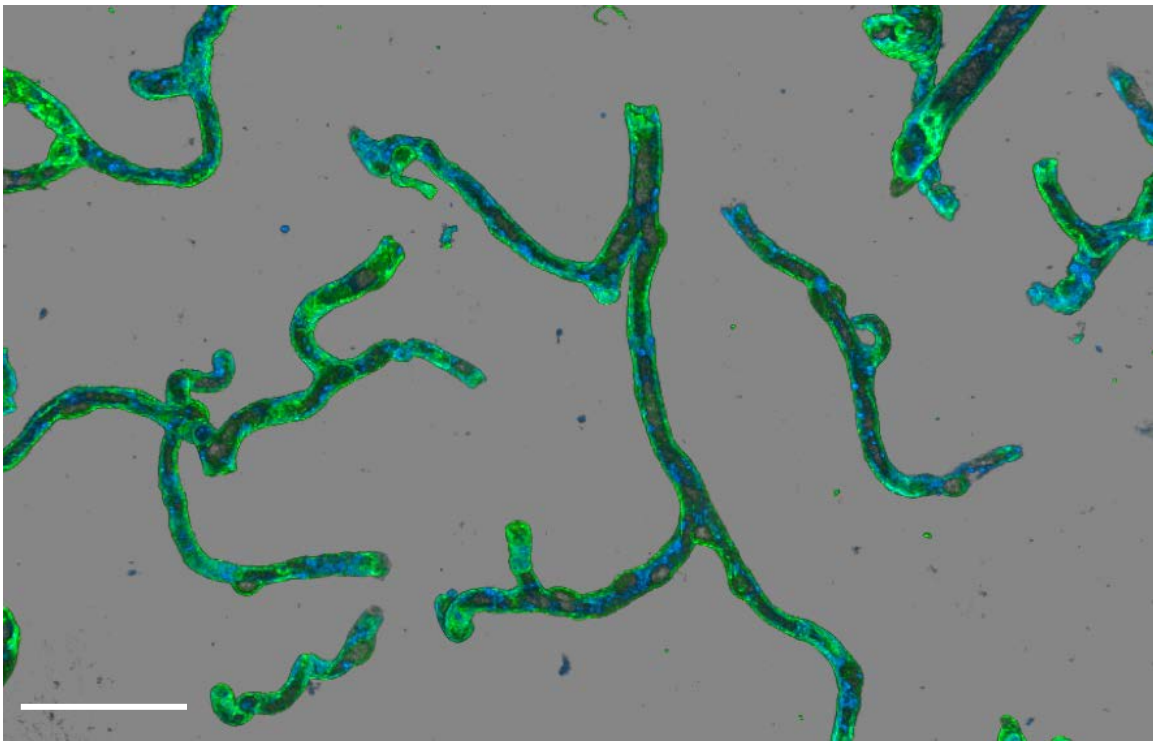

B

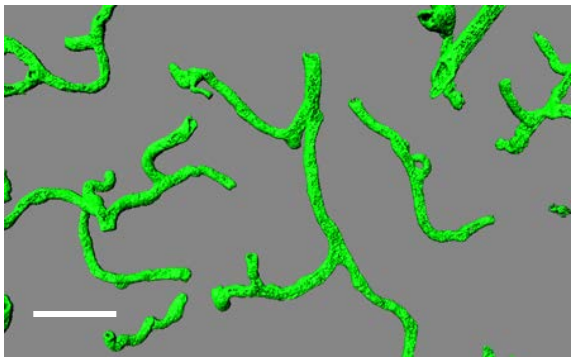

C

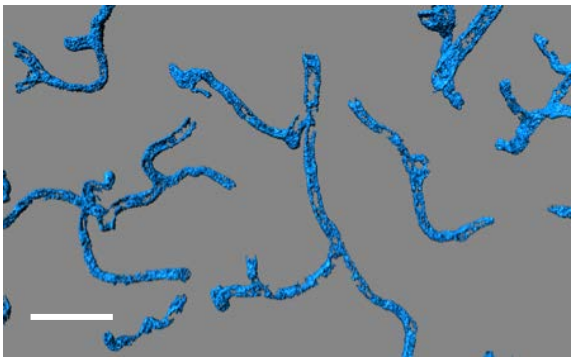

D

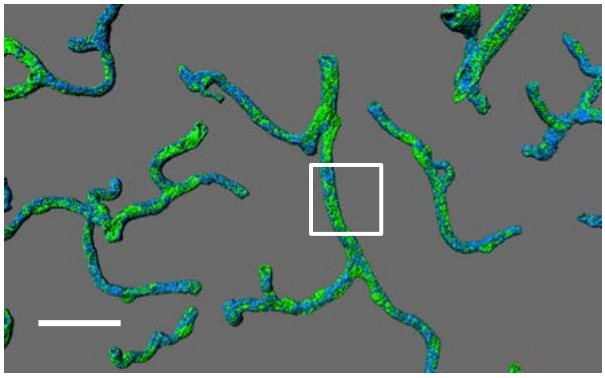

E

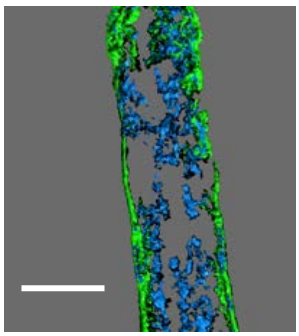

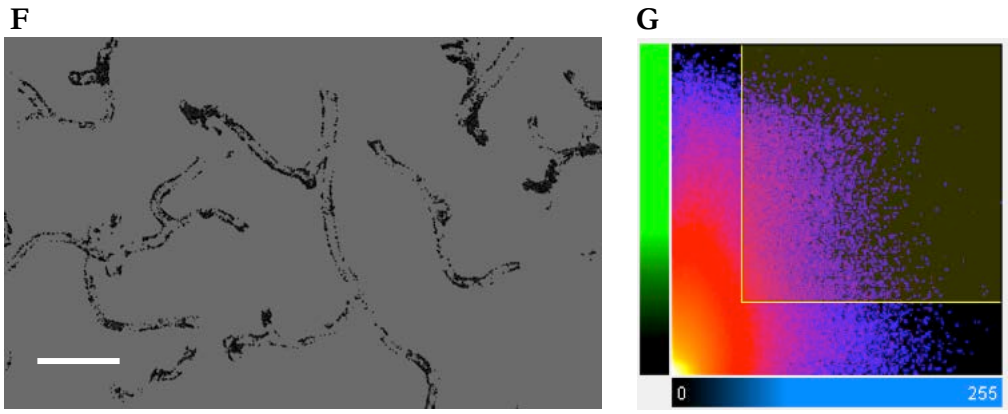

Figure 23. Basement membranes and endothelial cell lining are closely associated in intact BVs. Two channels of a confocal image (**A**) highlighting collagen IV in basement membranes (green) and CD31 expressing endothelial cells (blue). Collagen IV and CD31 channels (**B**) and (**C**), respectively, shown as 3D isosurfaces along with a merged view of the two (**D**). Detail (**E**) of a magnified view of the white-boxed area in image D. The last two images show the 3D reconstruction of the overlapping area (**F**) between isosurfaces shown in B and C and the luminance heat map (**G**) for the colocalizing isosurfaces. Scale bars A-D and F, 50 μm; E, 20 μm. Photos by author.

4.6.9 Microglia - Iba-1

Ionized calcium binding adaptor molecule 1 (Iba-1) is a microglial and macrophage-specific calcium-binding protein that is involved with the membrane ruffling and phagocytosis in activated microglia (Kettenmann, Hanisch, Noda, & Verkhratsky, 2011; Ohsawa, Imai, Kanazawa, Sasaki, & Kohsaka, 2000).

Iba-1 surface area, units and volume were measured in confocal image stacks by importing them into Bitplane's Imaris software and creating 3D isosurfaces (see Figure 24) using the "Surfaces" module.

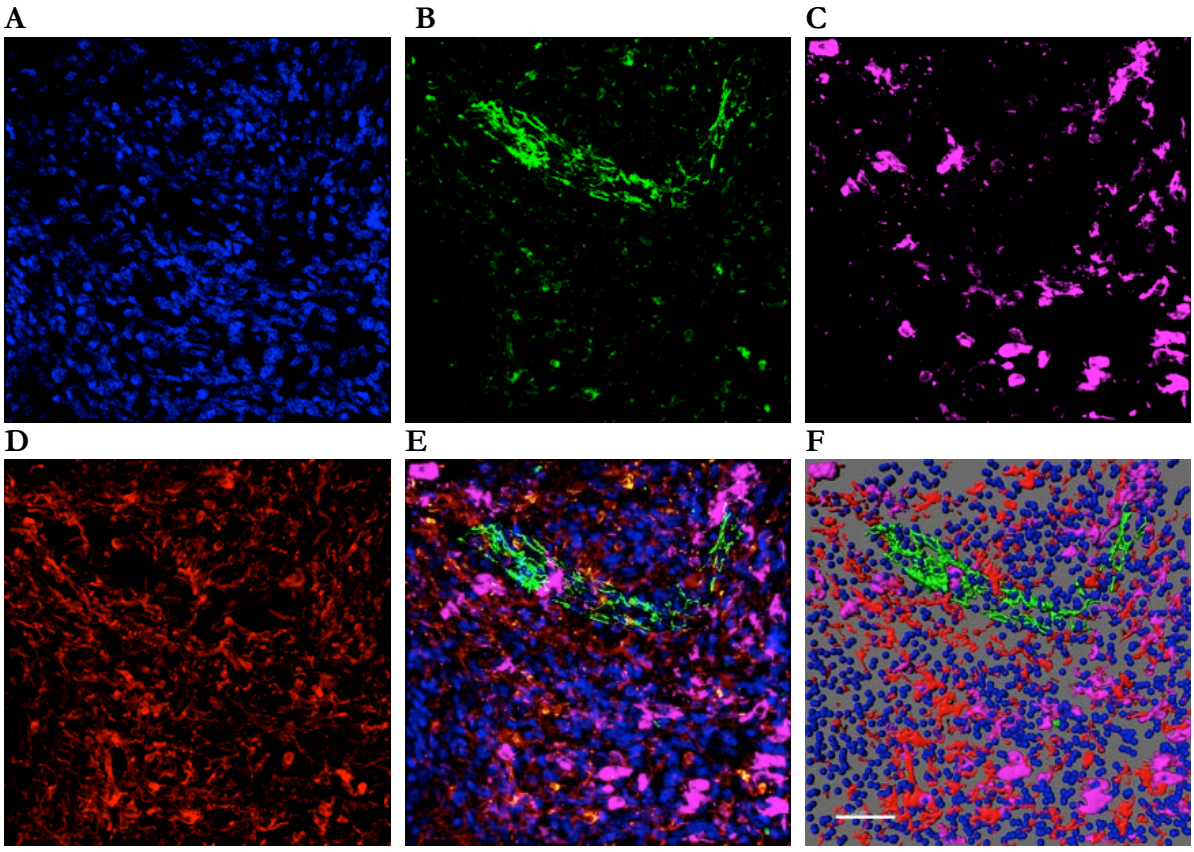

Figure 24. Iba-1 immunostaining can be used for locating Iba-1-rich areas in GBM. These images show the separate channels and merged view of a biopsy sample of a GBM tumor with a Ki67% index of 20%. Shown in the images are nuclei (blue, **A**), CD31 (green, **B**), Iba-1 (magenta, **C**) GFAP (red, **D**) and a merged view of all channels (**E**). The last image (**F**) is a 3D isosurface reconstruction of the same tumor sample. Scale bar 50 μm.

4.6.10 MHCII

MHC (major histocompatibility complex) class II molecules are markers for antigen presenting cells (APC), dendritic cells or mononuclear phagocytes.

Human GBM biopsy samples were immunostained marking type-IV collagen, GFAP, MHCII and nuclei. MHCII surface area, units and volume were then measured in confocal image stacks by importing them into Bitplane's Imaris software and creating 3D isosurfaces using the "Surfaces" module. A separate colocalization channel was created and isosurfaced to measure the total surface area of overlapping MHCII / GFAP areas (see Figure 25). In addition, MHCII-rich and GFAP-rich areas were isolated by selecting regions of interest (ROI) in Imaris and the area and volume of collagen IV expressed in each ROI was measured. Vessel diameters were also measured in each ROI (see Figure 26).

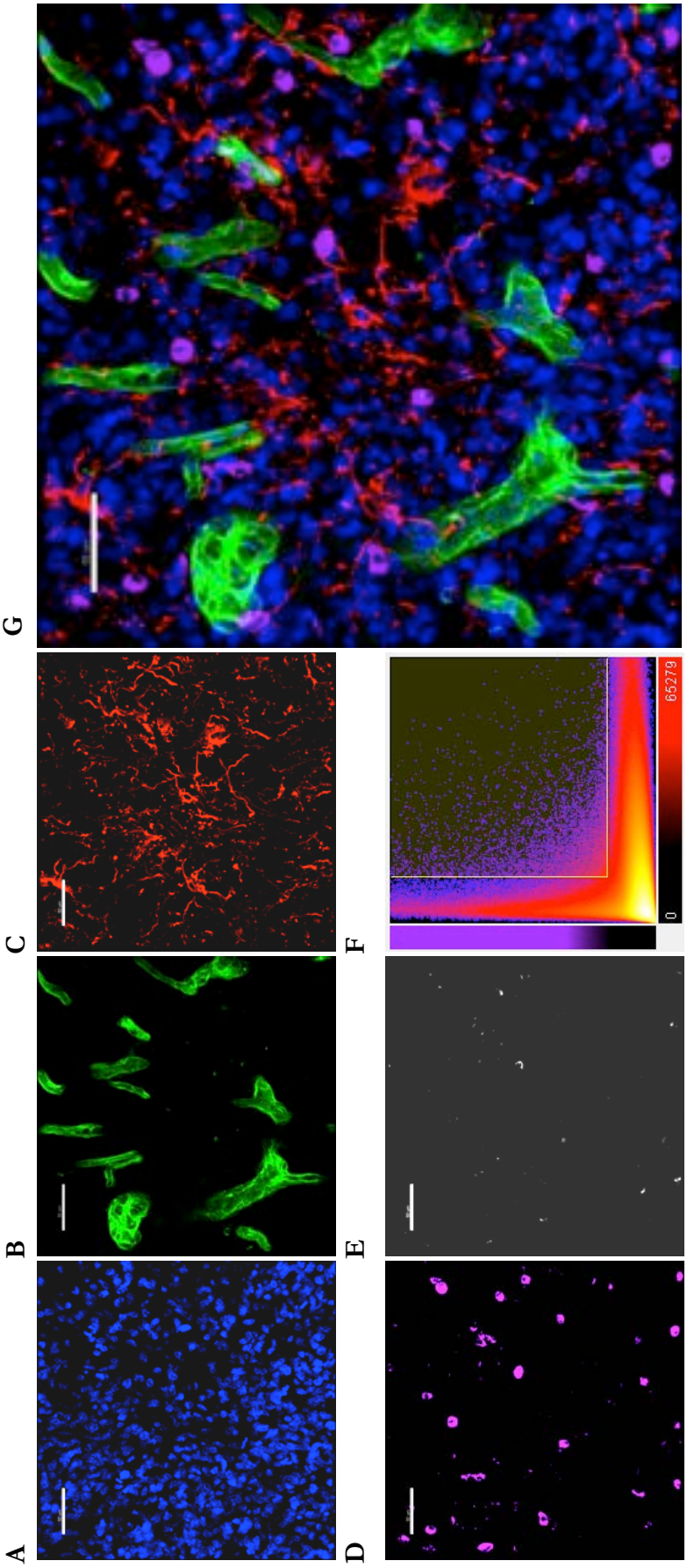

Figure 25. MHCII immunostaining can be used for locating MHCII-rich areas in GBM. Images showing the separate channels of a biopsy sample of a GBM tumor with a Ki67% index of 30%. Shown in the images are nuclei (blue, **A**), collagen IV (green, **B**), GFAP (red, **C**), MHCII (magenta, **D**) and the colocalization (white, **E**) of GFAP and MHCII. The fluorescence intensity heatmap (**F**) shows two separate peaks (horizontal and vertical) illustrating the separation of the two channels, i.e. practically no colocalization. The final image (**G**) is merged view of channels (A-D). Scale bars 50 µm.

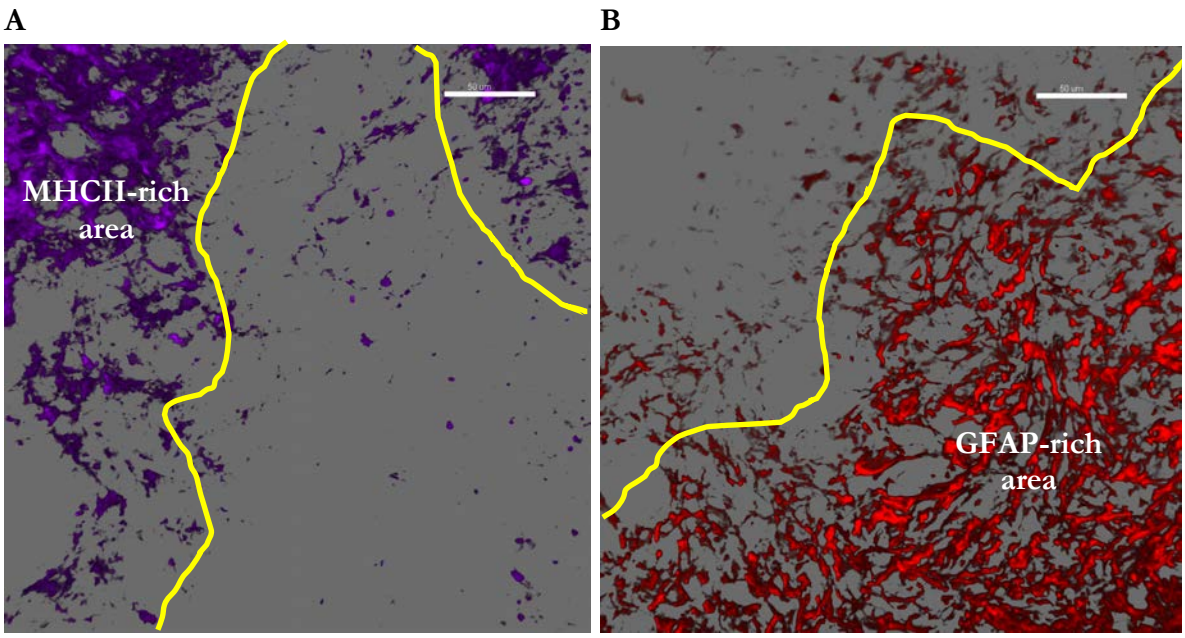

Figure 26. Collagen IV expression and blood vessel calibers can be measured separately in MHCII-rich and GFAP-rich areas. ROIs (regions of interest) can be used to isolate areas and measure vessel diameters and collagen IV-expression area and volume area by area. In this case, we were interested in measuring separately the MHCII-rich areas (magenta, **A**) and GFAP-rich areas (red, **B**). Scale bars 50 μm.

4.6.11 T cells - CD3

Cluster of differentiation 3 (CD3) is a membrane bound antigen found in all mature T cells and acts as a T-cell co-receptor that helps activate cytotoxic T cells and T helper cells. The CD3 antigen specificity and its universal expression at all T cell development stages make it an ideal immunological marker to detect T cells in tissue sections (Chetty & Gatter, 1994). In an effort to explore T-cell populations in GBM, tumor tissue samples were immunostained for CD3 and acquired confocal images were imported into Imaris software for analysis. The objective was to measure the extent of extravasation (i.e. movement of T cells away from vessels) and see if that bears any relation to membrane degradation in severe tumors. Total T cells in each image were counted using the Imaris "Spots" module and the distances from or contact with the nearest blood vessel were measured manually with the "Measurement Points" tool (see Figure 27).

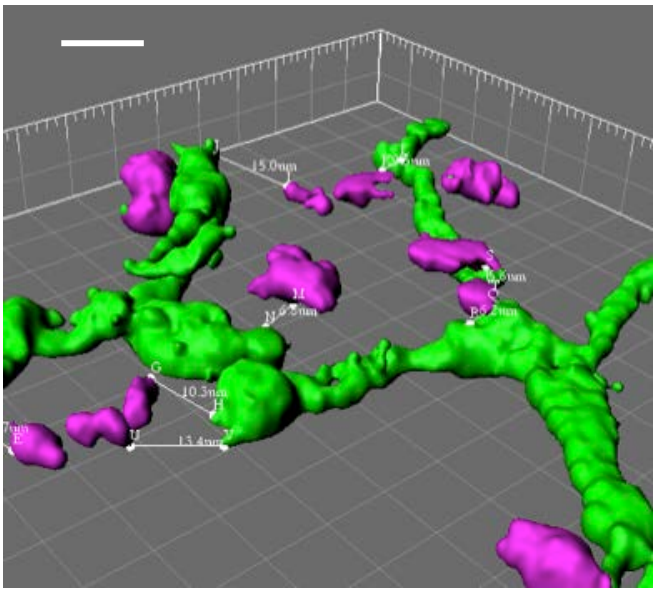

Figure 27. Exploring T cells in GBM by measuring the number of T cells inside BVs or in diapedesis or migrating from GBM microvasculature. Image shows 3D isosurfaces of T cells (magenta) and CD31 endothelial cells marking blood vessels (green). Imaris' "Measurement Points" tool is used to mark distances between T cells and vessels at the closest points between the two. Notice that some T cells are within vessels, some are in contact with the vessel surfaces and some more distant from vessels. Scale bar 15 μm.

4.7 Data Analysis

4.7.1 Statistical analyses

As noted in Section *2.3.2 Immunohistochemistry* in the materials and methods section, in order to clearly mark target structures without interferences or cross contamination deriving from antibody species conflicts, different combinations of antibodies were used; therefore, samples for different comparisons and analyses derive from different sample pools, all taken from the biopsies detailed in Table 1.

Data sets for statistical comparison derive from various sample combinations depending on the antibody combination used and the parameters to be determined (see Table 2).

Table 2. Sample pools and data sets for different parameters

Group	Parameters	Sample no.	Measures per sample	Lab ref. no.	Ki67% index (%)
Main (N=5)	cellularity, diameters, branching, density, basement membrane integrity GFAP and collagen IV areas and volumes	N	10	3.3	0
		1		11	10
		3		3.2	20
		7		4	30
		8		12	50
CD31* (N=4)	CD31, collagen IV and GFAP areas, cellularity, colocalization of CD31 and collagen IV, vessel integrity	N	6	3.3	0
		1		11	10
		2		2	20
		7		7	30
CD3 (N=5)	T cell count, extravasation or migration of T cells from nearest vessel	1	6	11	10
		3		32	20
		4		34	20
		5		31	30
		6		36	30
Iba-1 (N=6)	Iba-1 surface area, volume and units.	N	6	3.3	0
		1		11	10
		3		3.2	20
		4		3.4	20
		6		3.6	30
MHCII (N=6)	MHCII surface area, volume and units, colocalization of MHCII and GFAP, vessel areas, volumes and diameters in MHCII- and GFAP-rich areas.	N	6	3.3	0
		1		11	10
		3		3.2	20
		4		3.4	20
		6		3.6	30

* The CD31 group has fewer samples than the other groups because the immunostaining was started with samples from four tumor groups including the 50% Ki67 samples but, due to some technical problems while performing the staining, the protocol had to be repeated and at that point there was not sufficient tumor biopsy material left to include a new batch.

Results for cellularity, vessel characteristics (diameters, branching and density) and GFAP and type-IV collagen surface areas and volumes derive from samples immunostained for collagen IV and GFAP and counterstained with DAPI (N=5; normal cortical tissue and four tumors) with 50 data points (10 for normal and 10 each for Ki67 indices 10, 20, 30 and 50%). Basement membrane continuity results are drawn from the same sample pool with 50 data

sets (10 normal and 10 each for Ki67 indices 10, 20, 30 and 50%) with each data set comprising five separate sets of 33 luminance measurement points.

Results for CD31 surface area and multiple comparisons between cellularity, vessel continuity, type-IV collagen and CD31 surface areas, colocalization and GFAP surface area, derive from a sample set stained for collagen IV, CD31 and GFAP and counterstained with DAPI (N=4, one normal and three tumors; the biopsy tissue for 50% Ki67% was used up so it could not be included for these comparisons) with 24 data points for each variable, six normal and 18 for tumors (six each for Ki67 indices 10, 20 and 30%). Again, basement membrane continuity results are drawn from the same sample pool with 40 data sets (10 normal and 10 each for Ki67 indices 10, 20 and 30%) with each data set comprising five separate sets of 33 luminance measurement points.

Total T cell counts, and T cell extravasation and migration data were drawn from a sample pool of five, immunostained for CD31, CD3 and GFAP and counterstained with DAPI. Six separate areas were analyzed per sample.

Data for Iba-1 and MHCII derive from two sample groups (each with five normal and 25 tumor samples; tumors had Ki67% indices of 10, 20 and 30%). Iba-1 samples were immunostained for CD31, Iba-1 and GFAP and counterstained with DAPI. MHCII samples were immunostained for type-IV collagen, MHCII and GFAP and counterstained with DAPI.

For all statistical comparisons, we used the unpaired, two-tailed student t-test with Welch's correction, or one-way ANOVA (Dunnet's, Tukey's, Dunn's or Sidak's multiple comparisons test) with *$p<0.05$, **$p<0.01$, ***$p<0.001$, ****$p<0.0001$ unless otherwise stated in the text. Data are represented as mean ± SEM. F-tests were used to examine the similarity of the variance of the compared groups, and the appropriate tests were performed accordingly. See Appendix 3 for more information on statistical data and tests applied.

4.8 Limitations

All research is subject to certain constraints and limitations. There are three specific limitations affecting this thesis -methodological, procedural and theoretical- that bear mentioning.

The first deals with the small sample size which affects the power of any statistical conclusions drawn. This limitation is not unintentional as the decision was made to prioritize detail over

power in examining the parameters comprising this research. Creating a detailed topographic, morphometric picture of GBM characteristics required meticulous and thorough analysis of each parameter and the process was labor-intense and time-consuming, as well as requiring many resources. To analyze a sample pool large enough to increase the power would have been impossible in the context of this thesis. Thus, we opted to perform detailed analyses of a smaller sample pool at the expense of experimental power. Despite this limitation, and though the statistical results must be considered in this light, the detail obtained in confocal microphotographs and the resulting analyses shed great light on GBM morphology and TME topography.

The second main limitation relates to the experimental methodology, in particular immunostaining and confocal microphotography. Multiple immunostaining is complex and difficult in the best of circumstances but when dealing with free-floating, thick biopsy samples, the problems with sample handling due to tissue fragility and with antibody penetration increase substantially. Coupled with this are certain technical limitations inherent in the confocal microscope itself and the maximum number of lasers, and hence separate channels, that can be imaged. It would be ideal to stain and image all of the main GBM components under study simultaneously and create confocal image stacks composed of all elements of interest. Unfortunately, only a determined number of parameters could be measured at any one time due to microscopy limitations and antibody conflicts, which prevented combining certain pairs of markers because antibodies were derived from the same species. As a consequence, some parameters had to be compared indirectly, meaning that measures came from different sample sets though taken from the same tumor and immunostained identically but with different antibodies. Again, this is not the ideal scenario but nonetheless, despite this limitation, the results permit valid conclusions to be drawn.

And finally, there is an inherent contradiction in trying to obtain a precise topography and morphology and create an accurate 3D reconstruction of GBM. As is implicit in its traditional name, glioblastoma multiforme, GBM are heterogenous, macroscopically, genetically and at a cellular level (Aum et al., 2014; Inda et al., 2014; Parker et al., 2016; Patel et al., 2014; Soeda et al., 2015). Every tumor is an individual ecosystem and an accurate description of any single tumor is hard to generalize due to the high degree of inter- and intra-tumor variation. Constructing an atlas of GBM necessarily implies an idealized, generic approximation of GBM, highlighting its most salient characteristics.

Nevertheless, and particularly in light of the results obtained in our research, our methodology and the resulting imaging and 3D reconstructions provide an illuminating perspective and point the way to interesting further examination of the in situ spatial organizations of GBM TME components.

5 RESULTS

5.1 Cellularity

GBM is highly aggressive and this is reflected in increased cellularity deriving from intense tumor growth. On diagnosis, biopsy samples extracted from patients are assigned a Ki67% index by the hospital pathology department as an estimation of cellular proliferation. Our expectation was that our estimates of cellularity evidenced by DAPI-stained nuclei would increase as tumor aggressivity increased, effectively corroborating the assigned Ki67% indices. When comparing the confocal images of normal and GBM tissue (Figure 28), much higher density of DAPI-stained nuclei can be noted in GBM.

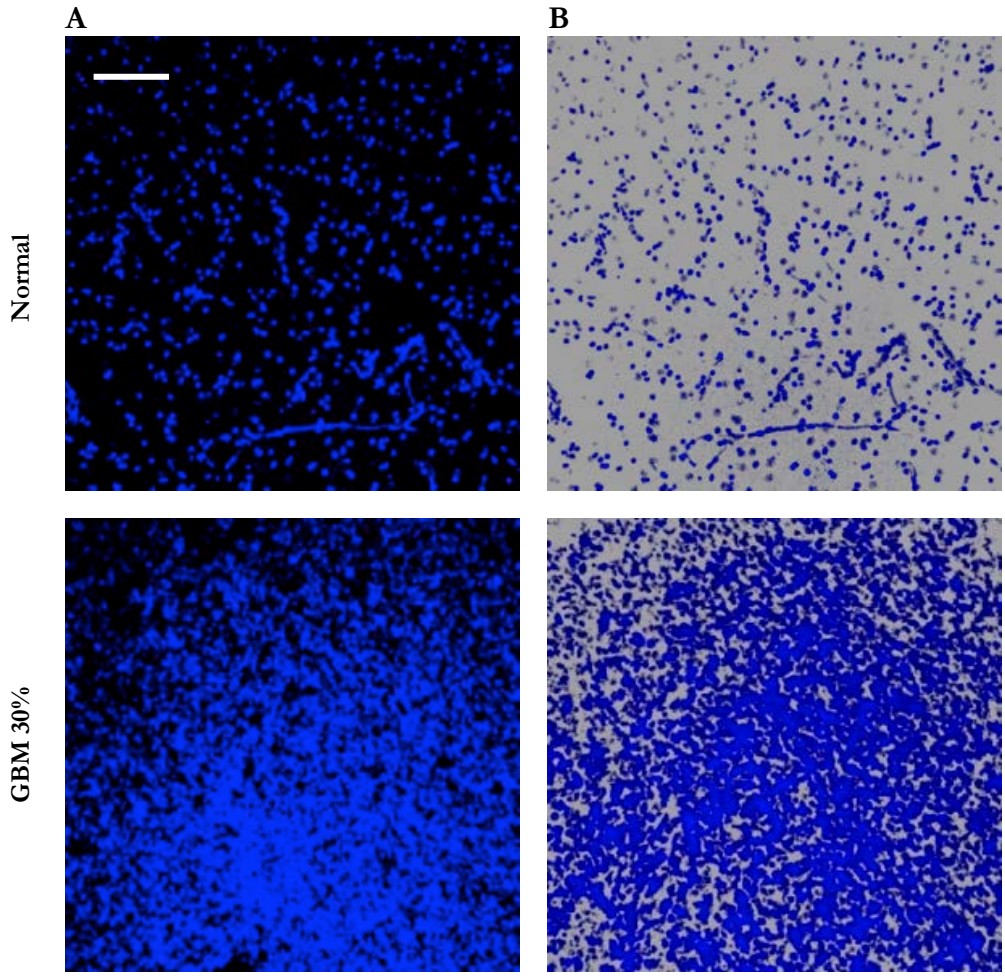

Figure 28. GBM growth is aggressive and the total cell count in these tumors is significantly higher than in normal tissue. Comparison of normal and tumor (Ki67%=30) in respective confocal images. The left view (**A**) is a maximum intensity projection of the DAPI channel (blue) from the original image stack and the right view (**B**) is a blend view on a light grey background. Scale bar 100 μm.

Our results not only support these increases in total cells but also show that there is a linear correlation between tumor aggressiveness as defined by Ki67% index and total cells. The relationship between the Ki67% index and cellularity is significant for the 10% ($p=0.001$),

30% and 50% groups (both p=0.0001). Respective mean total cells for normal and 10, 20, 30 and 50% groups were 970, 1511, 1239, 1744 and 2150. Results are shown graphically in Figure 29 and Table 3.

Therefore, our three-dimensional estimates of cellularity coincided with the pathology department assessment and corresponding Ki67% indices.

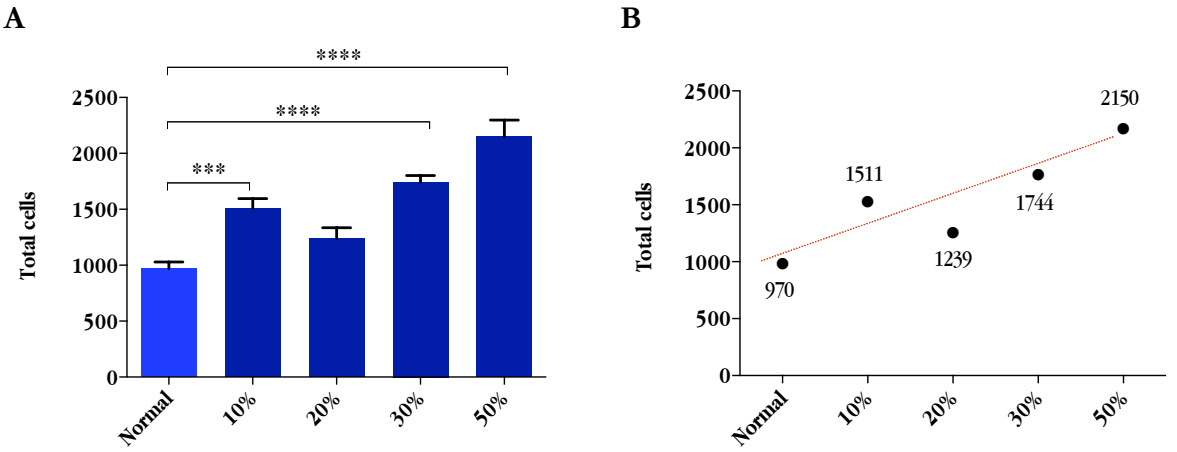

Figure 29. Cellularity increases proportionally with Ki67% index in GBM. Bar graph(**A**) plotting mean total cells versus proliferation as measured across groups according to Ki67% histological grading and a linear plot (**B**) of the mean total cells for each group with a tendency line in red.

Table 3. Mean, SD and SEM total cellularity across groups

	Normal	10%	20%	30%	50%
Mean	970.3	1511	1239	1744	2150
Std. Deviation	185.8	270.8	307.9	184.9	472.7
Std. Error of Mean	58.74	85.64	97.37	58.48	149.5
Significant?	-	***	ns	****	****

5.2 GFAP$^+$ astroglial and glioma cells

After substantiating the overall hypercellularity and confirming its correspondence with hospital-assigned Ki67% indices, we concentrated on the intratumor astroglial and tumor cell population as distinguished with the classical astroglial cell marker, GFAP, a marker also used by the pathology department for diagnosis, indicative of tumor aggressiveness.

5.2.1 GFAP-positive surface area

As an indication of how GFAP expression increased in relation to tumor aggressivity, we measured total GFAP surface area. Fifty measures were taken (10 each from one normal tissue sample and five different biopsy tissues with Ki67% indices of 10, 20, 30 and 50%). All GBMs highly expressed GFAP, as shown in total GFAP-positive surface areas and volumes (see Figure 30A). The results show significantly increased GFAP expression in GBM and surface areas vary proportionally with tumor Ki67% index. Differences between normal cortical tissue and GBM were significant for the 20 ($p<0.05$), 30 ($p<0.0001$) and 50% ($p<0.0001$) groups and when comparing normal vs. grouped GBM data ($p<0.001$) (see Figure 30B and C).

A

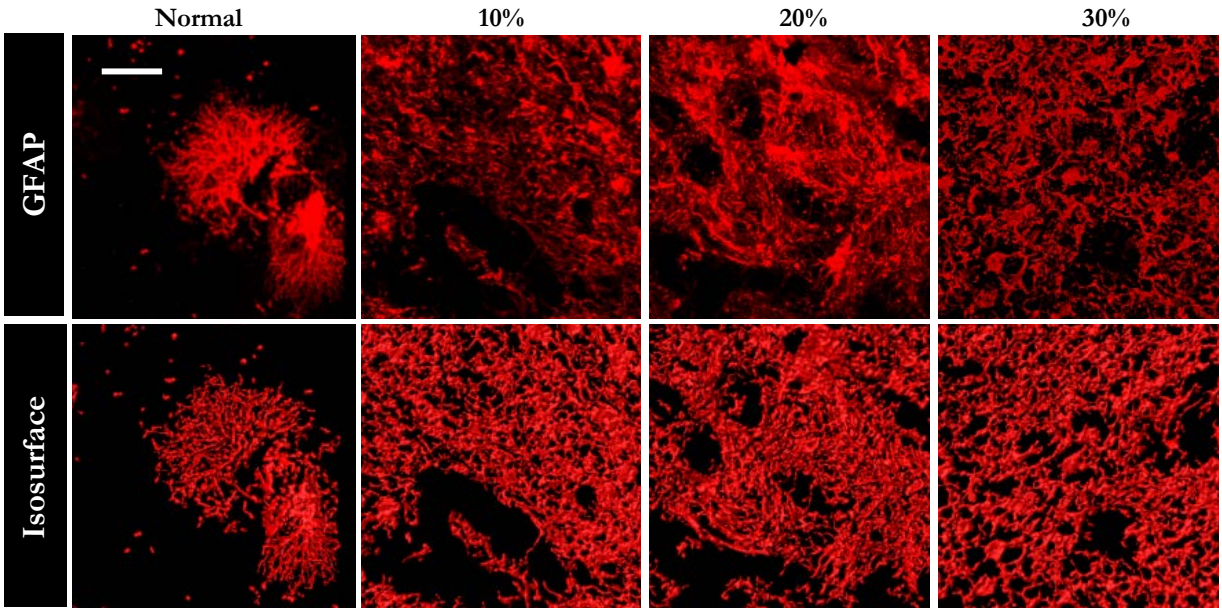

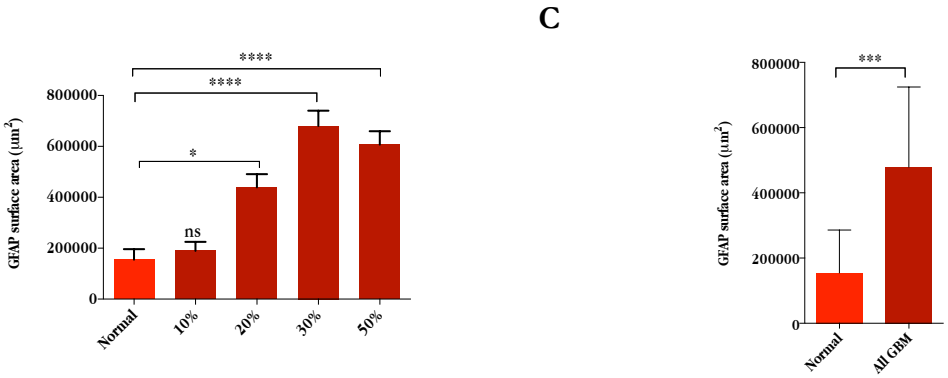

Figure 30. GFAP-expressing cells show a significant increase in GBM as reflected in greater surface areas and dispersion. Confocal images and corresponding isosurfaces (**A**) showing GFAP (red) expression and distribution. Mean GFAP areas compared between normal cortical tissue and individual groups with distinct Ki67% indices (**B**) and mean areas compared between normal tissue and all tumors (**C**). Scale bar 40 µm.

5.2.2 GFAP$^+$ cells - Distribution and Morphology

GFAP expression and astrocyte morphology vary highly across normal cortical tissue, peritumoral and tumor areas (Figure 31). In the first place, we found interlaminar astrocytes, which are exclusive to primates and are long fibrous astrocytes having cell bodies in cortical layer I with millimeter-long filaments extending to layers II, III or IV. More deeply, we found varicose projection astrocytes, also exclusive to primates, which reside in layers V or VI with one to five long processes often showing "rosary-bead" structures of evenly spaced varicosities. Around these layers we observed protoplasmic/reactive astrocytes, slightly enlarged with somewhat retracted projections and indicative of the peritumoral area. Additionally, we observed pregemistocytic astrocytes with plumper morphology and evidence of displacement of the cell nucleus, clear evidence of the tumor area itself, and usually observed in the deepest cortical layers.

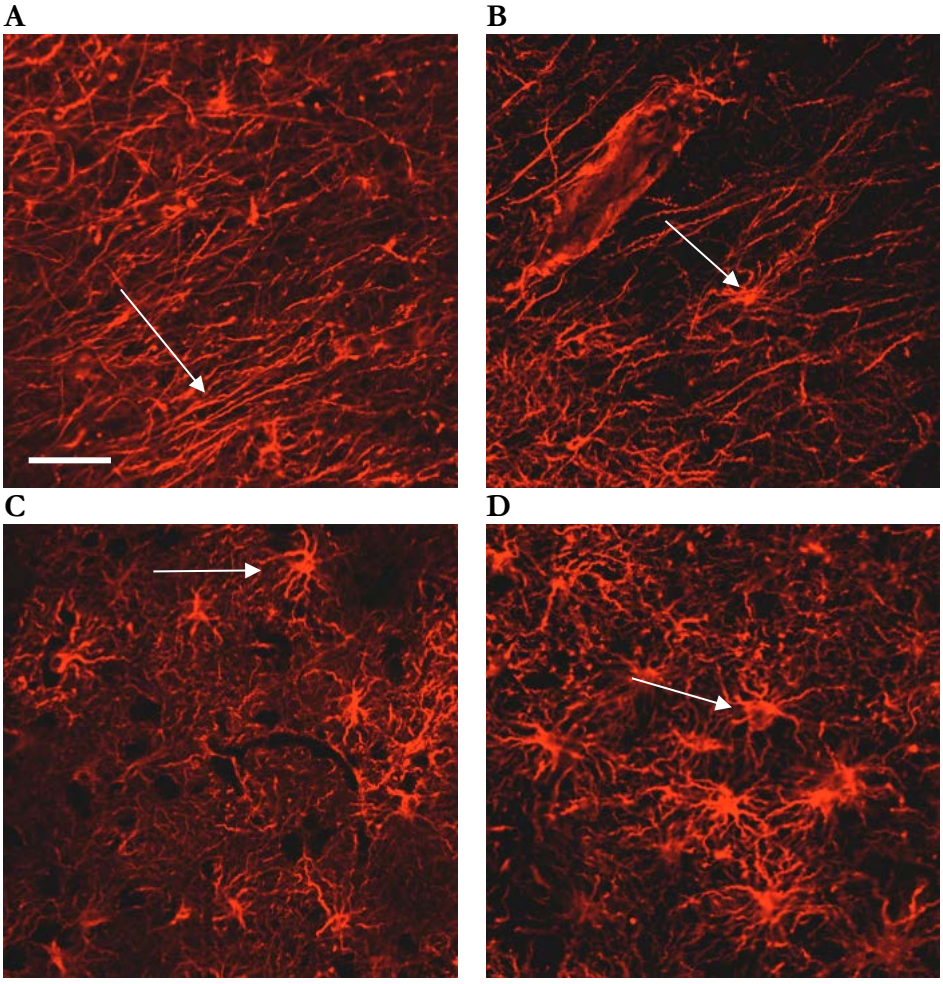

Figure 31. Progressive changes in GFAP expression across contiguous GBM peritumoral areas. Sequence (**A**-**D**) showing GFAP (red) expression variation across contiguous areas in a tumor biopsy sample with Ki67 index of 10%. From left to right, interlaminar astrocytes (**A**) in normal cortical tissue at the fringe of the biopsy to varicose projection astrocytes and protoplasmic/reactive astrocytes (**B** and **C**, respectively) and finally to the reactive pre-gemistocytic astrocytes in the last image (**D**). Scale bar 50 μm.

Figure 32 provides an atlas view that illustrates the wide morphological variation in astroglial and tumor cells evident in GBM. The confocal photographs show interlaminar astrocytes, protoplasmic astrocytes, varicose projection astrocytes (with associated "rosary-bead"-like formations), peritumoral reactive astrocytes, pregemistocytic and gemistocytic astrocytes, the latter typical of GBM (see Figure 34).

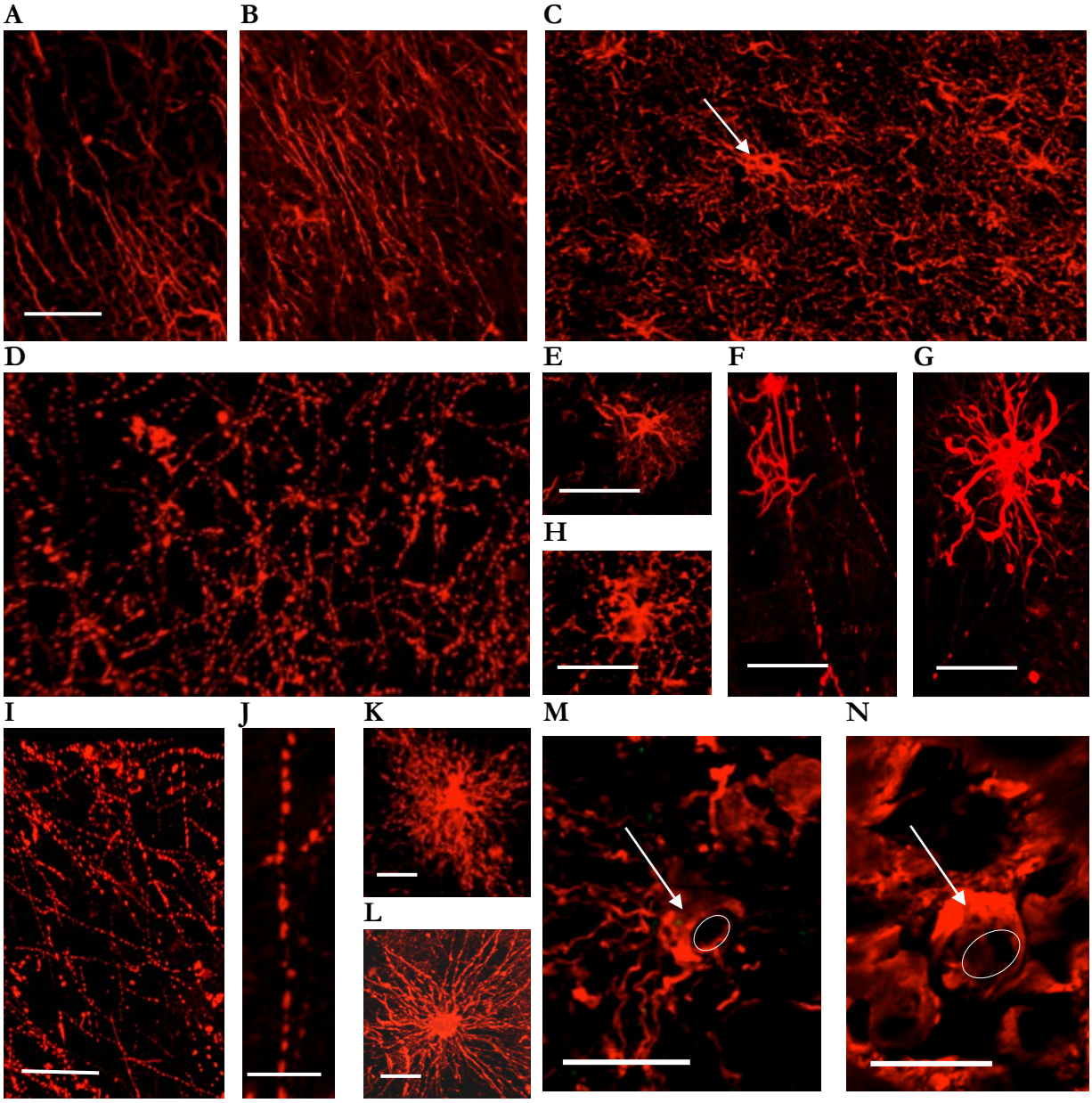

Figure 32. GFAP+ cells (astrocytes and glioma cells) in GBM show marked variations in expression and a high degree of morphological heterogeneity. Interlaminar astrocyte processes (**A**, **B**, **D** and **I**); rosary-bead like formations detail (**J**); protoplasmic astrocytes (**K** and **L**); peritumoral reactive astrocytes (**C**); varicose projection astrocyte (**E** to **H**); and pre-gemistocytic and gemistocytic (**M** and **N**, respectively). White ovals in M and N indicate position of nucleus. Scale bars A-D and I 50 μm, J 10 μm, K and E-H, N 20 μm and L and M 30 μm.

Figure 33 combines confocal photographs and drawings to highlight the connection between astrocyte morphology and cortical layer where distinct the phenotypes typically reside. It shows the same structures as in Figure 34 along with fibrous-malignant astrocytes. The latter are typical of pseudopalisades and distinct from the fibrous astrocytes characteristically associated with white matter.

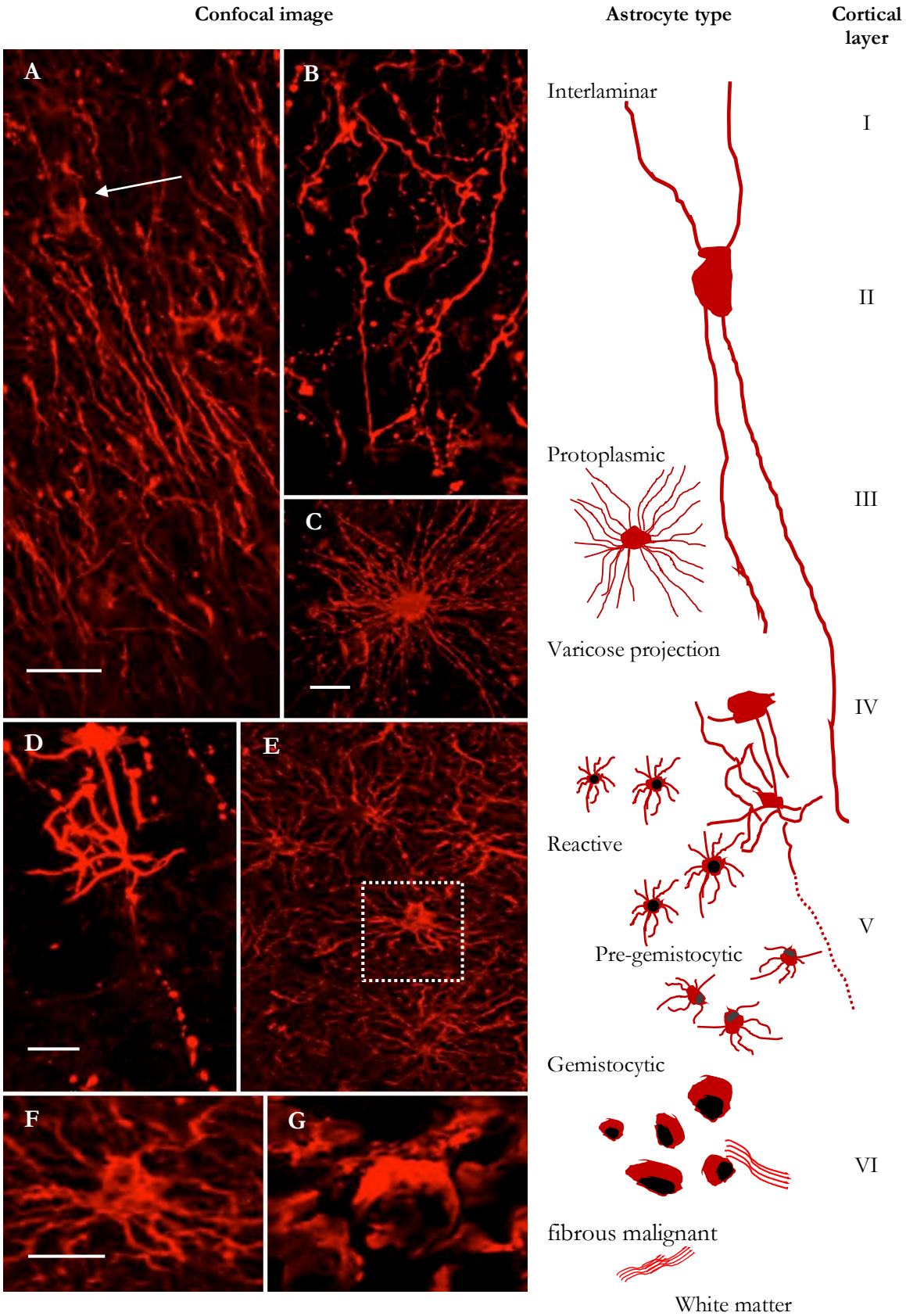

Figure 33. Astrocyte and glioma cell morphology variations give indications of cortical location of GBM. This image shows interlaminar astrocytes (**A** and **B**) in layers one to four; protoplasmic astrocytes (**C**) in layer three; varicose projection astrocytes (**D**) and reactive and pregemistocytic astrocytes (**E**) detail from white square in E (**F**), and gemistocytic astrocytes (**G**). Scale bar A, B and E 50 µm, C 30 µm, D, F and G 20 µm.

Interestingly, recent investigation (Lee et al., 2018) describing evidence that glioblastoma may arise from astrocyte-like NSCs migrating from the subventricular zone to other brain regions lends credence to the mapping shown in Figure 33; most of our tumor samples showed astrocyte phenotypes associated with deeper brain regions.

Figure 34 shows characteristic gemistocytic tumor cells (plump cells with eccentric nuclei) associated with GBM.

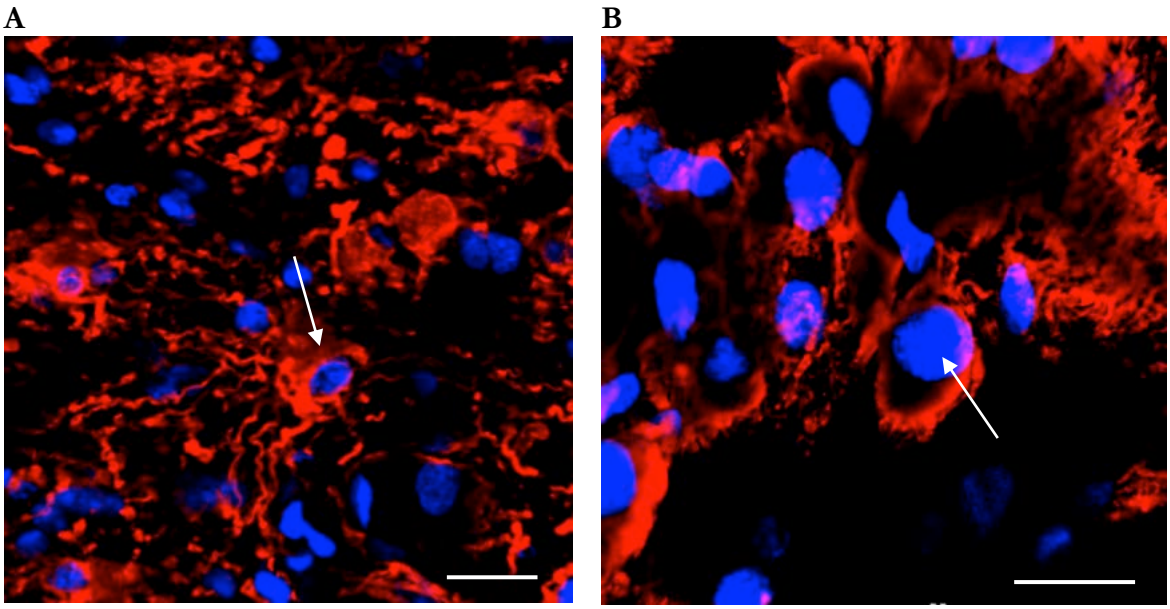

Figure 34. Two views of gemistocytes typical of GBM show pre-gemistocytic morphology and fully rounded gemistocytes. Various plump cells (**A**) in a human GBM biopsy sample. White arrow shows a pre-gemistocytic cell with some ramifications. The eccentric nuclei characteristic of gemistocytes are more apparent at greater magnification (**B**). White arrow shows a fully rounded gemistocyte with displaced nucleus. GFAP (red) and cell nuclei (blue). Both scale bars 20 μm.

5.3 Blood vessels

Glioma are highly vascular tumors essentially forming a dense vascular labyrinth surrounded by highly morphologically varied astrocytes and accompanied by TAMMS and tumor infiltrated lymphocytes (TILS). Tumor vasculature are essential for tumor propagation and growth and given the notable changes we observed in astrocyte morphology and the intimate relation between astrocytes and BVs, we thought it important to study in depth the GBM vascular network. Moreover, several fundamental hemodynamic principles associate vessel size (radius and length) and vessel wall integrity (cylinder stress) with vascular function so that any alterations in BV morphology might be mirrored in altered hemodynamic efficiency.

Our results confirm that there are radical changes in total vessels and in BV morphology and distribution, notably in those characteristics that may have a profound influence on hemodynamics. Results for type-IV collagen surface areas and volumes, vessel diameters, branching, vessel wall integrity, CD31 surface areas and volumes and the colocalization of collagen IV and CD31 are shown in Sections 5.3.1 to 5.3.7.

5.3.1 Type-IV collagen surface area and volume

Because type-IV collagen is a prominent component of basement membranes, increased vascularization in GBM should be reflected in increased overall expression of type-IV collagen. Using our protocol, we were able to label collagen IV^+ basement membranes and create images to highlight the tubular structure of BVs when seen in 3D. Figure 35 shows orthogonal views of normal and GBM BVs.

A

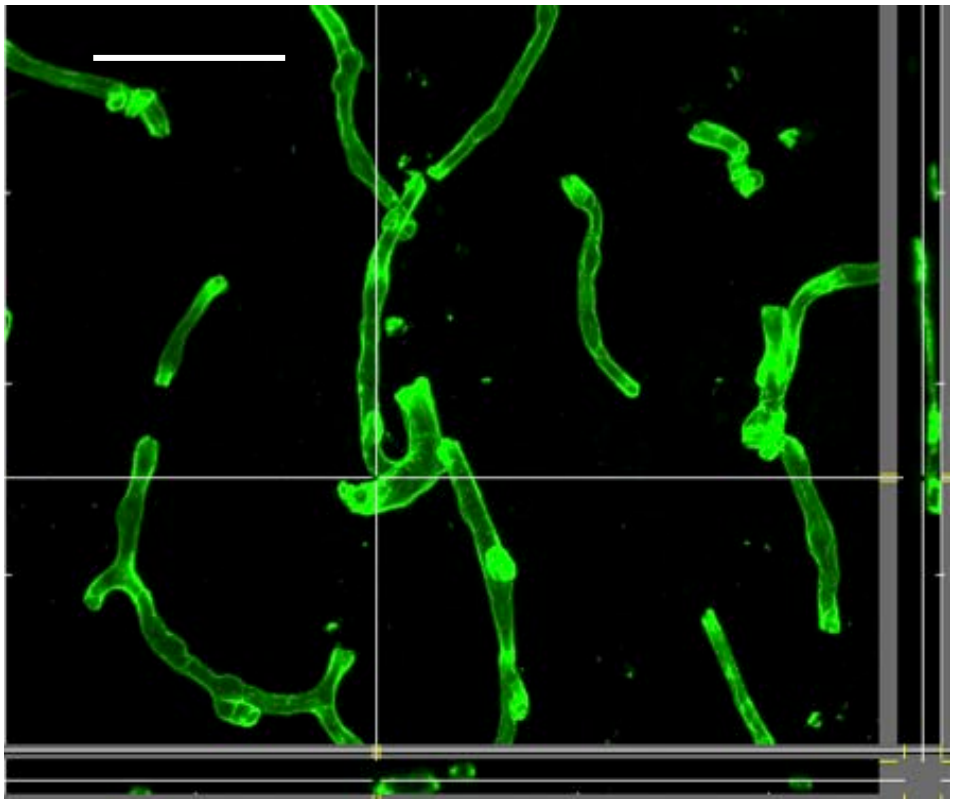

B

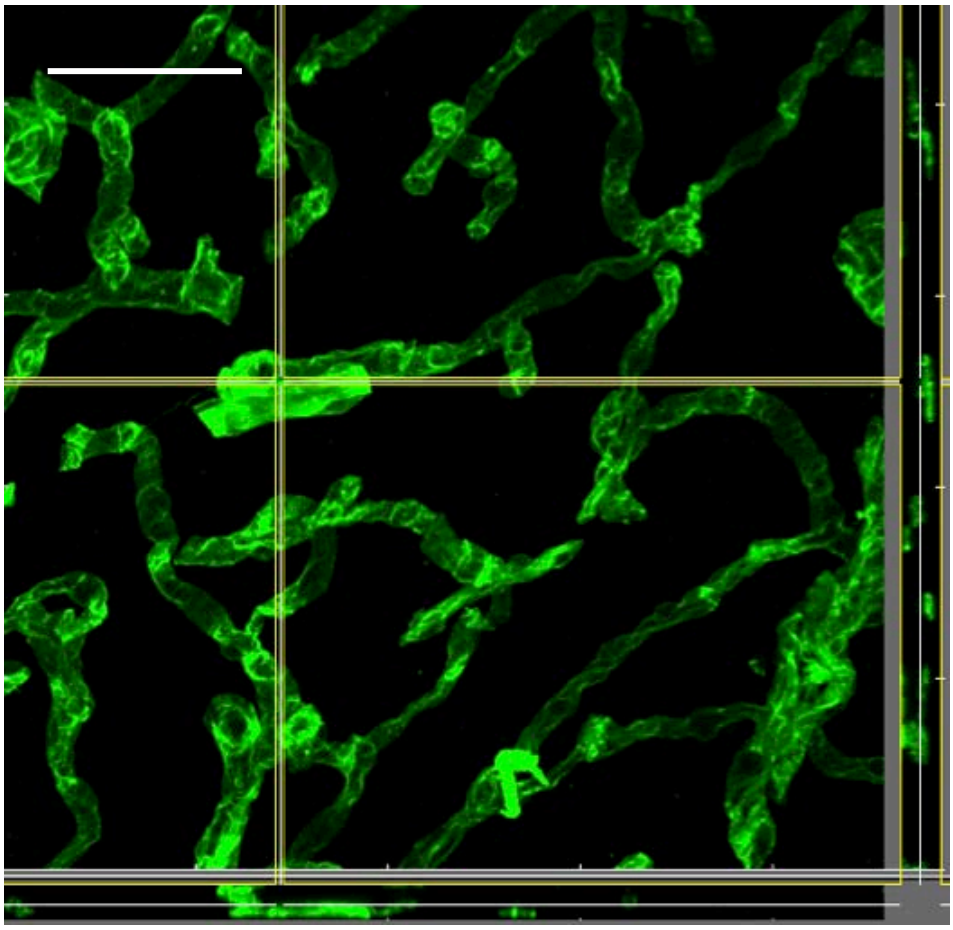

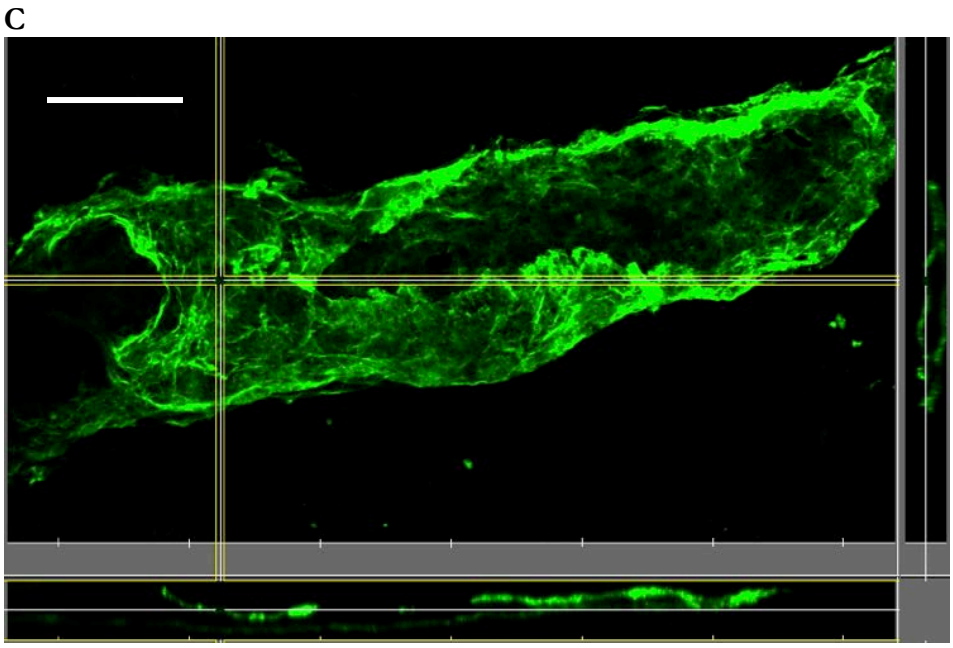

Figure 35. Three orthogonal views of GBM blood vessels showing the tubular structure as visualized in 3D. Orthogonal views illustrating the 3D structure of blood vessels from normal cortical tissue (**A**) and a GBM vascular network (**B**). Amplified view of a GBM vessel (C). Collagen IV (green). Both scale bars A and B, 70 μm and C, 40 μm.

We then created hypermosaics to visualize collagen-IV^{+} BV distribution over extended areas (approximately 4 mm^{2}) of normal cortical tissue and representative GBM tissue. Figure 36 juxtaposes two such hypermosaics and provides an overview of some general morphological differences in vasculature between the two. Figures 37 and 38 are amplified views from the two hypermosaics in Figure 36. The hypermosaics demonstrate convincingly the aberrant vessel organization associated with GBM. In the normal tissue vessel diameters seem for the most part uniform and cover the entire sample area whereas dispersion in GBM seems more erratic and vessel diameters appear more variable.

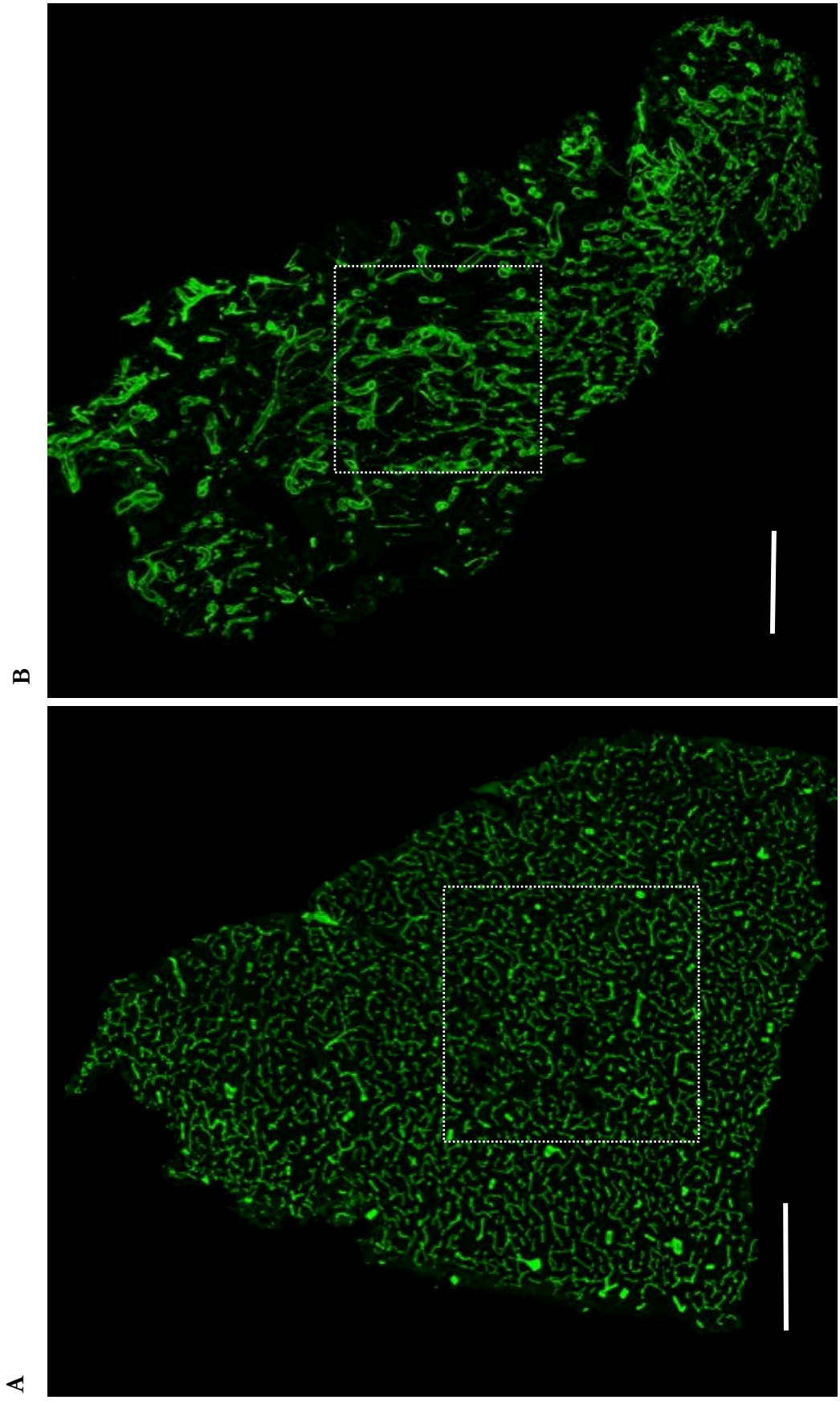

Figure 36. GBM vessel organization is much less ordered and vessel sizes are more variable than in normal cortical tissue. The two images above are hypermosaics of normal (**A**) and tumor (**B**) full sample tissue areas. Vessel sizes are less uniform and more extreme in GBM tissue than in normal tissue. BV distribution also appears less homogenous in GBM than in normal cortical tissue. Scale bars 1000 µm.

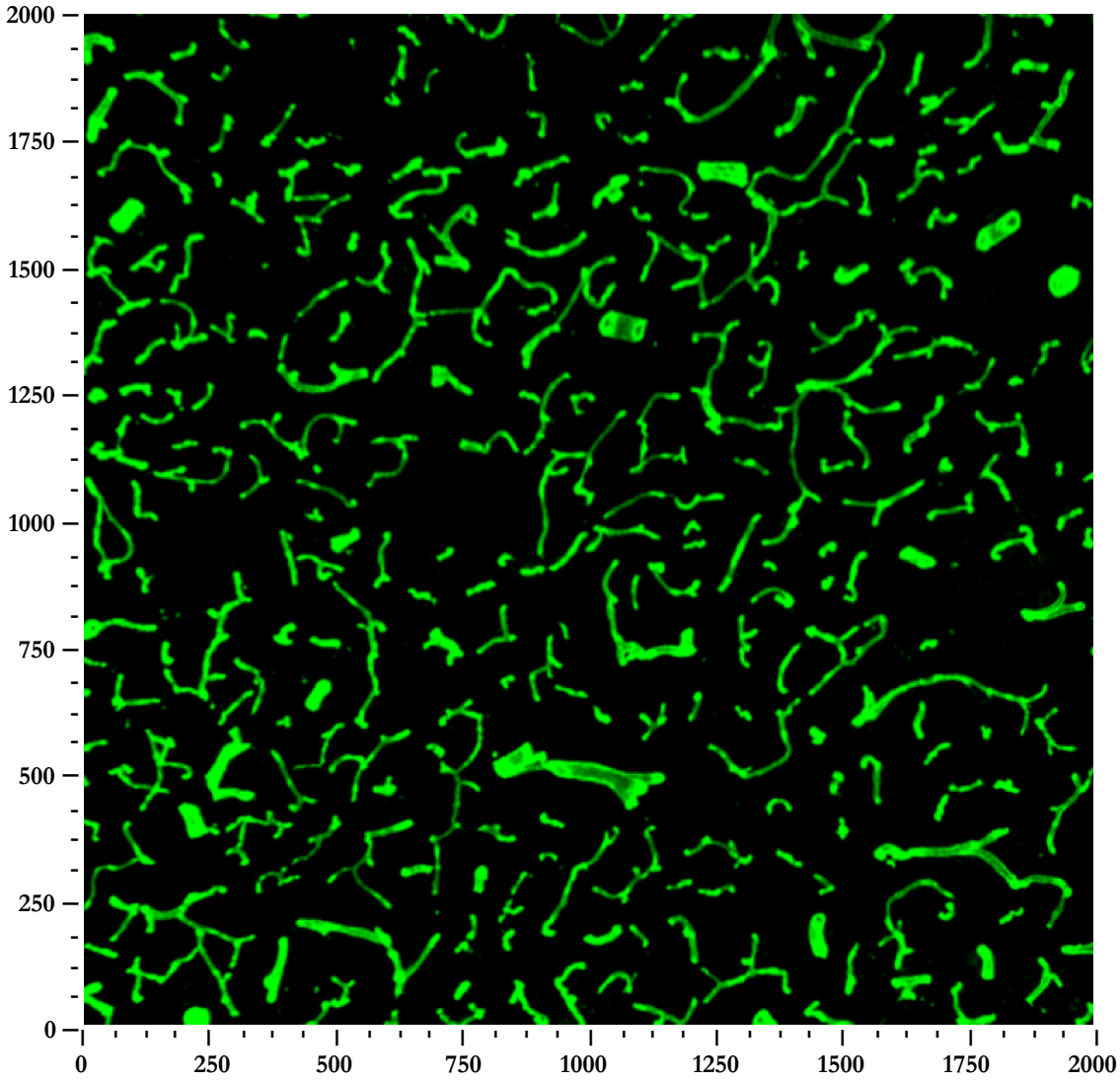

Figure 37. Amplified view of large area of normal cortical tissue showing orderly vessel organization and distribution and more uniform vessel sizes. The above image is shows a 4-mm² area amplified from the hypermosaic of normal cortical tissue in Figure 36(A). Note that while the size of vessels varies, in general the degree of variation is minimal.

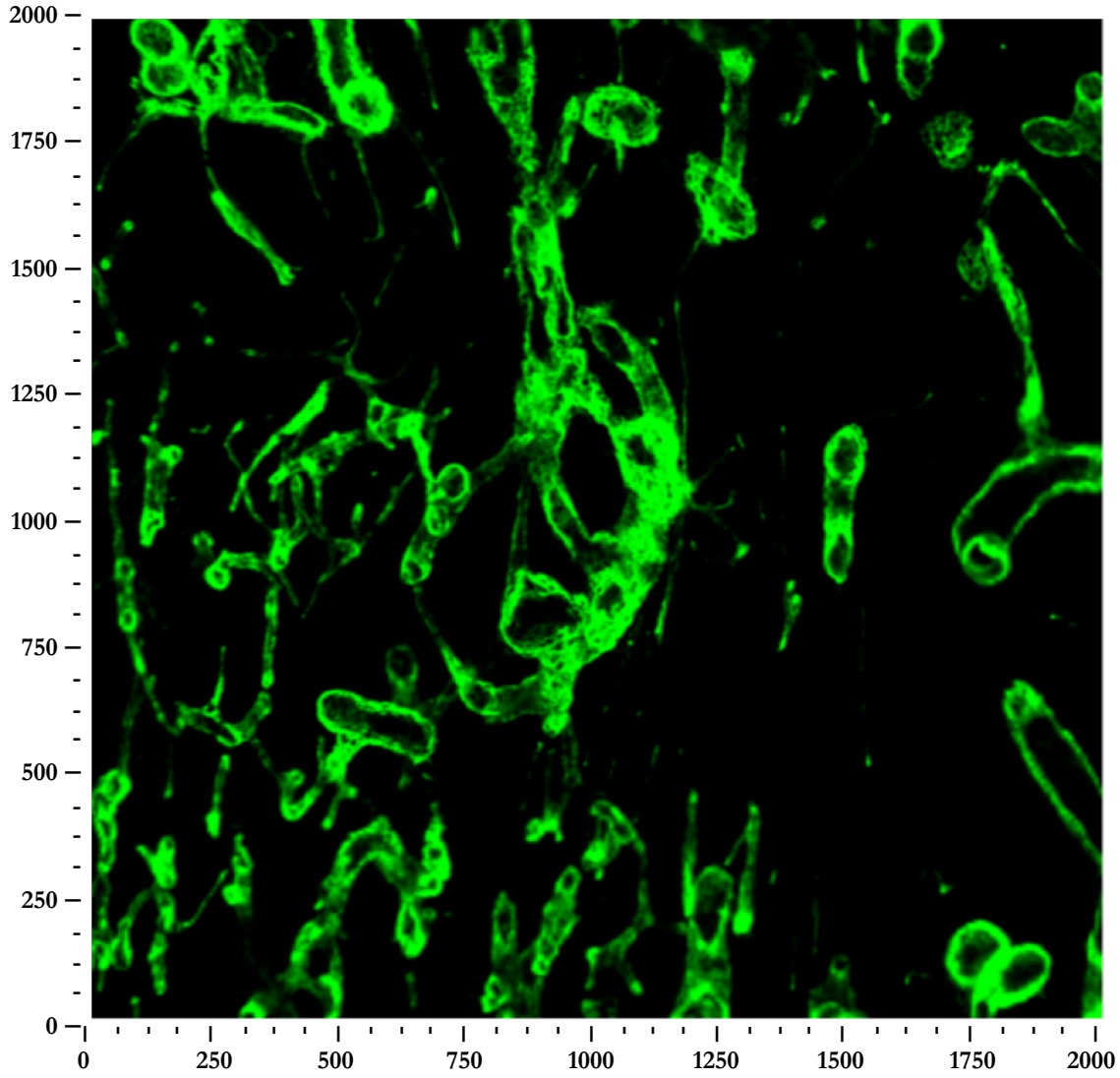

Figure 38. Amplified view of large area of GBM tissue showing disorganized vessel distribution and more variable sizes. The image shows a 4-mm² area amplified from the hypermosaic of GBM tissue in Figure 36(B). Note the generally greater variation in vessel size, higher variability in fluorescence and the disorganized spatial arrangement of the vessels.

We also observed differences in BV collagen IV distribution progressing from normal to more aggressive tumors (lower to higher Ki67% indices) (Figure 39). The vascular bed appears denser and more chaotic as Ki67% index increases and in the most aggressive tumors it is sometimes difficult to discern individual vessels from the mass.

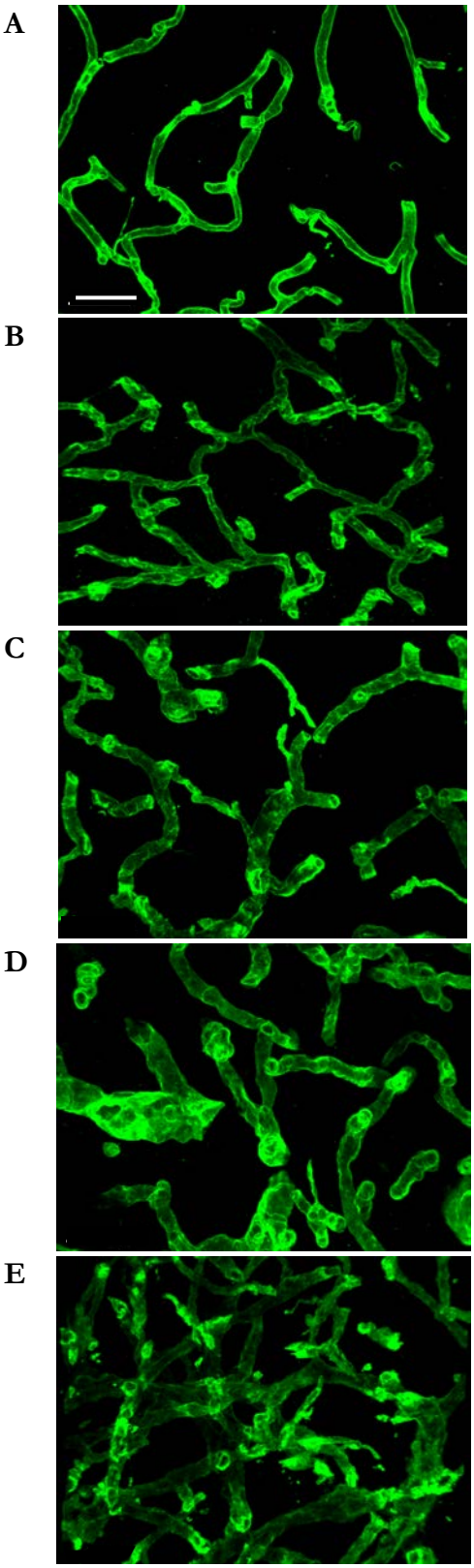

Figure 39. Normal and GBM tissue showing visible differences in BVs as tumors are progressively more aggressive. Blood vessels from normal (**A**) and GBM (**B**-**E**) samples (10, 20, 30 and 50% Ki67%, respectively). Collagen IV (green). Scale bar 50 μm.

We therefore measured collagen IV expression as total surface area and volume in normal cortical tissue and GBM biopsy samples. Our results show that there is significantly increased collagen IV expression in GBM and this increases with tumor Ki67% index but not always proportionally. Figure 40 shows confocal microphotographs and corresponding 3D reconstructions of collagen IV surface areas in one normal sample and four tumor samples with Ki67% indices of 20, 30 and 50%. Note the decreasing uniformity of vessel morphology as tumors are more aggressive and also the greatly increased type-IV collagen expression; vessel networks are both denser and more chaotic. Collagen IV surface areas vary significantly between normal and 10, 20 and 30% groups ($p<0.001$) and between normal and 50% ($p<0.0001$). A similar relation holds for normal vs. all tumors as a group ($p<0.001$).

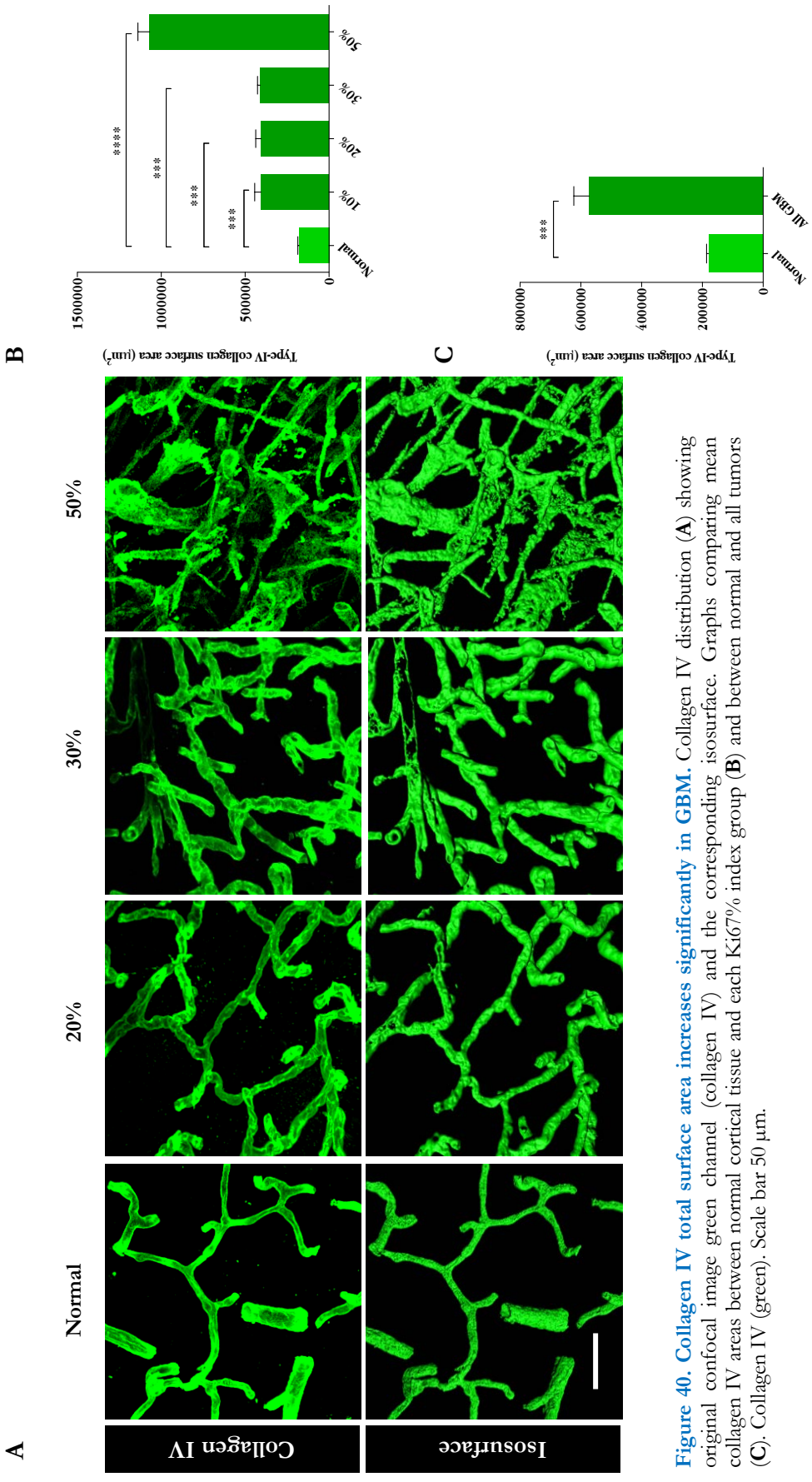

Figure 40. Collagen IV total surface area increases significantly in GBM. Collagen IV distribution (**A**) showing original confocal image green channel (collagen IV) and the corresponding isosurface. Graphs comparing mean collagen IV areas between normal cortical tissue and each Ki67% index group (**B**) and between normal and all tumors (**C**). Collagen IV (green). Scale bar 50 µm.

Furthermore, we measured vessel density or total collagen IV volume of the 3D isosurfaces created with Imaris software and compared these with increasing tumor aggressivity (Ki67% index). The microphotographs and 3D reconstructions in Figure 41 show the substantial increase in overall type-IV collagen expression and how vessel structure appears to degrade, and surfaces seem less continuous. Normal vessels (Figure 41A) are evenly distributed and uniform structurally, the 10% Ki67 vessels (Figure 41B) are larger and more numerous but still retain some degree of uniformity. The 20-50% Ki67 BVs (Figure 41C-E) are increasingly aberrant - denser, more chaotically distributed and with greater basement membrane disruption. Volume differences between groups with indices of 10, 30 and 50% were significant ($p<0.05$, 0.0001 and 0.0001 respectively) compared with the normal cortical tissue, as were the grouped measures for all tumors compared to normal (<0.0001). The 20% group was not significantly different from normal tissue (see Figure 42).

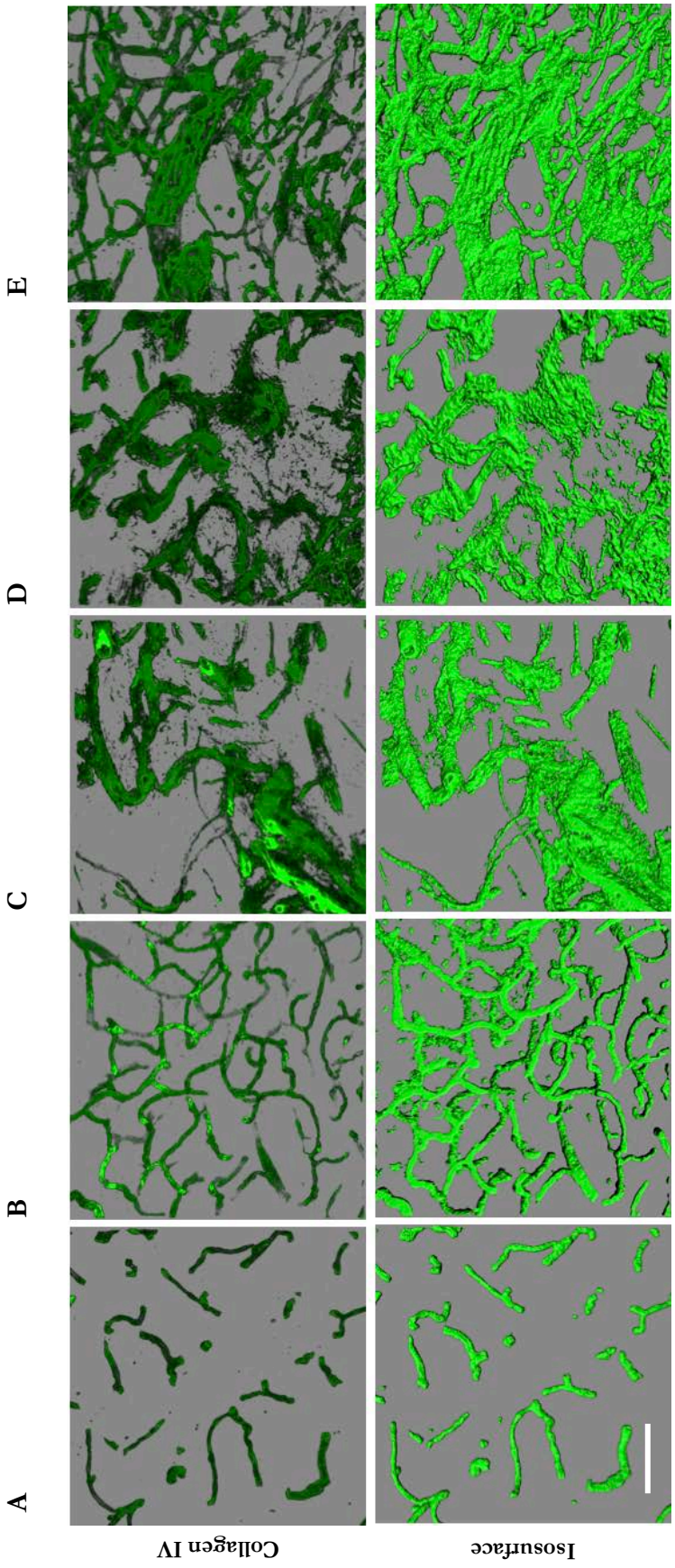

Figure 41. Vessel volume increases in GBM suggesting the creation of either more or larger vessels, or both. Normal (**A**) and tumor (**C-E**) confocal images (green channel marking collagen IV basement membrane) and 3-D isosurfaces (vessels also green) show a progressive increase in vessel density (as measured by total collagen IV volume) with increasing histological grade (tumor samples C-E are Ki67% 10, 20, 30 and 50%, respectively). Scale bar 100 μm.

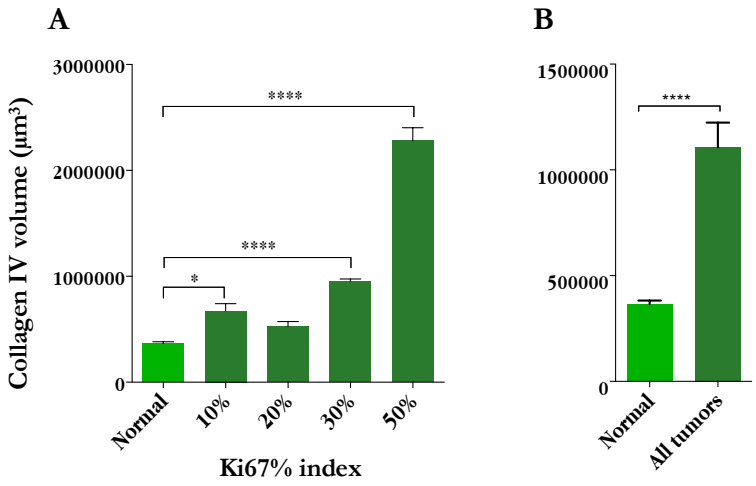

Figure 42. Collagen IV volume increases significantly in GBM as Ki67% index rises. Total collagen IV volume compared individually (A) between normal cortical tissue and separate tumor groups and between normal tissue grouped GBM samples (**B**).

With such striking differences between normal and GBM tissue with respect to type-IV collagen expression, we though it important to try to ascertain whether the significant increases in area and volume of collagen IV represented an increase in the number of BVs, their size or both. As such, we further studied certain vessel characteristics like vessel caliber, branching and vessel wall luminance in detail.

5.3.2 Diameters

Presented here are quantifications of blood vessel diameters in normal cortical tissue and four human GBM biopsy samples (Table 4 and Figure 43).

Table 4. Vessel diameter variations in GBM and normal tissue

Parameter	Control	GBM 10	GBM 20	GBM 30	GBM 50	All Tumors
Maximum	72.49	74.66	93.67	107.22	183.85	183.85
Minimum	0.64	0.26	0.56	1.36	0.88	0.255
Median	7.75	9.45	9.39	12.69	10.77	10.14
Standard Deviation	5.66	5.79	6.94	7.51	18.52	11.29

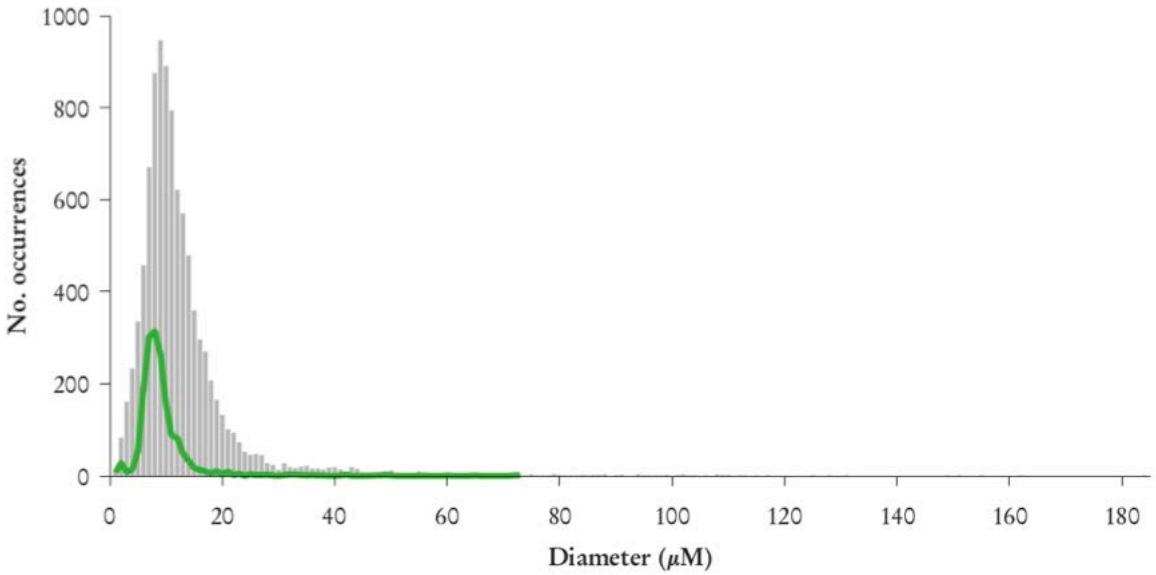

Figure 43. Blood vessel diameters are more varied in GBM than in normal tissue. Comparison of vessel diameter distributions between control (green line) and tumors (gray bar graph). The distributions have similar shapes but maximum, minimum and median size and standard deviation in tumors are extreme in contrast with normal vasculature.

Mean vessel diameters of all groups were compared separately with normal cortical tissue and all groups individually showed significant differences from the normal group (p=0.0001, all groups). The same applies for the comparison of all tumors (grouped values) with normal samples (p=0.0001). See Figure 44.

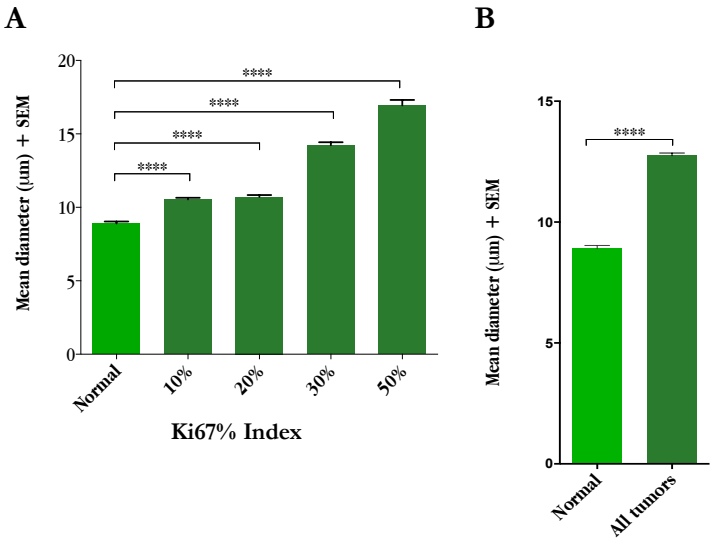

Figure 44. GBM blood vessel diameters are significantly greater than in normal vessels. All tumor groups (Ki67% 10-50) showed significant differences in BV diameters compared with the normal group (**A**) as did grouped values for all tumors compared with the normal samples (**B**).

Because one of the strategies linked with tumor-associated angiogenesis is the recruitment of "silent" BVs, so defined because their diameter is insufficient to permit blood cells to flow through them, we were interested in examining differences between the relative frequency of small vessels (arbitrarily 5 μm or less) in normal and tumor samples. The total number of BVs measuring ≤ 5 μm in diameter was counted in each sample and then compared with the total number of vessel measurements taken for that sample (Figure 45). The grouped results for tumors versus normal tissue were then compared.

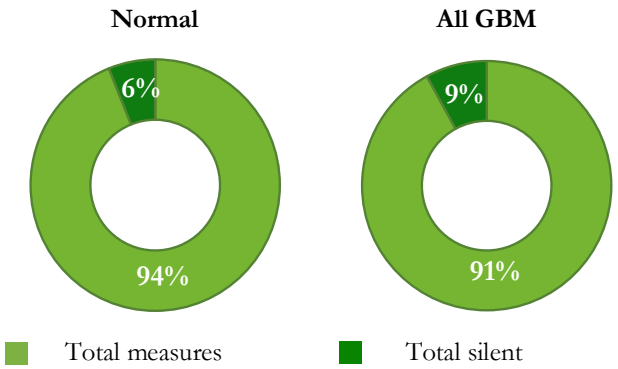

	Normal	All Tumors
Total silent vessels	110	826
Total vessels measured	1704	9546
Silent vessels as % of total	6.46	8.65

Figure 45. Percentage of blood vessels ≤5 μm diameter is not significantly different between tumor and normal cortical tissue samples. Samples varied in the number of BVs with small diameters but differences between GBM and normal samples were minimal.

Thus, according to our results, recruitment of silent vessels does not seem to play a prominent role as a neovascularization strategy.

5.3.3 Branching

Because of the importance of neovascularization in GBM tumor growth, we thought it relevant to investigate what effect, if any, on total BVs might be associated with tumor aggressivity. However, accurate quantification of BVs presents difficulties, particularly in the case of highly aggressive or advanced tumors where the vascular network is chaotic and extremely dense (for example Figure 41E). Because simply creating a new branch could be an effective basic strategy for vascularization, vessel branching might be seen as an indirect indication of the degree of neovascularization (i.e. more new vessels, more branches) and examining and quantifying branching types may provide clues as to what might be the preferred angiogenic strategies.

Figure 46 is a schematic depiction of the relative sizes and distribution of vessel branching points in Figures 37 and 38. Branching points are somewhat randomly distributed over the

entire sample implying fairly even blood perfusion throughout the tissue. On the other hand, the GBM vessels have larger diameters and are generally enlarged, more irregular and much less evenly distributed.

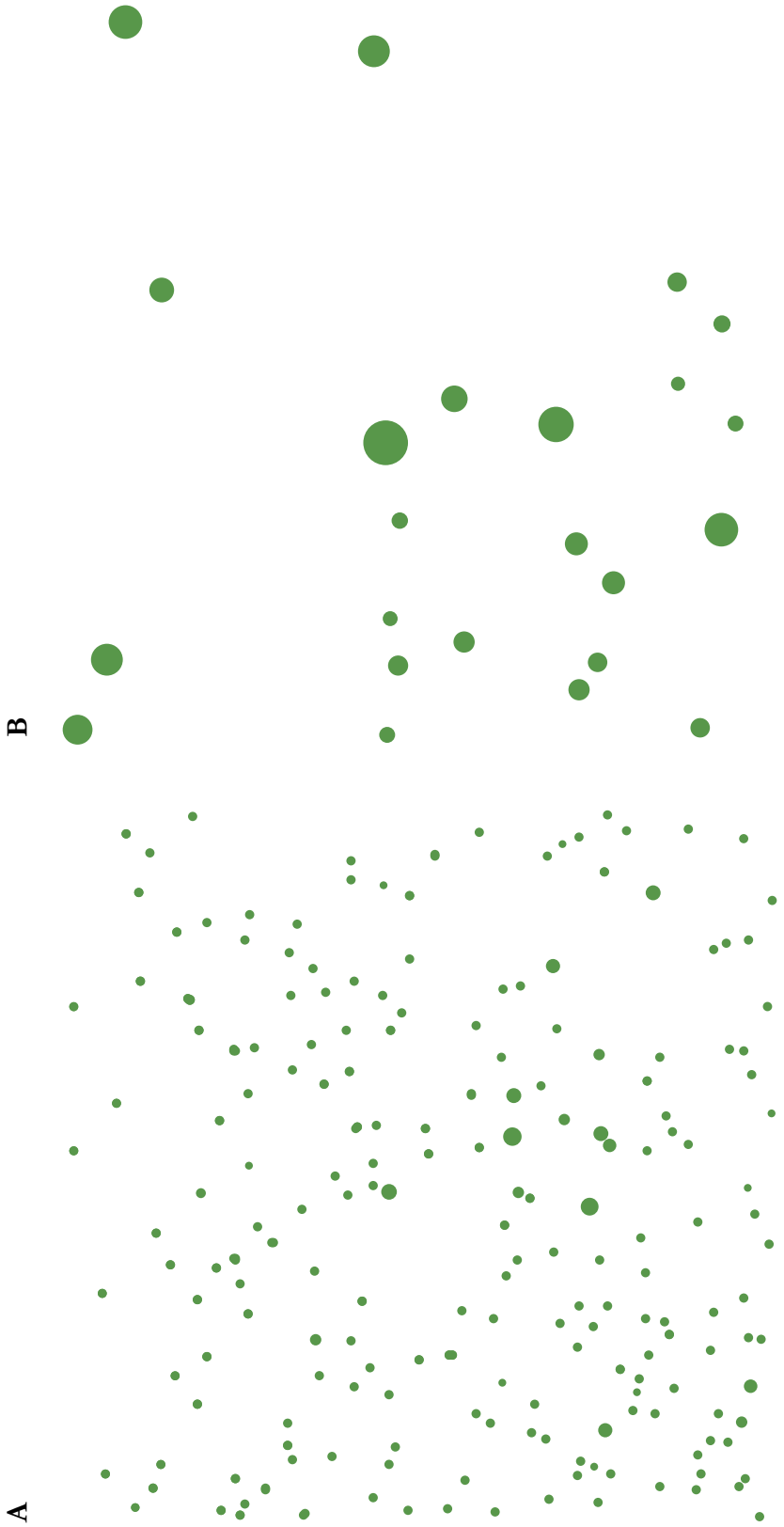

Figure 46. Distribution of branching points differs greatly between GBM and normal cortical tissue showing more disorderly vessel organization and uneven distribution of vessels as well as more variable vessel calibers in GBM. By extracting only the branching points from the two images in Figures 37 (**A**) and 38 (**B**), the level of disorganization and uneven distribution of vessels becomes more apparent. Each circle represents a branching point and the size of the circle is roughly proportional to the diameter of the branching vessels. Note that the dots in image **A** more or less cover the entire surface area of the sample whereas in **B** there are large areas without vessels and presumably without reliable blood supply.

As mentioned in the methods section, we ruled out using Imaris' "Filament Tracer" tool and opted to count BVs and branching points manually. In fact, quantifying single branching also happens to be the best stereological method for estimating BV counts (Nyengaard et al., 1988). As a first approximation, we classified three types of branching: primary (single ramifications), secondary (two ramifications) and tertiary (three or more ramifications). These were quantified and compared between normal cortical tissue and GBM. Figure 47 shows the relative numbers of the various branching types. Mean primary branching in tumors tends to increase with tumor severity (Figure 47A) but the trend is not significant.

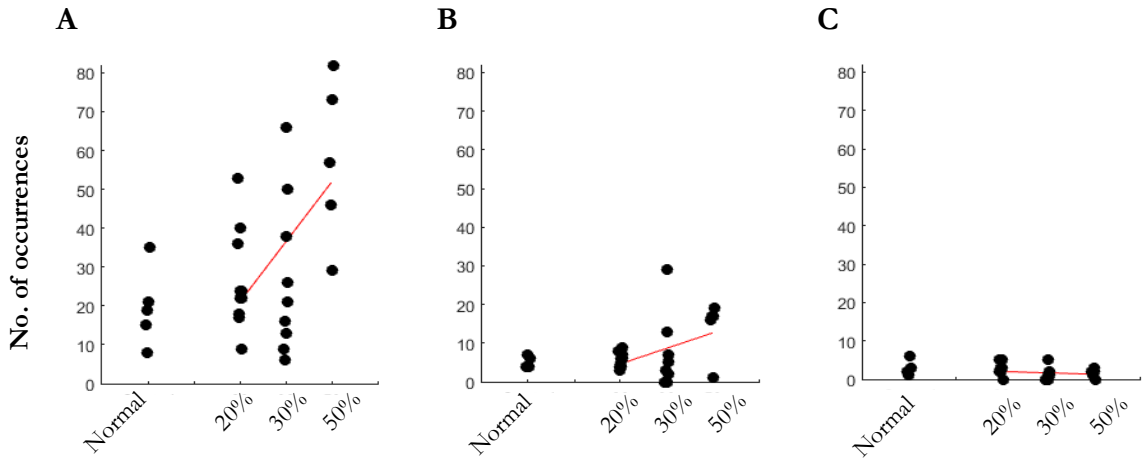

Figure 47. Primary, secondary and tertiary branching in GBM and normal vasculature. Scatterplots shows mean primary (**A**), secondary (**B**) and tertiary branching (**C**) in normal and GBM samples (x-axis shows Ki 67% indices).

Because tertiary branching (three-or more ramifications) occurred infrequently, to quantify vessel branching we decided to classify branches in two categories either single (simple bifurcations) or multiple (multiple bifurcations). There was little variation between tumors and normal samples with regards to single versus multiple branching, 71 and 29% and 78 and 22% single and multiple branching in normal tissue and tumors, respectively. An average of 20 single and eight multiple branches were counted per field in normal tissue and 32 single and nine multiple branches in tumor samples. The result is not statistically significant ($p=0.1473$). See Figure 48.

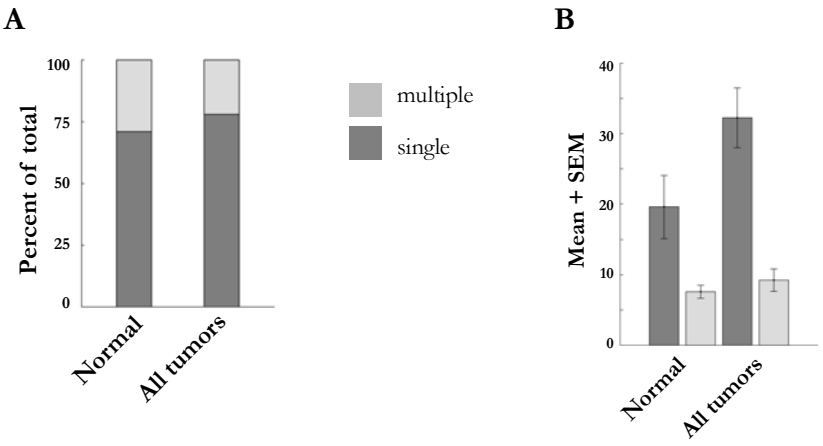

Figure 48. Branching in GBM and normal vasculature is preferentially by simple bifurcation. Single and multiple vessel branching compared in normal and GBM samples (**A**) and the mean+SEM of single (dark gray) and multiple (light gray) branching types in normal tissue and tumors (**B**).

5.3.4 Basement membrane deposition density and integrity

As mentioned previously, along with vessel diameters, the integrity and organization of the basement membrane is hemodynamically critical. We therefore devised a method to quantify collagen IV density along vessel walls to compare normal and GBM basement membranes. Although the highly disorganized distribution of vessels and large variations in vessel numbers, size and diameter in GBM are striking, the differences in the vessel walls themselves are perhaps even more remarkable (see Figure 49), with tumors showing multiple fenestrations and areas of uneven collagen IV deposition. By contrast, normal cortical tissue shows BVs with even layering of type-IV collagen and homogenous dispersion throughout the basement membrane surface.

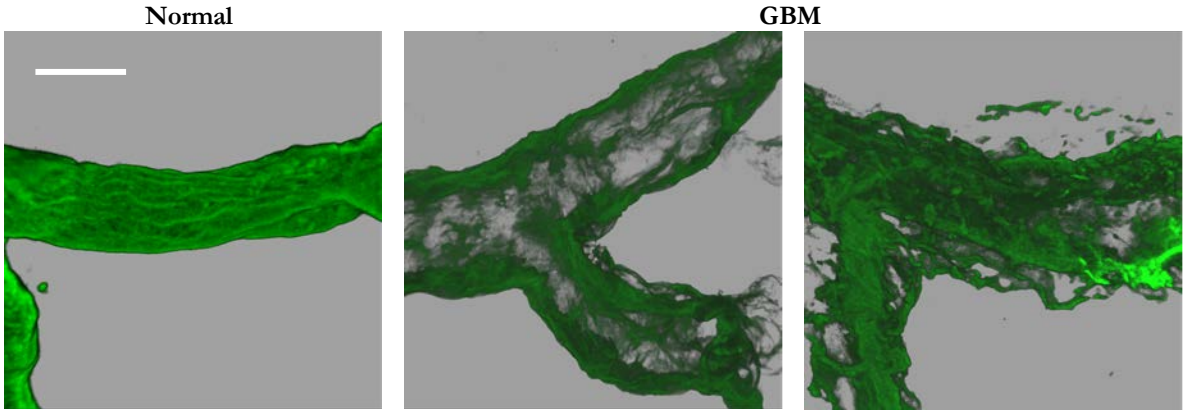

Figure 49. GBM BV basement membrane differs from normal cortical tissue and varies widely among different tumors. Normal cortical and GBM blood vessel show wide variations in the type-IV collagen relative fluorescence as seen in these confocal microphotographs. Scale bar 10 μm.

Figure 50 shows confocal photos alongside luminance surface plots generated in Fiji, which show collagen-IV luminance variations over a small area of BV membrane. Note that in GBM tissue the luminance is less uniform, i.e. peaks and valleys in the luminance surface plots are higher with more pronounced peaks and valleys. The tumors show areas of highly concentrated fluorescence and dark areas devoid of fluorescence, suggesting gaps or fenestrations in collagen-IV deposition as reflected in the luminance plots.

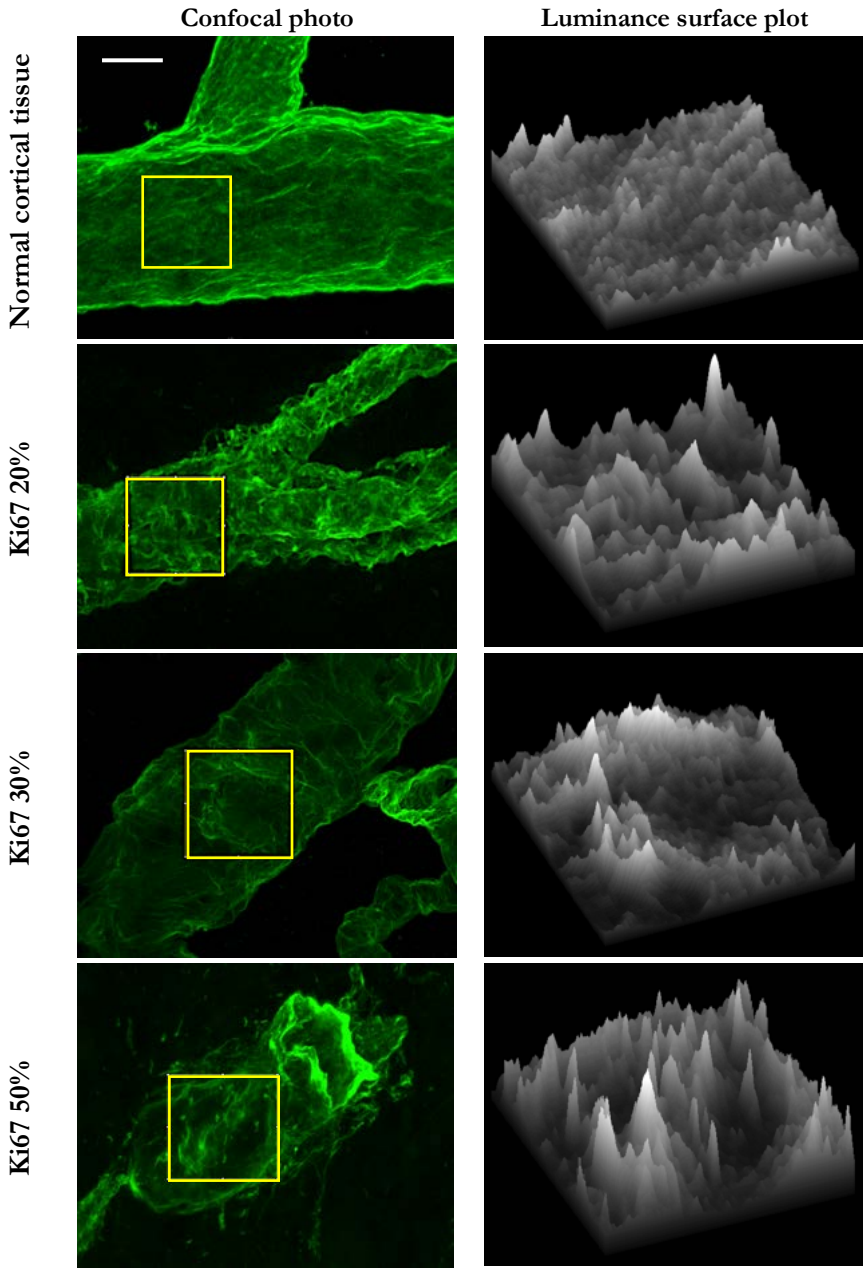

Figure 50. Collagen IV distribution is less uniform and more discontinuous in GBM. Comparing confocal photographs and luminance surface plots of type-IV collagen distribution in normal cortical tissue and GBM highlights the clear fenestration of vessel basement membranes and bright and dark areas of collagen IV concentration, showing the uneven dispersion of collagen IV. Scale bar 10 μm. Photos by author.

To quantify variations in BV relative fluorescence, forty images were analyzed, ten from each of the four samples (one normal and three GBM samples, with Ki67 indices of 20, 30 and 50%). Typical relative fluorescence profiles are shown in Figure 51.

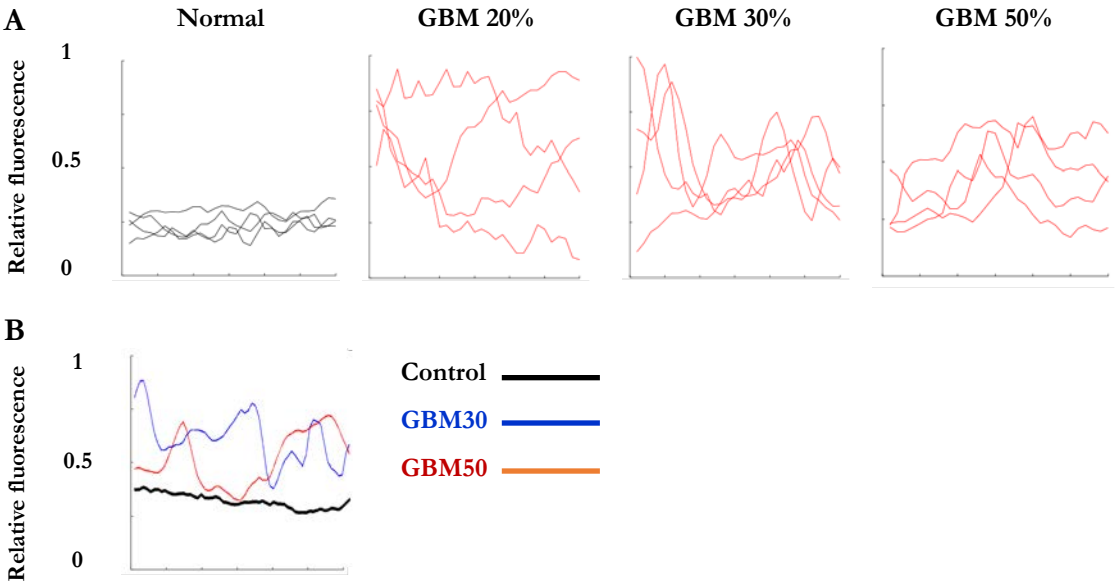

Figure 51. Collagen IV deposition is altered in GBM as reflected in the greater variability of basement membrane collagen IV relative fluorescence between normal and tumor samples. The figures show line plots (**A**) of relative fluorescence measures taken along short segments of normal and GBM BV walls. The x-axis represents the individual measures (n=30), and y is the corresponding normalized relative fluorescence value. The lower panel (**B**) superimposes relative fluorescence plots of three individual samples (one normal and GBM 30 and 50%).

Comparison of mean standard deviations of basement membrane vessel wall luminance between normal cortical tissue and GBM showed significant differences between the normal and 20 and 30% groups ($p=0.0001$). Differences between normal samples and combined tumor groups were also significant ($p=0.0001$). See Figure 52.

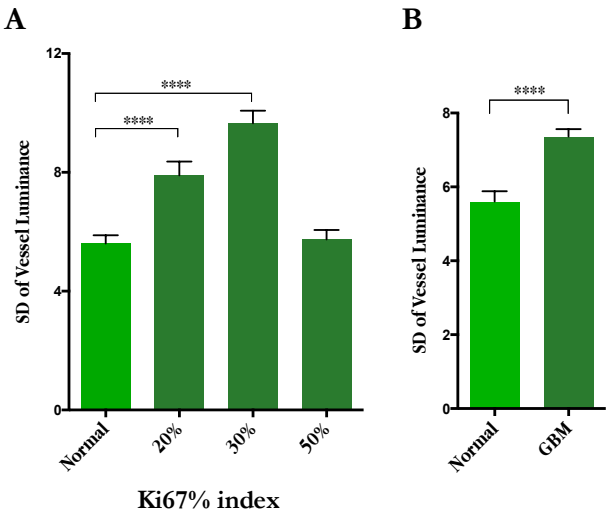

Figure 52. Vessel basement membrane collagen IV fluorescence shows significantly greater variability in GBM compared to normal vasculature. Mean standard deviations of GBM vessel wall relative fluorescence compared with that of normal vasculature individually (**A**) and across all tumors (**B**).

An interesting corollary benefit of our investigation of collagen IV deposition was finding evidence of the intussusceptive angiogenic process. Intussusception involves formation of an interstitial pillar such that opposing lumen fuse in the middle of an existing BV effectively forming two new vessels from one preexisting vessel. This process is illustrated in Figure 4 and shown in confocal image and 3D reconstruction in Figure 53.

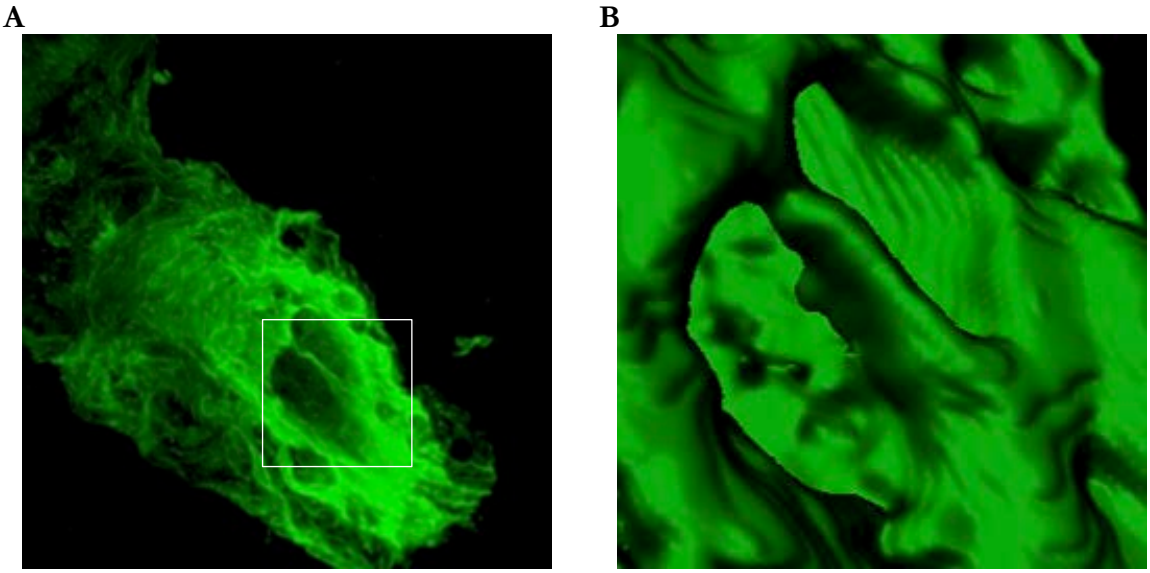

Figure 53. Intussusception is a rapid, effective means of generating new vasculature and could be an important strategy in GBM neovascularization. Confocal photograph (**A**) and amplified 3D reconstruction detail (**B**) of an interstitial pillar formation in a GBM vessel.

5.3.5 Relation of GFAP with collagen IV

Among the numerous morphological alterations involved in GBM, particularly striking are the changes in astrocyte morphology and GFAP expression and the altered relationship of astrocytes to BVs. The disruption of astrocyte-BV coupling has been well documented in murine studies like Watkins et al. (2014) and is widely believed to pave the way for the initial stages of tumor propagation. The figures below help illustrate some of these changes in human tissue. Figure 54 shows amplified views of blood vessels surrounded by GFAP-expressing astroglial or tumor cells. In normal tissue the astrocyte end feet maintain close contact with the basement membrane whereas the GBM tissue is surrounded by $GFAP^+$ cells which do not seem to make similar contact with BVs.

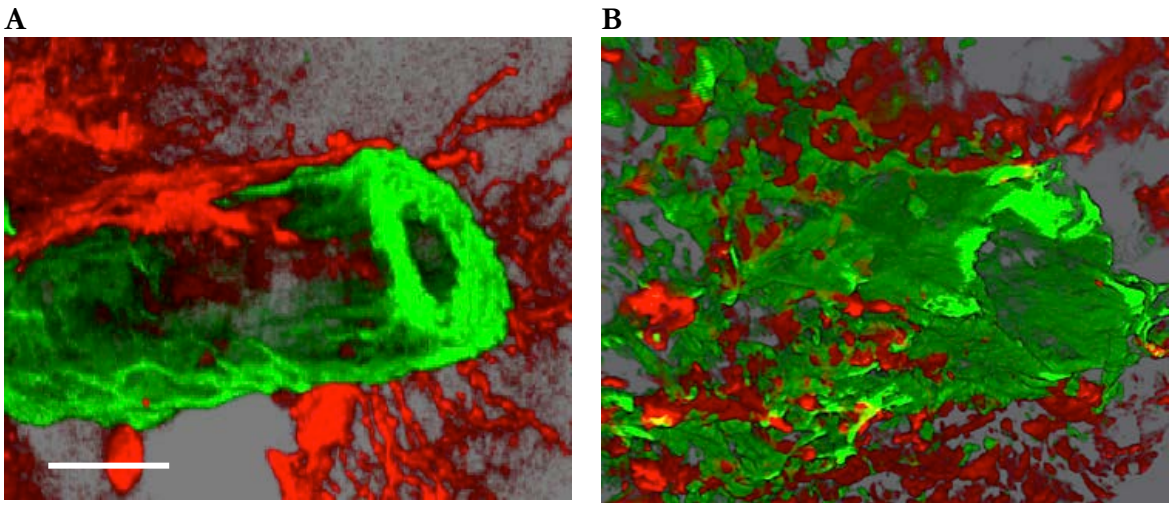

Figure 54. Close-up confocal photographs of normal and GBM tissue detail the altered spatial relationship between GFAP-expressing elements and vasculature. Normal cortical vessel with its surrounding astrocytes (**A**) and GFAP-expressing astroglial or tumor cells surrounding a GBM vessel (**B**). BVs (green), GFAP-positive astrocytes or tumor cells (red). Scale bar 10 μm.

Figure 55 shows the same samples as in Figure 30A with the addition of the collagen IV channel to show blood vessels in relation to $GFAP^+$ astroglial and tumor cells. Normal tissue shows clearly delineated BVs and a protoplasmic astrocyte. The GBM images show less clearly defined vessels and more disperse GFAP-expression and, particularly in Figure 55D, shapes characteristic of GBM, i.e. gemistocytic cells.

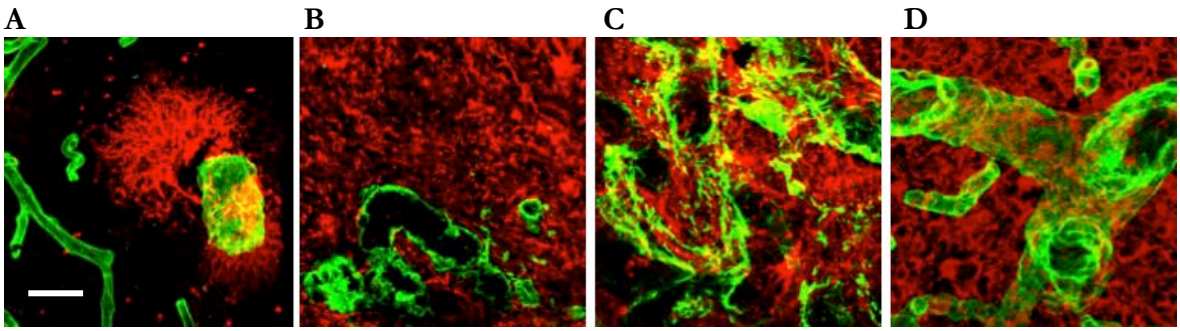

Figure 55. GFAP$^+$ astroglial and tumor cell distribution and their relationship with basement membrane varies with tumor severity. Merged view of GFAP (red) and collagen IV (green) showing normal cortical tissue (**A**) and tumors with Ki67% indices of 10 (**B**), 20 (**C**) and 30 (**D**). These are the same sample as in Figure 30A. Scale bar 40 μm.

Figure 56 shows 3D perspectives of isosurfaces depicting BVs and surrounding GFAP$^+$ elements in normal and GBM samples. These two images provide a three-dimensional view of the same phenomena described in the previous figures. The normal tissue sample shows a reconstruction of a BV and a nearby protoplasmic astrocyte. The GBM image illustrates how the GFAP$^+$ cells are more abundant and more disperse.

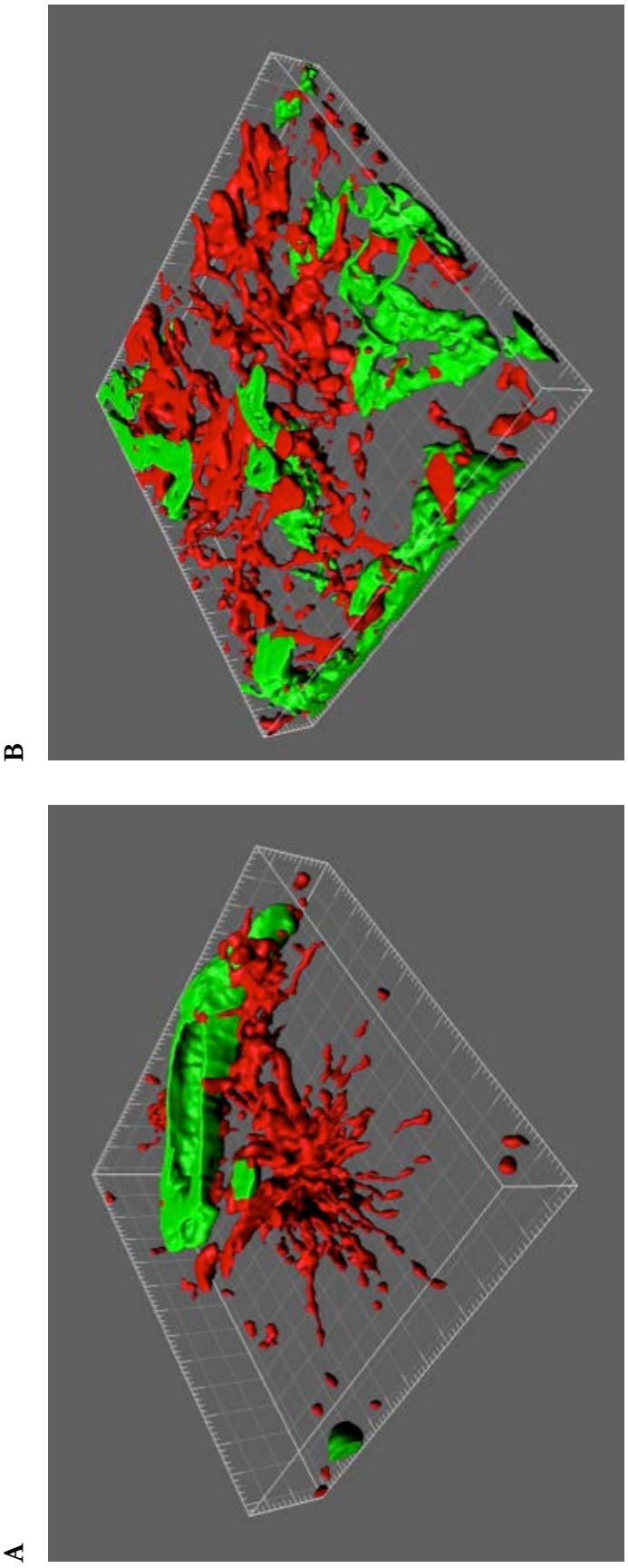

Figure 56. 3D reconstructions highlight differences in normal and GBM blood vessels in relation to surrounding GFAP-positive elements. The two images above compare three-dimensional reconstructions of normal (**A**) and tumor (**B**) BVs and the surrounding GFAP-expressing elements. Image **A** shows a typical protoplasmic astrocyte in relation to a cortical BV. **B** shows GFAP$^+$ tumor cells in relation to BVs. Collagen IV marked basement membranes (green) and GFAP-positive astrocytes or tumor cells (red). Scale bar 20 µm (large increments in frame are 10 µm).

It is generally accepted that in the initial stages of tumor invasion, GBM coopts existing vasculature and then later creates conditions for angiogenesis that result in new BVs to nourish subsequent tumor growth. Figure 57 shows what may be the initiation of the cooption process whereby a glioma cell interposes itself between the BV and surrounding cells (see Figure 2 for a graphical depiction of the same process). This process is fairly well characterized in murine models but poorly studied in humans.

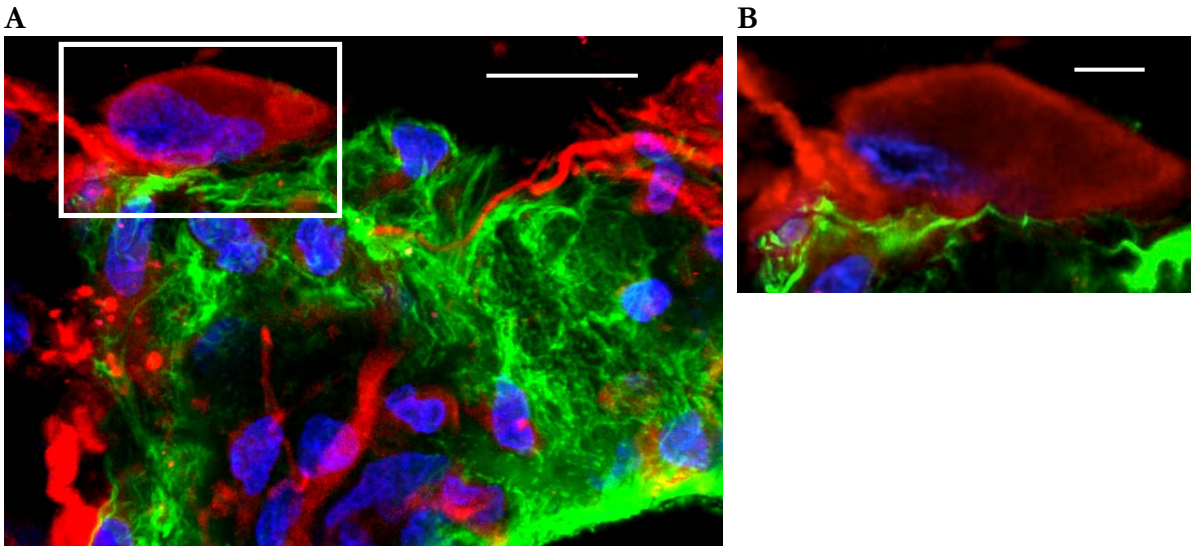

Figure 57. Evidence of glioma cell invasion or cooption along a blood vessel in human GBM. Typical gemistocytic tumor cell in an image suggesting that the cell is advancing along the BV membrane (**A**) and detail (**B**). Collagen IV (green) astrocytes and tumor cells (red), cell nuclei (blue). Scale bars A 20 μm and B 5 μm.

Pseudopalisades or hypercellular regions typically surrounding necrotic foci are pathognomonic for GBM. Figures 58 to 60 illustrate characteristic perinecrotic pseudopalisading tumor cells showing the typical cell clustering and central necrotic area and the surrounding radial $GFAP^+$ cell configuration.

A

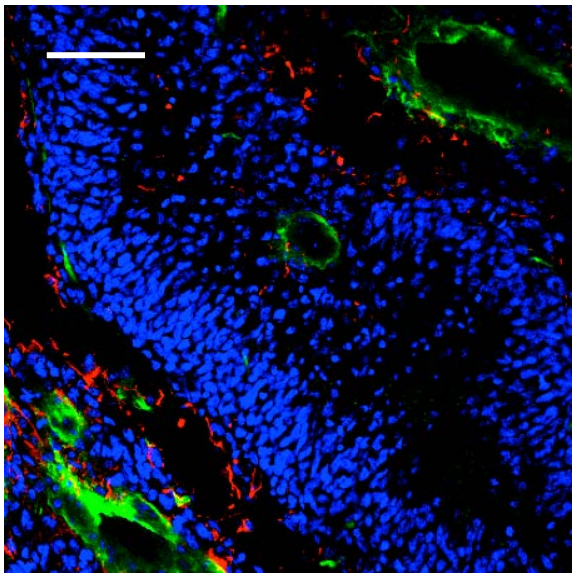

B

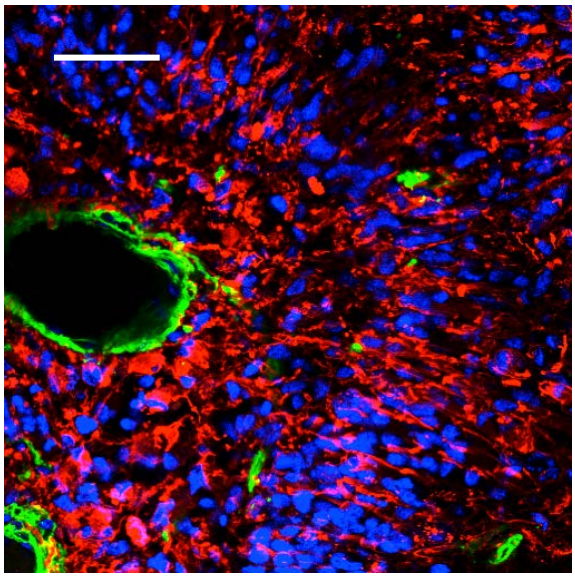

C

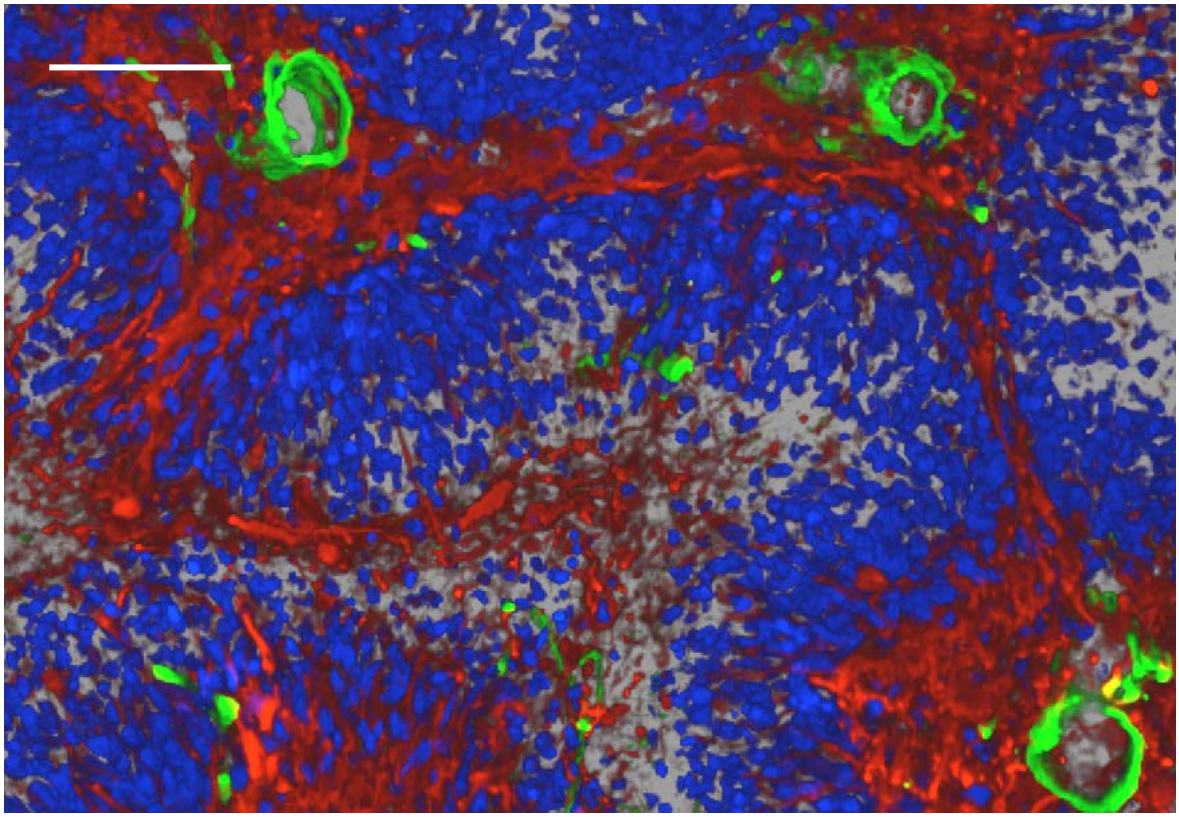

D

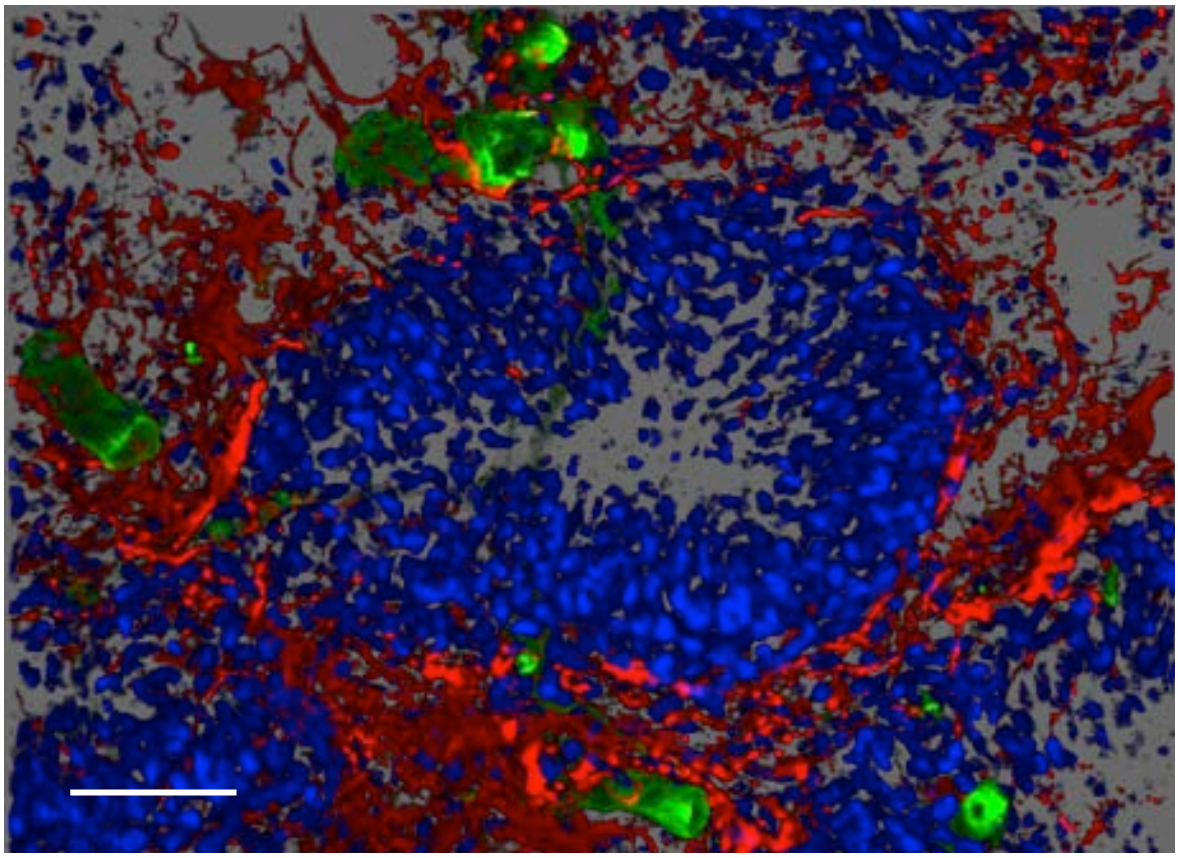

Figure 58. GBM's characteristic pseudopalisades show distinctive arrangements of BVs, GFAP$^+$ astroglial and tumor cells and cell clustering. Pseudopalisading cells in GBM tissue with a blood vessel fragment in the central necrotic area (**A**). **C**haracteristic radial arrangement of fibrous astrocytes and GFAP$^+$ tumor cells (**B**). Wider views incorporating these features (**C** and **D**). Basement membrane (collagen IV, green), astrocytes or tumor cells (GFAP, red) and nuclei (DAPI, blue) Scale bars A and D 100 μm, B 50 μm and C 70 μm.

Figure 59 juxtaposes two 3D confocal images showing a 3D perspective of the hypercellular area and surrounding GFAP$^+$ astroglial and tumor cells along with BVs in proximity to the pseudopalisading cells. Figure 60 shows a confocal image of pseudopalisading cells in GBM tissue with a central necrotic area and the surrounding fibrous astrocytes and GFAP$^+$ astroglial and tumor cells and a 3D reconstruction of the same image.

A

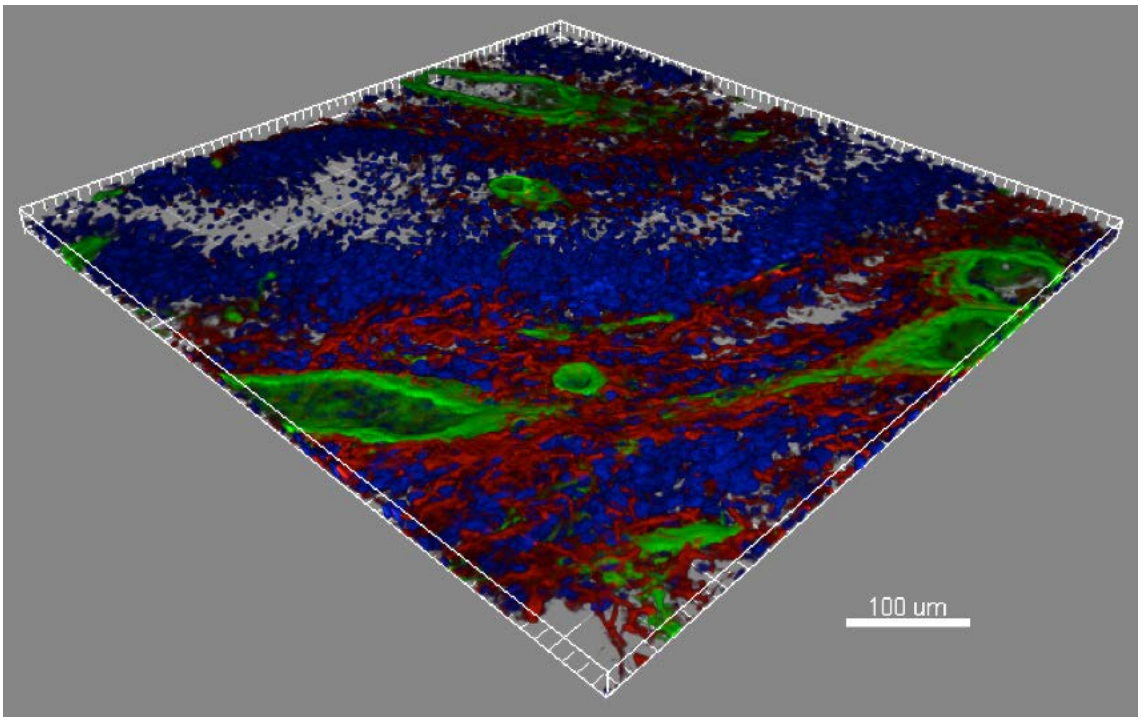

B

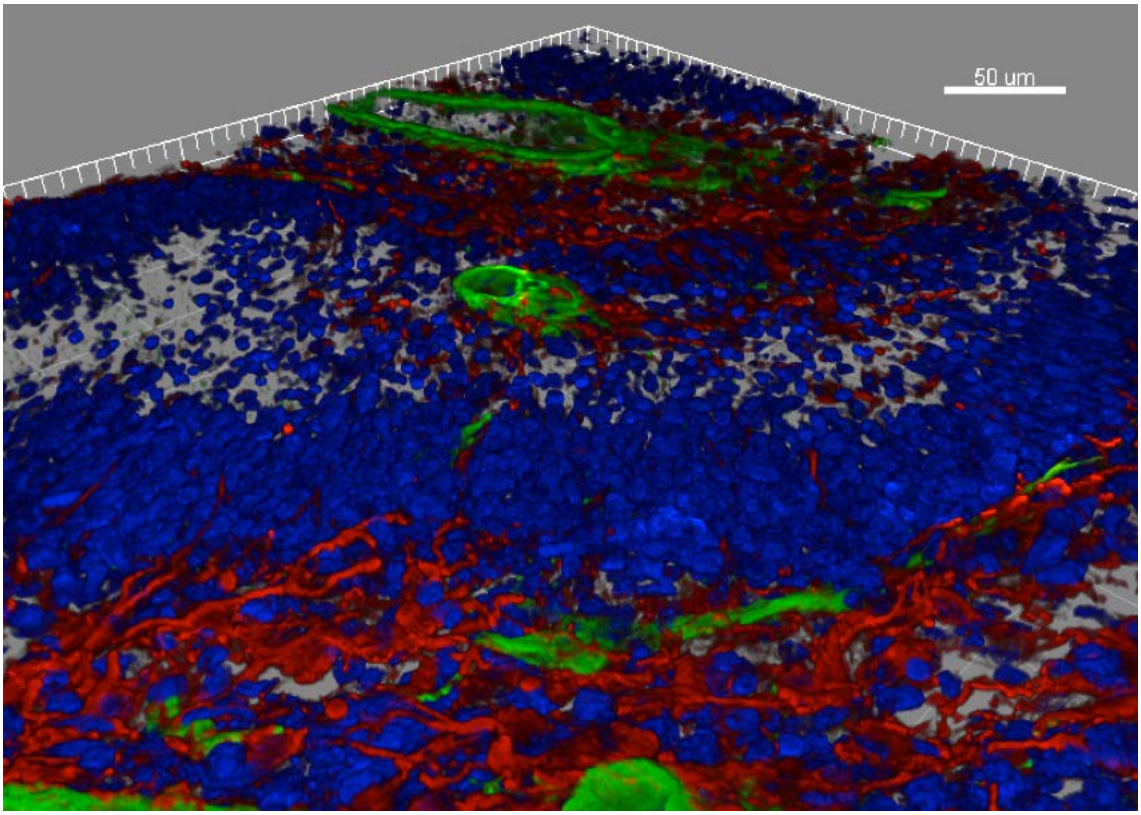

Figure 59. Astroglial and tumor cells align radially in proximity to GBM's characteristic pseudopalisade cell clusters. Pseudopalisading cells in GBM tissue with a blood vessel fragment in the central necrotic area and the characteristic radial arrangement of fibrous astrocytes and GFAP$^+$ tumor cells (**A**). Amplified view (**B**) of a section of A. Basement membrane (collagen IV, green), astrocytes or tumor cells (GFAP, red) and nuclei (DAPI, blue) Scale bars A 100 μm and B 50 μm.

A

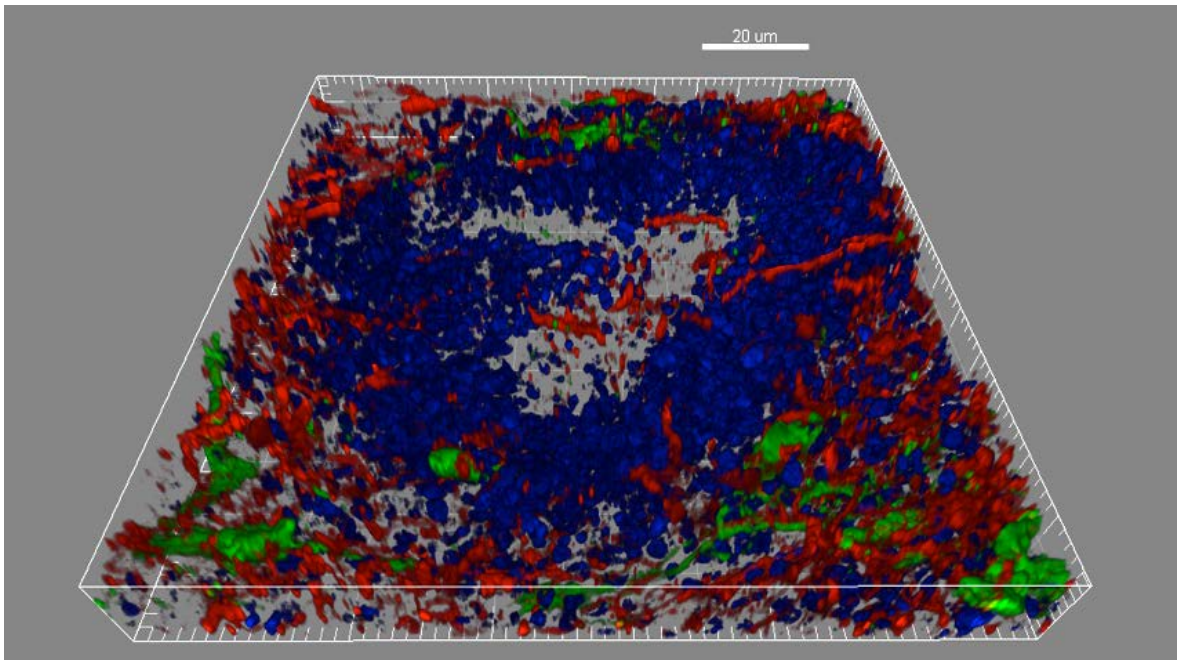

B

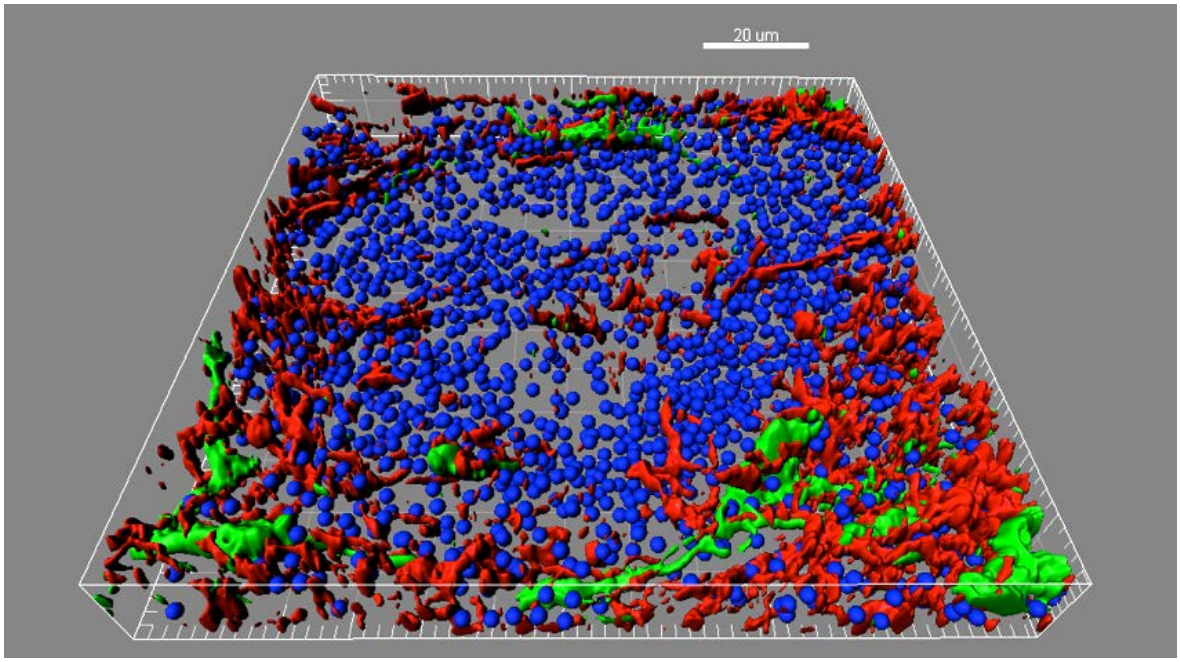

Figure 60. 3D perspective shows details of how pseudopalisades are arranged spatially. Confocal image of pseudopalisading cells in GBM tissue with a central necrotic area and the surrounding fibrous astrocytes and GFAP$^+$ tumor cells (**A**). 3D reconstruction of the same image (**B**). Basement membrane (collagen IV, green), astrocytes or tumor cells (GFAP, red) and nuclei (DAPI, blue). Scale bars 20 μm.

5.3.6 CD31 surface area and volume

Due to the abundant and significant changes in type-IV collagen expression and accompanying alterations in multiple BV parameters, we further examined BV microstructure and possible endothelial cell disruptions by measuring CD31 expression. As normal basement membrane is lined by endothelial cells, we thought that the disrupted collagen IV expression and vessel characteristics might be mirrored in changes in endothelial cells. Previous studies in mouse tumor models found evidence of disrupted basement membranes which included irregular thickness, defective association with endothelial cells and pericytes, multiple redundant layers and projections into the perivascular stroma (Baluk et al., 2014; Baluk, Morikawa, Haskell, Mancuso, & McDonald, 2003). We looked primarily at CD31 expression and later at interaction between type-IV collagen and CD31. Our results reveal that as well as an increase in collagen IV expression (described above) there is a significant increase in CD31 expression in GBM. More importantly, there appears to be a disassociation of the two which results in vessels that do not display a typical spatial organization of CD31 and collagen IV. Normal BVs have a fairly regular tubular shape and a continuous, intact endothelial lining, somewhat like a tube within a tube, whereas GBM BVs, although often tubular, displayed highly irregular shapes and showed discontinuous or, in some instances, absent endothelial linings (see Figures 61 to 64).

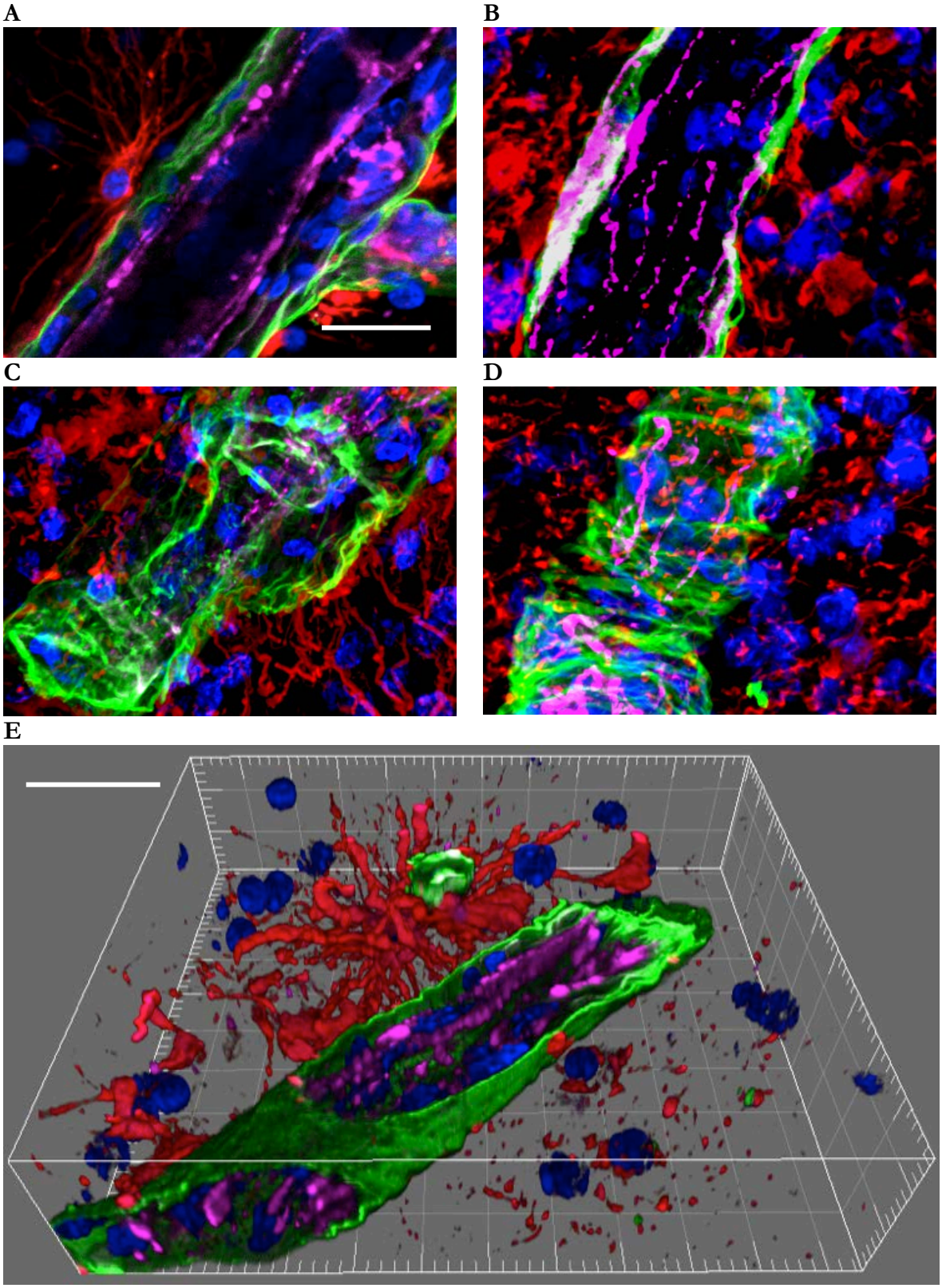

Figure 61. CD31 expression appears less regular in GBM than in normal cortical tissue and not as intimately associated with basement membranes. Typical spatial distribution of CD31 (magenta) and collagen IV (green) in normal cortical tissue (A). Note the protoplasmic astrocyte (GFAP - red) contacting the membrane surface. CD31 and collagen IV distribution in GBM (**B**-**D**) with 10, 20 and 30 Ki67% indices, respectively. 3D confocal image showing normal vessel structure (**E**). Scale bar 20 μm.

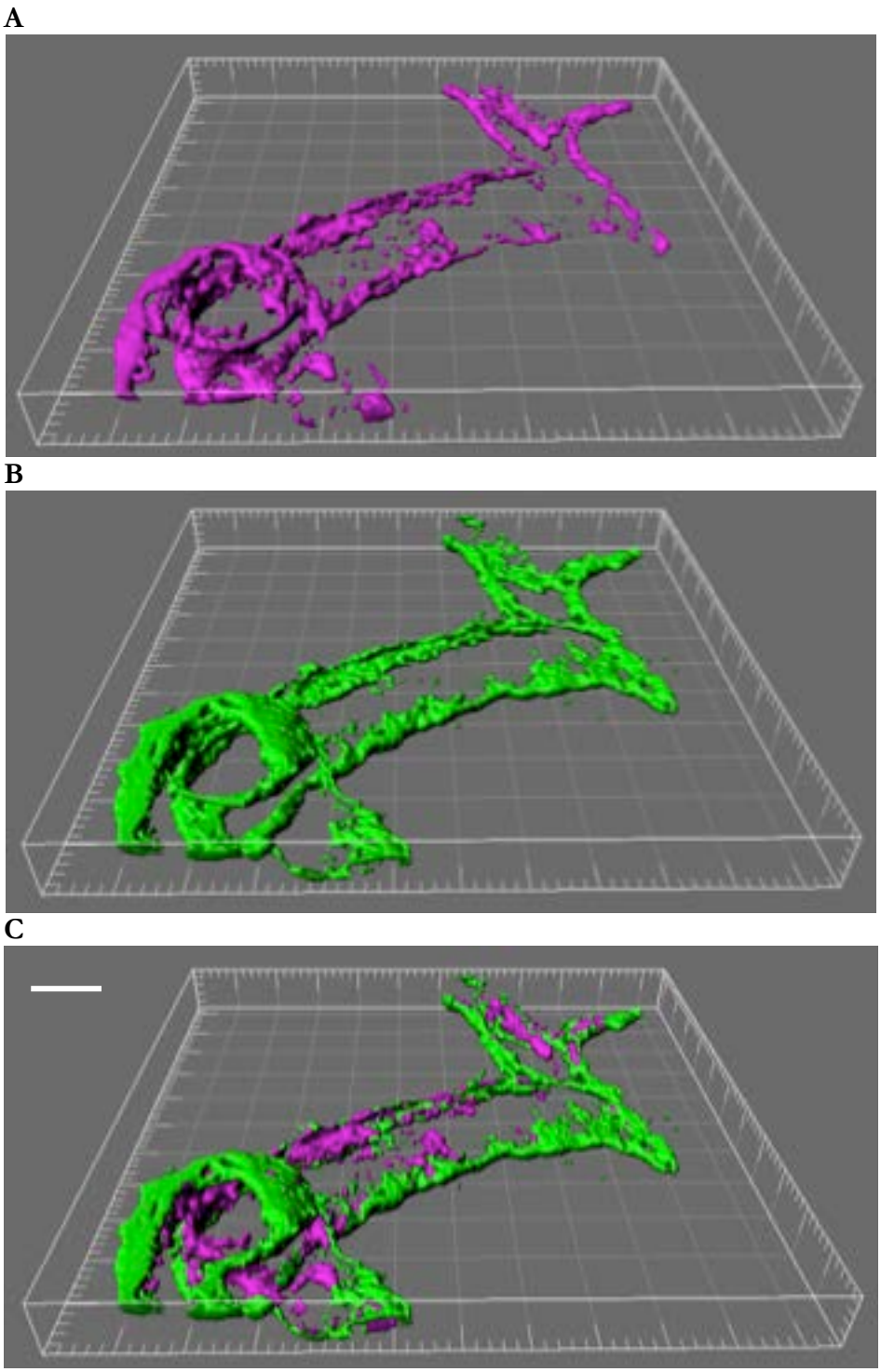

Figure 62. 3D isosurfaces demonstrate altered CD31 association with basement membranes in GBM. The three images show 3D reconstructions of CD31 (magenta) (**A**), collagen IV (green) (**B**) and a merged view of both (**C**) from GBM tissue. Scale bar 50 μm.

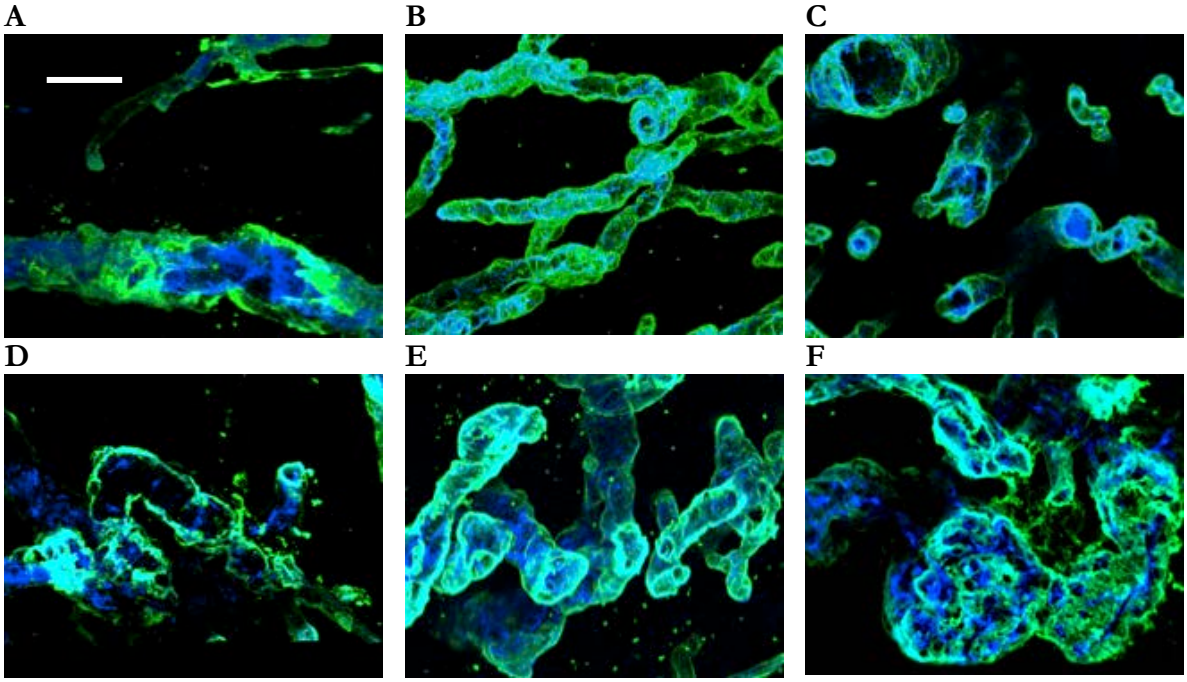

Figure 63. Additional views of disrupted CD31-collagen IV association in GBM. Six different examples (**A-F**) of the spatial organization disruption seen in GBM. Endothelial lining is discontinuous or absent, fluorescence is uneven and vessel structure is generally misshapen. Collagen IV (green) and CD31 (light blue). Scale bar 40 μm.

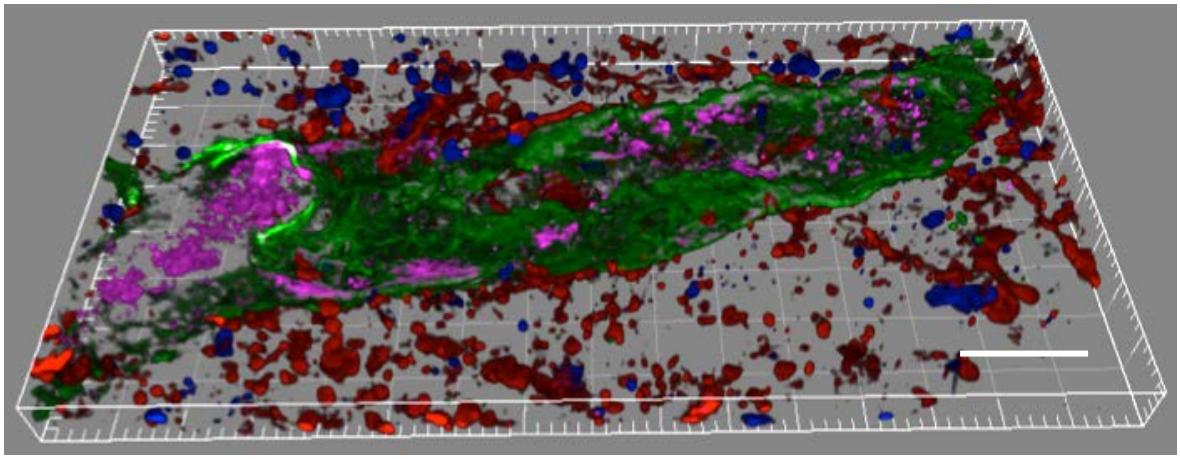

Figure 64. Three-dimensional view of GBM vessel showing relation of CD31 to collagen IV and surrounding astroglial or tumor cells. Endothelial lining is less continuous and, in some places, absent, vessel surface is uneven and surrounding GFAP$^+$ cells do not contact the basement membrane and are more dispersed than in normal tissue. Collagen IV (green), CD31 (magenta) and GFAP (red). Scale bar 40 μm.

Results from analysis of CD31 surface areas in GBM and normal samples show that CD31 expression tends to increase with tumor aggressiveness and there were significant differences between the normal cortical tissue and the 20 ($p<0.01$) and 30% GBM ($p<0.0001$) groups. Normal tissue vs. grouped GBM also showed significant differences ($p<0.01$) (see Figure 65, B and C).

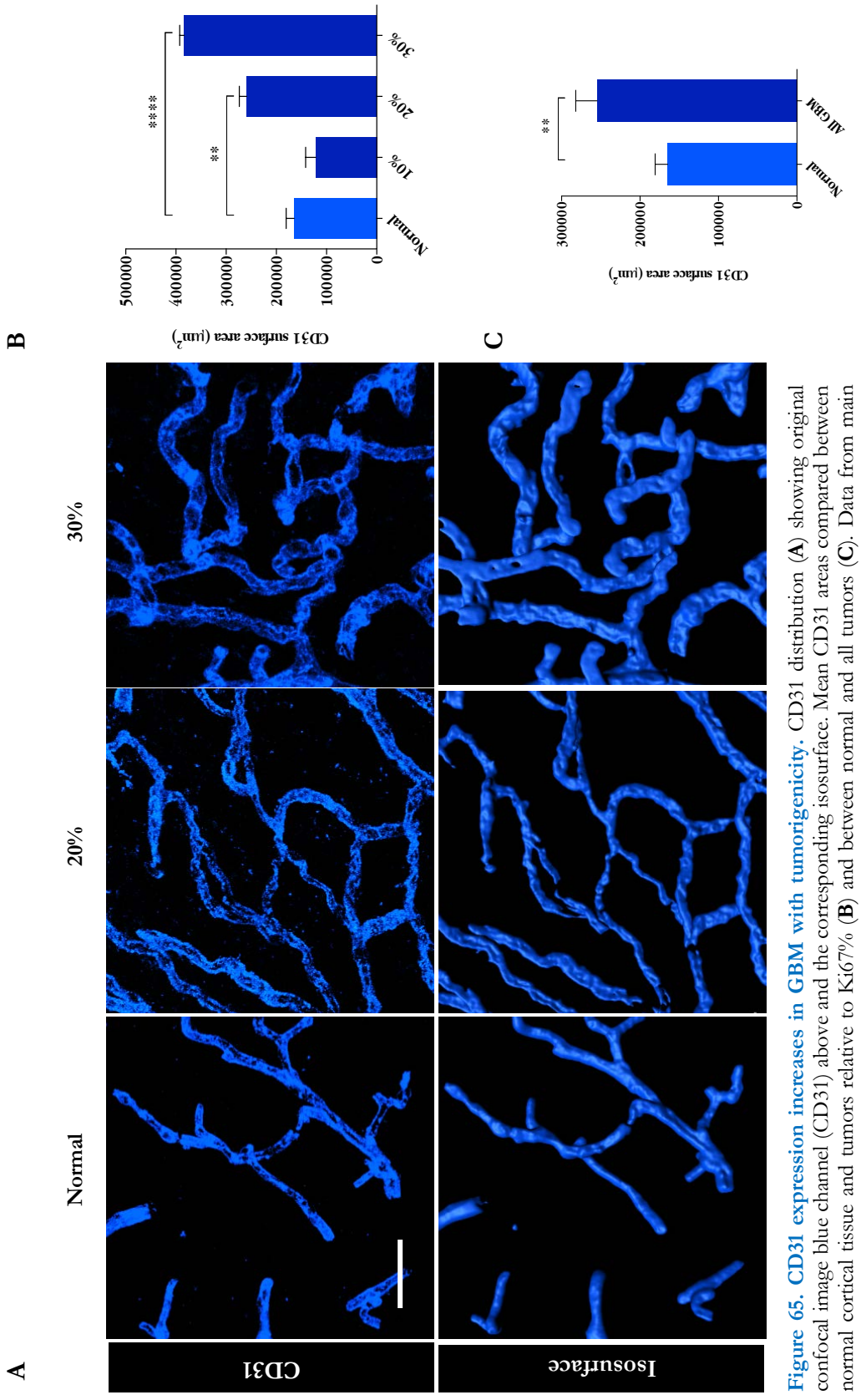

Figure 65. CD31 expression increases in GBM with tumorigenicity. CD31 distribution (**A**) showing original confocal image blue channel (CD31) above and the corresponding isosurface. Mean CD31 areas compared between normal cortical tissue and tumors relative to Ki67% (**B**) and between normal and all tumors (**C**). Data from main sample group. CD31 (blue). Scale bar 50 µm.

5.3.7 Interaction of collagen IV and CD31

Previous studies have reported basement membrane defects in various murine cancer models including loose association with endothelial cells and pericytes among other abnormalities (Baluk et al., 2003) but again, studies in humans in such detail are scarce if not absent. Thus, after having established that both collagen IV and CD31 surface areas increased significantly with tumor aggressivity, we then examined any correlations between the two to see if we could find evidence of any of the alterations described in animal models. So, additionally we analyzed this sample pool to determine differences in CD31 and collagen IV surface area ratios as well as to estimate the overall surface area of any colocalization of the two (i.e. surface-to-surface contact) as a means of quantifying the extent of any possible disruption in the relationship between basement membrane and endothelial cells. Whereas in normal vessels the endothelial lining appears like a tube within the outer tube of basement membrane, we thought that this analogy would not hold true for tumor vessels. Our results show significant increases in collagen IV ($p<0.05$) and CD31 ($p<0.05$) in tumors compared to normal cortical tissue but, interestingly, the area of colocalization remains similar between the GBM and normal groups (see Figure 66) meaning that the significantly increased type-IV collagen and CD31 did not seem to be tightly associated.

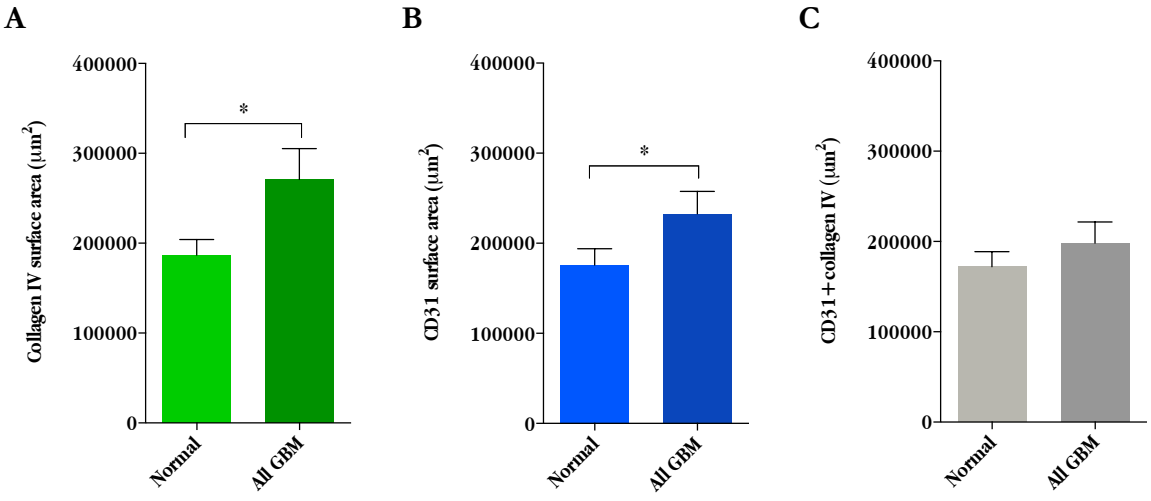

Figure 66. Collagen IV and CD31 surface areas increase in GBM while surface to surface contact between both remains stable in normal and GBM samples. Collagen IV surface areas compared between normal cortical tissue and GBM (**A**). CD31 surfaces in normal and GBM samples (**B**). Colocalization surface area between CD31 and collagen IV in normal and in all tumors (**C**)

Next, we examined the total collagen IV area and CD31 area as ratios of total colocalization area and, although both type-IV collagen and CD31 increased in tumors compared to normal

tissue, the ratios of total collagen IV and CD31 to colocalization actually decreased, again supporting the idea of a looser association of the two.

Figure 67 shows individual data for total collagen IV and CD31 as ratios of total colocalization in normal cortical tissue and GBM with Ki67 indices of 10, 20 and 30%. Percentage of total collagen IV that was colocalized tended to decrease with tumor severity but was only significant for the 50% group ($p<0.01$). The same tendency held for CD31 but in this case both the 10% ($p<0.01$) and the 50% ($p<0.05$) groups were significantly lower.

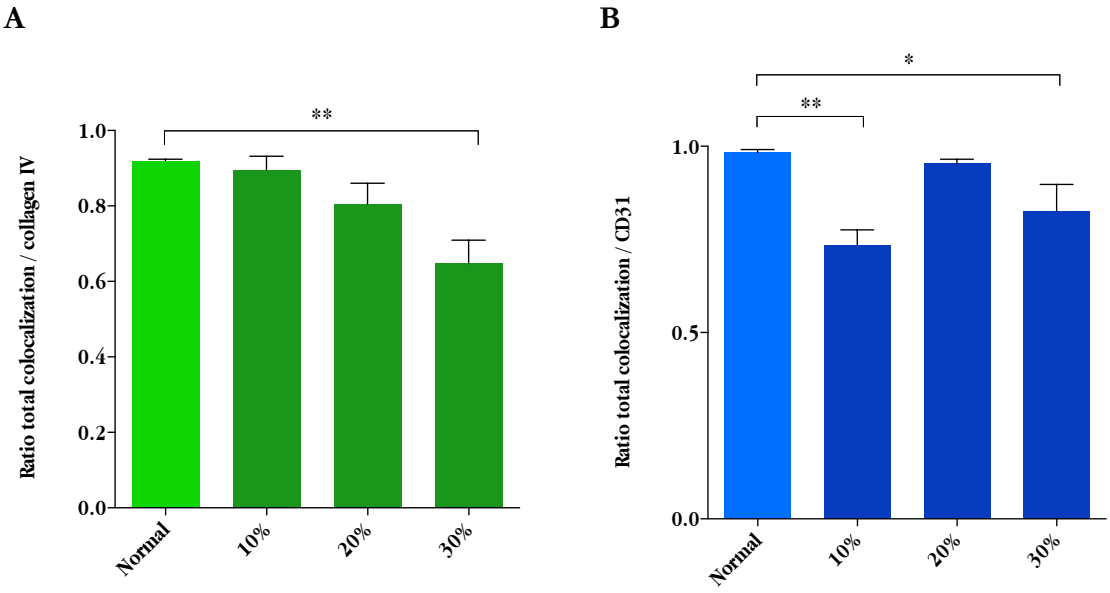

Figure 67. Total collagen IV and CD31 surface areas as ratios of total colocalized area decreased significantly in GBM. Graphs comparing the ratios of total collagen IV (**A**) and total CD31 (**B**) surface areas to total colocalized area for normal cortical tissue and different Ki67 indices of GBM.

Figure 68 juxtaposes color heatmaps for the colocalization channel showing the different patterns of colocalization across tumors and normal tissue. In normal tissue the colormap is slightly more concentric whereas the tumor samples show dispersion or separation of the green and blue channels at higher fluorescence values; this is best seen in Figure 68B.

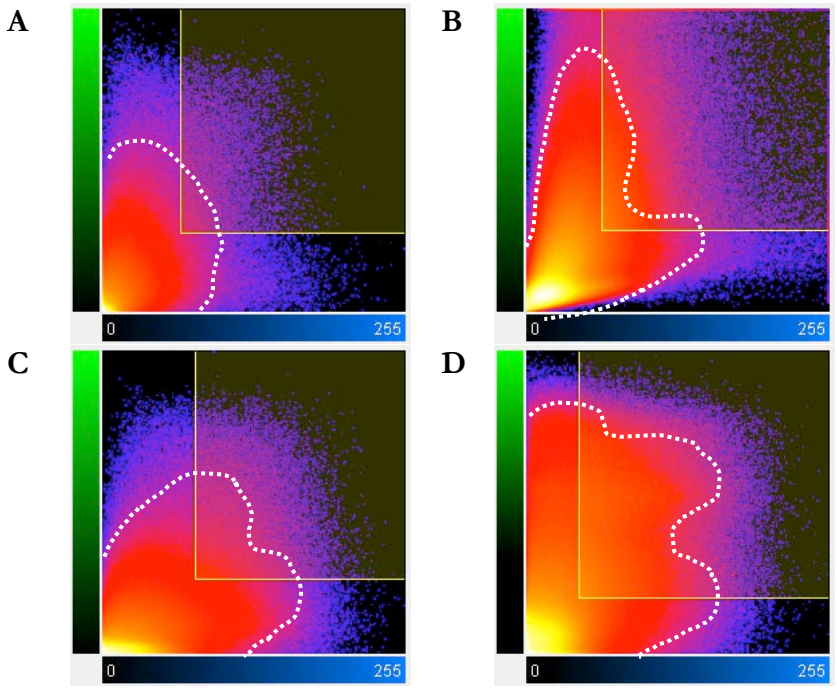

Figure 68. Colocalization color heatmaps show different patterns across normal and GBM samples. Heatmaps showing colocalization of collagen IV and CD31 surface areas for normal cortical tissue (**A**) and different Ki67 indices of GBM (**B**, 10%, **C**, 20% and **D**, 30%). The dotted white lines show the areas outline the areas of intense fluorescence for the two channels. High heat areas overlap substantially (they are nearly concentric) in A whereas in B-D there are two or three high intensity "tails" where the high fluorescence areas of the two channels overlap less than in A.

Figure 69 provides a more visual and detailed description of collagen IV and CD31 colocalization combining confocal images and 3D isosurfaces. It includes a Venn diagram of relative areas of collagen IV, CD31 and their colocalization. The circle sizes represent relative areas and the gray overlapping area shows the relative degree of colocalization.

The stacked bar graphs compare normal cortical tissue and combined GBM groups showing the percent of total collagen IV (92% normal cortical tissue, 78% GBM) and CD31 (98% normal cortical tissue, 83% GBM) that is colocalized. The results indicate that when comparing normal tissue to all GBM, there are significant decreases in colocalization percentage for both collagen IV (14%, $p<0.01$) and CD31 (15%. $p<0.001$).

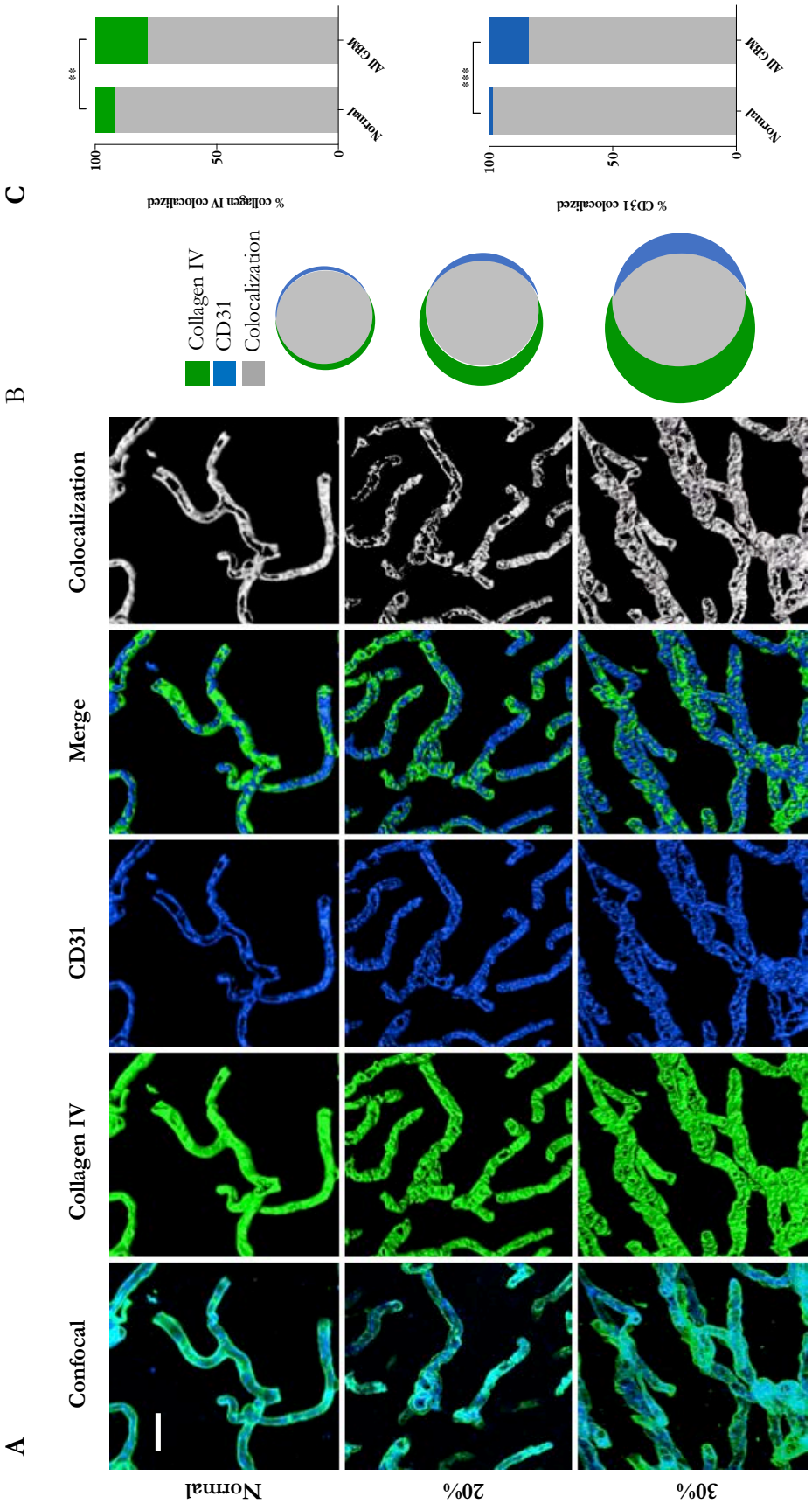

Figure 69. Endothelium and basement membrane are disrupted in GBM. Montage (**A**) showing confocal images with merged channels for collagen IV and CD31 (column 1); isosurfaces for collagen IV and CD31 and a merged view of the two channels (columns 2-4) and an isosurface of the colocalization of the collagen IV and CD31 channels (column 5). This latter channel approximates the degree of surface-to-surface contact of collagen IV-positive (basement membrane) and CD31-positive (endothelial cells) areas in normal and tumor vessels. Venn diagram (**B**) of relative collagen IV, CD31 and colocalization areas. Bar graphs (**C**) comparing the percent of total colocalized collagen IV (upper graph) and CD31 (lower graph) between normal cortical tissue and GBM. Collagen IV (green), CD31 (blue), merged (gray). Scale bar 40 µm.

Thus, after observing the increased CD31 expression in GBM, and in light of the disruptions in endothelial cells lining basement membranes, we focused on glomeruloid vascular structures, an important histopathological feature of GBM, which occur in the context of microvascular proliferation with hyperplastic endothelial cells but the precise cellular makeup of these structures and whether or not they contain tumor cells remains poorly studied (Rojiani & Dorovini-Zis, 1996). Here we demonstrate that glomeruloid vessels contain multiple type-IV collagen layers (basement membrane) and proliferative endothelial cells but show no evidence of $GFAP^+$ tumor cells. Figure 70 illustrates a typical glomeruloid tumor vessel.

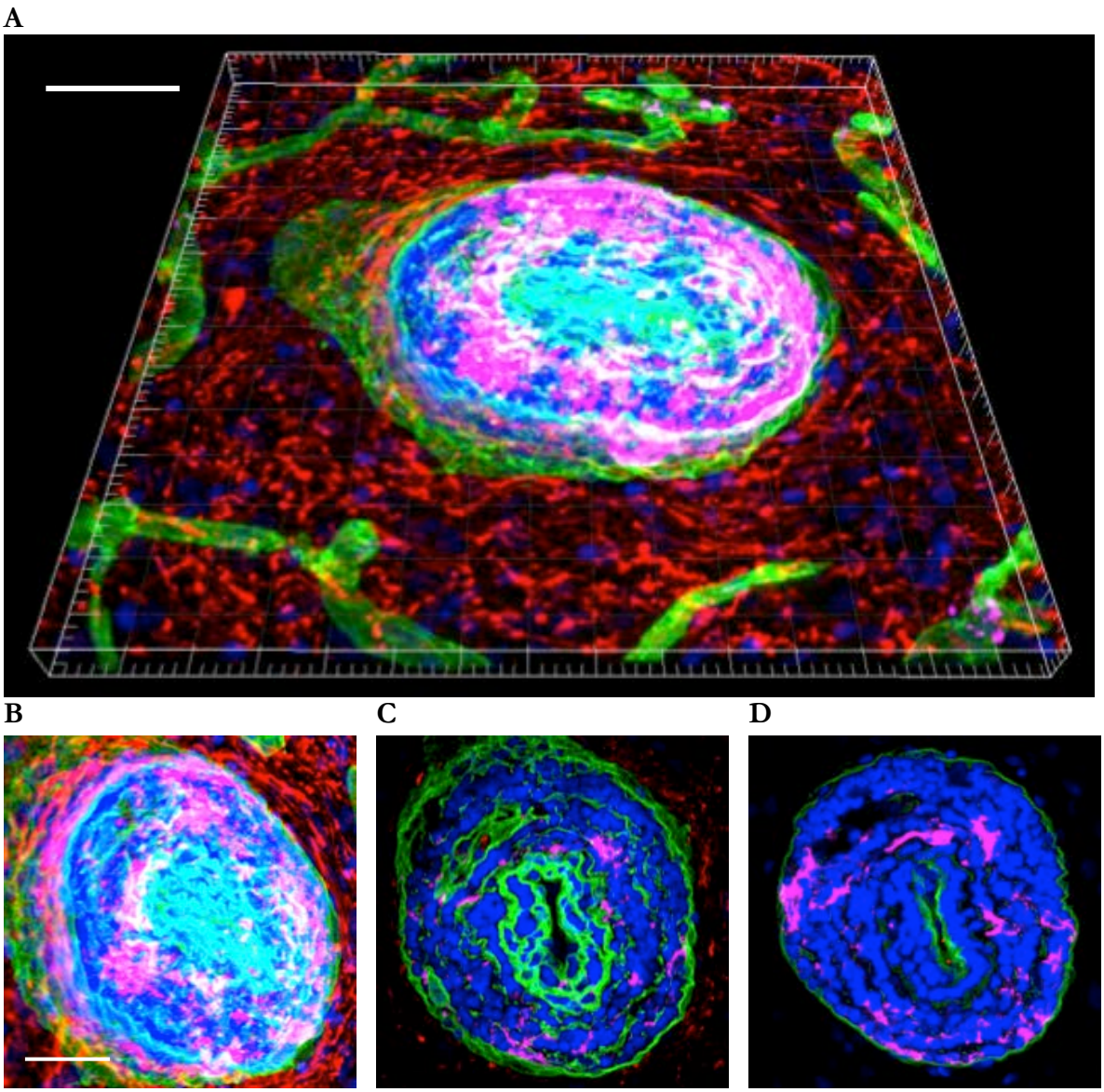

Figure 70. Endothelial cell hyperplasia leads to blood vessel abnormalities in glomeruloid vessels. Three microphotographs (**B**-**D**) taken at different depths of a confocal stack (**A**) illustrating characteristics typical of glomeruloid vessels. Clear differences in the amount of basement membrane type-IV collagen, the distribution and amount of CD31 expression and number of cell nuclei are visible across photos. Basement membrane (collagen IV, green), tumor cells (GFAP, red), endothelial cells (CD31, magenta) and nuclei (DAPI, blue). Scale bars A, 50 μm and B-D, 40 μm.

Though glomeruloid vessels are as yet not fully understood and it is still an open question as to whether they are an accelerated form of angiogenesis or dysfunctional hyperproliferation (Brat & Van Meir, 2001). Ultrastructural analysis has demonstrated that they are complex structures of newly formed vascular microchannels lined by hyperplastic endothelial cells and surrounded by basal lamina and an incomplete pericyte layer without astrocytes (Rojiani & Dorovini-Zis, 1996). Interestingly, plotting the relative luminance for the separate channels

supported some of these findings and corroborated the layering of the different membrane components and cells that was observed on visual analysis (see Figure 71).

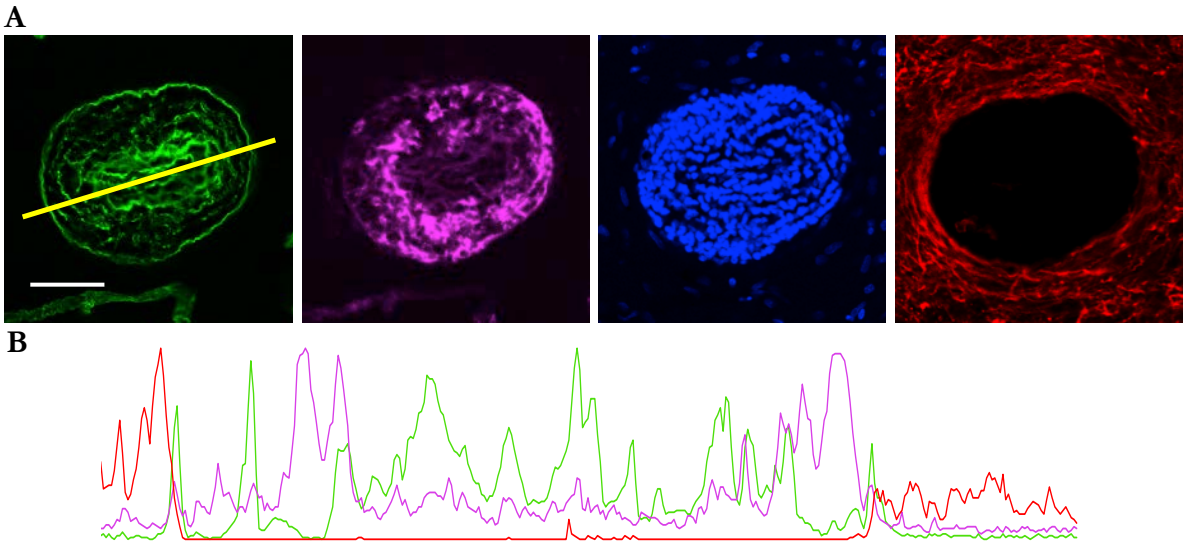

Figure 71. Plotting the relative fluorescence intensity profiles for separate channels to highlight the spatial organization of a glomeruloid tuft. Four microphotographs (**A**) of the separate channels taken from a confocal image of a glomeruloid vessel in a GBM biopsy sample. The yellow line shows the portion of the image where the relative fluorescence intensity was measured separately for each channel. The lower image (**B**) is an overlaid plot of all the green and magenta channels highlighting the separate layers of basement membrane and endothelial cells. Basement membrane (collagen IV, green), fibrous malignant astrocytes (GFAP, red), endothelial cells (CD31, magenta) and nuclei (DAPI, blue). Scale bar 50 μm.

5.4 Microglia and macrophages and T cells

Although the structural and morphological variations described above are important, equally so is an analysis of the cellular populations that form part of the TME to determine their makeup and particularly in the present context, their location. Accordingly, this section presents results for TME subpopulations including TAMMs and TILs. Parameters measured and reported include Iba-1 and MHCII surface areas, volumes and units and MHCII / GFAP colocalization, total T cells, total extravasating and migrated T cells, mean distances migrated and ratios of extravasating to migrated T cells.

5.4.1 Microglia and macrophages

Microglia are CNS resident macrophages and act as the first line of defense in the brain; however, in GBM microglia and infiltrated macrophages seem to be dormant and apparently may even assist tumor development. As in other tumor types, TAMMs are believed to be anti-inflammatory and promote tumor growth. However, little is known about the location and distribution of TAMMs with regard to BVs or malignant tissue. Our intention here was to

examine not only the spatial organization and distribution of TAMMs but also to discover if there were any increases in microglia/macrophage populations related to tumor severity, something poorly studied, particularly using Iba-1 as a marker.

We began by detecting for Iba-1, a microglia/macrophage-specific calcium-binding protein which detects microglia. Figure 72 shows microglia/macrophages marked with Iba-1 in which clear differences in cell morphology can be appreciated.

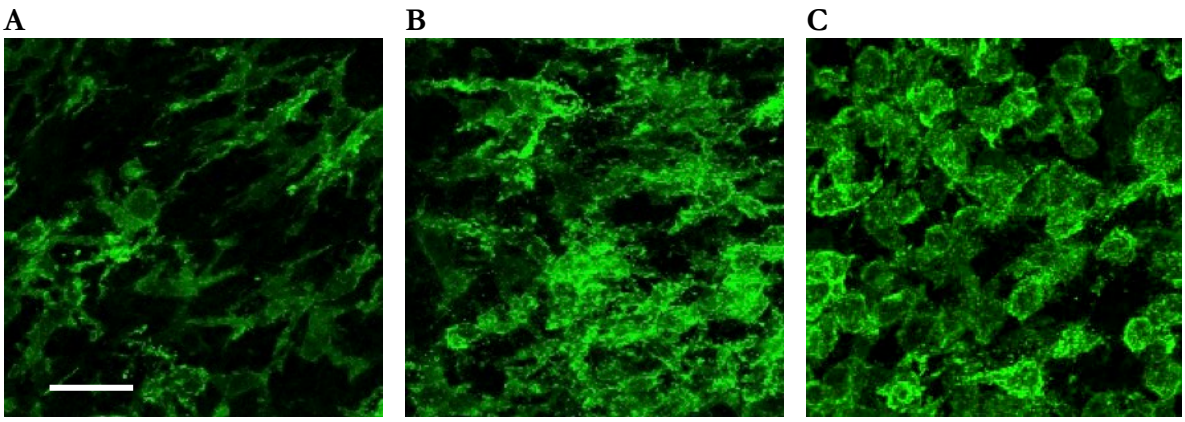

Figure 72. Iba-1 clearly demonstrates changes in microglia/macrophage morphology associated with GBM. The three images show different phenotypic variations in microglia/macrophages stained with Iba-1 (green), passing from more "spider-like" shapes in peritumoral areas (**A**), to a more fully ameboid shape (**C**) in tumoral areas, with a more diffuse intermediary stage (**B**) in intermediate areas. Scale bar 25 μm.

Figure 73 shows a deconstruction of a confocal image showing Iba-1 distribution in relation to BVs and $GFAP^+$ components. Bona fide microglia/macrophages are intermingled with malignant cells in GBM. Note the ameboid shape of TAMMS and the fibrous nature of the $GFAP^+$ astroglial or tumor cells.

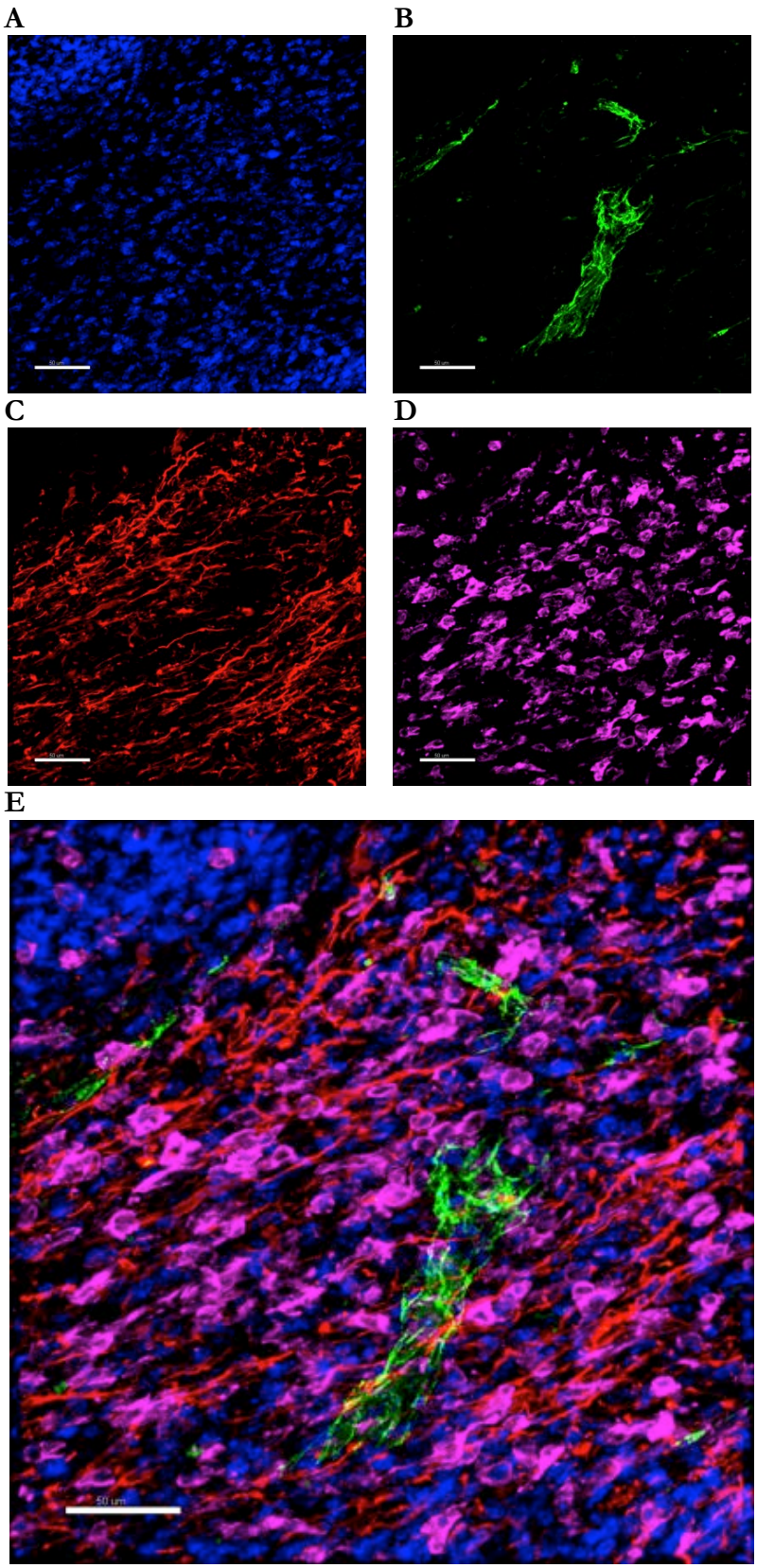

Figure 73. Confocal photograph deconstructed into separate channels to visualize microglia/macrophages, BV endothelium, GFAP⁺ astroglial cells and cell nuclei. Separate channels of a confocal image showing DAPI counterstained nuclei (blue) (**A**), tumor BVs (CD31, green) (**B**), GFAP⁺ cells (red) (**C**), Iba-1⁺ cells (magenta) (**D**) and a merged view (**E**) of A-D. Scale bar 50 μm.

Figure 74 shows a three-dimensional reconstruction of the Iba-1 distribution in relation to blood vessels and GFAP$^+$ astroglial and tumor cells in a GBM sample.

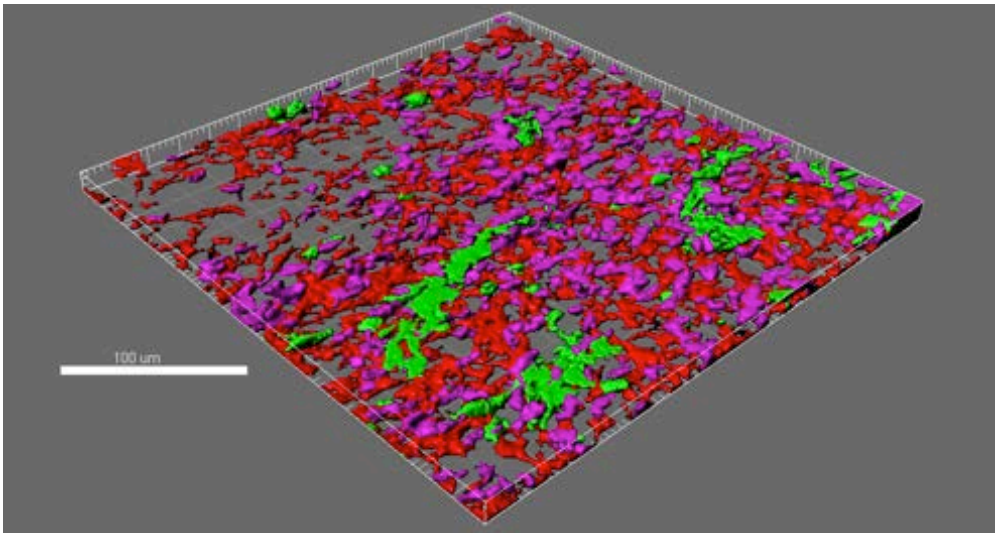

Figure 74. Three-dimensional reconstruction of GBM BVs showing Iba-1 expression. The image shows Iba-1-expressing cells (magenta) in relation to tumor BVs (green) and intermingled with GFAP-rich areas (red). Scale bar 100 μm.

We quantified activated microglia by immunofluorescence detection of Iba-1 and subsequent analysis of total surface areas, volumes and units for each sample. Thirty measurements were taken: six normal, six Ki67% 10, twelve Ki67% 20 and six Ki67% 30. All three Iba-1 measures -surface area, volume and units- increased with tumor severity. Our results show significant differences between normal and 20 and 30% groups for surface area ($p<0.05$ and $p<0.01$, 20 and 30% respectively) and volume ($p<0.05$ for both 20 and 30%) and between normal and 30% for units ($p<0.01$) (see Figure 75).

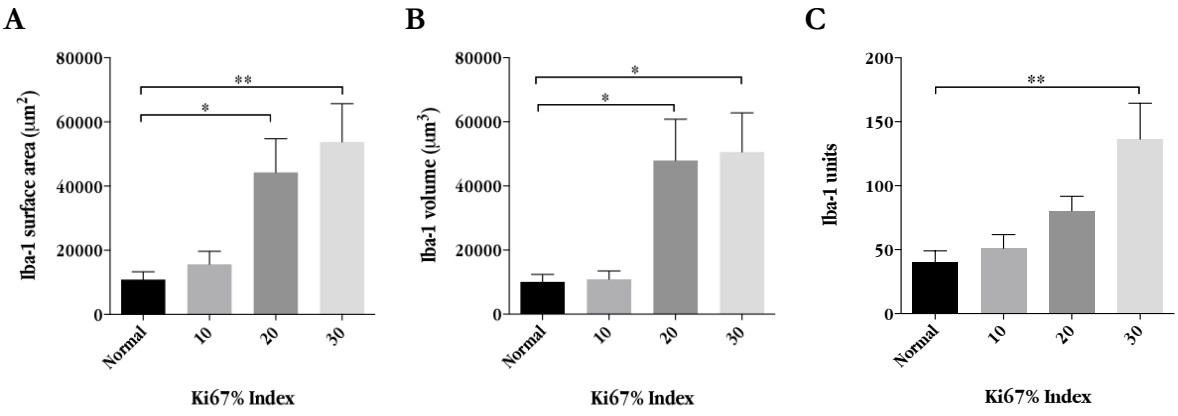

Figure 75. Iba-1 expression in GBM increases with increased tumor aggressiveness. Compared to normal tissue, all parameters measured increased relative to tumor aggressiveness. Bar graphs show significant increases in Iba-1$^+$ surface areas and volumes, (**A** and **B**, respectively) between normal and GBM 20 and 30% groups and a significant increase in Iba-1$^+$ units (**C**) between normal and GBM 30% groups.

Whereas Iba-1 exclusively identifies microglia and macrophages, MHCII, on the other hand, marks APCs, which can include cells other than TAMMs, such as some lymphocytes, like B cells, dendritic cells, neutrophils or eosinophils, although their presence in the brain is reduced. Nonetheless, as MHCII is a frequently used immunomarker for activated microglia/macrophages, we wanted to expand our examination of the TAMM population by incorporating results using a distinct immunomarker.

Figure 76 showing $MHCII^+$ cells, similarly to Figure 72 for Iba-1, shows morphological variations in microglia/macrophage morphology across tumor areas, with a transition from characteristic more "spider-like" shapes to more ameboid forms, passing through an intermediate area with less distinct shapes. $GFAP^+$ astroglial and tumor cells also display varied morphology, with activated astrocytes in the uppermost row and pregemistocytic and gemistocytic cells in the two lower rows.

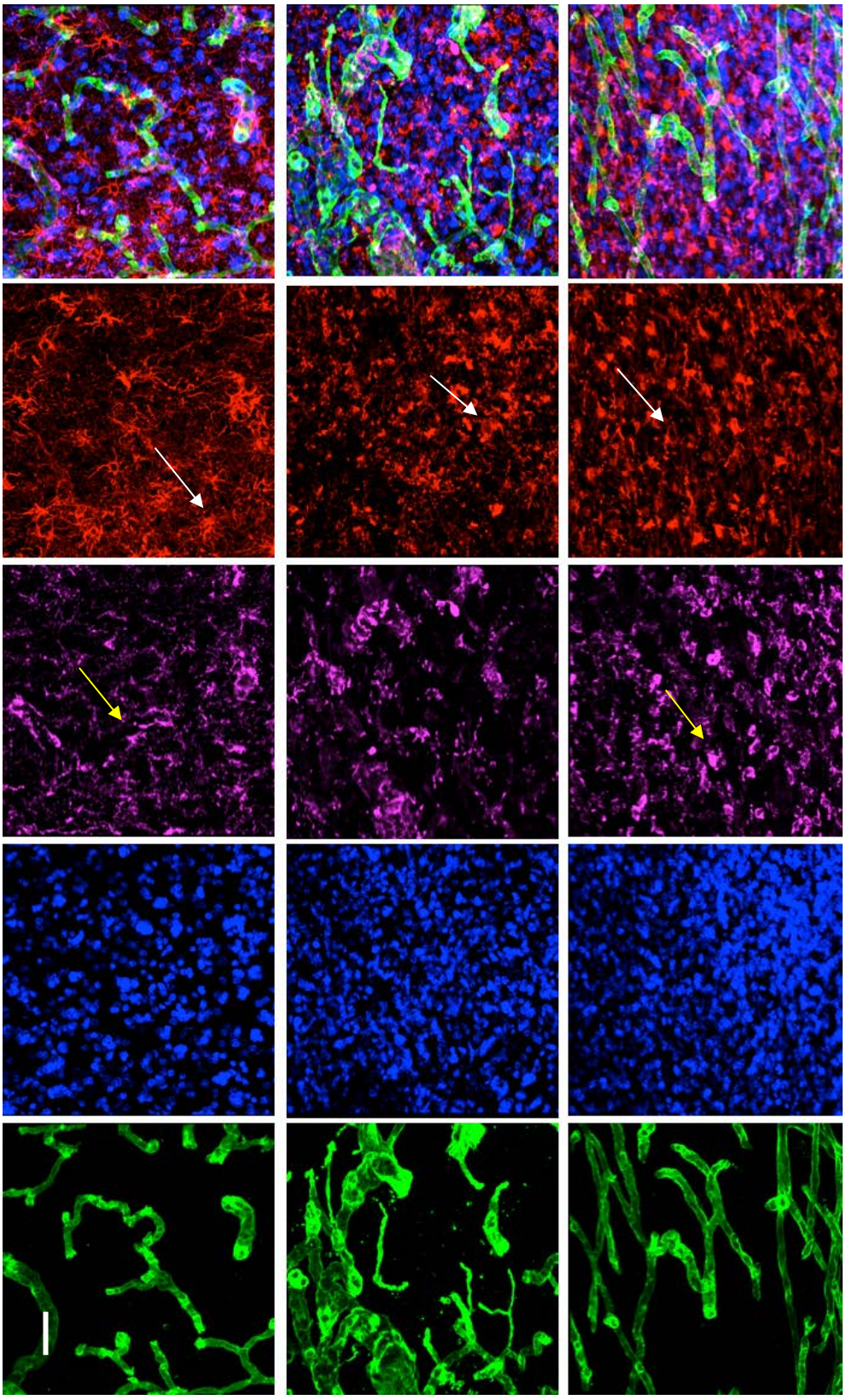

Figure 76. MHCII highlights changes in microglia/macrophage morphology associated with GBM. Three tumors (**A**-**C**) immunostained for collagen IV (green), nuclei (blue), MHCII (magenta) and GFAP (red) and a merged view of all channels. Note the variations in microglia/macrophages stained with MHCII (yellow arrows), passing from more "spider-like" shapes and perivascular TAMMs in the peritumoral area (**A**) to the tumor proper with more ameboid shapes (**C**) in tumoral areas and a more diffuse intermediary stage (**B**) in intermediate areas. Astroglial and tumor cell morphology also varies across tumors (white arrows), activated astrocytes in **A**, pregemistocytic and gemistocytic astrocytes in **B** and **C**, respectively. Scale bar 50 μm.

Figures 77 and 78, respectively, show a deconstructed confocal image showing separate channels individually along with the original merged view and a 3D reconstruction of the same image.

A

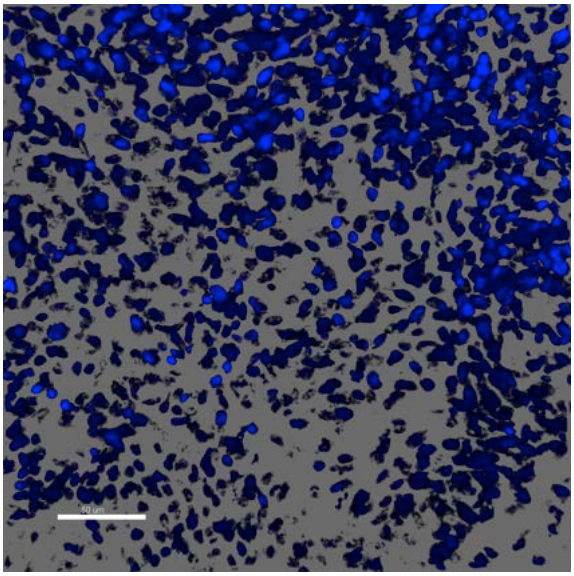

B

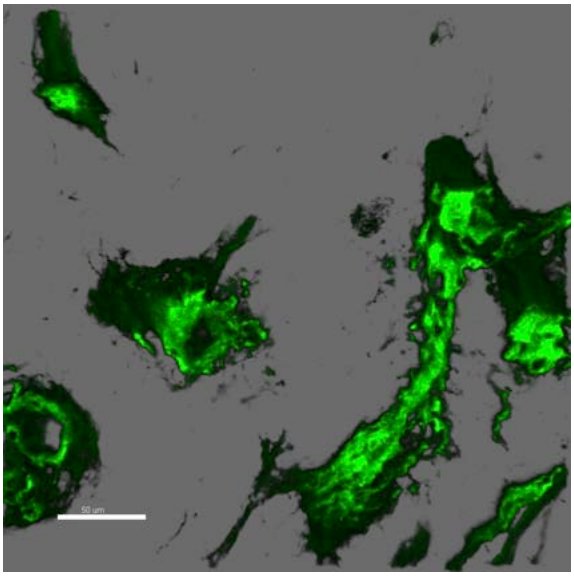

C

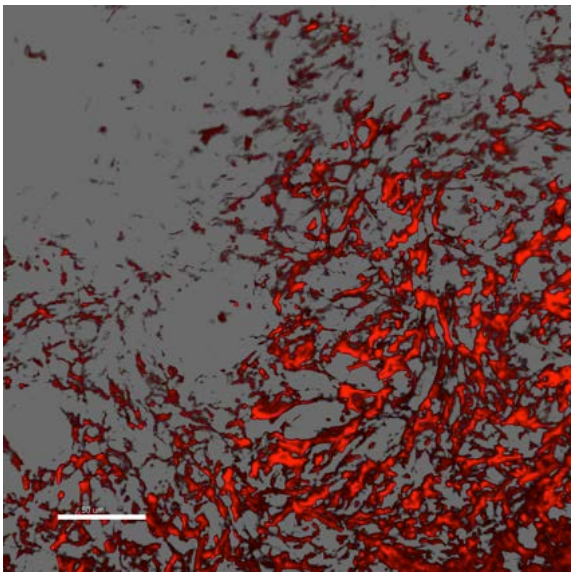

D

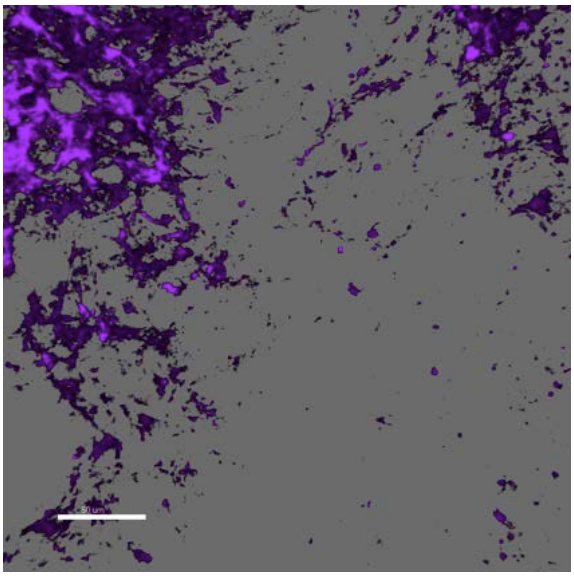

E

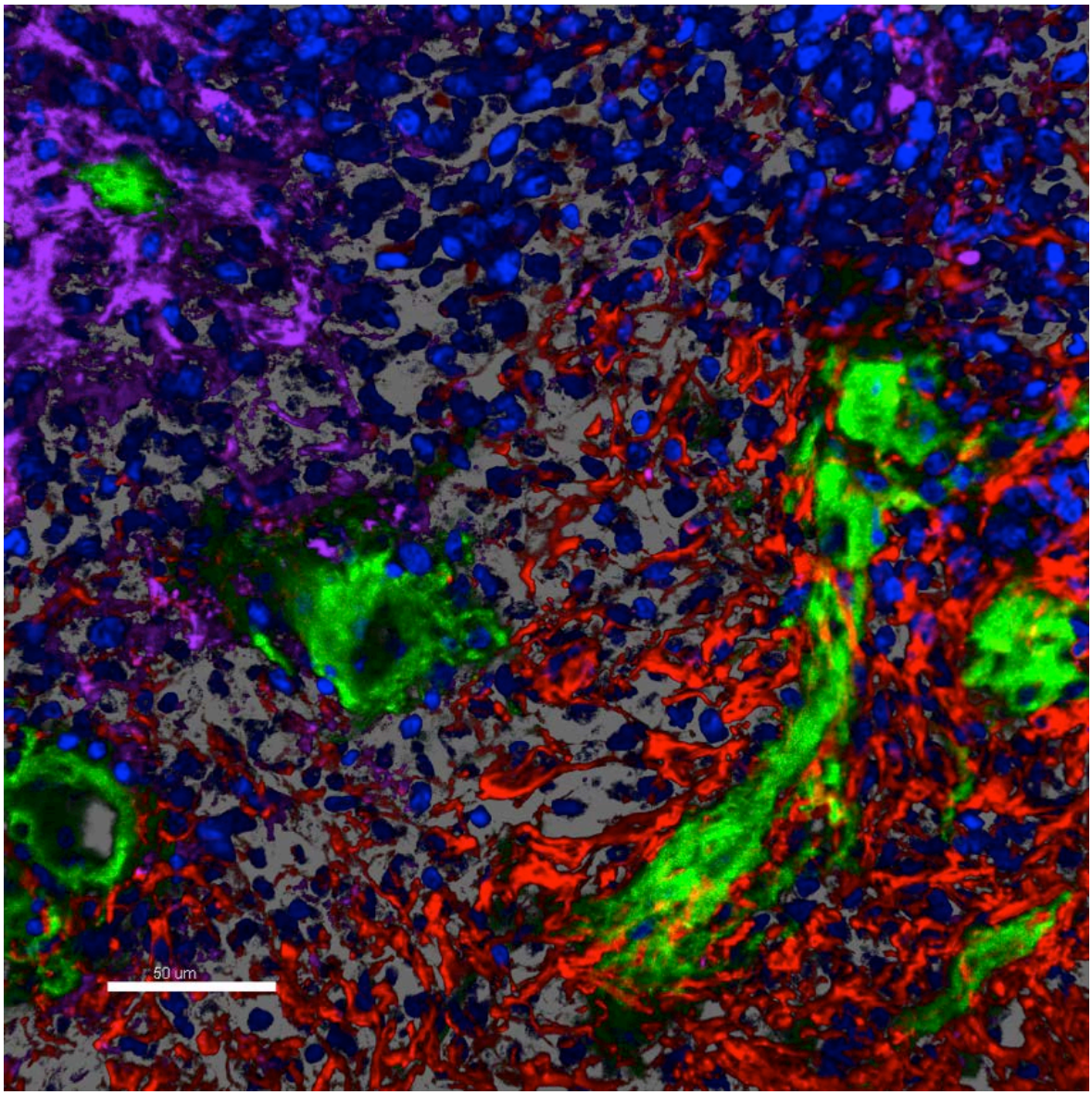

Figure 77. Confocal photograph deconstructed into separate channels to visualize MHCII$^+$ cells, BV endothelium, GFAP$^+$ astroglial and tumor cells and cell nuclei. The image shows MHCII-expressing cells (magenta) in relation to tumor BVs (green) and intermingled with GFAP$^+$ astroglial or tumor cells (red) and DAPI counterstained nuclei (blue). Nuclei (**A**), collagen IV (**B**), GFAP (**C**), MHCII (**D**) and merged view of all channels (**E**). Scale bar 50 μm.

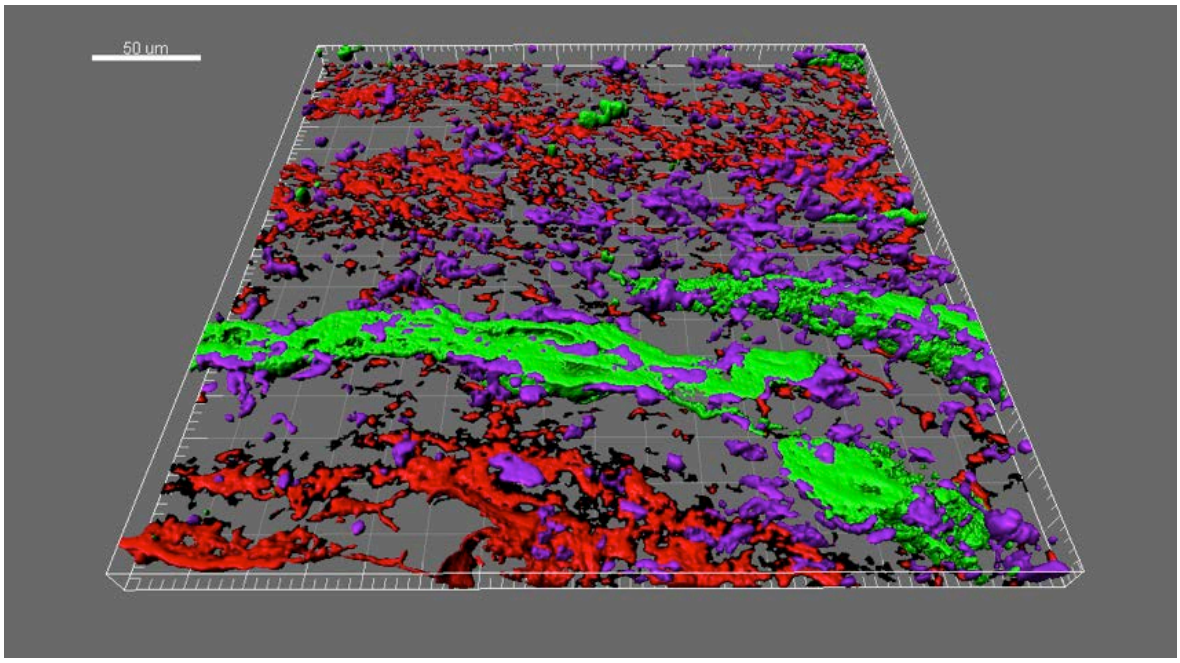

Figure 78. Three-dimensional reconstruction of GBM BVs showing non-overlapping MHCII-rich and GFAP-rich areas. The image shows a 3D isosurface reconstruction of MHCII-expressing cells (magenta) inside and surrounding a tumor BV (collagen IV, green) and flanked on both sides by GFAP-rich areas (red). Scale bar 50 μm.

Much the same as for Iba-1, we quantified TAMMs by immunostaining for MHCII and measuring total surface areas, volumes and units for each sample. Again, 30 measurements were taken: six normal, six Ki67% 10, twelve Ki67% 20 and six Ki67% 30. Similarly to Iba-1, all three MHCII measures -surface area, volume and units- increased with tumor severity.

Our results for MHCII show significant differences between normal and 20 and 30% groups for surface area ($p<0.01$ and $p<0.0001$, 20 and 30%, respectively), volume ($p<0.01$ and $p<0.0001$, 20 and 30%, respectively) and units ($p<0.001$ for both 20 and 30%) (see Figure 79).

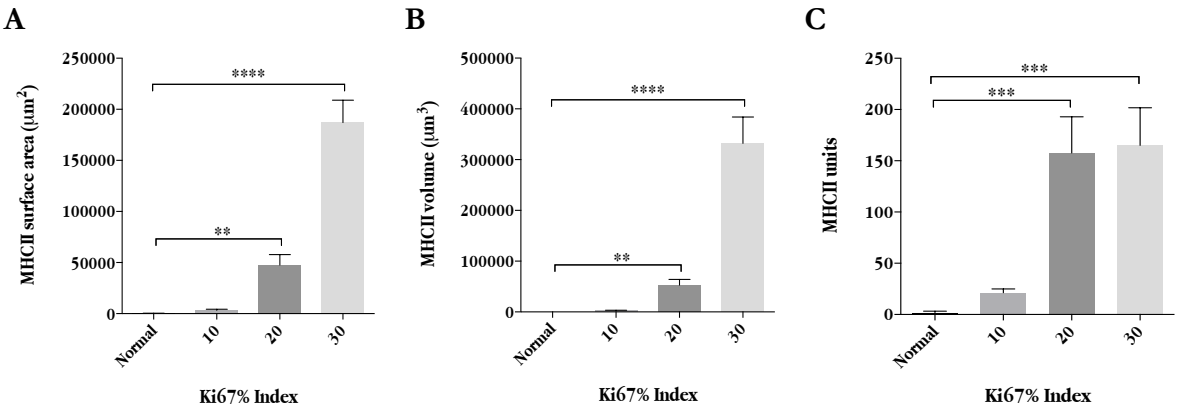

Figure 79. MHCII expression in GBM varies in relation to tumor aggressiveness. Compared to normal tissue, all parameters measured increased relative to tumor aggressiveness. Surface areas (**A**) volumes (**B**) and units (**C**) all show significant increases between normal cortical tissue and GBM 20 and 30% groups.

While not always the case, on first examination it appeared that, unlike Iba-1, which was fairly evenly distributed throughout the samples, MHCII$^+$ and GFAP$^+$ cell populations appear to occupy distinct niches in the TME, a MHCII-rich stromal and a GFAP-rich tumoral area (see Figure 77). Given this preliminary data, we further examined the relation between MHCII- and GFAP-rich areas, initially mainly to determine if these two components interact. Using Imaris' colocalization feature, we were able to establish that there was minimal interaction (overlap) of the two components. In general, GFAP$^+$ cells seemed to occupy tumoral zones and MHCII$^+$ cells, stromal areas.

There were no significant differences between any groups in absolute terms, comparing total MHCII interacting with GFAP (Figure 80A). Furthermore, the interacting MHCII was less than one percent of total MHCII for every group (Figure 80B).

A

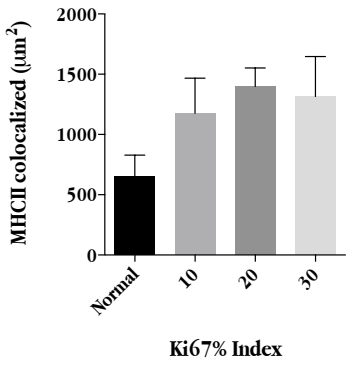

B

Ki67%	% colocalized MHCII to total MHCII
Normal	0.98
10%	0.42
20%	0.02
30%	0.08

Figure 80. MHCII⁺ positive areas do not overlap with GFAP⁺ areas in GBM regardless of tumor aggressiveness. MHCII-expressing cell populations and GFAP-expressing populations occupy unique niches in the GBM TME. Colocalization surface areas (**A**) are not significantly different between any groups and the percentage of total MHCII that colocalizes with GFAP is less than 1% in all groups (**B**).

Interestingly, MHCII⁺ cells were often observed in proximity to or inside BVs as shown in Figures 81 and 82. The former suggests initial monocyte infiltration from a large TABV and the latter shows microglia/macrophages in relation to a characteristic pseudopalisade.

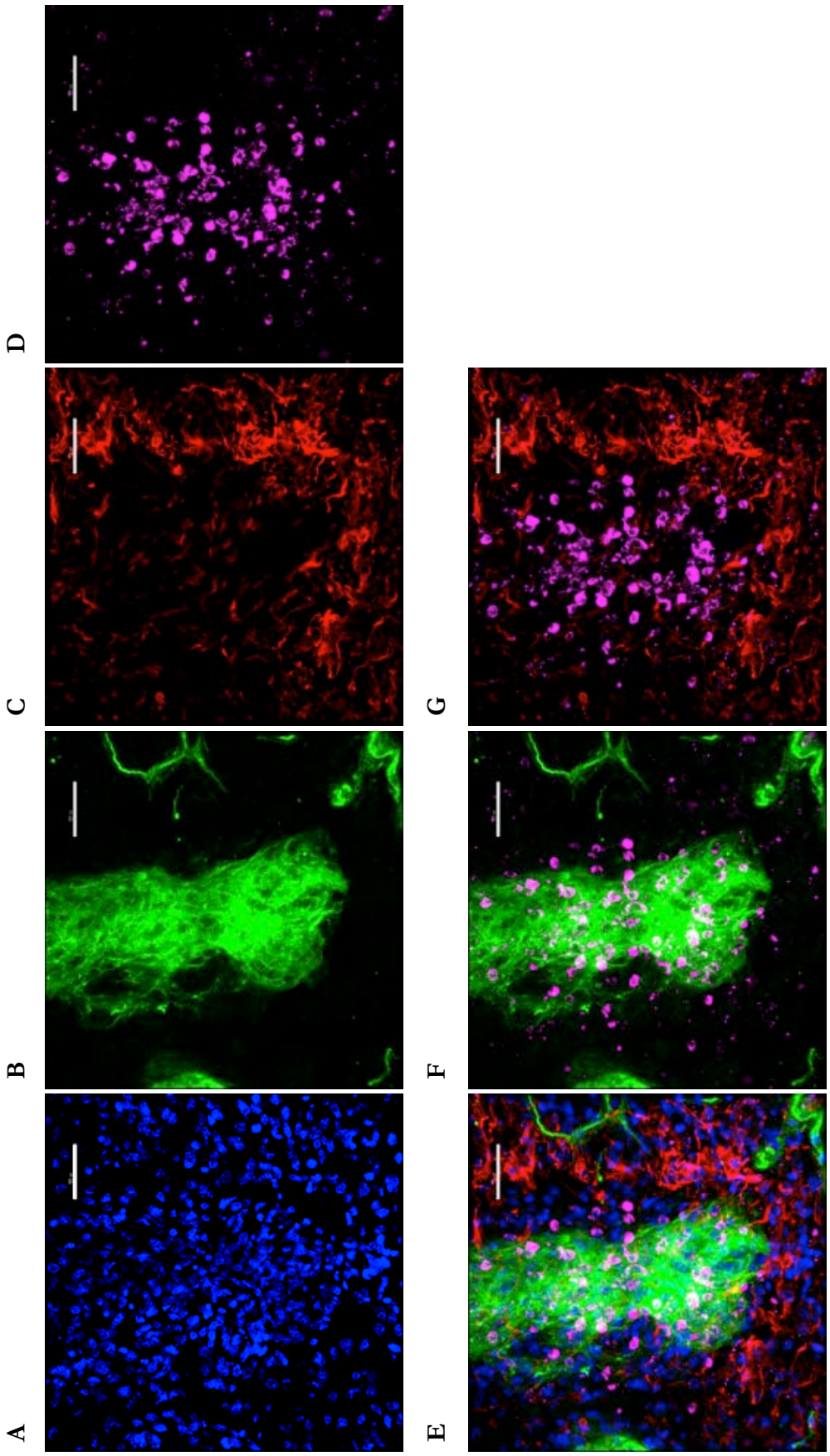

Figure 81. MHCII⁺ cells can be seen inside and in close proximity to the BV in this GBM sample. Confocal photos (**A-D**) show maximum intensity projections of nuclei (blue), collagen IV basement membrane (green) GFAP-expressing cells (red) MHCII-expressing cells (magenta) and a merged view (**E**) of channels (A-D). Image **F** shows the collagen IV and MHCII channels highlighting the close proximity of microglia/macrophages to the BV and **G** is a merged view of the MHCII and GFAP channels and shows how MHCII and GFAP occupy distinct niches in the GBM TME. Scale bar 50 µm.

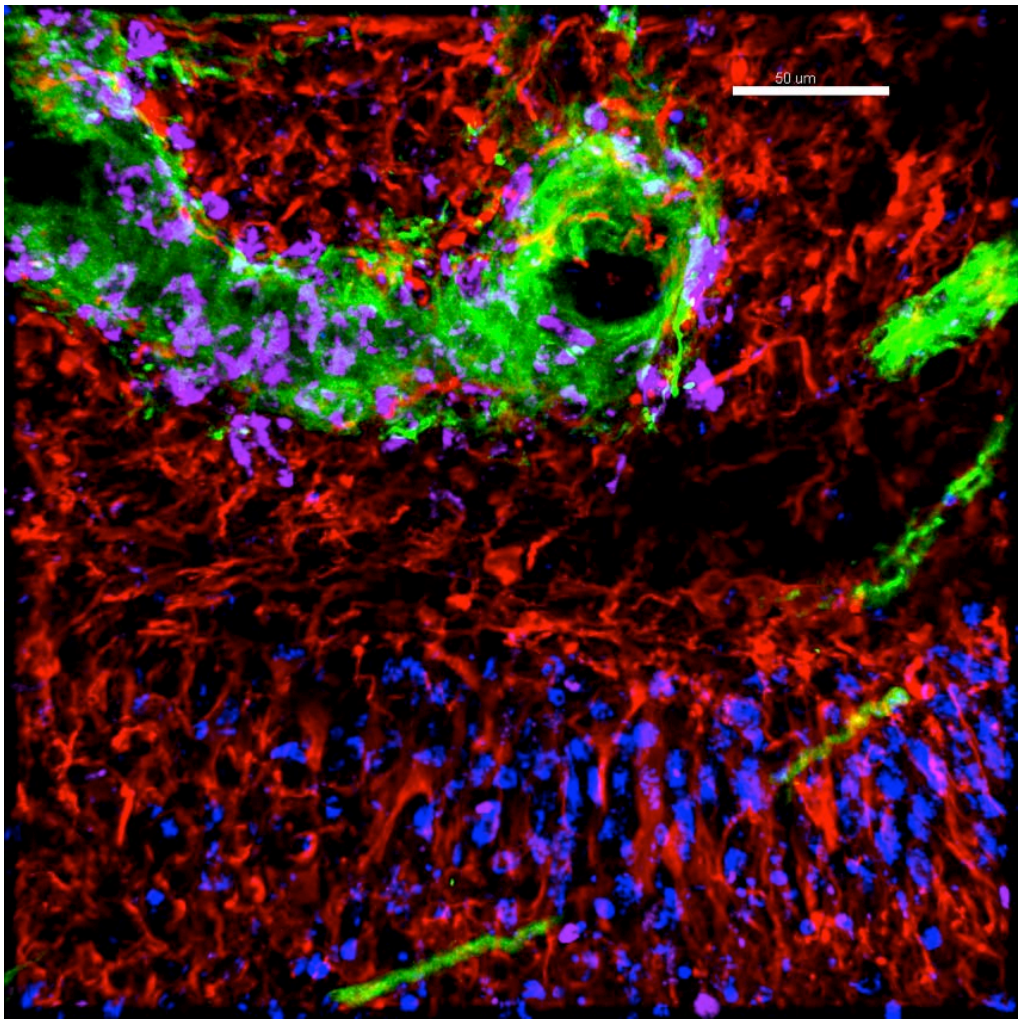

Figure 82. MHCII$^+$ cells inside or in close proximity to BVs are separate from cell clusters and radially distributed GFAP in this classic example of a GBM pseudopalisade. Maximum intensity projection of nuclei (blue), collagen IV basement membrane (green) GFAP-expressing cells (red) and MHCII-expressing cells (magenta). Scale bar 50 μm.

Previous results in our lab had demonstrated that GBM samples double stained to detect both Iba-1 and MHCII revealed Iba-1$^+$ cells that did not mark positive for MHCII (see Figures 83 and 84). In the former, there is a large Iba-1-positive area to the right which seems devoid of MHCII. Iba-1 should also be positive for MHCII, which is probably very low or undetectable in these areas. Panels C and E of the higher resolution image show those areas where Iba-1 and MHCII coincide in yellow and also the green, Iba-1-only, areas. Figure 85 shows heatmap plots corresponding to Figures 83 and 84 showing the relative overlap between the fluorescence for Iba-1 and MHCII channels. The fluorescence profiles suggest that Iba-1 expression does not vary much over the image area whereas MHCII expression does, including areas with high expression and areas with MHCII practically undetectable.

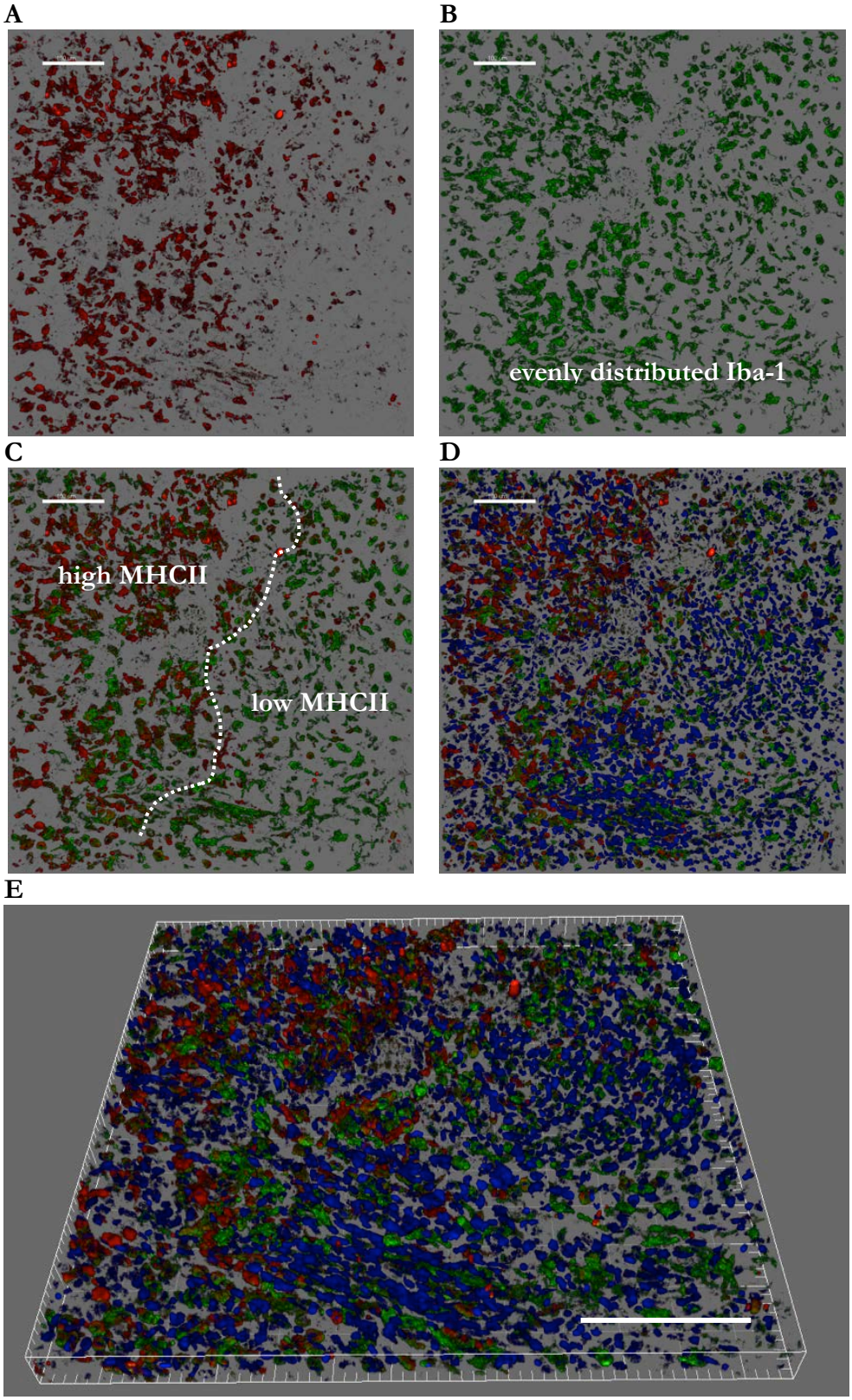

Figure 83. Confocal blend view of double immunostaining for Iba-1 and MHCII shows a substantial subpopulation of Iba-1 expressing cells that do express detectable levels of MHCII. Confocal photograph showing MHCII (red) (**A**), Iba-1 (green) (**B**), a merged view (**C**) of A and B, the same merged view (**D**) including nuclei (blue) and a 3D merged view (**E**) of all channels. Scale bar A-D 100 µm, E 150 µm. Photos by Elena Saavedra López, used with permission.

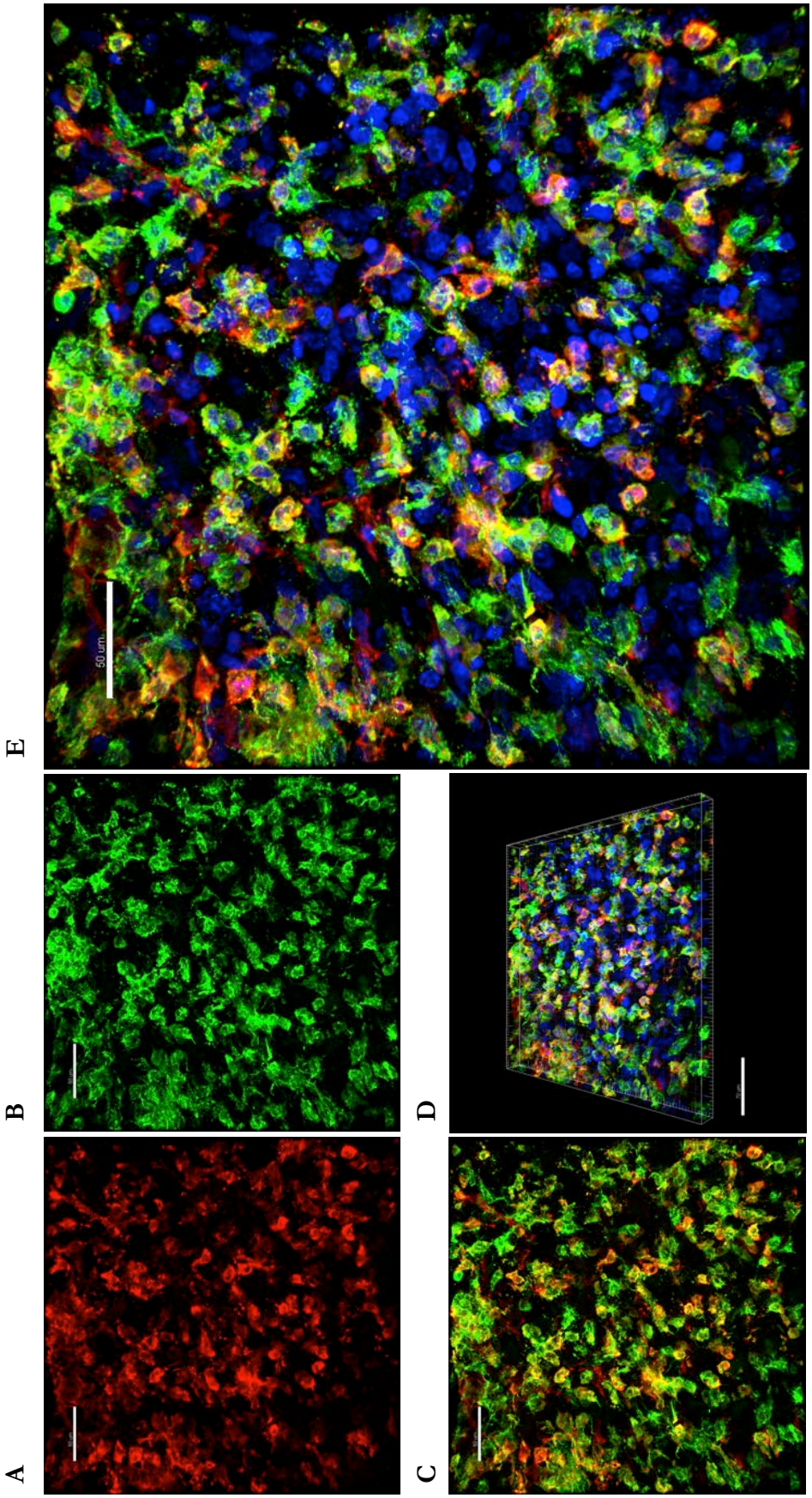

Figure 84. Confocal maximum intensity projection view of a stromal area with double immunostaining for Iba-1 and MHCII shows Iba-1 expressing cells that do express detectable levels of MHCII. Some Iba-1$^+$ cells (green) show high MHCII (red) expression whereas some show low or undetectable MHCII expression. MHCII (red) (**A**), Iba-1 (green) (**B**), merged view (A and B) (**C**), merged view (A, B and nuclei) (**E**) and a merged 3D view (with nuclei, blue) (**D**). Scale bar A-C and E 100 µm, D 150 µm. Photos by Elena Saavedra López, used with permission.

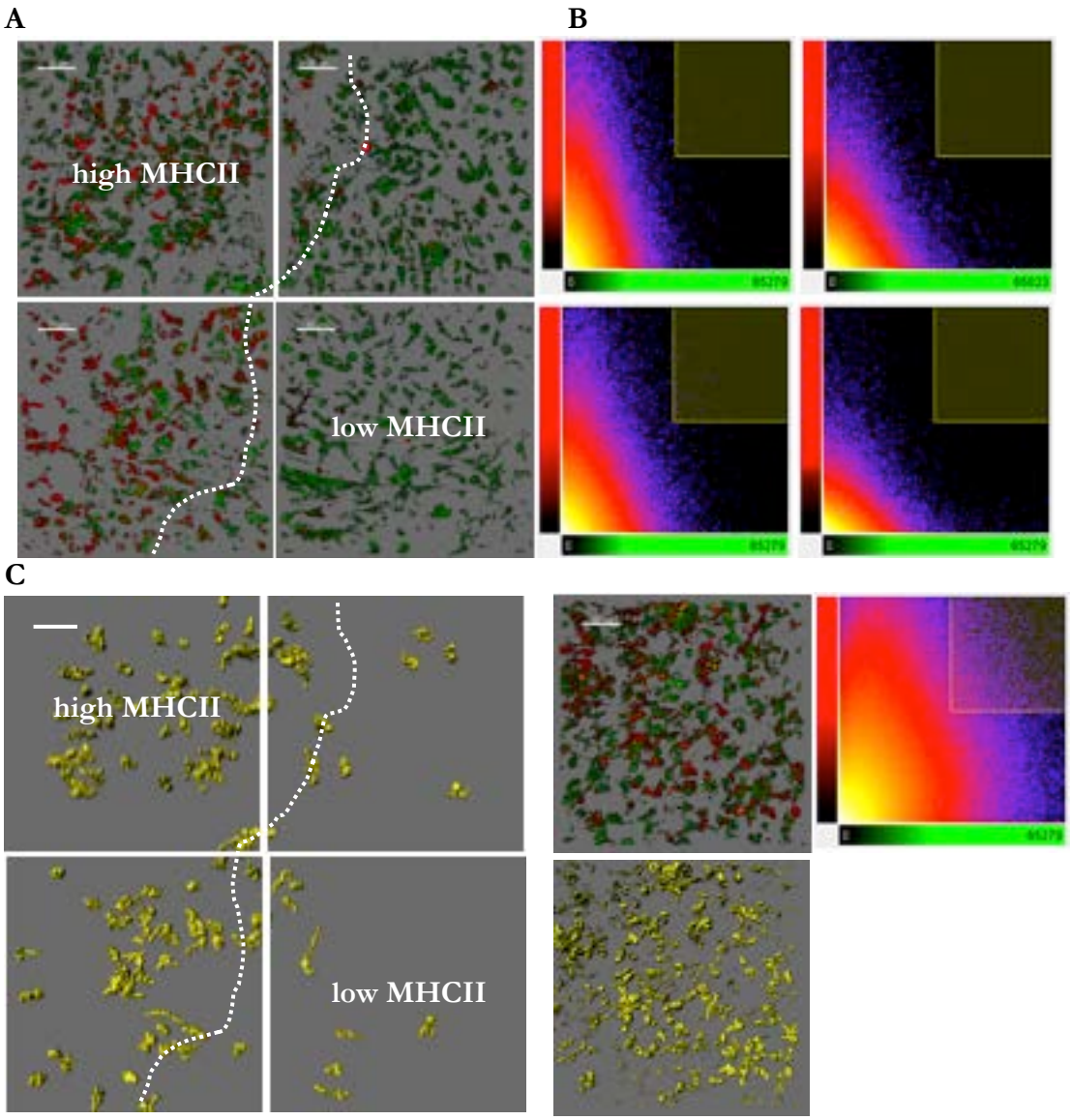

Figure 85. Heatmap plots highlighting high and low fluorescence areas of MHCII expression. Two images **A** (Figure 83 divided into four quadrants, upper and lower right and left) and **B**, the respective heatmaps showing the relative fluorescence for Iba-1 and MHCII channels. Stromal areas (mainly left quadrants) show high MHCII expression whereas malignant areas (right quadrants) show low MHCII expression. Image C show an isosurface of the colocalization between MHCII and Iba-1 in each quadrant of A. Image **D** shows a blend view of the same image as in Figure 84 and its corresponding heatmap and colocalization isosurface. Scale bar 50 μm.

It appears that Iba-1 expression is fairly consistent across tumor areas whereas MHCII expresses highly in stromal areas and much less so (being practically undetectable) in malignant areas. Importantly, our results also demonstrate that high $GFAP^+$ areas correspond to areas of low MHCII expression and vice versa. Hypothetically, stromal and tumoral areas host microglia/macrophages with different phenotypes for MHCII expression (see Figure 86).

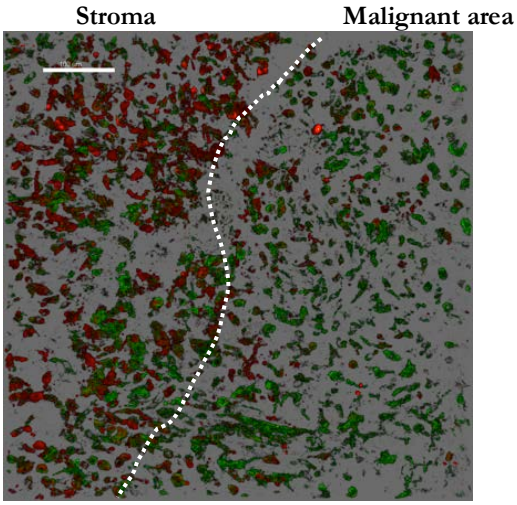

Figure 86. Schematic description of differences between tumor and stromal areas with regard to Iba-1, GFAP and MHCII expression. Image shows Iba-1-expressing cells and MHCII-expressing cells (red). Scale bar 100 μm.

Regardless of the accuracy of this hypothetical schema, the observed differences between stromal and malignant tumor areas were sufficient to merit further investigation and to do so, we measured the expression of collagen IV and also the diameter of BVs in each region.

As expected, overall collagen IV area and volume increased significantly between normal and tumor samples ($p<0.0001$ and $p<0.01$, respectively). However, on comparing the two areas (stromal and malignant) in normal tissue our results show practically no difference in surface area or volume of type-IV collagen expression or in BV diameters. On the other hand, in GBM both the area and volume of collagen IV expressed in MHCII-rich areas increase significantly ($p<0.001$ and $p<0.01$, area and volume, respectively) compared to normal tissue. Type-IV collagen expression in GFAP-rich areas does not vary significantly from normal tissue. Vessel diameters were not different in MHCII-rich areas but were significantly greater ($p<0.05$) in GFAP-rich areas. See Figure 87.

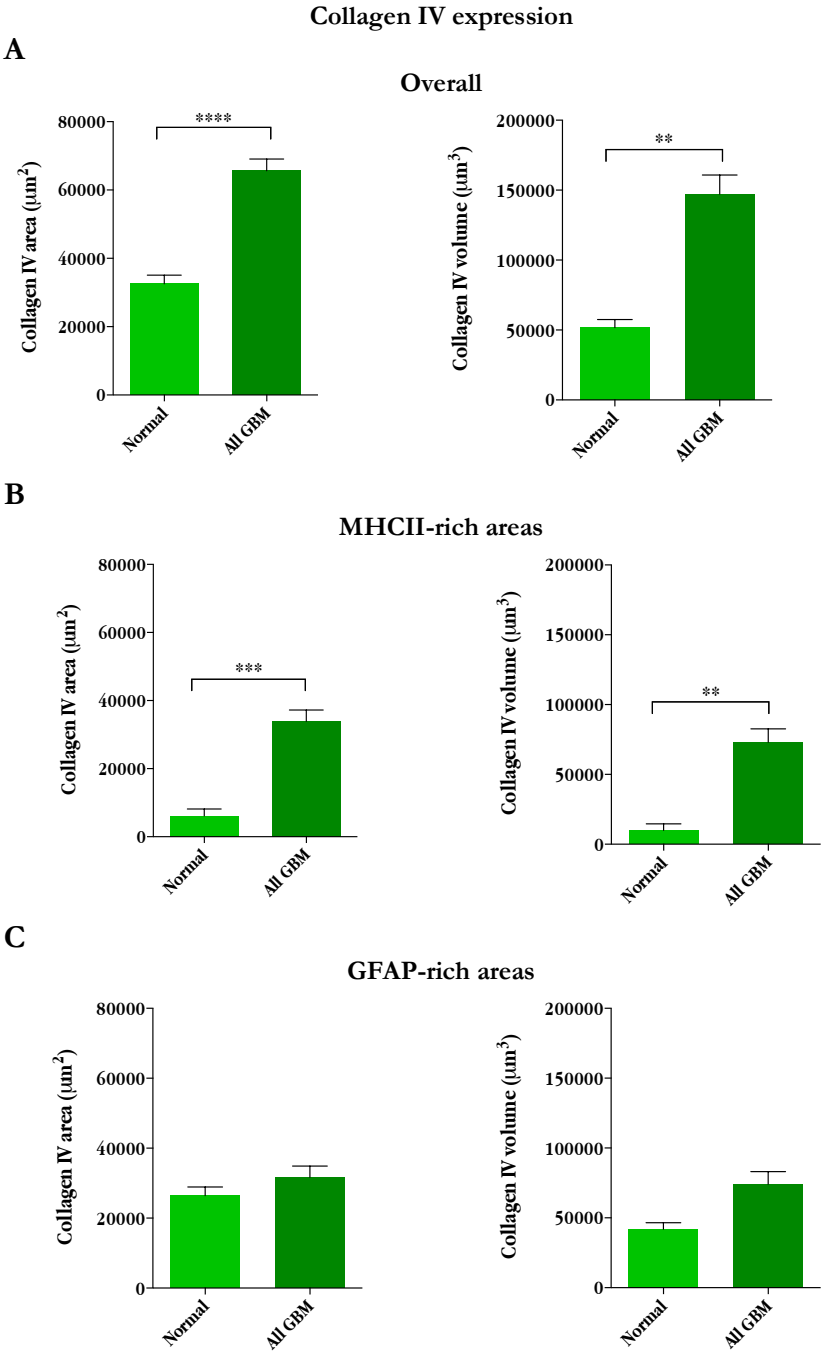
Collagen IV expression
A
Overall
Collagen IV area (µm²)
80000
60000
40000
20000
0
****
Normal
All GBM
Collagen IV volume (µm³)
200000
150000
100000
50000
0
**
Normal
All GBM
B
MHCII-rich areas
Collagen IV area (µm²)
80000
60000
40000
20000
0
***
Normal
All GBM
Collagen IV volume (µm³)
200000
150000
100000
50000
0
**
Normal
All GBM
C
GFAP-rich areas
Collagen IV area (µm²)
80000
60000
40000
20000
0
Normal
All GBM
Collagen IV volume (µm³)
200000
150000
100000
50000
0
Normal
All GBM

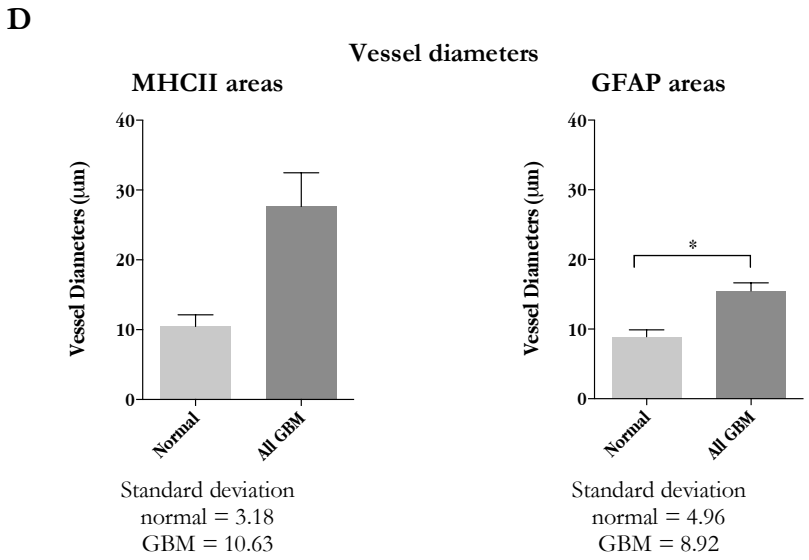

Figure 87. MHCII⁺ and GFAP⁺ areas show differences in collagen IV expression and BV diameters compared to normal tissue. Type-IV-collagen expression, overall (**A**) and separately in MHCII⁺ (**B**) and GFAP⁺ (**C**) areas. Bar graphs (**D**) show vessel diameters in MHCII⁺ and GFAP⁺ areas.

Comparing MHCII-rich vs. GFAP-rich areas revealed no significant differences in collagen IV expression, neither areas nor volumes. Vessel diameters were significantly larger ($p<0.05$) in MHCII-rich areas as opposed to GFAP-rich areas. Comparing vessel diameters in MHCII-rich and GFAP-rich areas as a function of tumor aggressivity showed significant differences only in the GFAP-rich areas between the 10 and 20% and 10 and 30% groups. Results are shown in Figure 88.

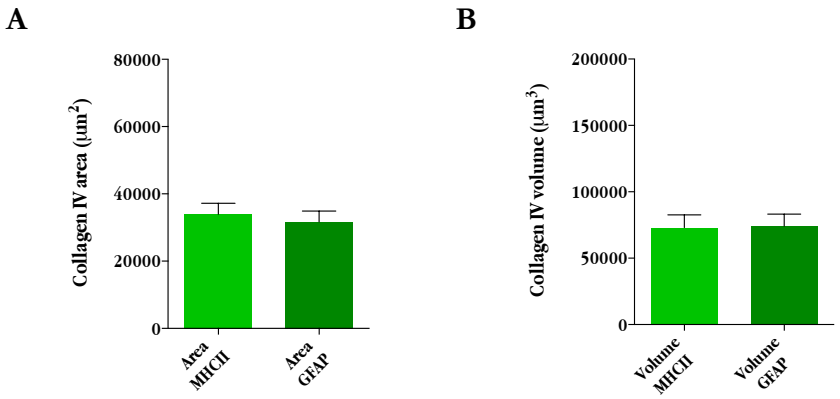

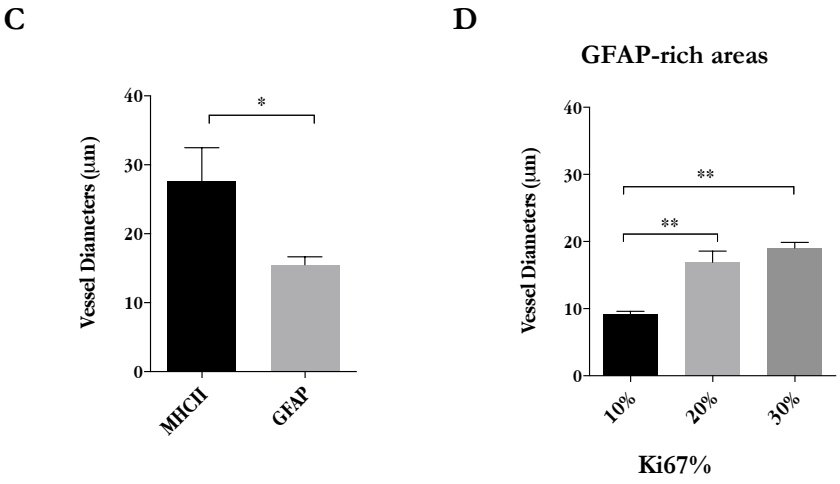

Figure 88. MHCII⁺ and GFAP⁺ areas showed no differences in collagen IV expression but showed larger BV diameters in MHCII⁺ areas and vessel diameters vary depending on tumor aggressiveness in GFAP-rich areas. Type-IV-collagen expression as area (**A**) and volume (**B**) compared between MHCII⁺ and GFAP⁺ areas. The lower bar graphs show vessel diameters in MHCII⁺ and GFAP⁺ areas (**C**) and GFAP expression across tumors in GFAP⁺ areas (**D**).

5.4.2 T cells

Given the importance of T cell participation for an effective immune response and given the vascular aberrations seen in GBM, we analyzed a five-sample pool of GBM biopsy tissues to quantify the total number of T cells and examine their distribution and location within GBM tissue and compare these measurements with BV data. To define location, T cells were divided into two conditions, etravasating or migrated. Extravasating is defined in terms of vascular interaction, i.e. being either inside or in contact with the BV, whereas migration is movement away from BVs inwards towards malignant or stromal tissue. Observe the distribution of T cells marked with CD3 in Figure 89 and the relation to GFAP-rich tumor areas and notice that some T cells maintain intimate contact with the BVs and appear to be in diapedesis whereas others are located some distance away from the vessel. To quantify these attributes, total T cells marked with CD3 were counted and extravasation (number of cells) and migration (numbers and distances) were measured.

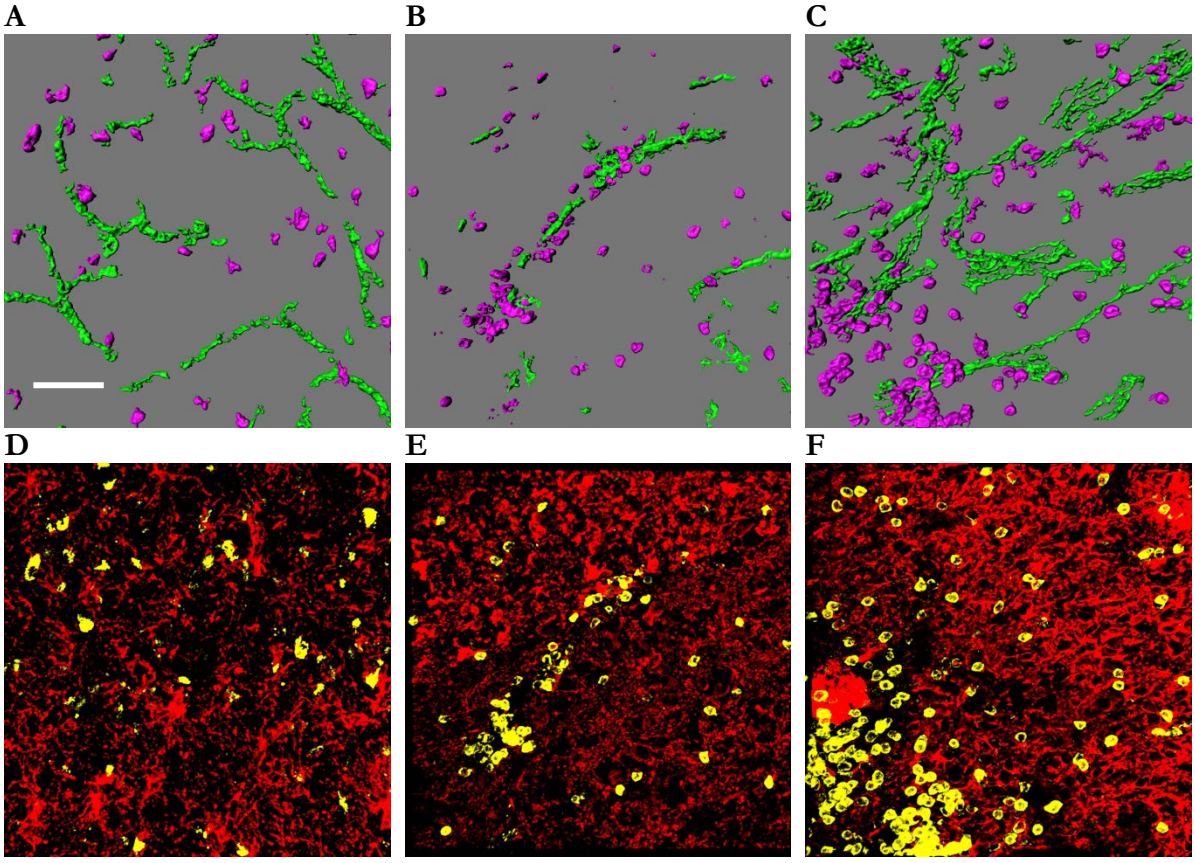

Figure 89. Some T cells are in contact with or in close proximity to BVs and others are in stromal or malignant tissue at varying distances from the BVs. 3D reconstructions (**A**-**C**) of GBM with 10, 20 and 30% Ki67, respectively, illustrating how T cell (magenta) numbers and locations relative to BVs (green) vary across GBM samples. Confocal images (**D**-**F**) show the relation between GFAP$^+$ elements (red) and T cells (yellow) in the same samples. Notice in some tissues there is a greater proportion of T cells near or in contact with BVs whereas in other cases there is a wider dispersion. Collagen IV (green), CD3 (magenta, A-C; yellow, D-F) and GFAP (red). Scale bar 50 μm.

Figures 90 and 91 show T cells in relation to BV endothelium, some as they pass through the basement membrane presumably to enter tumor or stromal areas.

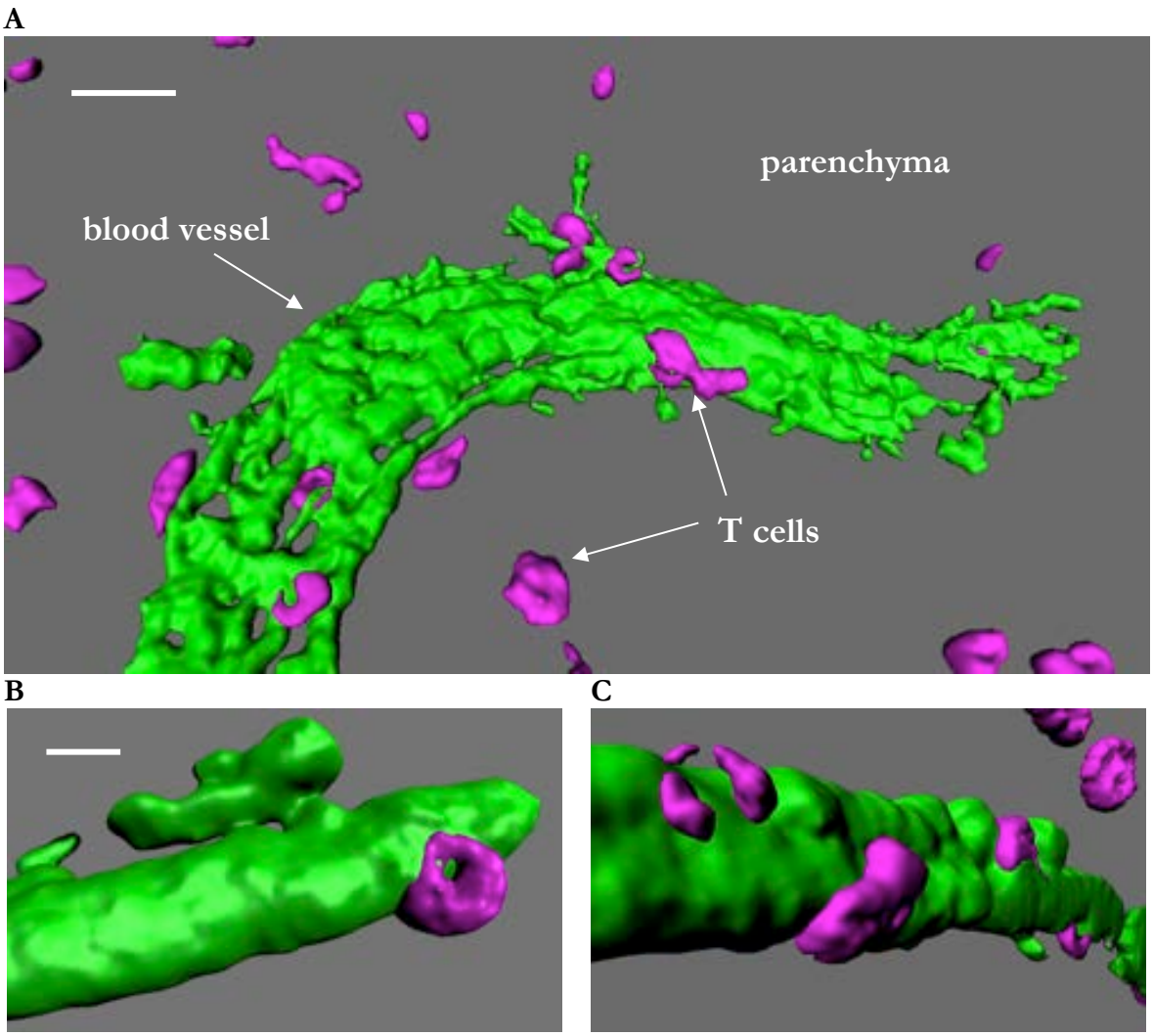

Figure 90. T cells shown in relation to the BV endothelium presumably poised to enter stromal or malignant tissue. 3D isosurface reconstructions of TABV endothelium (CD31, green) and T cells (CD3, magenta) (**A**) and BV segments (**B** and **C**) with T cells apparently passing through the BV endothelium in a GBM sample. Scale bars A, 20 μm, B and C, 10 μm.

A

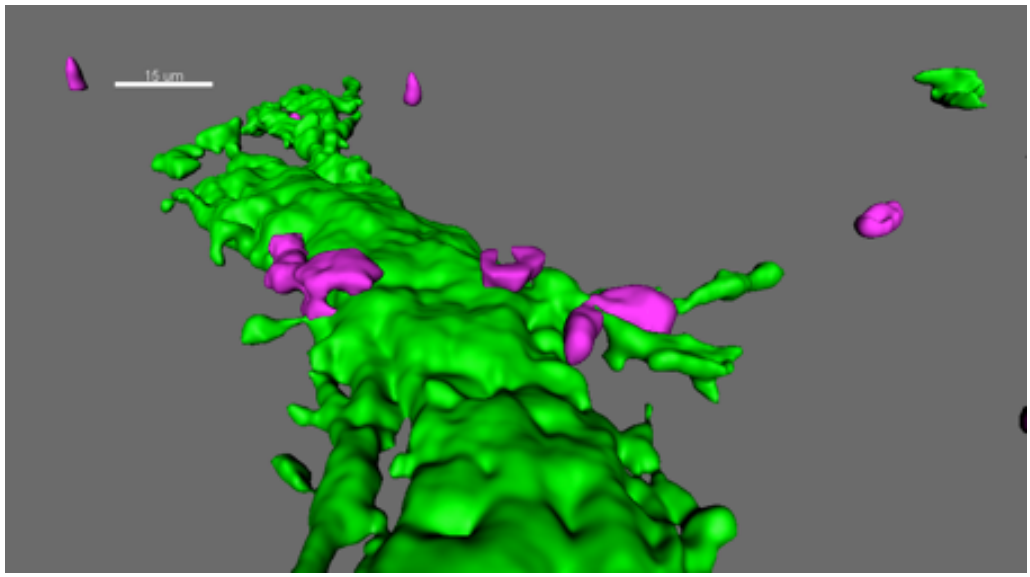

B

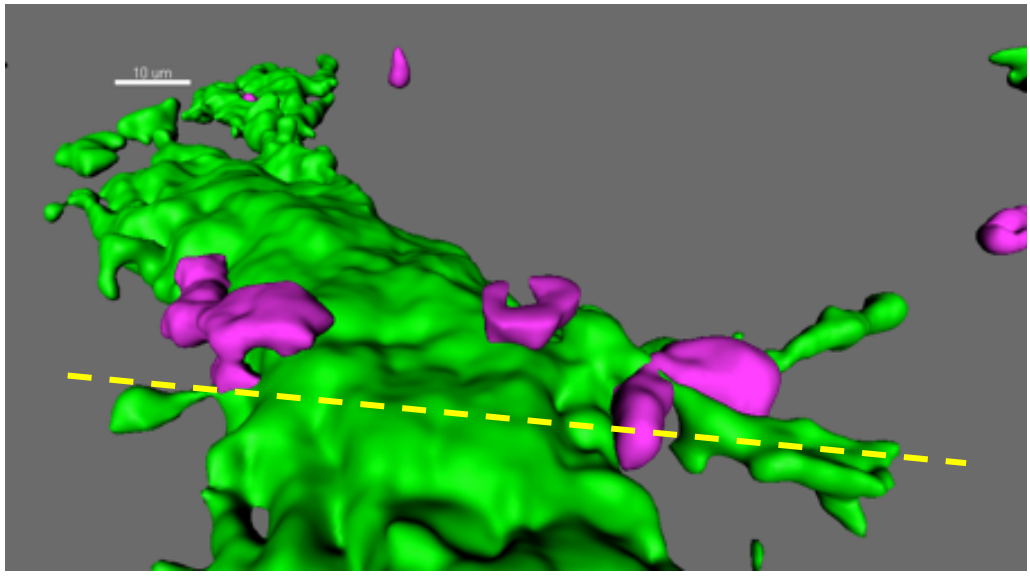

C

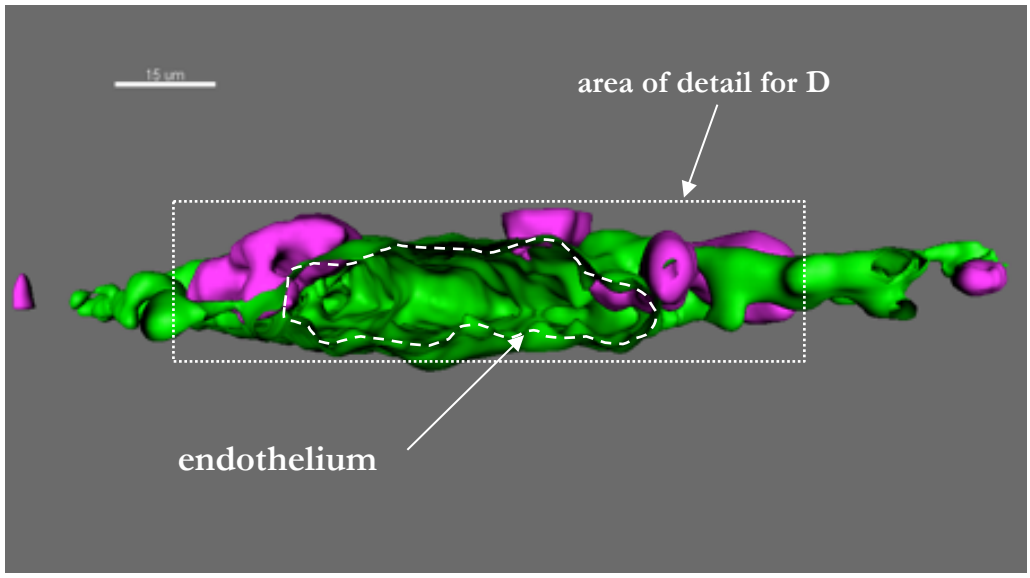

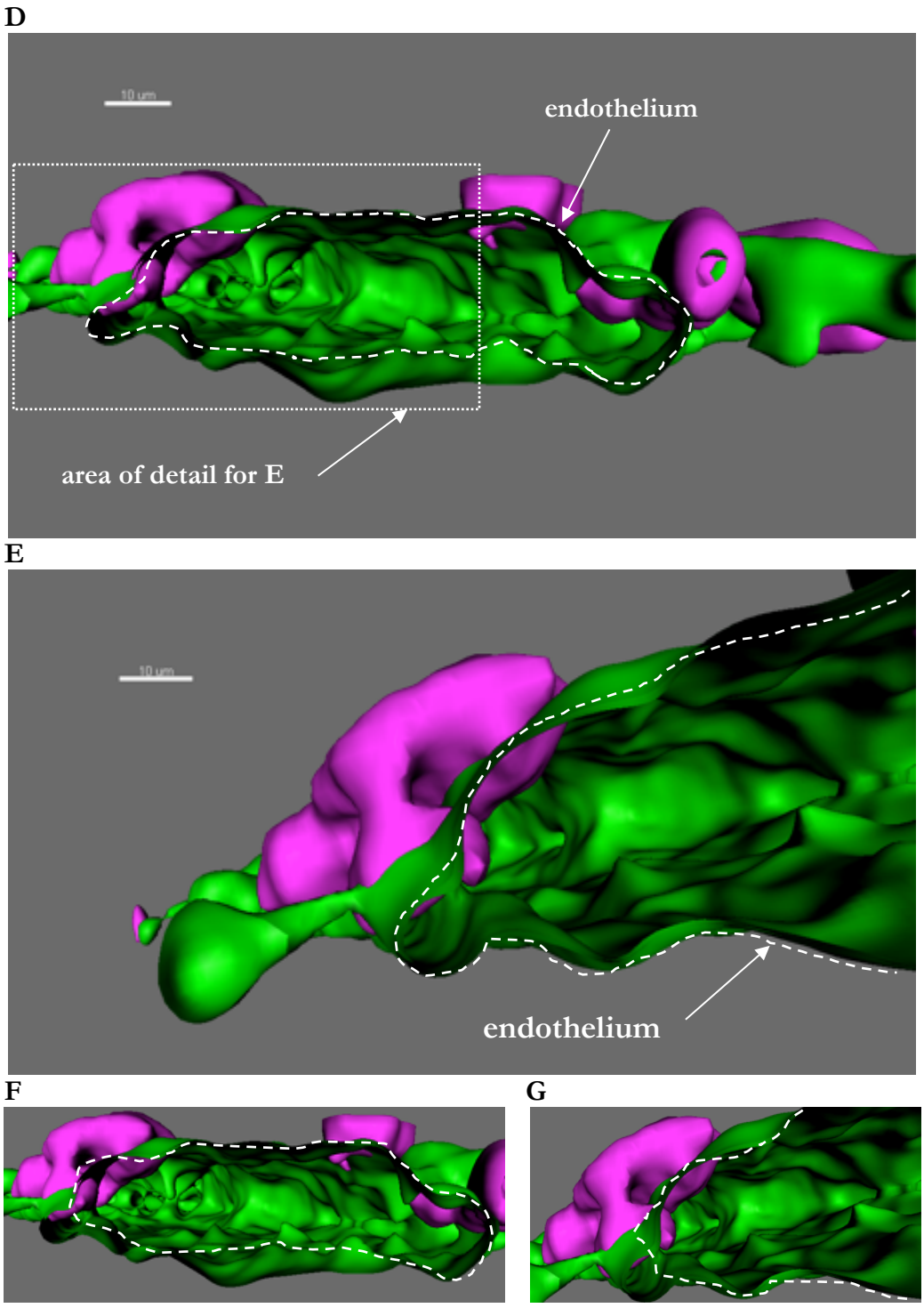

Figure 91. 3D reconstructions showing leukocyte extravasation across BV endothelium in GBM samples. Five views at different zooms showing blood vessel endothelium (green) and partially extravasated T cells (magenta) (**A** and **B**) and three increasing zooms (**C**-**E**) of the clipping plane at the yellow dashed line shown in B. Detailed views (**F** and **G)** of images D and E, respectively, show the outline of the BV endothelium (white dashed line) in relation to the T cells (magenta). Note how the T cells appear to be crossing through the BV endothelium. Scale bars 20 μm (A, C) and 10 μm (B, D and E).

Even though T cells are able to enter and survey the brain parenchyma in conditions without BBB damage or neuroinflammation, T cells in this context show limited motility and exit quickly unless they encounter cognate antigens; naïve T cells in healthy CNS parenchyma only show relatively stationary behavior (Díaz et al., 2018; Herz et al., 2011; Hickey, Hsu, & Kimura, 1991; Wekerle, Sun, Oropeza-Wekerle, & Meyermann, 1987). Thus, for the purposes of the quantifications done here, we considered normal tissue as having a T cell count of zero.

Five GBM biopsy tissues with Ki67% indices of 10, 20 and 30% were analyzed (six areas sampled from each biopsy tissue). Results showed that total T cells increased with Ki67% index and both 20 and 30% samples differed significantly from normal tissue ($p<0.01$ and $p<0.05$, respectively) as shown in Figure 92.

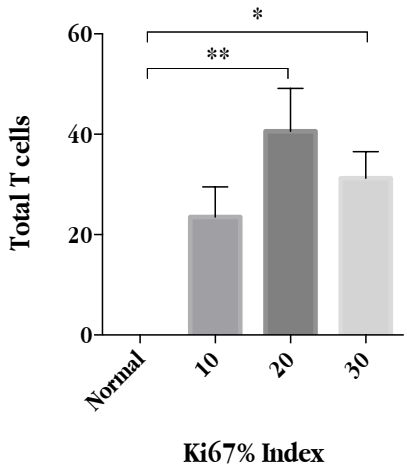

Figure 92. The total number of T cells increases in GBM though not strictly tied to increasing Ki67% indices. T cells tend to increase as Ki67% index increases although not linearly. Higher indices resulted in significant differences but not the 10% group.

Differences in total number of cells either in close proximity to or inside BVs were not significant between samples regardless of Ki67% index (Figure 93A); however, migration or extravasation of T cells tended to increase in samples with higher Ki67% indices. This increase was significant ($p<0.05$) between 10 and 20% Ki67 indices (Figure 93B).

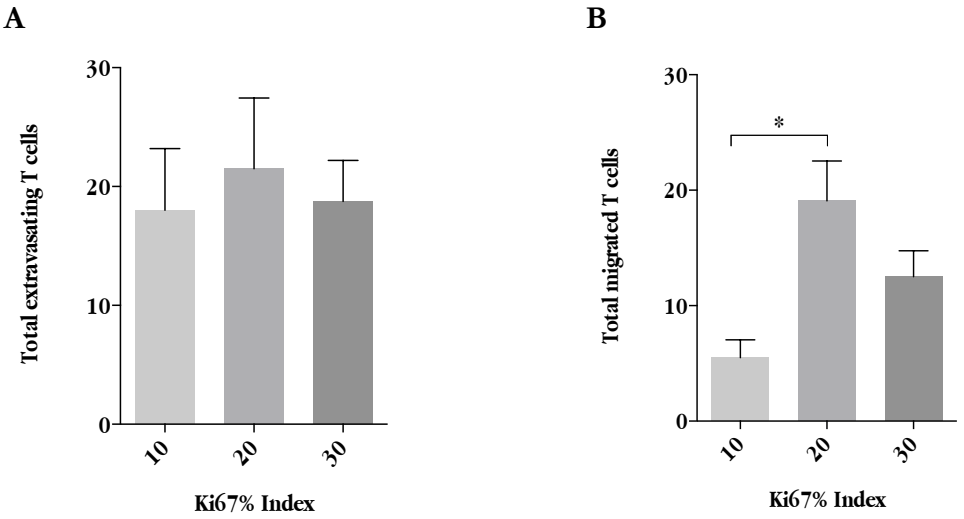

Figure 93. Extravasation (T cell-vascular interaction) remains relatively unaffected by tumor severity, but migration of T cells tends to increase with more aggressive GBM. Despite different Ki67% indices, the total number of extravasating T cells (**A**) remains similar in human GBM samples whereas the number of migrated T cells (**B**) varies significantly from Ki67 10 to 20%.

Interestingly, the ratio of extravasating to migrated cells decreases significantly ($p<0.01$) between samples with 10 and 20% and 10 and 30% Ki67% indices (Figure 94 A and B).

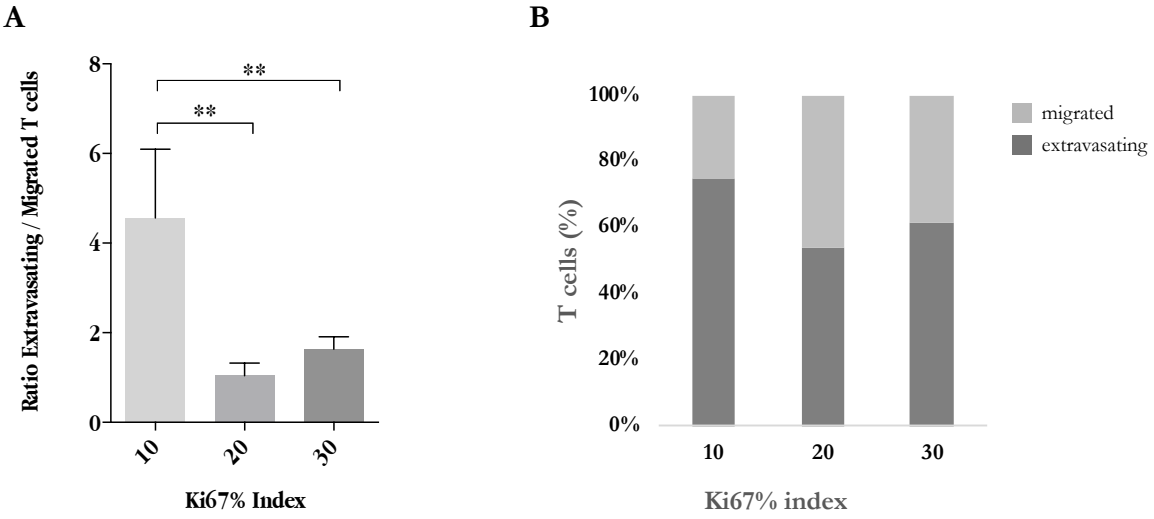

Figure 94. More aggressive GBM seems related to a decreased ratio of extravasating to migrated T cells. Ratios of extravasating to migrated T cells across three groups with Ki67% indices of 10, 20 and 30% (**A**). The same data presented as a stacked bar graph (**B**) with the respective percentages of extravasating and migrated T cells on a single bar for each group.

And finally, Figure 95 shows the mean distances travelled by migrated T cells measured from the nearest blood vessel. This parameter could also be understood as a rough estimate of intervessel distance as, presumably, the longest distance migrated is the halfway point between

two BVs. Differences were significant ($p<0.05$) when comparing the 10 and 20% Ki67% index groups.

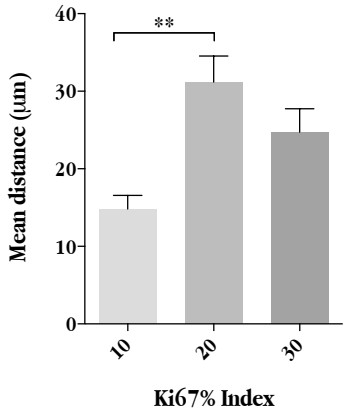

Figure 95. The mean distance T cells migrate into the stromal or malignant tissue tends to increase in more aggressive GBM. The graph shows the mean distance in µm that T cells migrate as measured from the nearest BV. The three bars represent 10, 20 and 30% Ki67% indices, respectively.

5.5 Cross comparisons between multiple parameters

Looking beyond significant differences in individual parameters between normal cortical tissue and GBM, this section presents results highlighting cross comparisons among parameters to explore possible interactions. Interrelations between all parameters measured were examined and the following grids summarizing Pearson correlation coefficients and scatterplots of individual values for these parameters were created. Section 5.5.1 shows data for the main sample pool (Table 5 and Figure 96, Pearson correlations and scatterplots, respectively). Section 5.5.2 shows the data for the CD31 sample pool (Table 6 and Figure 97 Pearson correlations and scatterplots, respectively).

5.5.1 Main sample pool

In general terms, there are significant correlations between all parameters measured although branching was somewhat of an exception (see Table 5). These parameters also showed significant differences between normal cortical tissue and GBM in the results presented in Sections 5.1 to 5.4.

Total cellularity correlated with mean vessel diameter ($p<0.0001$), vessel continuity ($p<0.0001$), collagen IV surface area and volume (both $p<0.0001$) and GFAP surface area and volume (both $p<0.001$). Mean vessel diameter correlated with branching ($p<0.01$), vessel continuity ($p<0.0001$), collagen IV surface area and volume (both $p<0.0001$) and GFAP surface area and volume (both $p<0.0001$). Branching correlated with GFAP area ($p<0.05$). Vessel continuity correlated with collagen IV surface area and volume (both $p<0.0001$) and GFAP surface area and volume (both $p<0.0001$). Collagen IV surface area correlated with GFAP surface area ($p<0.01$) and volume ($p<0.001$). And lastly, collagen IV volume correlated with GFAP surface area ($p<0.0001$) and volume ($p<0.0001$).

5.5.1.1 Pearson correlations – main sample pool

Table 5. Grid summarizing Pearson correlation results from multiple parameter comparisons for main sample pool

Note: asterisks in **red** denote negative correlations and asterisks in **black**, positive ones.

	Total cells	Mean vessel diameter	Total branches	Vessel continuity	Collagen IV area	Collagen IV volume	GFAP area
Total cells							
Mean vessel diameter	****						
Total branches	ns	**					
Vessel continuity	****	****	ns				
Collagen IV area	****	****	ns	****			
Collagen IV volume	****	****	ns	****	****		
GFAP area	***	****	*	****	**	****	
GFAP volume	***	****	ns	****	***	****	****

5.5.1.2 Scatterplots – main sample pool

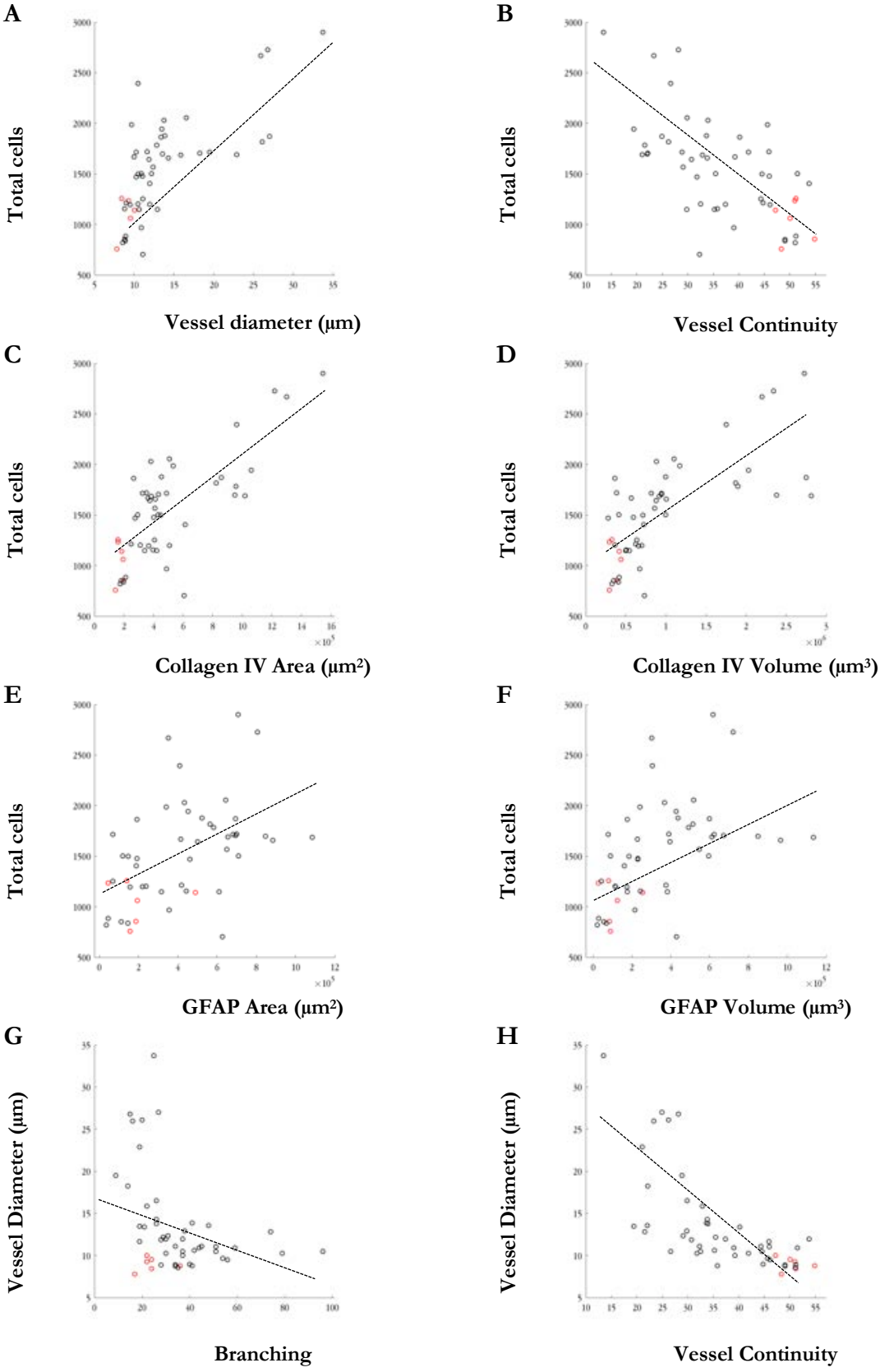

Figure 96. Scatterplots- main group. Total cells vs. vessel diameter, vessel continuity, collagen IV area and volume and GFAP area and volume, (**A**-**F**, respectively). Vessel diameter vs. branching and vessel continuity (**G** and **H**, respectively). Normal cortical tissue data in **red** and GBM data in **black**.

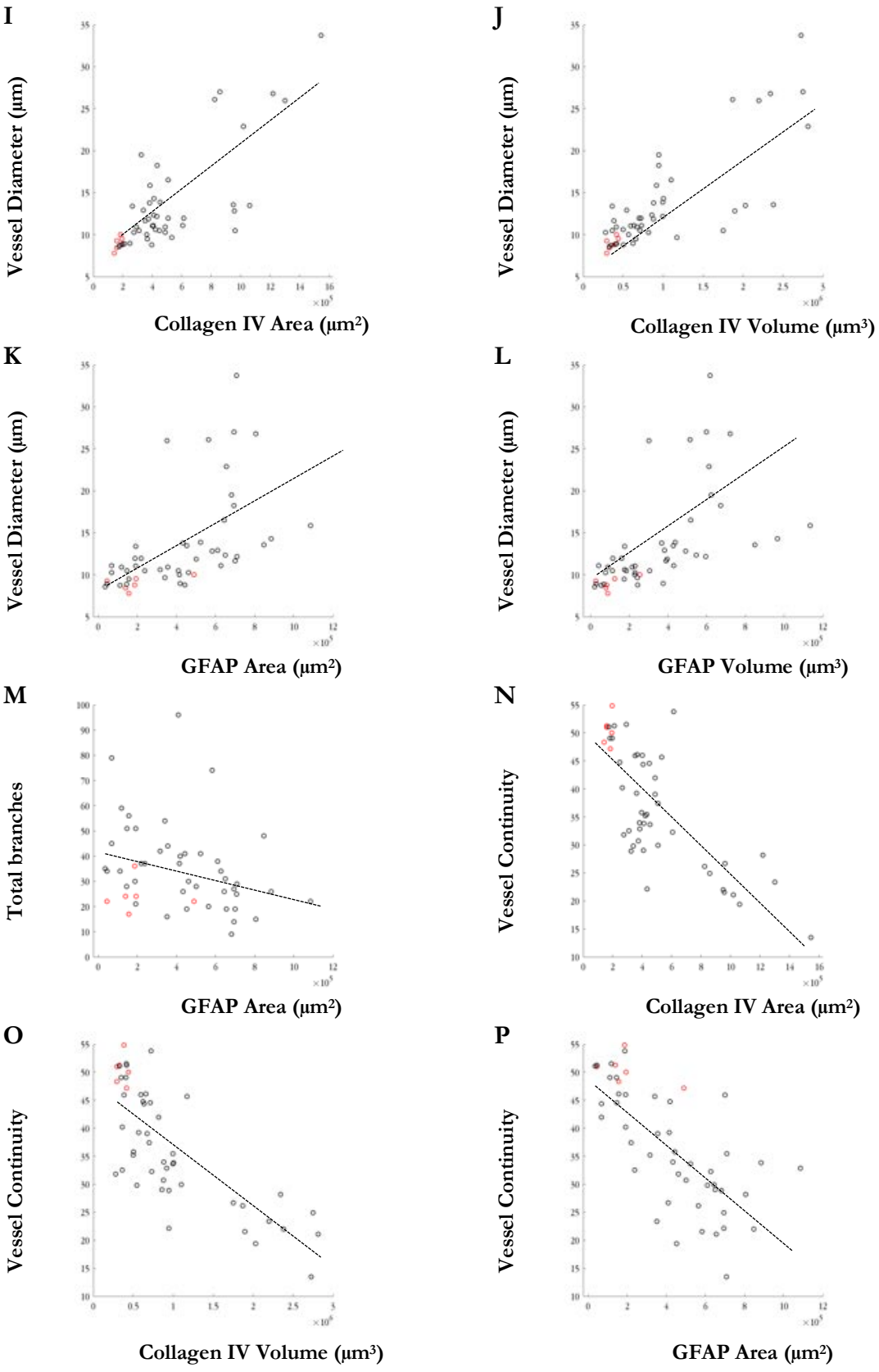

Figure 96 (cont.). Scatterplots- main group. Vessel diameter vs. collagen IV area and volume and GFAP area and volume (**I**-**L**, respectively). Total branches vs. GFAP area (**M**) and vessel continuity vs. collagen IV area and volume and GFAP area (**N**-**P**, respectively). Normal cortical tissue data in **red** and GBM data in **black**.

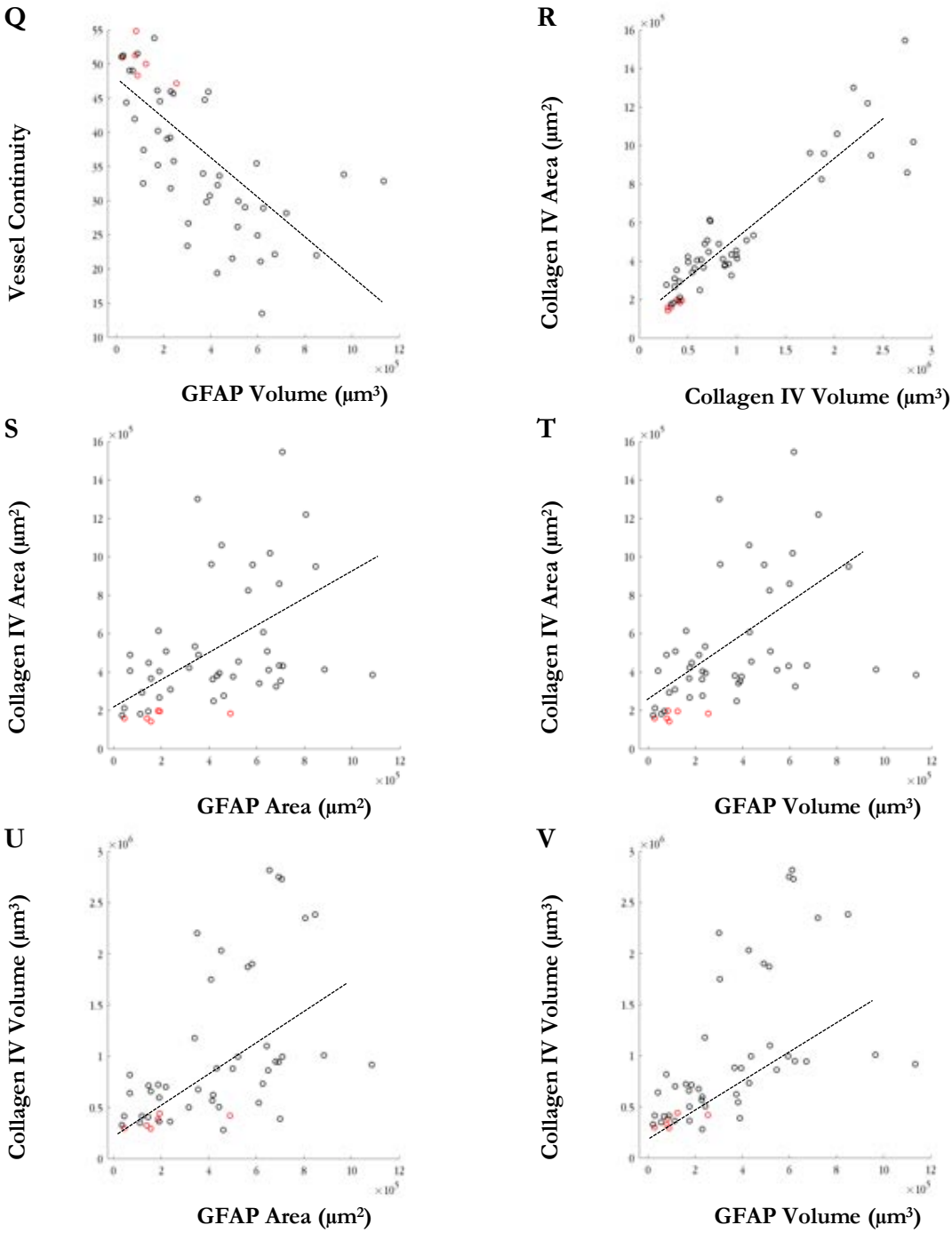

Figure 96 (cont.). Scatterplots- main group. Vessel continuity vs. GFAP volume (**Q**), collagen IV area vs. collagen IV volume and GFAP area and volume (**R**-**T**, respectively) and collagen IV volume vs. GFAP area and volume (**U**-**V**). Normal cortical tissue data in **red** and GBM data in **black**.

5.5.2 CD31 sample pool

5.5.2.1 Pearson correlations – CD31 sample pool

Table 6 shows a grid summarizing Pearson correlation results for multiple comparisons between parameters for the CD31 sample pool. In general terms, there are strong correlations between almost all parameters measured although colocalization in this case was an exception. Again, these parameters also showed significant differences between normal cortical tissue and GBM in the results presented previous sections.

Total cellularity correlated with vessel continuity ($p<0.001$), collagen IV surface area ($p<0.01$), CD31 surface area ($p<0.01$) and GFAP surface area ($p<0.01$). Vessel continuity correlated with collagen IV surface area ($p<0.0001$), CD31 surface area ($p<0.001$), colocalization ($p<0.01$) and GFAP surface area ($p<0.0001$). Collagen IV surface area correlated with CD31 surface area ($p<0.0001$), colocalization ($p<0.0001$) and GFAP surface area ($p<0.01$). CD31 surface area correlated with colocalization ($p<0.0001$) and GFAP surface area ($p<0.01$).

Table 6. Grid summarizing Pearson correlation results from multiple parameter comparisons for CD31 sample pool

Note: asterisks in **red** denote negative correlations and asterisks in **black**, positive ones.

	Total cells	**Vessel continuity**	**Collagen IV area**	**CD31 area**	**Colocalization (CD31 and Col IV)**	**GFAP area**
Total cells						
Vessel continuity	***					
Collagen IV area	**	****				
CD31 area	**	***	****			
Colocalization (CD31 and Col IV)	ns	**	****	****		
GFAP area	**	****	**	**	ns	

5.5.2.2 Scatterplots – CD31 sample pool

Figure 97 shows scatterplots of individual data comparing each of the parameters that showed significant correlations as seen in Table 6.

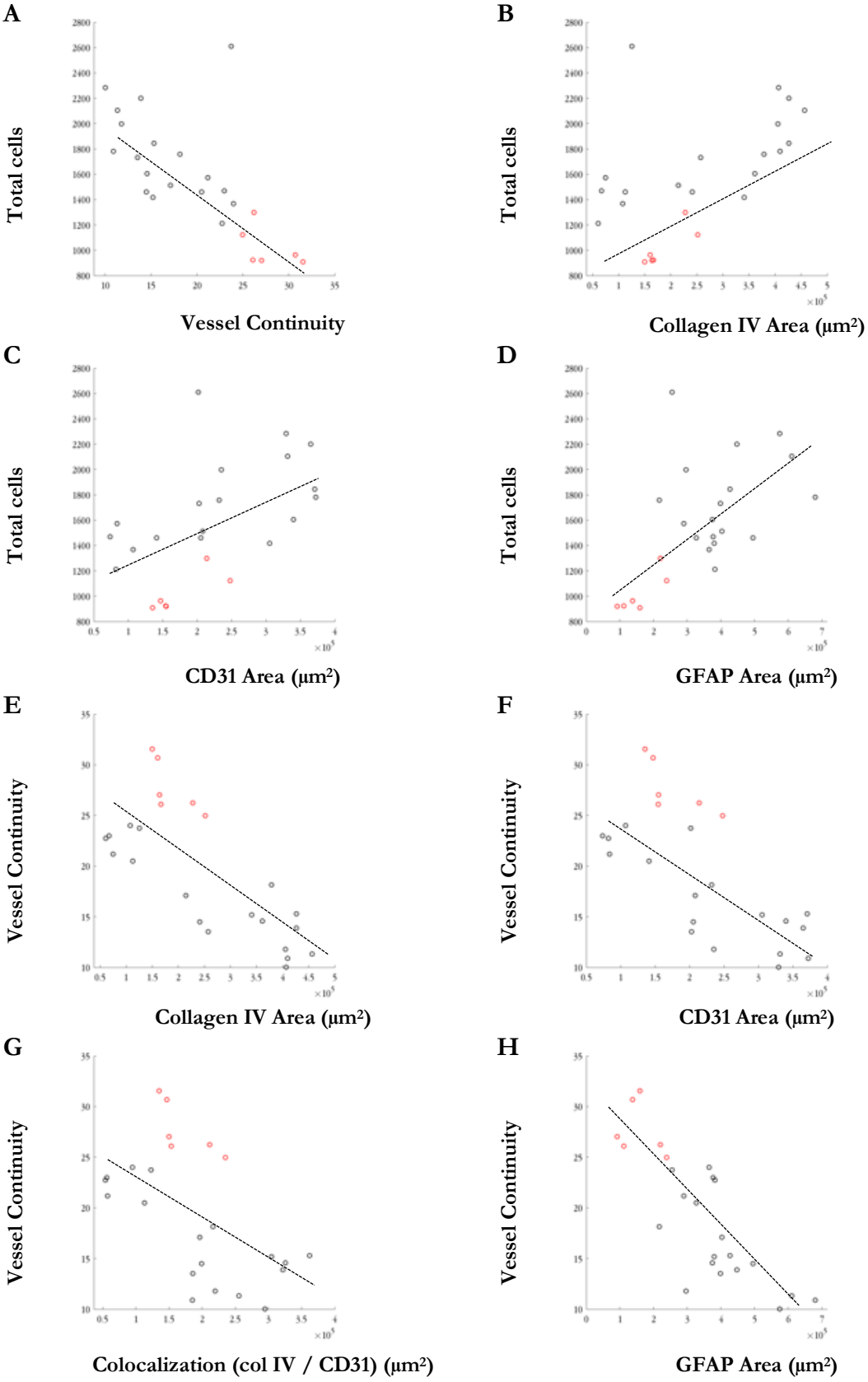

Figure 97. Scatterplots- CD31 group. Total cells vs. vessel continuity, collagen IV area, CD31 area and GFAP area, (**A**-**D**, respectively). Vessel continuity vs. collagen IV area, CD31 area, colocalization (collagen IV : CD31) and GFAP area (**E H**, respectively). Normal cortical tissue data in **red** and GBM data in **black**.

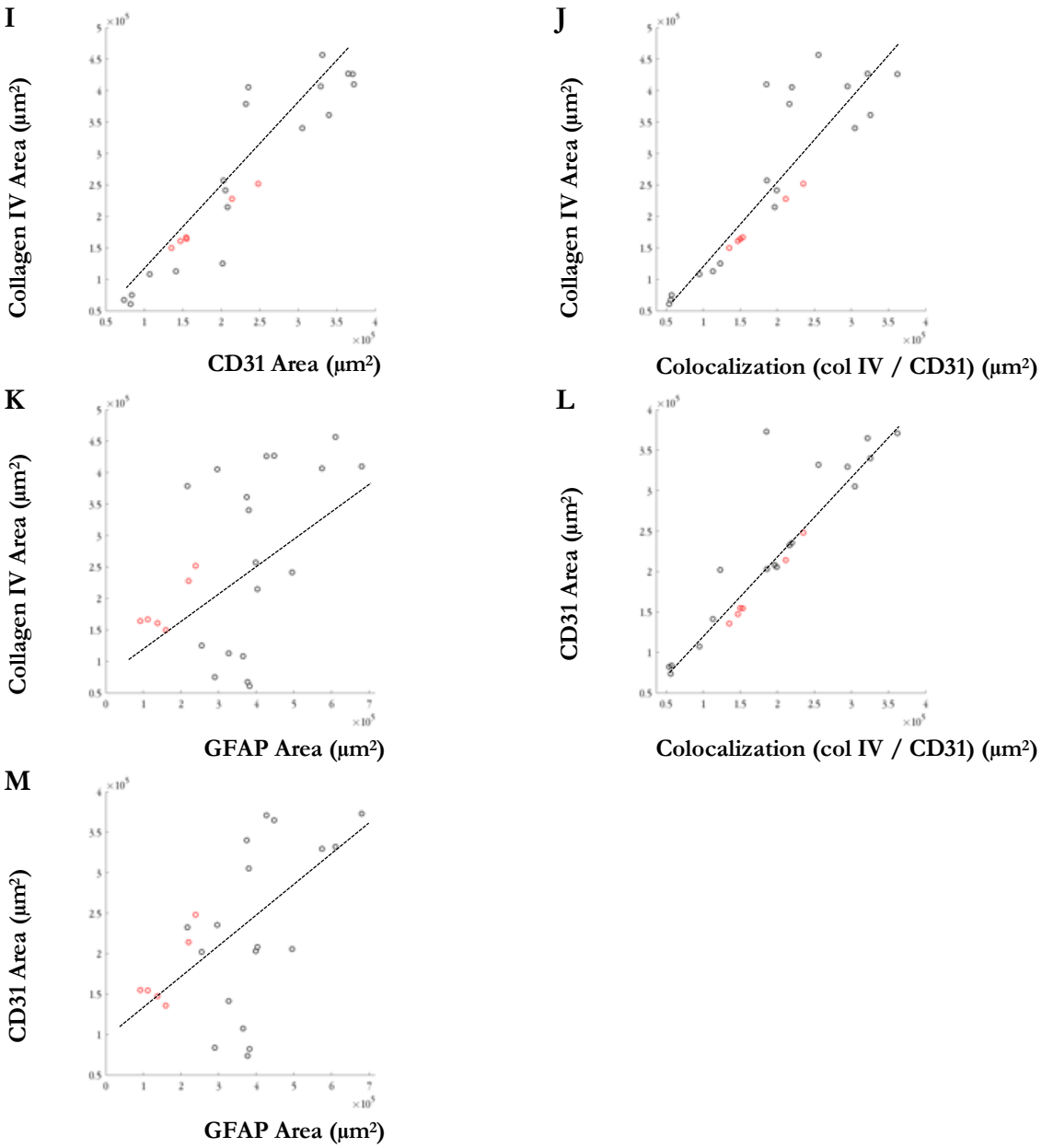

Figure 97 (cont.). Scatterplots- CD31 group. Collagen IV area vs. CD31 area, colocalization (collagen IV : CD331) and GFAP area, (**I**-**K**, respectively) and CD31 area vs. colocalization (collagen IV : CD331) and GFAP area (**L**-**M**). Normal cortical tissue data in **red** and GBM data in **black.**

6 DISCUSSION

This research describes GBM from a novel perspective after carefully examining the tumor topology in thick-section human biopsy samples immunostained so as to substantially preserve tissue structure. In contrast to the vast majority of studies referencing thin mount tissue preparations, which obfuscate any 3D spatial relationships between TME components, our results focus on these relationships and emphasize the importance of understanding GBM biology in context and, if nothing else, reinforce the enormous morphological heterogeneity of glioblastoma. Some of our results corroborate previously published information regarding GBM but in many cases the results move one step further in illustrating phenomena in human GBM biopsy samples that have previously been described in murine models or in vitro studies. Where relevant this will be pointed out.

Overall cellularity seems a good starting point not only because hypercellularity is a known hallmark of GBM but also because tumors are routinely graded for severity after biopsy by assigning Ki67% indices, as Ki67 is a specific marker for cell proliferation. This also makes overall cellularity an interesting benchmark against which to measure and compare other parameters. As expected, our results for total cell counts correlate well with the independently assigned Ki67% indices, thus indirectly confirming the diagnostic criteria and inversely indirectly validating our staining procedure.

It was expected that GFAP-positive surface areas would increase with tumor aggressivity (defined as Ki67% index) and that increased cellularity would correlate with the GFAP surface area parameter. This was in fact the case. Unfortunately, given our methods, it is neither possible to determine what contribution increased $GFAP^+$ cells make to overall hypocellularity nor to determine what proportions other TME subpopulations contribute.

Furthermore, $GFAP^+$ surface area increased significantly with higher individual Ki67% indices and correlated with all other parameters measured. These results have several important implications. Firstly, the high degree of correlation between $GFAP^+$ surface areas and type-IV collagen surface areas and the fact that both increase significantly with higher Ki67% indices imply that these are somehow parallel processes in tumorigenicity and neovascularization. Thus, it may be that new vessel growth is associated with increases in the astroglial cell population supporting the idea of cooption-induced neovascularization. Further support for this claim comes from the correlation between total branching (an indicator of new vessel formation) and $GFAP^+$ surface areas, which, by the way, is the only factor for which vessel branching showed significant correlation.

Characterization and modeling of normal cortical vasculature has been well-studied (Lauwers, Cassot, Lauwers-Cances, Puwanarajah, & Duvernoy, 2008; Lorthois, Cassot, & Lauwers, 2011) and studies have also been done to characterize GBM vessels in vivo using MRI or ToF angiography (Radbruch et al., 2014) in an attempt to improve differential diagnosis of GBM and aid in predicting response to treatment and prognosis. Numerous studies have examined blood vessel diameters in mouse models including cross comparisons of different mouse GBM models to characterize the vascular features across models. Especially relevant to this thesis is research by Watkins et al. (2014) which examined the relative affinity of glioma cells to different diameter vessels. Of the few studies that exist to examine GBM vasculature, an important one studies three animal tumor models (Baluk et al., 2003). Ours is perhaps one of the first to characterize human GBM vessel networks in 3D using thick tissue sections and creating large scale mosaics to understand the structural and topographical organization in normal samples and observe how that changes in GBM samples. As expected, we found overall increased vessel density and one of the more obvious differences shown by GBM tumor vasculature is the wider range of vessel calibers, the smallest vessels are smaller and the larger vessels, larger than in normal tissue. Moreover, differences in standard deviation of vessel diameters are also more pronounced in GBM samples. This has direct implications on not only tumor blood supply but also on therapeutic drug delivery as vessel diameter is a crucial hemodynamic factor affecting the flow rate and volume of fluid flowing through a vessel.

As a result of measuring vessel diameters, we were also able to estimate the number of microvessels (diameter ≤ 5 μm) present in normal tissue and tumors. Statistically, the differences were not significant but, nevertheless, this data is important. The microvessels observed in normal tissue generally had the appearance of being intact, connected vessels whose diameter was insufficient to permit blood flow. It has been described that silent vessels can be recruited as a ready means of neovascularization and this seems a logical conclusion. In the case of injury or sudden need for increased blood supply, it is an extremely rapid and effective first response to enlist an existing vessel, albeit one needing to increase in diameter, rather than create a new one. The fact that there is a slightly higher percent of microvessels in GBM does not contradict this. The microvessels observed in GBM samples generally had the appearance of being incomplete or immature in contrast to the well-formed normal microvessels. The massive neovascularization occurring in GBM probably results in greater numbers of immature, nonfunctional vessels.

Branching patterns in GBM may give clues to possible angiogenic strategies and similarly to BV diameter, vessel branches have an impact on vessel hydrodynamics and functionality. Numerous variations of branching type are discernable across tumors with different Ki67% indices as well as in normal tissue. In fact, in some of the samples from more highly aggressive tumors the degree of membrane degradation is so severe that it is not only difficult to appreciate vessel outlines but also nearly impossible to distinguish branching points, if they exist at all. Nevertheless, in the majority of samples simple and more complex branching is clearly evident. Our results show that simple bifurcations are by far the most frequent but there are plentiful examples in both normal tissue and GBM of more complex three- or four-branch junctions, or in some cases networks which appear to give rise to even more ramifications. That simple bifurcation is the predominant branching strategy is fully understandable given that the majority of angiogenic strategies including standard angiogenesis, intussusception, sprouting, looping and recruitment of silent collateral vessels would all logically lead to simple branching.

Ironically, although GBM facilitate their own survival by creating new vessels, these new vessels or tumor associated blood vessels (TABVs) are somehow underdeveloped and dysfunctional. They are typically tortuous and disorganized and show morphological alterations, e.g. leakiness, disconnection, dilation and uneven diameters, excessive branching, endothelial fenestrae, widened interendothelial junctions, pericyte coverage disruption and absent or discontinuous basement membrane (Bergers & Benjamin, 2003; Carmeliet & Jain, 2000; Jain et al., 2007; Stacey Watkins & Sontheimer, 2012). Hence, vessels are often immature with corresponding variability in vessel permeability and differential interstitial fluid pressure (IFP) and compromised perfusion of surrounding tissue, this latter also having important therapeutic implications by affecting drug delivery (De Palma, Biziato, & Petrova, 2017; Jain et al., 2007; M & Baluk, 2002; Plate & Mennel, 1995). Much of this information is based on animal studies or thin tissue human samples; however, we were able to visualize and, in some cases, quantify these vessel aberrations in human GBM biopsy samples.

Perhaps most striking when first visualizing immunostained GBM vasculature is the heightened expression of type-IV collagen and the progressively more chaotic organization and disrupted morphology of tumor BVs reflected in erratic collagen IV deposition, haphazard distribution and vessel wall discontinuity. The disrupted relationship between vessel basement membrane and endothelial cells lining the vessels is also noteworthy.

In fact, the more severe the tumor, the more aberrant the BVs appear in our images. This can be appreciated best in our hypermosaics of extended tumor areas in which normal vessels appear fairly evenly distributed and vessel diameters are more or less consistent and uniform in contrast with GBM vessels which are the opposite, erratically distributed and with widely varying diameters. The erratic distribution of BVs in tumor areas might have direct implications on perfusion, or rather lack of, in certain tumor areas. The differences in diameter are clearly reflected in our results which show significant differences between normal and GBM vessel calibers, GBM vessels being more extreme in all measures, largest vessels are larger, smallest vessels are smaller and median vessel diameter and standard deviation are greater in GBM compared to normal cortical tissue.

Increased type-IV-collagen-positive surface areas and volumes are presumably a direct consequence of increased collagen IV expression, and our results show that both collagen-IV surface areas and vessel density, as measured by collagen IV volume, increase consistently across tumors with increasing Ki67% indices.

Importantly, this increased collagen IV expression, while leading to more new BVs does not necessarily equate with more functional BVs. This is perhaps most evident in the notable discontinuity of GBM vessel membrane and in the disruption between type-IV collagen in basement membranes and CD31-expressing endothelial cells lining the vessels. Our results show concrete evidence of vessel disruption and support that tumor BVs are indeed poorly formed and most likely dysfunctional.

Although frequently observed and widely accepted that GBM basement membranes are structurally aberrant, quantifying the changes and comparing the differences across tumors and against normal cortical tissue is difficult. Our approach measured the absolute intensities and standard deviations of variation in relative fluorescence along small vessel wall segments and compared them statistically. Our reasoning was that differences in type-IV collagen deposition and distribution in BV walls would be reflected in changes in luminance intensity of relative fluorescence along the vessel walls. This approach proved fruitful and examining the line plots of relative fluorescence standard deviations for normal tissue and GBM and the corresponding statistical analyses, it is clear that variation is significantly greater for tumor vasculature. The lines are spikier and the ranges greater for tumors in contrast to normal tissue, supporting the idea that variation in basement membrane fluorescence increases in tumors as they become more aggressive and implying that collagen IV deposition is altered,

i.e. more discontinuous, more uneven, with fenestrations, etc. Alterations at this level could support the vessel leakiness reported previously and generally accepted. Our results provide direct visual and numerical support for this leakiness, which carries important implications in terms of extravasation of plasma components normally excluded by the intact BBB and poor delivery of blood-borne therapeutic agents because BVs are defective.

Further along these same lines, our data for CD31 expression supports that endothelial cells increase in GBM in relation to tumor aggressiveness and moreover provides evidence of disrupted basement membrane-endothelial cell interactions in GBM. Total CD31 surface area increased significantly in GBM compared to normal tissue as did type-IV collagen and both parameters were highly correlated. Interestingly, the colocalization of collagen IV and CD31, though correlated with increases in both, did not differ significantly between tumors and normal tissue. This finding suggests for normal vessels, increases in collagen IV are paralleled with increases in CD31 and colocalization is nearly 100% because intact, healthy basement membranes also have intact endothelial cell linings. By contrast, this relation appears severed in GBM because although both parameters increase significantly in more severe tumors their colocalization does not reflect these increases. This could support the idea of malformed, immature and dysfunctional vessels if the de novo vessels do not have intact endothelial cell linings.

TAMMs are known to constitute 30-50% of GBM tissue (Hambardzumyan et al., 2015; Morantz, Wood, Foster, Clark, & Gollahon, 1979). Our results for both Iba-1 and MHCII expression confirm significant occupation of GBM tissue by TAMMs. For both markers, surface area, volume and units of marked cells increased significantly with increased tumor Ki67% index, the result being more pronounced in the case of $MHCII^+$ cells. Additionally, $MHCII^+$ and $GFAP^+$ cells seem to occupy mutually exclusive TME niches. This does not appear to be the case for Iba-1. Our lab has previously found that even though the majority of Iba-1 marked cells should also be detected by MHCII, a substantial subpopulation of Iba-1 expressing cells do not express detectable levels of MHCII. Thus, there may be distinct subpopulations of TAMMs which differ in MHCII expression, some expressing higher levels and thus detected by immunostaining and others expressing lower, essentially undetectable levels of MHCII. This along with our results showing that $MHCII^+$ cells and $GFAP^+$ cells appear to occupy mutually exclusive niches in stromal and malignant areas, respectively,

support the notion that phenotypically distinct microglia/macrophage subpopulations reside in distinct TME areas.

Our results show increased total T cells in GBM, significantly so for Ki67 indices of 20 and 30%, though not linearly correlated with increasing Ki67% index. They also give indications of possible variations in tissue distribution of T cells associated with increasing tumorigenicity. Total extravasating T cells (inside or in close proximity to BVs) are not significantly different in absolute terms for normal and GBM samples but the ratio of extravasating to migrated (located at varying distances from BVs) T cells decreases significantly in tumors with higher Ki67% indices. Thus, our results indicate that higher tumorigenicity is associated with greater T-cell migration in absolute terms and mirrored in a significantly lower ratio of extravasating to migrated T cells. This corroborates previously reported results supporting massive T cell infiltration in GBM scenarios (Carpentier & Meng, 2006; Díaz et al., 2018). Moreover, mean distance migrated increases though not linearly with increasing tumor aggressiveness. Even though distribution of T cells in tumor and stromal areas was not quantified in this study, infiltrated T cells did not seem to show a clear preference for stromal or malignant areas, which would support previous work in the lab (Díaz et al., 2018, in press). These results taken together with our results indicating increased vessel wall discontinuity and collagen IV-CD31 disruption suggest that T cells enter CNS parenchyma under GBM conditions not only in response to activating factors and cues but also because their entry is facilitated by more permeable BV membranes.

From the outset, it was clear that any conclusions based purely on the statistical analyses of the small number of samples studied would be difficult to support because of the limited power. Nevertheless, perhaps the most convincing evidence provided herein is founded on the exquisite imaging resulting from the meticulous staining, imaging and analysis of the small cohort chosen.

Above and beyond the morpho-topographical data obtained from the parameters assessed, this thesis research has provided equally important non-numerical information to the study of GBM, namely an accurate, reproducible immunostaining protocol for thick-tissue sections and an extensive and growing collection of high-quality confocal image stacks and the resulting images extracted from them. It is, and always was, a primary objective of this thesis to compile sufficient parametric data to permit the 3D reconstruction of GBM vascular networks and TME components. We have largely succeeded in this objective and our method enables

visualization of 20-80-micron thick human GBM biopsy samples and offers glimpses of intra-tumoral organization on a level not previously attempted. It opens the possibility of acquiring high-resolution information from largely intact tissues and provides the opportunity to learn about organizational principles that would otherwise be difficult or impossible to study. To our knowledge there are no other techniques or structural approaches using three-dimensional imaging techniques capable of or thus far employed for this kind of detailed analysis of multiple individual components of human GBM in the same tissue sample.

We believe that large tumor areas can be assessed with this approach and this makes it plausible to reconstruct entire tumors with reasonable accuracy. Even the purely manual reconstruction of smaller areas should provide insights into topographical questions and provide information that could be valuable for targeting tumor subpopulations either via drug therapy or immunotherapy.

Although it may be unrealistic to expect that an entire GBM tumor will ever be completely reconstructed, we believe this research meets the requirements for a technique to compile a full 3D atlas of human GBM and hopefully contributes to providing the incentive to do so.

It is said that one picture is worth a thousand words and hopefully, the images presented herein are sufficiently eloquent to convey the narrative embracing the multiple facets of GBM which despite its lethality can inspire a sense of awe for its astounding survival ability and for the beauty of the images it engenders.

7 CONCLUSIONS AND FUTURE DIRECTIONS

The following conclusions can be drawn from the results described above:

- Analyses confirm correlation of cell density and tumor severity (internal control).
- Vessels caliber range and variability increase positively with tumor severity.
- Collagen IV$^+$ vessel branching increases with tumor severity.
- Single branching (i.e. simple bifurcation) seems to be the predominant angiogenic strategy in GBM. Multiple branching (new ramifications at existing branching points) occurs infrequently and is probably not an important angiogenic strategy in GBM.
- Blood vessel wall disruption increases with tumorigenicity in terms of collagen IV deposition in basement membranes and in terms of increased dissociation of CD31 and collagen IV in basement membranes.
- Both CD31 and collagen IV expression increase with tumor severity whereas colocalization (i.e. surface-to-surface contact) between the two decreases, suggesting that pro-angiogenic forces stimulate neovascularization through separate processes involving collagen IV and endothelial cell production.
- T cells increase with tumorigenicity whereas the ratio of T cells inside of or in the proximity of vessels to those having migrated some distance from vessels decreases. T cells migrate further from vessels in more aggressive tumors.
- T cell migration correlates positively with increased vessel discontinuity.
- TAMMs increase with tumor severity.
- MHCII$^+$ cells and GFAP$^+$ cells occupy mutually exclusive niches in the GBM TME.

Consistent with the intentions driving the research of which this thesis is a result and based on the often-unanticipated beauty and clarity of the images generated in this process, a logical extension of the ideas and techniques elaborated herein would be to submit a journal article that fully exploits the possibilities of the material and fulfils the concept of an atlas. Moreover, in conjunction with such an article it would be desirable to make a portion of the original images publicly accessible for further exploration on the part of other interested researchers. There are certain precedents involving journal articles describing other types of tissue or cell systems, but the idea of taking this project to its logical conclusion is intriguing. As such, preliminary steps have been made to write an article which could form the basis for establishing a small database of GBM images for public consultation.

BIBLIOGRAPHY

Abbott, N. J., Rönnbäck, L., & Hansson, E. (2006). Astrocyte-endothelial interactions at the blood-brain barrier. *Nature Reviews Neuroscience*, *7*(1), 41–53. https://doi.org/10.1038/nrn1824

Adeberg, S., Bostel, T., König, L., Welzel, T., Debus, J., & Combs, S. E. (2014). A comparison of long-term survivors and short-term survivors with glioblastoma, subventricular zone involvement: A predictive factor for survival? *Radiation Oncology*, *9*(1), 95. https://doi.org/10.1186/1748-717X-9-95

Agnihotri, S., Burrell, K. E., Wolf, A., Jalali, S., Hawkins, C., Rutka, J. T., & Zadeh, G. (2013). Glioblastoma, a brief review of history, molecular genetics, animal models and novel therapeutic strategies. *Archivum Immunologiae et Therapiae Experimentalis*. https://doi.org/10.1007/s00005-012-0203-0

Aum, D. J., Kim, D. H., Beaumont, T. L., Leuthardt, E. C., Dunn, G. P., & Kim, A. H. (2014). Molecular and cellular heterogeneity: the hallmark of glioblastoma. *Neurosurgical Focus*, *37*(6), E11. https://doi.org/10.3171/2014.9.FOCUS14521

Ausiello, C. M., Palma, C., Maleci, A., Spagnoli, G. C., Amici, C., Antonelli, G., … Cassone, A. (1991). Cell mediated cytotoxicity and cytokine production in peripheral blood mononuclear cells of glioma patients. *Eur.J.Cancer*, *27*(5), 646–650. Retrieved from http://www.ncbi.nlm.nih.gov/pubmed/1711354

Bailey, P., & Cushing, H. (1926). *A classification of the tumors of the glioma group on a histogenetic basis : with a correlated study of prognosis*. Philadelphia PA: Lippincott. Retrieved from https://www.worldcat.org/title/classification-of-the-tumors-of-the-glioma-group-on-a-histogenetic-basis-with-a-correlated-study-of-prognosis/oclc/3459260

Baluk, P., Morikawa, S., Baluk, P., Kaidoh, T., Haskell, A., Jain, R. K., & Mcdonald, D. M. (2014). Abnormalities in Pericytes on Blood Vessels and Endothelial Sprouts in Tumors Abnormalities in Pericytes on Blood Vessels and Endothelial Sprouts in Tumors. *The American Journal of Pathology*, *9440*(April), 985–1000. https://doi.org/10.1016/S0002-9440(10)64920-6

Baluk, P., Morikawa, S., Haskell, A., Mancuso, M., & McDonald, D. M. (2003). Abnormalities of Basement Membrane on Blood Vessels and Endothelial Sprouts in Tumors. *American Journal of Pathology*, *163*(5), 1801–1815. https://doi.org/10.1016/S0002-9440(10)63540-7

Barcia, C., Gómez, A., Gallego-Sanchez, J. M., Perez-Vallés, A., Castro, M. G., Lowenstein, P. R., … Herrero, M. T. (2009). Infiltrating CTLs in human glioblastoma establish immunological synapses with tumorigenic cells. *American Journal of Pathology*, *175*(2), 786–798. https://doi.org/10.2353/ajpath.2009.081034

Bauchet, L., Mathieu-Daude, H., Fabbro-Peray, P., Rigau, V., Fabbro, M., Chinot, O., … Honnorat, J. (2010). Oncological patterns of care and outcome for 952 patients with newly diagnosed glioblastoma in 2004. *Neuro-Oncology*, *12*(7), 725–735. https://doi.org/10.1093/neuonc/noq030

Bergers, G., & Benjamin, L. E. (2003). Tumorigenesis and the angiogenic switch. *Nature Reviews Cancer*, *3*(6), 401–410. https://doi.org/10.1038/nrc1093

Brat, D. J., & Van Meir, E. G. (2001, March). Glomeruloid microvascular proliferation orchestrated by VPF/VEGF: A new world of angiogenesis research. *American Journal of Pathology*. American Society for Investigative Pathology. https://doi.org/10.1016/S0002-9440(10)64025-4

Brennan, C., Momota, H., Hambardzumyan, D., Ozawa, T., Tandon, A., Pedraza, A., & Holland, E. (2009). Glioblastoma subclasses can be defined by activity among signal transduction pathways and associated genomic alterations. *PLoS ONE*, *4*(11). https://doi.org/10.1371/journal.pone.0007752

Bushong, E. a, Martone, M. E., Jones, Y. Z., & Ellisman, M. H. (2002). Protoplasmic astrocytes in CA1 stratum radiatum occupy separate anatomical domains. *The Journal of Neuroscience : The Official Journal of the Society for Neuroscience*, *22*(1), 183–192. https://doi.org/22/1/183 [pii]

Carmeliet, P., & Jain, R. K. (2000). Angiogenesis in cancer and other diseases. *Nature*, *407*(6801), 249–257.

Carpentier, A. F., & Meng, Y. (2006). Recent advances in immunotherapy for human glioma. *Current Opinion in Oncology*. https://doi.org/10.1097/01.cco.0000245321.34658.f4

Chen, Y., Jing, Z., Luo, C., Zhuang, M., Xia, J., Chen, Z., & Wang, Y. (2012). Vasculogenic mimicry-potential target for glioblastoma therapy: An in vitro and in vivo study. *Medical Oncology*, *29*(1), 324–331. https://doi.org/10.1007/s12032-010-9765-z

Chen, Y. S., & Chen, Z. P. (2014). Vasculogenic mimicry: A novel target for glioma therapy. *Chinese Journal of Cancer*, *33*(2), 74–79. https://doi.org/10.5732/cjc.012.10292

Cheng, L., Wu, Q., Guryanova, O. A., Huang, Z., Huang, Q., Rich, J. N., & Bao, S. (2011). Elevated invasive potential of glioblastoma stem cells. *Biochemical and Biophysical Research Communications*, *406*(4), 643–648. https://doi.org/10.1016/j.bbrc.2011.02.123

Chetty, R., & Gatter, K. (1994). CD3: Structure, function, and role of immunostaining in clinical practice. *The Journal of Pathology*. https://doi.org/10.1002/path.1711730404

Cohen, A. L., Holmen, S. L., & Colman, H. (2013). IDH1 and IDH2 mutations in gliomas. *Current Neurology and Neuroscience Reports*. https://doi.org/10.1007/s11910-013-0345-4

Coutu, D. L., Kokkaliaris, K. D., Kunz, L., & Schroeder, T. (2017). Three-dimensional map of nonhematopoietic bone and bone-marrow cells and molecules. *Nature Biotechnology*. https://doi.org/10.1038/nbt.4006

Cuddapah, V. A., Robel, S., Watkins, S., & Sontheimer, H. (2014). A neurocentric perspective on glioma invasion. *Nature Reviews. Neuroscience*, *15*(7), 455–465. https://doi.org/10.1038/nrn3765

De Palma, M., Biziato, D., & Petrova, T. V. (2017). Microenvironmental regulation of tumour angiogenesis. *Nature Reviews Cancer*, *17*(8), 457–474. https://doi.org/10.1038/nrc.2017.51

Díaz, L. R., Saavedra-López, E., Romarate, L., Mitxitorena, I., Casanova, P. V, Cribaro, G. P., … Barcia Jr, C. (2018). Imbalance of immunological synapse-kinapse states reflects tumor escape to immunity in glioblastoma. *JCI Insight*, *3*(18).

Dix, A. R., Brooks, W. H., Roszman, T. L., & Morford, L. A. (1999). Immune defects observed in patients with primary malignant brain tumors. *Journal of Neuroimmunology*, *100*, 216–232. Retrieved from www.elsevier.comrlocaterjneuroim

Doetsch, F. (2003). The glial identity of neural stem cells. *Nature Neuroscience*. https://doi.org/10.1038/nn1144

Dubois, L. G., Campanati, L., Righy, C., Dâ€™Andrea-Meira, I., Spohr, T. C. L. de S. e, Porto-Carreiro, I., … Moura-Neto, V. (2014). Gliomas and the vascular fragility of the blood brain barrier. *Frontiers in Cellular Neuroscience*, *8*. https://doi.org/10.3389/fncel.2014.00418

Duda, D. G., Cohen, K. S., Kozin, S. V., Perentes, J. Y., Fukumura, D., Scadden, D. T., & Jain, R. K. (2006). Evidence for incorporation of bone marrow-derived endothelial cells into perfused blood vessels in tumors. *Blood*, *107*(7), 2774–2776. https://doi.org/10.1182/blood-2005-08-3210

Dvorak, H. F. (1986). Tumors: wounds that do not heal. Similarities between tumor stroma generation and wound healing. *The New England Journal of Medicine*, *315*(26), 1650–1659. https://doi.org/10.1056/NEJM198612253152606

El Hallani, S., Boisselier, B., Peglion, F., Rousseau, A., Colin, C., Idbaih, A., … Sanson, M. (2010). A new alternative mechanism in glioblastoma vascularization: Tubular vasculogenic mimicry. *Brain*, *133*(4), 973–982. https://doi.org/10.1093/brain/awq044

Eng, L. F., Vanderhaeghen, J. J., Bignami, A., & Gerstl, B. (1971). An acidic protein isolated from fibrous astrocytes. *Brain Research*, *28*(2), 351–354. https://doi.org/10.1016/0006-8993(71)90668-8

Fecci, P. E., Heimberger, A. B., & Sampson, J. H. (2014). Immunotherapy for primary brain tumors: No longer a matter of privilege. *Clinical Cancer Research*. https://doi.org/10.1158/1078-0432.CCR-14-0832

Fecci, P. E., Mitchell, D. A., Whitesides, J. F., Xie, W., Friedman, A. H., Archer, G. E., … Sampson, J. H. (2006). Increased regulatory T-cell fraction amidst a diminished CD4 compartment explains cellular immune defects in patients with malignant glioma. *Cancer Research*, *66*(6), 3294–3302. https://doi.org/10.1158/0008-5472.CAN-05-3773

Halliday, J. J., & Holland, E. C. (2011, August 3). Connective tissue growth factor and the parallels between brain injury and brain tumors. *Journal of the National Cancer Institute*, *103*(15), 1141–1143. https://doi.org/10.1093/jnci/djr261

Hambardzumyan, D., Gutmann, D. H., & Kettenmann, H. (2015). The role of microglia and macrophages in glioma maintenance and progression. *Nature Neuroscience*, *19*(1), 20–27. https://doi.org/10.1038/nn.4185

Hardee, M. E., & Zagzag, D. (2012). Mechanisms of glioma-associated neovascularization. *American Journal of Pathology*. https://doi.org/10.1016/j.ajpath.2012.06.030

Herz, J., Paterka, M., Niesner, R. A., Brandt, A. U., Siffrin, V., Leuenberger, T., … Radbruch, H. (2011). In vivo imaging of lymphocytes in the CNS reveals different behaviour of naïve T cells in health and autoimmunity. *Journal of Neuroinflammation*, *8*. https://doi.org/10.1186/1742-2094-8-131

Hickey, W. F., Hsu, B. L., & Kimura, H. (1991). T-lymphocyte entry into the central nervous system. *Journal of Neuroscience Research*. https://doi.org/10.1002/jnr.490280213

Hillen, F., & Griffioen, A. W. (2007). Tumour vascularization: Sprouting angiogenesis and beyond. *Cancer and Metastasis Reviews*, *26*(3–4), 489–502. https://doi.org/10.1007/s10555-007-9094-7

Holash, J., Maisonpierre, P. C., Compton, D., Boland, P., Alexander, C. R., Zagzag, D., … Wiegand, S. J. (1999). Vessel cooption, regression, and growth in tumors mediated by angiopoietins and VEGF. *Science*, *284*(5422), 1994–1998. https://doi.org/10.1126/science.284.5422.1994

Inda, M. del M., Bonavia, R., & Seoane, J. (2014). Glioblastoma multiforme:A look inside its heterogeneous nature. *Cancers*, *6*(1), 226–239. https://doi.org/10.3390/cancers6010226

Jafri, N. F., Clarke, J. L., Weinberg, V., Barani, I. J., & Cha, S. (2013). Relationship of glioblastoma multiforme to the subventricular zone is associated with survival. *Neuro-Oncology*, *15*(1), 91–96. https://doi.org/10.1093/neuonc/nos268

Jain, R. K. (2013). Normalizing tumor microenvironment to treat cancer: Bench to bedside to biomarkers. In *Journal of Clinical Oncology* (Vol. 31, pp. 2205–2218). https://doi.org/10.1200/JCO.2012.46.3653

Jain, R. K., di Tomaso, E., Duda, D. G., Loeffler, J. S., Sorensen, a G., & Batchelor, T. T. (2007). Angiogenesis in brain tumours. *Nature Reviews. Neuroscience*, *8*(8), 610–622. https://doi.org/10.1038/nrn2175

Jiang, Y., & Uhrbom, L. (2012). On the origin of glioma. *Upsala Journal of Medical Sciences*, *117*(2), 113–121. https://doi.org/10.3109/03009734.2012.658976

Jung, C. S., Foerch, C., Schänzer, A., Heck, A., Plate, K. H., Seifert, V., … Sitzer, M. (2007). Serum GFAP is a diagnostic marker for glioblastoma multiforme. *Brain*, *130*(12), 3336–3341. https://doi.org/10.1093/brain/awm263

Kalluri, R. (2003). Basement membranes: structure, assembly and role in tumour angiogenesis. *Nature Reviews. Cancer*, *3*(June), 422–433. https://doi.org/10.1038/nrc1094

Kettenmann, H., Hanisch, U.-K., Noda, M., & Verkhratsky, A. (2011). Physiology of Microglia. *Physiological Reviews*, *91*(2), 461–553. https://doi.org/10.1152/physrev.00011.2010

Kirkpatrick, D. B. (1984). The first primary brain-tumor operation. *Journal of Neurosurgery*, *61*(5), 809–813. https://doi.org/10.3171/jns.1984.61.5.0809

Kmiecik, J., Poli, A., Brons, N. H. C., Waha, A., Eide, G. E., Enger, P. Ø., … Chekenya, M. (2013). Elevated CD3+ and CD8+ tumor-infiltrating immune cells correlate with prolonged survival in glioblastoma patients despite integrated immunosuppressive mechanisms in the tumor microenvironment and at the systemic level. *Journal of Neuroimmunology*, *264*(1–2), 71–83. https://doi.org/10.1016/j.jneuroim.2013.08.013

Kreuger, J., & Phillipson, M. (2016). Targeting vascular and leukocyte communication in angiogenesis, inflammation and fibrosis. *Nature Reviews Drug Discovery*, *15*(2), 125–142. https://doi.org/10.1038/nrd.2015.2

Kros, J. M., Schouten, W. C. D., Janssen, P. J. A., & van der Kwast, T. H. (1995). Proliferation of gemistocytic cells and glial fibrillary acidic protein (GFAP)-positive oligodendroglial cells in gliomas: a MIB-1/GFAP double labeling study. *Acta Neuropathologica*, *91*(1), 99–103. https://doi.org/10.1007/s004010050398

Kurz, H., Burri, P. H., & Djonov, V. G. (2003). Angiogenesis and vascular remodeling by intussusception: from form to function. *News in Physiological Sciences : An International Journal of Physiology Produced Jointly by the International Union of Physiological Sciences and the American Physiological Society*, *18*(12), 65–70. Retrieved from http://www.ncbi.nlm.nih.gov/pubmed/12644622

Lacroix, M., Abi-Said, D., Fourney, D. R., Gokaslan, Z. L., Shi, W., DeMonte, F., … Sawaya, R. (2001). A multivariate analysis of 416 patients with glioblastoma multiforme: prognosis, extent of resection, and survival. *Journal of Neurosurgery*, *95*(2), 190–198. https://doi.org/10.3171/jns.2001.95.2.0190

Lauwers, F., Cassot, F., Lauwers-Cances, V., Puwanarajah, P., & Duvernoy, H. (2008). Morphometry of the human cerebral cortex microcirculation: General characteristics and space-related profiles. *NeuroImage*, *39*(3), 936–948. https://doi.org/10.1016/j.neuroimage.2007.09.024

Lee, J. H., Lee, J. E., Kahng, J. Y., Kim, S. H., Park, J. S., Yoon, S. J., … Lee, J. H. (2018). Human glioblastoma arises from subventricular zone cells with low-level driver mutations. *Nature*, *560*(7717), 243–247. https://doi.org/10.1038/s41586-018-0389-3

Li, Z., Wang, H., Eyler, C. E., Hjelmeland, A. B., & Rich, J. N. (2009). Turning cancer stem cells inside out: an exploration of glioma stem cell signaling pathways. *The Journal of Biological Chemistry*, *284*(25), 16705–16709. https://doi.org/10.1074/jbc.R900013200

Lim, D. A., Cha, S., Mayo, M. C., Chen, M.-H., Keles, E., VandenBerg, S., & Berger, M. S. (2007). Relationship of glioblastoma multiforme to neural stem cell regions predicts invasive and multifocal tumor phenotype. *Neuro-Oncology*, *9*(4), 424–429. https://doi.org/10.1215/15228517-2007-023

Lorthois, S., Cassot, F., & Lauwers, F. (2011). Simulation study of brain blood flow regulation by intra-cortical arterioles in an anatomically accurate large human vascular network: Part I: Methodology and baseline flow. *NeuroImage*, *54*(2), 1031–1042. https://doi.org/10.1016/j.neuroimage.2010.09.032

Louis, D. N., Perry, A., Reifenberger, G., von Deimling, A., Figarella-Branger, D., Cavenee, W. K., … Ellison, D. W. (2016). The 2016 World Health Organization Classification of Tumors of the Central Nervous System: a summary. *Acta Neuropathologica*. https://doi.org/10.1007/s00401-016-1545-1

M, D. M., & Baluk, P. (2002). Significance of blood vessel leakiness in cancer. *Cancer Research*, *62*(18), 5381–5385.

Maniotis, A. J., Folberg, R., Hess, A., Seftor, E. A., Gardner, L. M., Pe'er, J., … Hendrix, M. J. (1999). Vascular channel formation by human melanoma cells in vivo and in vitro: vasculogenic mimicry. *Am J Pathol*, *155*, 739–752. https://doi.org/S0002-9440(10)65173-5 [pii]\r10.1016/S0002-9440(10)65173-5

Mantovani, A., Allavena, P., Sica, A., & Balkwill, F. (2008). Cancer-related inflammation. *Nature*. https://doi.org/10.1038/nature07205

Maxwell, P. H., Pugh, C. W., & Ratcliffe, P. J. (2001). Activation of the HIF pathway in cancer. *Current Opinion in Genetics and Development*. https://doi.org/10.1016/S0959-437X(00)00193-3

Mirzaei, R., Sarkar, S., & Yong, V. W. (2017). T Cell Exhaustion in Glioblastoma: Intricacies of Immune Checkpoints. *Trends in Immunology*. https://doi.org/10.1016/j.it.2016.11.005

Montana, V., & Sontheimer, H. (2011). Bradykinin Promotes the Chemotactic Invasion of Primary Brain Tumors. *Journal of Neuroscience*, *31*(13), 4858–4867. https://doi.org/10.1523/JNEUROSCI.3825-10.2011

Morantz, R. A., Wood, G. W., Foster, M., Clark, M., & Gollahon, K. (1979). Macrophages in experimental and human brain tumors. *Journal of Neurosurgery*, *50*(3), 305–311. https://doi.org/10.3171/jns.1979.50.3.0305

Nyengaard, J. R., Bendtsen, T. F., & Gundersen, H. J. (1988). Stereological estimation of the number of capillaries, exemplified by renal glomeruli. *APMIS Suppl*, *4*, 92–99. Retrieved from http://www.ncbi.nlm.nih.gov/entrez/query.fcgi?cmd=Retrieve&db=PubMed&dopt=Citation&list_uids=3224028

Ohsawa, K., Imai, Y., Kanazawa, H., Sasaki, Y., & Kohsaka, S. (2000). Involvement of Iba1 in membrane ruffling and phagocytosis of macrophages/microglia. *Journal of Cell Science*, *113 (Pt 1*, 3073–3084.

Ostrom, Q. T., Gittleman, H., Liao, P., Rouse, C., Chen, Y., Dowling, J., … Barnholtz-Sloan, J. (2014). CBTRUS Statistical Report: Primary Brain and Central Nervous System Tumors Diagnosed in the United States in 2007-2011. *Neuro-Oncology*, *16*(suppl 4), iv1-iv63. https://doi.org/10.1093/neuonc/nou223

Parker, N. R., Hudson, A. L., Khong, P., Parkinson, J. F., Dwight, T., Ikin, R. J., … Howell, V. M. (2016). Intratumoral heterogeneity identified at the epigenetic, genetic and transcriptional level in glioblastoma. *Scientific Reports*. https://doi.org/10.1038/srep22477

Patel, A. P., Tirosh, I., Trombetta, J. J., Shalek, A. K., Gillespie, S. M., Wakimoto, H., … Bernstein, B. E. (2014). Single-cell RNA-seq highlights intratumoral heterogeneity in primary glioblastoma. *Science (New York, N.Y.)*, *344*(6190), 1396–1401. https://doi.org/10.1126/science.1254257

Plate, K. H., & Mennel, H. D. (1995). Vascular morphology and angiogenesis in glial tumors. *Experimental and Toxicologic Pathology*. https://doi.org/10.1016/S0940-2993(11)80292-7

Preibisch, S., Saalfeld, S., & Tomancak, P. (2009). Globally optimal stitching of tiled 3D microscopic image acquisitions. *Bioinformatics*, *25*(11), 1463–1465. https://doi.org/10.1093/bioinformatics/btp184

Qiao, L., Liang, N., Zhang, J., Xie, J., Liu, F., Xu, D., … Tian, Y. (2015). Advanced research on vasculogenic mimicry in cancer. *Journal of Cellular and Molecular Medicine*, *19*(2), 315–326. https://doi.org/10.1111/jcmm.12496

Radbruch, A., Eidel, O., Wiestler, B., Paech, D., Burth, S., Kickingereder, P., … Heiland, S. (2014). Quantification of tumor vessels in glioblastoma patients using time-of-flight angiography at 7 Tesla: A feasibility study. *PLoS ONE*, *9*(11), e110727. https://doi.org/10.1371/journal.pone.0110727

Rojiani, a M., & Dorovini-Zis, K. (1996). Glomeruloid vascular structures in glioblastoma multiforme: an immunohistochemical and ultrastructural study. *Journal of Neurosurgery*, *85*(6), 1078–1084. https://doi.org/10.3171/jns.1996.85.6.1078

Rueden, C. T., Schindelin, J., Hiner, M. C., DeZonia, B. E., Walter, A. E., Arena, E. T., & Eliceiri, K. W. (2017). ImageJ2: ImageJ for the next generation of scientific image data. *BMC Bioinformatics*, *18*(1). https://doi.org/10.1186/s12859-017-1934-z

Sanai, N., Alvarez-Buylla, A., & Berger, M. S. (2005). Neural stem cells and the origin of gliomas. *The New England Journal of Medicine*, *353*(8), 811–822. https://doi.org/10.1056/NEJMra043666

Santarelli, J. G., Udani, V., Yung, Y. C., Cheshier, S., Wagers, A., Brekken, R. A., … Tse, V. (2006). Incorporation of bone marrow-derived Flk-1-expressing CD34+ cells in the endothelium of tumor vessels in the mouse brain. *Neurosurgery*, *59*(2), 374–381. https://doi.org/10.1227/01.NEU.0000222658.66878.CC

Scherer, H. J. (1938). Structural development in gliomas. *American Journal of Cancer*, *34*(3), 333–351. https://doi.org/10.1158/ajc.1938.333

Scherer, H. J. (1940). a Critical Review: the Pathology of Cerebral Gliomas. *Journal of Neurology and Psychiatry*, *3*(2), 147–177. https://doi.org/10.1136/jnnp.3.2.147

Schindelin, J., Arganda-Carreras, I., Frise, E., Kaynig, V., Longair, M., Pietzsch, T., … Cardona, A. (2012). Fiji: An open-source platform for biological-image analysis. *Nature Methods*. https://doi.org/10.1038/nmeth.2019

Siebzehnrubl, F. A., Reynolds, B. A., Vescovi, A., Steindler, D. A., & Deleyrolle, L. P. (2011). The origins of glioma: E Pluribus Unum? *GLIA*, *59*(8), 1135–1147. https://doi.org/10.1002/glia.21143

Soda, Y., Marumoto, T., Friedmann-Morvinski, D., Soda, M., Liu, F., Michiue, H., … Verma, I. M. (2011). Transdifferentiation of glioblastoma cells into vascular endothelial cells. *Proceedings of the National Academy of Sciences of the United States of America*, *108*(11), 4274–4280. https://doi.org/10.1073/pnas.1016030108

Soda, Y., Myskiw, C., Rommel, A., & Verma, I. M. (2013). Mechanisms of neovascularization and resistance to anti-angiogenic therapies in glioblastoma multiforme. *Journal of Molecular Medicine*. https://doi.org/10.1007/s00109-013-1019-z

Soeda, A., Hara, A., Kunisada, T., Yoshimura, S. I., Iwama, T., & Park, D. M. (2015). The evidence of glioblastoma heterogeneity. *Scientific Reports*, *5*, 7979. https://doi.org/10.1038/srep07979

Stupp, R., Mason, W., van den Bent, M. J., Weller, M., Fisher, B. M., Taphoorn, M. J. B., … Mirimanoff, R. O. (2005). Radiotherapy plus Concomitant\nand Adjuvant Temozolomide for Glioblastoma. *The New England Journal of Medicine*, 987–996. https://doi.org/10.1056/NEJMoa043330

Tabatabai, G., & Weller, M. (2011). Glioblastoma stem cells. *Cell and Tissue Research*, *343*(3), 459–465. https://doi.org/10.1007/s00441-010-1123-0

Verhaak, R. G. W., Hoadley, K. A., Purdom, E., Wang, V., Qi, Y., Wilkerson, M. D., … Hayes, D. N. (2010). Integrated Genomic Analysis Identifies Clinically Relevant Subtypes of Glioblastoma Characterized by Abnormalities in PDGFRA, IDH1, EGFR, and NF1. *Cancer Cell*, *17*(1), 98–110. https://doi.org/10.1016/j.ccr.2009.12.020

Wang, R., Chadalavada, K., Wilshire, J., Kowalik, U., Hovinga, K. E., Geber, A., … Tabar, V. (2010). Glioblastoma stem-like cells give rise to tumour endothelium. *Nature*, *468*(7325), 829–835. https://doi.org/10.1038/nature09624

Watkins, S., Robel, S., Kimbrough, I. F., Robert, S. M., Ellis-Davies, G., & Sontheimer, H. (2014). Disruption of astrocyte-vascular coupling and the blood-brain barrier by invading glioma cells. *Nature Communications*, *5*(May), 4196. https://doi.org/10.1038/ncomms5196

Watkins, S., & Sontheimer, H. (2011). Hydrodynamic Cellular Volume Changes Enable Glioma Cell Invasion. *Journal of Neuroscience*, *31*(47), 17250–17259. https://doi.org/10.1523/JNEUROSCI.3938-11.2011

Watkins, S., & Sontheimer, H. (2012). Unique biology of gliomas: Challenges and opportunities. *Trends in Neurosciences*, *35*(9), 547–556. https://doi.org/10.1016/j.tins.2012.05.001

Wekerle, H., Sun, D., Oropeza-Wekerle, R. L., & Meyermann, R. (1987). Immune reactivity in the nervous system: modulation of T-lymphocyte activation by glial cells. *Journal of Experimental Biology*, *132*, 43–57.

Wen, P. Y., & Kesari, S. (2008). Malignant gliomas in adults. *The New England Journal of Medicine*, *359*(5), 492–507. https://doi.org/10.1056/NEJMra0708126

Woroniecka, K., Chongsathidkiet, P., Rhodin, K. E., Kemeny, H. R., Dechant, C. A., Farber, S. H., … Fecci, P. E. (2018). T Cell Exhaustion Signatures Vary with Tumor Type and are Severe in Glioblastoma. *Clinical Cancer Research : An Official Journal of the American Association for Cancer Research*. https://doi.org/10.1158/1078-0432.CCR-17-1846

Zhu, Y., & Parada, L. F. (2002). The molecular and genetic basis of neurological tumours. *Nature Reviews Cancer*. https://doi.org/10.1038/nrc866

THESIS DIRECTOR CERTIFICATE

This is to certify that the work embodied in the accompanying thesis entitled "**Three-Dimensional Atlas of Vascular Networks in Human Glioblastoma**" has been carried out entirely by the candidate as a research scholar under my direct supervision and guidance and that the candidate has fulfilled the requirements of the regulations laid down for the Doctor of Philosophy (Neuroscience) Degree of the *Institut de Neurociències* of the *Universitat Autònoma de Barcelona.*

Doctoral candidate: George Paul Cribaro

Department: *Institut de Neurociències (Universitat Autònoma de Barcelona)*

Thesis director: Carlos Barcia González

12-09-2018

Signature Date

Carlos Barcia González
Thesis Director

APPENDICES

APPENDIX 1 – IMMUNOFLUORESCENCE PROTOCOL

The full protocol along with approximate timings for each step is shown schematically below:

IMMUNOFLUORESCENCE GENERAL PROTOCOL		
Step	**Time**	**Elapsed time (per session)**
Days 1 and 2		
1. Wash samples three times in PBS	10' 3x	30’
Antigen retrieval:		
2. Incubate samples in citrate (pH 6, 60 °C)	20’	50’
3. Wash in PBS	5’	55’
4. Wash in TBS-triton	5’	60’
Blocking		
5. Incubate in horse serum at 10%	60’	120’
6. Wash in horse serum at 1%	5’	125’
7. Wash in TBS	5’	130’
8. Add primary antibody in HS1% and incubate 48 h	30’ (about 5 min per sample)	160’
Day 3		
9. Wash samples three times in TBS-Triton	10' 3x	30’
10. Secondary antibody in HS1%	24 h	(about 5 min per sample) + 24 h
Day 4		
11. Wash samples three times in PBS	10' 3x	30’
12. Incubate in DAPI / PBS (1:1000)	30’	60’
13. Wash samples three times in PBS	10' 3x	90’

1. Immunohistochemistry

This section describes in detail the immunostaining procedure employed, including preparation of the necessary reagents, sample preparation, the procedure itself and sample mounting on slides for image acquisition.

1.1 Reagents

All reagent solutions were prepared in appropriate volumetric containers and stored in glass containers at room temperature until use. Ingredients were weighed and dissolved using a magnetic bar stirrer in distilled water (except for horse serum). Once all components were fully dissolved, the solution was topped up to the mark and the pH was measured and adjusted as necessary.

PBS with sodium azide pH= 7.4 (200 mL)
NaCl 2 g
Na_2HPO_4 0.36 g
NaH_2PO_4 0.06 g
NaN_3 0.02 g
Fill to mark with distilled H_2O and adjust pH.

Citrate pH=6 (500 mL)
Citric acid 1.05 g
Fill to mark with distilled H_2O and adjust pH.

PBS pH= 7.4 (800 mL)
NaCl 8 g
Na_2HPO_4 1.44 g
NaH_2PO_4 0.24 g
Fill to mark with distilled H_2O and adjust pH.

TBS-triton 0.5% pH=7.4 (500 mL)
Trizma base 3.5 g
NaCl 4.5 g
Triton 2.5 g
Fill to mark with distilled H_2O and adjust pH.

Horse Serum 10% (30 mL)
HS 3 mL
NaN3 0.3 g
TBS-triton make to mark.

Horse Serum 1% (30 mL)
HS10% 3 mL
NaN3 0.03 g
TBS-triton make to mark.

All the above volumes can be adjusted depending on the final volume desired as long as the proportions of the ingredients remain the same.

1.2 Protocol

Tissue sections approximately 50- to 70 μm thick had been previously cut from tumor samples deriving from the sample pool described in Table 1 and stored refrigerated in PBS with sodium azide. Samples were normally processed in batches of six including one normal cortical tissue sample and five GBM samples. The full IHC protocol spans four days and comprises antigen retrieval in citrate buffer, blocking promiscuous binding sites with horse serum and marking with a combination of primary and secondary antibodies for collagen IV, GFAP, CD31, CD3, Iba-1 and MHCII, as needed, and DAPI.

Immunohistochemical protocol for human tissue:

1. Take a six-well Falcon plate and fill the necessary number of wells each with 1-2 mL PBS. Choose samples and label the plate top with the desired sample numbers using a permanent marker.

2. Remove the corresponding samples from the refrigerator, carefully remove the parafilm and remove top. Using a fine-tipped brush take a sufficiently large, intact piece of tissue and transfer it to a well. Carefully reseal the sample container with parafilm and set aside. Repeat for each of the samples being used. When finished, return the unused samples to the refrigerator. Be careful to ensure that the correct sample is in the corresponding previously labeled well.

3. Do three ten-minute washes with PBS (1-2 mL per well), removing and discarding the PBS with a pipette after each ten-minute cycle and replacing it with fresh solution. Place the cover on the plate and the plate on a plate shaker at about 200 rpm (gentle agitation) during each wash.

4. In the meanwhile, heat the citrate for the next step. Add sufficient citrate for the number of samples (at least 1-2 mL per well) to a 50-mL flask, insert a magnet and place on a hotplate/stirrer. Put a thermometer in the solution and cover with aluminum foil to prevent evaporation. Set the temperature to 60 ºC with gentle stirring.

5. After removing the PBS after the third wash in step 3, pipette the heated citrate into the wells to cover the samples sufficiently. Cover and place the Falcon plate on the shaker and leave for twenty minutes.

6. Pipette the citrate from the wells and discard and add PBS (1-2 mL per well) and wash for five minutes, placing the Falcon plate on the shaker.

7. Remove and discard PBS and add 1-2 mL TBS-Triton per well and wash for five minutes, placing the plate on the stirrer.

8. Remove and discard TBS-Triton and add 1-2 mL 10% horse serum to each well. Incubate for one hour under agitation on the plate stirrer.

9. Prepare primary antibodies while waiting for step 8 to finish. See Box 1a below.

Box 1a. Preparation of primary antibodies

Prepare sufficient amount (approximately 1-1.5 mL per well) for the number of wells in use. (Can be prepared while waiting for step 8 to end.)

Remove antibodies from refrigerator or freezer; they should be stored in small aliquots. Take the required amount with an automatic pipette (after thawing if aliquots were frozen) and add to a tapered-bottom tube with the corresponding amount of 1% HS.

Note: Before removing the antibody from the aliquoted mini-Eppendorf tube, concentrate it at the bottom of the tube by centrifuging briefly and then open carefully.

Tissue target	Molecular target	Species	Manufacturer	Proportion/ amount per mL
Basement membrane	Collagen IV	rabbit	Abcam, Cambridge, UK	1:200 / 5 μL
Astrocyte, tumor cells	GFAP	mouse chicken	Millipore, Temecula, CA, USA Abcam, Cambridge, UK	1:500 / 2 μL 1:200 / 5 μL
Endothelial cells	CD31	mouse	Abcam, Cambridge, UK	1:400 / 2.5 μL
Antigen-presenting cells	HLA-DP, DQ, DR (MHCII)	mouse	Dako Cytomation; Glostrup, Denmark	1:100 / 10 μL
T cells	CD3	rabbit	Dako Cytomation; Glostrup, Denmark	1:100 / 10 μL
Microglia/macrophages	Iba-1	rabbit	Wako Pure Chemical Industries, Ltd.; Osaka, Japan	1:500 / 2 μL

10. Remove 10% horse serum and add 1-2 mL 1% horse serum per well. Cover plate and leave for five minutes on the plate stirrer.

11. Remove the 1% horse serum, discard and add 1-2 mL TBS-Triton to each well. Leave for five minutes on the plate stirrer.

12. Add primary antibodies to small, capped bottles (to prevent evaporation) and label with corresponding sample numbers. Gently remove samples from the Falcon plate and put into the respective bottles. Cap and leave for 48 hours under gentle agitation.

13. Prepare secondary antibodies. See Box 2a.

Box 2a. Preparation of secondary antibodies

Prepare sufficient amount (approximately 1-1.5 mL per well) for the number of wells in use.

Remove antibodies from refrigerator or freezer; they should be stored in small aliquots. After thawing, if frozen, take the required amount with an automatic pipette and add to an aluminum foil-wrapped, tapered-bottom tube with the corresponding amount of 1% HS. (Protect secondary antibodies from light as much as possible).

Note: Before removing the antibody from the aliquoted mini-Eppendorf tube, concentrate it at the bottom of the tube by centrifuging briefly and then open carefully.

Target	Species	Manufacturer	Proportion	Per mL
AlexaFluor® α-rabbit 488	goat	Invitrogen, Carlsbad, CA, USA	1:1000	1 μL
AlexaFluor® α-mouse 555	goat	Invitrogen, Carlsbad, CA, USA	1:500	2 μL
AlexaFluor® α-chicken 555	goat	Invitrogen, Carlsbad, CA, USA	1:500	2 μL
AlexaFluor® α-mouse 647	goat	Invitrogen, Carlsbad, CA, USA	1:500	2 μL

14. Remove primary antibodies and add 1-2 mL TBS-Triton solution to each well. Do three ten-minute washes, removing and discarding the TBS-Triton with a pipette after each ten-minute cycle and replacing it with fresh solution.

15. After the last wash, wrap each of the small sample bottles with aluminum foil to prevent light from entering. All steps from this point on should protect the samples from light as much as possible.

16. Add 1. 1.5 mL of the secondary antibody solution per bottle, cap the bottles and place on the plate stirrer. Leave to incubate 24 hours on the plate stirrer.

17. At the end of the incubation period, perform three 10-minute washes PBS, keeping the samples inside the small bottles and taking care to protect them from light as

much as possible. As previously, remove and discard the PBS with a pipette after each ten-minute cycle and replace it with fresh solution (again 1-2 mL per bottle).

18. Prepare a solution of DAPI and PBS (at 1:1000). After the third wash in the previous step, remove and discard the PBS from each bottle and pipette 1-1.5 mL of the DAPI:PBS solution into each bottle. Cap and incubate on the plate stirrer for 30 minutes.

19. Wash the samples as before, three times for ten minutes, removing and discarding the PBS and replacing it with fresh solution for successive washes.

1.3 Mounting

Immunostained tissue samples are mounted on non-gelatinized slides using ProLong® Gold antifade reagent. A T-shaped ribbon of ProLong® Gold is drawn on the coverslip and the slide is then gently lowered onto the coverslip to disperse the Prolong Gold evenly and prevent bubbles from forming on the sample (see steps a-f in the figure below). Slides are left to dry before image acquisition.

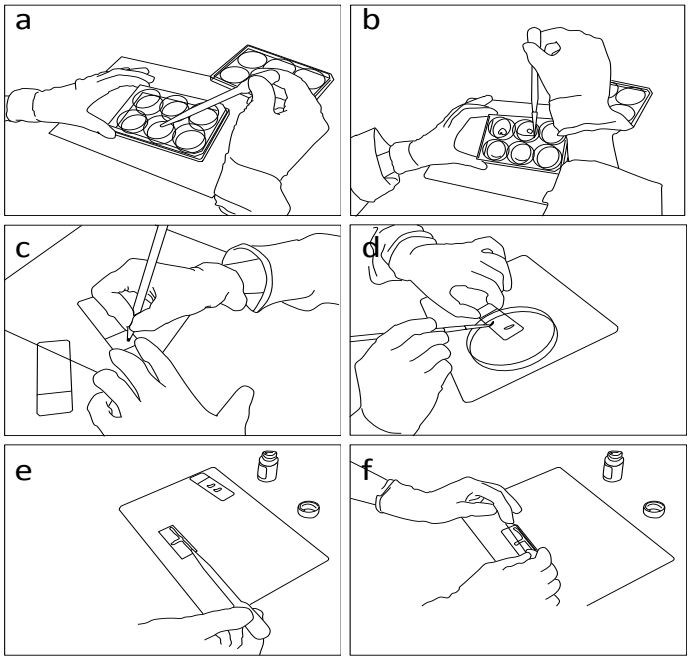

APPENDIX 2 - RAW DATA

MAIN GROUP

TOTAL CELL COUNT				
0	**10**	**20**	**30**	**50**
758	1404	969	1879	1784
1236	1501	1200	2054	2394
1257	1863	705	1705	2669
1142	1213	1149	1567	2729
1061	1988	1154	1504	2902
856	1714	1150	1642	1872
851	1479	1203	2029	1942
838	1499	1720	1717	1698
819	1254	1469	1659	1818
885	1195	1669	1685	1689

GFAP SURFACE AREA (µm²)				
0	**10**	**20**	**30**	**50**
156445	188493	356032	522356	582128
43783	118845	219758	644152	409421
139842	192151	628055	694980	352009
489513	418353	315666	648926	806869
193940	340512	442408	708902	707237
187122	69486	611072	500344	693893
111775	191334	237417	433484	452460
145287	147315	699464	681589	848103
34881	68299	462322	883872	565064
44915	156153	414950	1085230	655797

GFAP VOLUME (µm³)				
0	**10**	**20**	**30**	**50**
89720	160603	214896	437250	491977
27081	88192	115599	518047	304774
80403	175874	429593	672660	302048
255334	375458	176197	545577	720975
124002	241339	243340	594933	617176
83360	77495	382419	395793	599522
55751	230013	112926	366963	428516
68421	185138	390694	622560	848698
22135	42121	229371	965257	513789
29485	174519	227642	1135110	612589

COLLAGEN IV SURFACE AREA (µm²)				
0	**10**	**20**	**30**	**50**
142357	612774	488275	453276	957431
158228	291646	506431	507502	961618
159086	266211	606610	432400	1299600
184017	248220	422034	409976	1218810
194340	533418	395175	430108	1545150
196848	488620	340807	375151	858303
181592	402405	308753	380587	1060730
195967	448429	352173	325084	950057
175096	405295	275231	411829	824086
211761	366407	360783	384860	1017670

COLLAGEN IV VOLUME (µm³)				
0	**10**	**20**	**30**	**50**
292168	721562	672678	996539	1899210
295788	413259	702092	1099040	1751000
324382	363191	732538	944815	2201270
416806	624218	498942	858773	2347800
442111	1175050	503268	995017	2728580
383400	819280	544922	879248	2751360
347559	594094	362122	881908	2030800
406313	712942	386941	946267	2384160
327637	638195	280662	1006100	1871820
415012	658090	565539	916569	2814520

MEAN DIAMETER				
0	**10**	**20**	**30**	**50**
7.81	11.94	10.91	13.85	12.83
9.28	10.92	11.95	16.53	10.49
8.44	13.38	11.1	18.26	25.94
10.02	8.97	10.61	12.36	26.79
9.54	9.64	8.8	12.17	33.72
8.81	10.25	12.9	11.88	27.01
8.77	11.05	10.5	13.77	13.46
8.9	10.50	11.64	19.49	13.56
8.56	11.07	10.28	14.31	26.11
8.91	9.50	10	15.88	22.88

BRANCHING - TOTAL				
0	**10**	**20**	**30**	**50**
17	30	44	41	74
22	59	37	26	96
24	21	34	14	16
22	40	42	31	15
24	54	41	29	25
36	79	38	28	27
34	51	37	26	19
28	51	19	9	48
35	45	30	26	20
34	56	37	22	19

BRANCHING - SINGLE				
0	**10**	**20**	**30**	**50**
16	28	38	40	64
19	53	33	22	84
22	20	33	12	15
19	37	39	29	15
23	47	38	25	24
33	71	35	25	27
30	45	36	24	18
25	49	19	9	46
33	42	29	24	19
32	51	34	19	16

BRANCHING - MULTIPLE				
0	**10**	**20**	**30**	**50**
1	2	6	1	10
3	6	4	4	12
2	1	1	2	1
3	3	3	3	0
1	7	3	4	1
3	8	3	3	0
4	6	1	2	1
3	3	0	0	2
2	3	1	2	1
2	5	3	3	3

VESSEL CONTINUITY - MEAN STD				
0	**10**	**20**	**30**	**50**
20	14.53	29.29	34.70	46.77
17.33	16.82	30.96	38.44	41.69
17.11	28.15	36.06	46.24	44.96
21.16	23.59	33.11	39.29	40.18
18.31	22.7	32.53	32.91	54.86
13.48	26.41	38.52	37.64	43.42
19.28	22.33	35.83	34.37	48.94
19.32	23.79	22.42	39.44	46.31
17.30	23.99	36.53	34.53	42.15
17.11	22.22	29.1	35.45	47.28

CD31 GROUP

TOTAL CELL COUNT			
0	**10**	**20**	**30**
922	1211	1460	2199
919	1470	1418	1781
962	1574	1732	1844
909	2610	1513	1999
1300	1367	1604	2106
1123	1461	1759	2284

VESSEL CONTINUITY - MEAN STD			
0	**10**	**20**	**30**
15.49	18.84	27.07	27.69
14.52	18.57	26.37	30.67
10.87	20.4	28.03	26.26
10.02	17.82	24.46	29.79
15.34	17.58	27	30.24
16.59	21.06	23.42	31.55

COLLAGEN IV SURFACE AREA (μm^2)			
0	**10**	**20**	**30**
167013	60414	241425	426604
163831	66990	340616	409718
160597	74749	257334	426469
149592	125113	214835	405672
228069	108063	361307	456705
251673	112456	378883	406892

CD31 SURFACE AREA (µm²)			
0	**10**	**20**	**30**
154264	81955	205470	364946
154976	73480	305389	372714
147162	83795	202941	371150
135576	202046	208111	235141
214210	107216	340094	331779
248152	141143	232273	329574

COLOCALIZATION SURFACE AREA (µm²)			
0	**10**	**20**	**30**
153656	54236	199124	322132
150023	56408	305016	185353
146880	57472	186095	362366
135316	123102	196515	219775
211566	94721	325929	255632
235364	112973	216345	295106

Iba-1

Iba-1 Area (µm²)			
Normal	**10**	**20**	**30**
22501	16116	33764	85870
9226	16510	9814	68486
11458	4414	11862	56746
5968	14421	24076	18864
8413	33673	13221	17096
7828	8467	22330	75418
		97694	
		121496	
		45771	
		42947	
		27427	
		80730	

Iba-1 volume (µm³)			
Normal	**10**	**20**	**30**
21054	10205	37574	82768
8223	9931	7156	59466
11046	4651	9065	48518
5461	10781	18735	16670
7432	23011	10048	14975
7366	6530	18810	81141
		105370	
		145101	
		42939	
		56871	
		27260	
		96084	

Iba-1 units			
Normal	**10**	**20**	**30**
81	60	44	211
39	77	28	165
39	10	37	154
25	41	80	46
31	79	48	106
29	39	69	303
		143	
		143	
		118	
		62	
		83	
		108	

MHCII

MHCII area (µm²)			
Normal	**10**	**20**	**30**
0	1963	109377	213492
349	7913	105912	196718
962	2657	68748	179334
0	1275	37071	234160
0	2370	38102	84802
0	3854	82889	214254
		6612	
		20147	
		38324	
		9471	
		23757	
		30926	

MHCII volume (µm³)			
Normal	**10**	**20**	**30**
0	1824	124559	456925
332	6216	120514	218864
816	1727	67755	404456
0	846	35654	359360
0	1673	31345	133845
0	2754	90208	418754
		7307	
		26587	
		49671	
		11292	
		30042	
		36595	

MHCII units			
Normal	**10**	**20**	**30**
0	8	366	194
2	31	318	297
9	27	209	72
0	13	212	214
0	22	271	59
0	27	220	154
		25	
		44	
		77	
		31	
		61	
		58	

CD3

TOTAL CD3		
10	**20**	**30**
34	47	55
26	73	22
11	86	8
45	69	7
20	78	13
5	47	15
	23	38
	11	39
	7	52
	15	38
	10	30
	21	58

TOTAL EXTRAVASATING		
10	**20**	**30**
23	21	31
23	58	14
10	51	2
38	28	4
12	48	5
2	23	11
	5	29
	4	17
	2	33
	6	29
	2	16
	10	34

TOTAL MIGRATED		
10	**20**	**30**
11	26	24
3	15	8
1	35	6
7	41	3
8	30	8
3	24	4
	18	9
	7	22
	5	19
	9	9
	8	14
	11	24

RATIO EXTRAVASATING/MIGRATED		
10	**20**	**30**
2.09	0.81	1.29
7.67	3.87	1.75
10.00	1.46	0.33
5.43	0.68	1.33
1.50	1.60	0.63
0.67	0.96	2.75
	0.28	3.22
	0.57	0.77
	0.40	1.74
	0.67	3.22
	0.25	1.14
	0.91	1.42

MEAN DISTANCE MIGRATED (µm)		
10	**20**	**30**
11.894	25.610	19.180
16.395	29.237	55.067
22.495	24.718	26.851
12.814	28.512	28.920
10.579	20.796	17.969
14.711	25.739	21.765
	30.921	17.681
	28.099	24.283
	54.340	28.466
	33.686	17.854
	54.312	18.597
	18.270	20.152

APPENDIX 3 - RAW STATISTICAL DATA

Parameter	Dunnett's multiple comparisons test	Mean Diff.	95% CI of diff.	Significant?	Summary
Cellularity	Normal vs. 10%	-540.7	-884.2 to -197.2	Yes	***
(Figure 29A)	Normal vs. 20%	-268.5	-612.0 to 75.01	No	ns
	Normal vs. 30%	-773.8	-1117 to -430.3	Yes	****
	Normal vs. 50%	-1179	-1523 to -835.9	Yes	****
GFAP surface area	Normal vs. 10%	-34344	-266467 to 197779	No	ns
(Figure 30B)	Normal vs. 20%	-283964	-516087 to -51841	Yes	*
	Normal vs. 30%	-525633	-757756 to -293510	Yes	****
	Normal vs. 50%	-452548	-684671 to -220425	Yes	****
Collagen IV surface area	Normal vs. 10%	-226413	-366985 to -85842	Yes	***
(Figure 40B)	Normal vs. 20%	-225698	-366269 to -85127	Yes	***
	Normal vs. 30%	-231148	-371720 to -90577	Yes	***
	Normal vs. 50%	-889416	-1.030e+006 to -748845	Yes	****
Collagen IV volume	Normal vs. 10%	-306871	-558425 to -55316	Yes	*
(Figure 42A)	Normal vs. 20%	-159853	-411407 to 91702	No	ns
	Normal vs. 30%	-587310	-838865 to -335755	Yes	****
	Normal vs. 50%	-1.913e+006	-2.164e+006 to -1.661e+006	Yes	****
Mean BV diameter - individual	Normal vs. 10%	-1.645	-2.419 to -0.8709	Yes	****
(Figure 44A)	Normal vs. 20%	-1.814	-2.581 to -1.046	Yes	****
	Normal vs. 30%	-5.331	-6.249 to -4.413	Yes	****
	Normal vs. 50%	-8.040	-8.837 to -7.242	Yes	****
Vessel luminance (SD)	Normal vs. 20%	-2.295	-3.565 to -1.024	Yes	****
(Figure 52A)	Normal vs. 30%	-4.048	-5.318 to -2.778	Yes	****
	Normal vs. 50%	-0.1355	-1.406 to 1.135	No	ns
CD31 surface area	Normal vs. 10%	42995	-12896 to 98886	No	ns
(Figure 65B)	Normal vs. 20%	-94325	-150216 to -38434	Yes	**
	Normal vs. 30%	-218971	-274862 to -163080	Yes	****
Colocalized collagen IV ratio	Normal vs. 10%	0.02401	-0.1388 to 0.1868	No	ns
(Figure 67A)	Normal vs. 20%	0.1144	-0.04843 to 0.2773	No	ns
	Normal vs. 30%	0.2723	0.1095 to 0.4351	Yes	**

Parameter	Dunnett's multiple comparisons test	Mean Diff.	95% CI of diff.	Significant?	Summary
Colocalized CD31 ratio	Normal vs. 10%	0.2480	0.09740 to 0.3986	Yes	**
(Figure 67B)	Normal vs. 20%	0.02958	-0.1210 to 0.1802	No	ns
	Normal vs. 30%	0.1566	0.005992 to 0.3072	Yes	*

Parameter	Sidak's multiple comparisons test	Mean Diff.	95% CI of diff.	Significant?	Summary
Vessel diameter - GFAP-rich areas	10% vs. 20%	-7.781	-13.43 to -2.131	Yes	**
(Figure 88D)	10% vs. 30%	-9.896	-16.42 to -3.372	Yes	**
	20% vs. 30%	-2.115	-7.765 to 3.535	No	ns

Parameter	Tukey's multiple comparisons test	Mean Diff.	95% CI of diff.	Significant?	Summary
MHCII colocalized	Normal vs. 10	-526.3	-1507 to 454.2	No	ns
(Figure 80A)	Normal vs. 20	-747.3	-1597 to 101.8	No	ns
	Normal vs. 30	-665.8	-1646 to 314.7	No	ns
Total T cells	Normal vs. 10	-23.50	-56.74 to 9.743	No	ns
(Figure 92)	Normal vs. 20	-40.58	-69.37 to -11.79	Yes	**
	Normal vs. 30	-31.25	-60.04 to -2.460	Yes	*
T cells extravasating	10% vs. 20%	-3.500	-23.52 to 16.52	No	ns
(Figure 93A)	10% vs. 30%	-0.7500	-20.77 to 19.27	No	ns
	20% vs. 30%	2.750	-13.60 to 19.10	No	ns
T cells migrated	10% vs. 20%	-13.58	-25.07 to -2.098	Yes	*
(Figure 93B)	10% vs. 30%	-7.000	-18.49 to 4.485	No	ns
	20% vs. 30%	6.583	-2.794 to 15.96	No	ns
T cell extravasating to migrated	10% vs. 20%	3.522	1.239 to 5.804	Yes	**
(Figure 94A)	10% vs. 30%	2.928	0.6447 to 5.210	Yes	**
	20% vs. 30%	-0.5942	-2.458 to 1.270	No	ns
Mean distance - migration	10% vs. 20%	-16.37	-28.92 to -3.828	Yes	**
(Figure 95)	10% vs. 30%	-9.917	-22.46 to 2.627	No	ns
	20% vs. 30%	6.455	-3.788 to 16.70	No	ns

Parameter	Dunn's multiple comparisons test	Mean rank diff.	Significant?	Summary
Iba-1 surface area	Normal vs. 10%	-3.667	No	ns
(Figure 75A)	Normal vs. 20%	-12.580	Yes	*
	Normal vs. 30%	-15.330	Yes	**
Iba-1 volume	Normal vs. 10%	-0.667	No	ns
(Figure 75B)	Normal vs. 20%	-10.580	Yes	*
	Normal vs. 30%	-13.176	Yes	*
Iba-1 units	Normal vs. 10%	-3.500	No	ns
(Figure 75C)	Normal vs. 20%	-9.000	No	ns
	Normal vs. 30%	-16.830	Yes	**
MHCII surface area	Normal vs. 10%	-6.167	No	ns
(Figure 79A)	Normal vs. 20%	-15.08	Yes	**
	Normal vs. 30%	-23.67	Yes	****
MHCII volume	Normal vs. 10%	-6.000	No	ns
(Figure 79B)	Normal vs. 20%	-15.00	Yes	**
	Normal vs. 30%	-24.00	Yes	****
MHCII units	Normal vs. 10%	-6.250	No	ns
(Figure 79C)	Normal vs. 20%	-17.29	Yes	***
	Normal vs. 30%	-18.33	Yes	***

	Unpaired t test with Welch's correction				
Parameter	**P value**	**P value summary**	**Significant? (p<0.05)**	**One- or two-tailed P value**	**Welch-corrected t, df**
GFAP surface area (Figure 30C)	0.0002	***	Yes	Two-tailed	t=4.005 df=48
Collagen IV surface area - grouped (Figure 40C)	0.0003	***	Yes	Two-tailed	t=3.863 df=48
Collagen IV volume - grouped (Figure 42B)	< 0.0001	****	Yes	Two-tailed	t=6.277 df=40.62
Mean BV diameter - grouped (Figure 44B)	< 0.0001	****	Yes	Two-tailed	t=21.43 df=4563
Branching (Figure 48B)	0.0607	ns	No	Two-tailed	t=2.056 df=12.86
Vessel luminance (SD) - grouped (Figure 52B)	< 0.0001	****	Yes	Two-tailed	t=5.090 df=107.8
CD31 surface area (Figure 65C)	0.0094	**	Yes	Two-tailed	t=2.849 df=21.89
Collagen IV surface area - grouped (Figure 66A)	0.0406	*	Yes	Two-tailed	t=2.176 df=21.90
CD31 surface area - grouped (Figure 66B)	0.0498	*	Yes	Two-tailed	t=1.845 df=20.25
Colocalization (Figure 66C)	0.3749	ns	No	Two-tailed	t=0.4303 df=18.41
Colocalization ratio collagen IV (Figure 69C)	0.0021	**	Yes	Two-tailed	t=3.605 df=17.45
Colocalization ratio CD31 (Figure 69C)	0.0006	***	Yes	Two-tailed	t=4.138 df=18.86
Collagen IV area (Figure 87A)	<0.0001	****	Yes	Two-tailed	t=4.638 df=28
Collagen IV volume (Figure 87A)	0.0020	**	Yes	Two-tailed	t=3.408 df=28

	Unpaired t test with Welch's correction				
Parameter	**P value**	**P value summary**	**Significant? (p<0.05)**	**One- or two-tailed P value**	**Welch-corrected t, df**
Collagen IV area - MHCII-rich (Figure 87B)	0.0003	***	Yes	Two-tailed	t=4.138 df=28
Collagen IV volume - MHCII-rich (Figure 87B)	0.0031	**	Yes	Two-tailed	t=3.235 df=28
Collagen IV area - GFAP-rich (Figure 87C)	0.4266	ns	No	Two-tailed	t=0.8068 df=28
Collagen IV volume - GFAP-rich (Figure 87C)	0.0917	ns	No	Two-tailed	t=1.746 df=28
Vessel diameters - MHCII-rich (Figure 87D)	0.0917	ns	No	Two-tailed	t=1.746 df=28
Vessel diameters - GFAP-rich (Figure 87D)	0.0103	*	Yes	Two-tailed	t=2.749 df=28
Collagen IV area - MHCII- vs. GFAP-rich (Figure 88A)	0.6272	ns	No	Two-tailed	t=0.4890 df=46
Collagen IV volume - MHCII- vs. GFAP (Figure 88B)	0.9340	ns	No	Two-tailed	t=0.0833 df=46
Vessel diameters - MHCII- vs. GFAP-rich (Figure 88C)	0.0185	*	Yes	Two-tailed	t=2.443 df=46